Concentration préférentielle de particules inertielles : la structure et la dynamique de clusters

Sholpan Sumbekova

Communauté
UNIVERSITÉ Grenoble Alpes

THÈSE

Pour obtenir le grade de

DOCTEUR DE LA COMMUNAUTÉ UNIVERSITÉ GRENOBLE ALPES

Spécialité : **Mécanique des fluides, Energétiques, Procèdes**

Arrêté ministériel : 25 mai 2016

Présentée par

Sholpan Sumbekova

Thèse dirigée par **Alain Cartellier** et
codirigée par **Mickael Bourgoin**

préparée au sein du **Laboratoire des Ecoulements Géophysiques et Industriels**
dans **l'École Doctorale I-MEP 2**

Clustering of inertial sub-Kolmogorov particles: Structure of clusters and their dynamics

Thèse soutenue publiquement le **15 Décembre 2016**
devant le jury composé de :

Mr Christophe Baudet
Professeur des Universités, Université Grenoble Alpes, President
Mme Véronique Roig
Professeur, Institut de Mécanique des Fluides de Toulouse, Rapporteur
Mr Romain Monchaux
Professeur, École Nationale Supérieure de Techniques Avancées, Paris Tech Université, Rapporteur
Mr Alain Cartellier
Directeur de Recherche au CNRS, directeur de thèse
Mr Mickael Bourgoin
Directeur de Recherche au CNRS, co-directeur de thèse
Mr Christos Vassilicos
Professeur Étranger, Imperial College London, Examinateur
Mr Alberto Aliseda
Professeur Étranger, University of Washington, Examinateur

"*Begin at the beginning," the King said, very gravely, "and go on till you come to the end: then stop."*

"*It would be so nice if something made sense for a change"*

"*Take care of the sense, and the sounds will take care of themselves"*

Charles Lutwidge Dodgson, Alice in Wonderland

Acknowledgements

This work would have not been possible to achieve without the help and support of many people. First of all, I would like to thank the reviewers and examinators of this thesis for being very understanding and signing up for a 200 page read. Not everyone wants to be a reviewer, and a special thanks is for reviewers Romain Monchaux and Véronique Roig for revising this work carefully.

Second of all, I would like to acknowledge the technicians of LEGI who were there when I most needed their help, and most importantly, who tried to reduce the delay in their work to a minimum. This is a very important factor to consider when one works in the experimental science. Without the help of Stephane, Joseph, Vincent, Tristan and Laure, not many things would have been achieved during my thesis.

Next, a "grand merci" to my PhD supervisors: Alain Cartellier and Mickael Bourgoin. I would like to thank you for the patience and persistence you have given to this work, for the discussions that we have, even during the time when you have been at the conferences, at home during the weekend or at work during a jour ferie. Your dedication and engagement made a lot of things possible during this thesis. The results we obtained would have not been there if you were not in my team. I truly enjoyed working with you as there was a lot of problem-solving involved and fruitful discussions.

The big part of the thesis is the amount of support you get from other people in your working environment. I would like to thank my friends: Diego, Amie, Isabel, Antoine, Quentin, Chakry, Prasanta, Markku, Shrey, Jade, Julian, Keshav, Cruz, Jean-Bastien and Yves for passing a great time together during the last 3 years. During the times when nothing seemed to be working and during the times when we celebrated the submission of important works. Not to forget, I would like to thank all the people who work in LEGI for showing their kindness and understanding.

Furthermore, I would like to thank my family for making me the person I am and supporting me a lot during my studies. Last but not least, I want to thank you to Adam, my greatest friend and favourite companion. I doubt I would have made it to this point of writing acknowledgements without you, your constant support and care (cooking and doing dishes included). I am very lucky to have you, guys, in my life.

I think one more thing that I have to thank is the chance. I have found this PhD entirely by chance, and I think I was quite lucky enough to meet, work and achieve results with some truly great people during the last 3 years.

Contents

Chapter 1

Introduction

1.1 Origins of preferential concentration

Turbulent flows laden with inertial particles are very common in industrial applications and nature. Some examples of such flows would be rain droplets, dispersion of pollutants in the atmosphere, sprays that are used to clean computers, marine snow which is an accumulated organic matter falling from upper water level to the deep ocean, sedimentation of sand in rivers, planetesimals which are huge grains of cosmic dust traveling in the cosmic gas that collide and form new planets. Some of the examples of such flows are shown in fig.1.1.

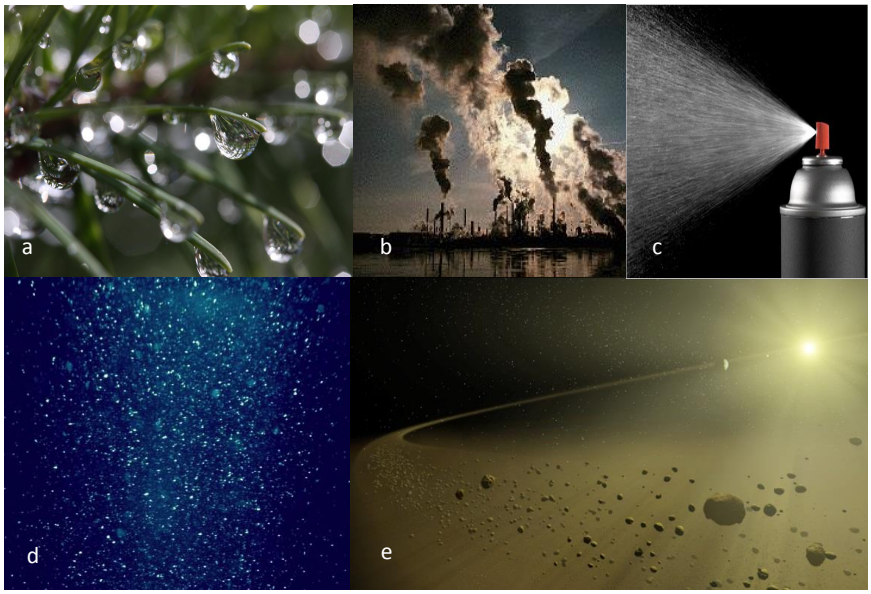

FIGURE 1.1: Examples of flows with inertial particles: (a) rain droplets, (b) aerosol pollutants, (c) cleaning spray, (d) marine snow and (e) planetestimals

In these examples, a flow consist of two-phases: the carrier fluid and seeded particles which are denser than the carrying fluid. Due to significant differences in densities, particles no longer follow the flow but lag behind it. Also, due to having a non-negligible inertia and interaction with the flow structures, the particle field is not homogeneous. In all of these examples clustering plays an important role as a catalysis of important physical processes to follow. The initially random field of water droplets clustering together will result in the rain formation. Clustering serves an important role promoting the collision of particles which is crucial, for example, in combustion chambers to increase the efficiency of the fuel intake.

Figure 1.2 shows that how initially homogeneous particle field changes its homogeneity with increasing inertia. This phenomenon is commonly known as "clustering" or "preferential concentration". The regions of high concentration of particles best known as ***clusters*** and low concentration of particles best known as ***voids*** can be clearly identified.

Another problem that is related to clustering of inertial particles is the question

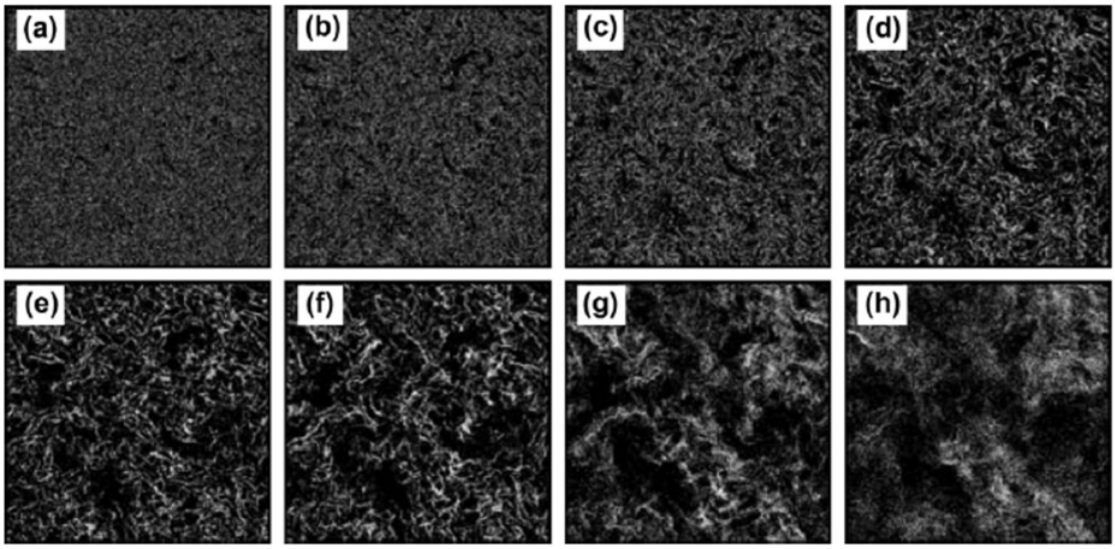

FIGURE 1.2: Simulation from Yoshimoto & Goto [78]: (a) St = 0.05, (b) 0.1, (c) 0.2, (d) 0.5, (e) 1, (f) 2, (g) 5 and (h) 10

of the settling velocity. The questions as to how the settling velocity of inertial particles i.e. their dynamics change in the presence of the turbulence still remain unanswered. The distinct feature of inertial particles not following the carrier flow exactly results in significant differences between the dynamics of the flow and inertial particles. However, the interaction between the two can not be neglected.

Empirical models for clustering and settling of inertial particles are also difficult to develop as both processes involve many ingredients whose specific role has not

been clearly identified yet: particles inertia (itself related to their size and density), turbulence intensity, gravitational settling, global seeding concentration, etc.

In this context, the present thesis reports a systematic experimental exploration of preferential concentration and settling of inertial particles as several control parameters known to influence it are varied.

Chapter 2

Bibliography

2.0.1 Equations of motion of the inertial particle

The dynamics of turbulent flows with inertial particles remains an open problem which has been tackled by both numerical and experimental studies. The very early ideas on formulating the equation of motion of the inertial particle was suggested by Basset [5], Boussinesq [13] and Oseen [57] after investigating the motion of the sphere under gravity in a fluid at rest at low Re numbers.

However, the final model of the equation of motion of the particle following Stokes regime at low Re number was given by Maxey & Riley [44] and Gatignol [30] giving us the equation of motion of particle in a flow:

$$m_p\frac{d\vec{v}}{dt} = 3\pi\mu_f d_p(\vec{u}-\vec{v})+\frac{1}{2}m_f\frac{d(\vec{u}-\vec{v})}{dt}+m_f\frac{D\vec{u}}{Dt}+\frac{3}{2}{d_p}^2\sqrt{\pi\rho_f\mu_f}\int_{-\infty}^{t}\frac{d(\vec{u}-\vec{v})}{dt}\frac{d\tau}{\sqrt{t-\tau}}+(m_p-m_f)\vec{g} \tag{2.1}$$

where $\vec{v}$ is a particle velocity, $\vec{u}$ is a velocity field of unperturbed carrier flow, d_p is a diameter of a particle, $m_f = \rho_f\pi\frac{d_p^3}{6}$ is a mass of the fluid transferred by the particle and μ_f is a dynamic viscosity of the carrier fluid, ρ_p and ρ_f is corresponding densities of the particle and fluid. The terms of the right-hand side of the equation are:

i) Stokes drag force (due to the differences in velocities of particles and fluids)

ii) force exerted by the displayed fluid

iii) pressure gradient term, which is equivalent to the fluid particle acceleration acting at the particle center

iv) history term taking into account the previous motion of particle up to time t

v) Archimedes or buoyancy force for the weight of the particle

Evidently, the equation 2.1 is valid for vanishing particle's Reynolds number $Re_p = d_p \frac{|\vec{v}-\vec{u}|}{\nu} \ll 1$ where $\vec{u}$ is a velocity of the fluid at the particle position and $\vec{v}$ is a velocity of the particle, supposing a Stokes flow around the particle due to mismatch of the velocities of the fluid and particle, and also valid for particles with a size smaller than smallest lengthscales of the flow. Hence, this *point particle model* is the most used analytical expression for describing the particle-fluid interaction.

Simplifying terms of the equation 2.1 on the right hand side [69], many studies assume that the only dominant force on the particle is a drag force caused by the relative motion between the particle and the flow, giving:

$$\frac{d\vec{v}}{dt} = \frac{1}{\tau_p}(\vec{u} - \vec{v}) \tag{2.2}$$

Particle inertia is then described by the single non-dimensional parameter St number which is the ratio between particle response time and a typical flow timescale that quantifies particles inertia. More about an influence of particle inertia on the motion of particles in the turbulent flows and as a relevant control parameters will be discussed in the section 2.1.1.

2.1 Control parameters

The modelling of clustering does not only depend on the particles inertia represented by the St number, it is also greatly affected by the presence of other parameters which impact different physical processes. For instance, the role of turbulence is characterised by the Re number of the flow, collective effects that are respresented by the volume fraction ϕ_v and gravity influence given by the Ro number are of a particular importance and will be further discussed in this section.

2.1.1 Stokes number/Particles inertia

Inertia is generally associated to the particle Stokes number $St = \frac{\tau_p}{\tau_\eta}$, the ratio between the particle viscous relaxation time τ_p and the dissipation time of the carrying turbulence $\tau_\eta = \sqrt{\frac{\nu}{\epsilon}}$ (where ν is the fluid's kinematic viscosity and ϵ is the turbulent energy dissipation rate per unit mass). For small particles (with diameter d_p much smaller than the dissipation scale of the flow $\eta = (\nu^3/\epsilon)^{1/4}$, the Stokes number can be simply related to the particle to fluid density ratio $\Gamma = \frac{\rho_p}{\rho_f}$ and to the ratio Φ between the particle diameter d_p and the dissipation scale η as $St = \frac{\Phi^2}{36}(1 + 2\Gamma)$.

The Stokes number therefore combines into one single parameter the joint influence of particle size and density on its inertia. Note that this is a strong hypothesis, which as shown by several recent experiments and simulations, does not apply to situations where particles are significantly larger than the dissipation scale [62, 61, 75, 41, 36, 26, 21].

2.1.2 Reynolds number/Turbulence intensity

Turbulence intensity is mostly associated to the Reynolds number of the carrier flow $Re = \frac{u\prime L}{\nu}$ (with $u\prime$ and L respectively the standard deviation and the correlation length of the velocity fluctuations). In the present work we will use the Re_λ number which is defined as:

$$R_\lambda = \frac{u\prime\lambda}{\nu}. \tag{2.3}$$

where λ is the Taylor-scale of the flow.

2.1.3 Rouse number/Gravitational settling

Gravitational settling is primarily controlled by the density ratio $\Gamma = \rho_p/\rho_f$ and the particle size. The question is however much subtler when dealing with settling in a turbulent background. Gravitational settling modifies the way particles interact with the background turbulence (by promoting for instance crossing trajectories effects [18] or preferential sweeping effects [43]), what in turn may impact the settling rate of the particles as well as their clustering properties. Note that, in addition to the Stokes number, an extra parameter then appears defined as the ratio of the terminal velocity to some characteristic turbulent velocity [76, 31]. The Γ parameter alone may not be sufficient enought o describe the role of gravity, and in turbulence Ro number is usually used. It is defined as:

$$Ro = \frac{U_{St}}{u\prime} \tag{2.4}$$

where U_{St} is the Stokes velocity of the particle and $u\prime$ is the standard deviation of the turbulent fluctuations.

2.1.4 Volume fraction/Collective effects

Global seeding concentration is characterized by the volume fraction ϕ_v of particles. Volume fraction is known to impact particles/turbulence interaction at various levels. In dilute situations (typically $\phi_v < 10^{-5}$, it is mostly the turbulence that affects

the particles dynamics with no global modification of the hydrodynamic properties of the flow due to the presence of particles (although subtle collective effects, possible reminiscent of local modification of hydrodynamics within the dense clustered regions, have been reported even in such dilute conditions [1]), a regime called *one-way coupling*.

At higher volume fractions *two-way coupling* effects emerge, with a modification of the carrier turbulence due to the presence of the particles, although no clear answer has been found yet to the question of when and how turbulence is reduced or enhanced by the presence of particles. At even higher seeding concentration *four-way* coupling mechanisms with additional particle-particle (collisions) interactions appear. The loadings considered in the present study are $\phi_v < 10^{-5}$, so that no significant modification of the turbulence in the carrier phase is expected.

Other parameters, such as polydispersity (both in particles size and/or density), particle's shape anisotropy, etc. can also influence clustering properties, but will not be addressed here.

As previously mentioned, although clear trends of clustering with these parameters have been evidenced in experiments and simulations, the exact impact of each of these parameters on preferential concentration (and its specific consequences) is not clearly understood yet. For instance, available numerical studies (mostly carried in the limit of pointwise particles) and the few available experiments, indicate that the Stokes number directly influences the clustering, with a maximum degree of clustering for particles with $St = \mathcal{O}(1)$. Existing results also suggest that clustering level increases with increasing Reynolds number of the carrier flow [55]. Similarly it was recently shown that global seeding concentration has a non-trivial effect on clustering [47], with a non-linear dependency of the over-concentration within clusters with the global concentration (even in situations of one-way coupling, where no global modulation of the carrier turbulence is expected due to the presence of the particles). Aliseda *et al.* [1] have also shown that gravitational settling is non-trivially connected to the preferential concentration phenomenon and to the global volume fraction and can be collectively enhanced within clusters. A better insight into such behaviors is now required in order to clearly disentangle the role of Stokes number, Reynolds number and volume fraction and eventually start paving the way towards possible strategies to develop predicting and accurate models of preferential concentration.

One of the difficulties to clearly characterize the specific role of these parameters relies in the practical complexity to disentangle unambiguously and systematically their specific contribution in actual experiments. For instance, for a given class

of particles (fixed size and density), varying the Reynolds number of the carrier flow (for instance by reducing the viscosity ν of the fluid or increasing the energy injection rate ϵ) also results in a change of the particle Stokes number (as the dissipation scale $\eta = (\nu^3/\epsilon)^{1/4}$, and hence the ratio $\Phi = d/\eta$ also varies). Similarly, regarding the volume fraction ϕ_v, even if it is maintained low (typically $\phi_v < 10^{-5}$) so that only *one-way coupling* effects are expected (meaning that the turbulence transports the particles without being modified by it) the number density within clusters may be larger, due precisely to preferential concentration, inducing subtler particle/turbulence and particle/particle interactions, which may in turn result in non-trivial collective dynamics of particles and of clusters of particles out of reach of usual point particle models.

2.2 Mechanisms of Clustering

Several mechanisms can be invoked to explain clustering. Some are very general, not intuitively related to the structure of turbulence, some on the contrary are very dinstinctively explaining the interaction between particle and underlying turbulence.

2.2.1 Dissipative dynamical system approach

Let us consider a dynamical system characterised by a state vector $\vec{q} = (q_1, q_2, ..., q_n)$ of a given state Ω. For a system to be dynamical, the state vector can evolve in time following the equation:

$$\frac{d\vec{q}}{dt} = \vec{f}(\vec{q}) \tag{2.5}$$

given that $\vec{q} \in \Omega$ and with the initial condition $\vec{q}(t = 0) = \vec{q_0}$ and where f is an evolution function called "flow". Hence, a probability density function of $\vec{q}$ is defined as $\rho(\vec{q}, t = 0)$ and should be satisfying $\int_\Omega \rho(\vec{q}, t = 0)d\vec{q} = 1$. The $\rho(\vec{q}, t = 0)d\vec{q}$ represents the probability to find the system around the state $\vec{q}$ at time $t = 0$. Introducing a linear perturbation around the density of states $\rho(\vec{q}, t)$ at $t > 0$ results in the following equation:

$$\frac{\mathrm{D}\rho}{\mathrm{D}t} = \frac{\partial\rho}{\partial t} + \frac{\partial\rho}{\partial\vec{q}} \cdot \frac{\partial\vec{q}}{\partial t} = \partial_t\rho + \vec{f} \cdot \vec{\bigtriangledown}\rho = -\rho\vec{\bigtriangledown} \cdot \vec{f} \tag{2.6}$$

which turns out to be a continuity equation giving that at $t > 0$, $\rho(\vec{q}, t)$ is a probability density function satisfying $\int_\Omega \rho(\vec{q}, t)d\vec{q} = 1$. Two important results can be concluded from the value of $\vec{\bigtriangledown} \cdot \vec{f}$

- if $\vec{\nabla} \cdot \vec{f} = 0$, then the equation 2.6 simply becomes $\frac{\mathrm{D}\rho}{\mathrm{D}t} = 0$ which is a continuity equation for an incompressible flow $\vec{f}$ meaning that the density of states in space is preserved. Dynamical systems $\vec{f}$ with the property $\vec{\nabla} \cdot \vec{f} = 0$ are called *conservative*.

- if $\vec{\nabla} \cdot \vec{f} < 0$, then $\frac{\mathrm{D}\rho}{\mathrm{D}t} > 0$. Thus the density along the Lagrangian trajectories in the state space grows. Since the total integral of ρ over the whole state space is 1, consequently the density of the states should decrease in some regions. Such an evolution of states would yield the presence of highly dense regions and depleted regions at the same time. Such a dynamical system possessing a property of $\vec{\nabla} \cdot \vec{f} < 0$ is called *dissipative*. Contraction of such a state space would give a rise to *attractors* towards which system will try to organise itself.

Now let's apply this state space analysis on the dynamics of the flows with particles:

- on the one hand, for Lagrangian tracers the state of the dynamic system is simply defined as $\vec{q} = \vec{x}$ where $\vec{x}$ is a position of the fluid particle. Given that the particles follow the carrier flow and $\vec{u} = \vec{v}$, and $derivative\vec{x} = \vec{u}$. For single-phase incompressible flows the following $\vec{\nabla} \cdot \vec{u} = 0$, hence the dynamical system f is conservative. This results in homogeneity of particles distribution i.e. an initially uniform distribution of particles remains uniform. To sum up lagrangian fluid tracers in incompressible flows do not form clusters.

- on the other hand, the dynamical system for inertial particles is dissipative. This follows from the minimal Stokesian model given by eq 2.2 where dynamics of particles is strongly coupled to the dynamics of the fluid by the Stokes drag. In this case we can define the dynamical system as : $\vec{q} = f(\vec{q_1}, \vec{q_2}) = (\vec{x}, \vec{v})$ and the f function being equal to $\vec{f} = (f_1, f_2) = (\vec{v}, {\tau_p}^{-1}(\vec{u} - \vec{v}))$
  Hence, if taking $\vec{\nabla} \cdot \vec{f} = \partial_{q_1} f_1 + \partial_{q_2} f_2 = -d({\tau_p}^{-1}) < 0$ where d is a dimension of physical space. Thus, the dynamical system is no longer conservative, leading to eventual contraction of physical space and emerging of clusters. Furthermore, the clustering properties are expected to depend strongly on the structure of the carrying flow and the mechanism of interaction with the inertial particles (see Mehlig and Wilkinson, 2004, Mehlig et al. 2005, Bec et al 2007). The centrifugal mechanism (described in the next section), generally invoked to interpret preferential concentration, is such an example.

2.2.2 Centrifugation mechanism

Now, let us examine closely eq. 2.2. Let's define $\frac{d\vec{u}}{dt} = \vec{a}$ and assume that $\frac{d\vec{v}}{dt}$ is locally the same as $\frac{d\vec{u}}{dt}$ in the limit of vanishing particles' Stokes number and Rouse number ($St = \frac{\tau_p}{\tau_\eta} << 1$). Hence eq. 2.2 becomes:

$$\vec{v} = \vec{u} - \tau_p \vec{a} \tag{2.7}$$

Next step we are going to take divergence of the eq. 2.7, giving:

$$\vec{\bigtriangledown} \cdot \vec{v} = -\tau_p \vec{\bigtriangledown} \cdot \vec{a} = -\tau_p \vec{\bigtriangledown} \cdot (\vec{u} \cdot \vec{\bigtriangledown} \vec{u}) = -\tau_p (S_{ij} S_{ij} - 4 R_{ij} R_{ij}) \tag{2.8}$$

where $S_{ij} = \frac{1}{2}(\partial_j u_i + \partial_i u_j)$ is the flow strain tensor, and $R_{ij} = \frac{1}{2}(\partial_j u_i - \partial_i u_j)$ is the vorticity tensor. Now in the case of heavy dense particles $\vec{\bigtriangledown} \cdot \vec{v} < 0$ and the $S_{ij} > R_{ij}$ meaning that the heavy dense inertial particles tend to cluster in the regions of high strain and low vorticity which is consistent with the argument of centrifugal expulsion of heavy particles from the vortex cores and their preferential accumulation in the regions of high strain.

However, in the case of light particles we need to include added mass term $\beta \frac{D\vec{u}}{Dt}$ in the equation of motion of particles with $\beta = \frac{3\rho_f}{\rho_f + 2\rho_p}$. Consequently, eq. 2.8 evolves to:

$$\vec{v} = \vec{u} - \tau_p (1 - \beta) \vec{a} \tag{2.9}$$

and the divergence of $\vec{v}$ evolves to:

$$\vec{\bigtriangledown} \cdot \vec{v} = -(1 - \beta) \tau_p (S_{ij} S_{ij} - 4 R_{ij} R_{ij}) \tag{2.10}$$

For dense particles $\beta < 1$ and $\vec{\bigtriangledown} \cdot \vec{v} < 0$ which is consistent with our previous argument for clustering of heavy dense particles. Furthermore, for light particles $\beta > 1$ and $\vec{\bigtriangledown} \cdot \vec{v} > 0$ and hence particles accumulate at low strain and high vorticity regions i.e. they concentrate preferentially in the rotating regions of the flow.

This centrifugation mechanism proposed by Maxey [43] is a signature of small scales as it assumes a continuous description of particle velocity field and is based on the compressibility of "meso-scale ensemble of particles". It is nothing but the analytical expression of the classical view of particles being expelled from small scale turbulent eddies, as illustrated by the following studies.

Eaton and Fessler [24] covered the range of studies focusing on the preferential concentration of the particles and their response to flow structures. The explanation

they proposed is following. Heavy particles can not follow the fluid path (see Figure 2.1). Hence, they get centrifuged out of the vortex core, cross the paths of fluid streamlines and finish off by accumulating in the regions of high strain and low vorticity. Thus, these regions tend to have higher concentration of particles and vortex cores tend to have low concentration of particles. This correlation between prefer-

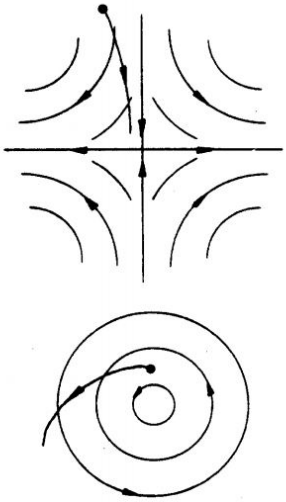

FIGURE 2.1

ential concentration and high strain & low vorticity has been extensively studied through simulations by Squires and Eaton [66], Wang and Maxey [73], Vaillancourt et al [27]. It is worth noting that this centrifugation mechanism is a signature of small scales. The DNS of monodisperse inertial particle two-phase flows [73, 24, 8, 9] has been consistently reporting the maximum dependence of clustering at $St = 1$, invoking a better resonance between particle response time and smallest scales of turbulence.

2.2.3 Sweep Stick Mechanism

Goto & Vassilicos [15] suggested a new mechanism responsible for clustering of inertial particles which is compatible with multiscale regime [32]. Next, Coleman & Vassilicos [17] did a detailed comparison with 3D simulation. Their numerical study shows that for particles with Stokes number larger than unity, clustering is primarily driven by the "sweep-stick" mechanism [17] by which particles tend to preferentially sample the zero-acceleration points of the carrier flow.
The "sweep-stick" mechanism could be explained considering a linearised Maxey-Riley equation (see eq.2.7):

$$\vec{v} = \vec{u} - \tau_p \vec{a} \tag{2.11}$$

Whenever $\vec{a} = \vec{0}$, $\vec{v} = \vec{u}$ that follows from eq.2.11. The zero-acceleration points of the flow are swept with the flow, inertial particles "stick" to these zero-acceleration poins of the flow with the velocity $\vec{u}$. Whereas the particles on the fluid non-zero acceleration points move away from the zero-acceleration points with relative velocity $\tau_p\vec{a}$. Here, the degree of "stickiness " is defined by the characteristic time of the particle τ_p.

It is important to note that, contrary to the centrifugation mechanism which is indeed *clustering* mechanism, the "sweep-stick" is a preferential *sampling* mechanism, and clustering only emerges as a consequence of the low-acceleration points in a turbulent flow organizing in multi-scale clusters [32] what is a purely hydrodynamic property intrinsic to single phase turbulence.

In this framework, clustering properties are driven by turbulence characteristics across scales, while particle properties only influence the ability of particles to preferentially stick to the aforementioned zero-acceleration points. The main constraint for particles to efficiently stick to zero-acceleration points is that their viscous relaxation time τ_p be small compared to the life-time of those zero-acceleration points. These points are known from numerical simulations to be very persistent [32], and this can be related to the experimental finding that the correlation time of the acceleration magnitude of tracer particles is of the order of the integral time-scale T_{int} of the carrier turbulence [50].

As a consequence, as long as $\tau_p \ll T_{int}$ (or equivalently $St_L = \frac{\tau_p}{\tau_L} << 1$, where St_L is the Stokes number based on the integral time scale rather than dissipation time scale of the flow), particles will respond much faster than the typical time of evolution of ZAP, hence having sufficient time to efficiently stick to them, and thus, no significant dependency of clustering by the "sweep-stick" mechanism on the Stokes number is expected. A significant decrease of the efficiency of the mechanism will only occur for particles with response times approaching the integral time scale of the flow [32].

2.2.4 Conclusion

It is important to note that preferential concentration of the particles due to explusion from vortex cores and their accumulation in the regions of high strain and low vorticity is a signature of small scales. Thus, this clustering of small scales reaches its maximum for $St = 1$. This centrifugation mechanism fails to explain the preferential concentration of the particles when St exceeds unity.
"Sweep-stick" mechanism could possibly explain both clustering at St above and

below unity. According to the simulations of [17], all particles preferentially sample zero-acceleration points. When $St < 1$ particles velocity is the same as the fluid and the particles are swept with the flow at a constant velocity $\vec{u}$. Hence, the centrifugation mechanism is very well satisfied. However, at $St > 1$ the particles stick to the zero-acceleration points, and at this level the clustering occurs as a consequence of preferential sampling of the zero-acceleration points.

2.3 Settling Velocity

The setting velocity of small dense (or light) particles embedded in a turbulent field has been observed in various flow conditions to differ from their corresponding terminal velocity, the latter being defined for an isolated particle in a still fluid. Let us briefly review available contributions mostly for homogeneous isotropic turbulent flow fields, either from experiments (see Table 2.1) or from simulations (see Table 2.2).

Experiments in an oscillating grid turbulence show that droplets or solid particles exhibit either an increase or a decrease in their settling velocity depending on the Rouse number (see Nielsen [54] and the data reported therein). Retardation as well as enhancement has also been observed by Zhou and Cheng [80] on solid particles in a oscillating grid experiment, with settling relative velocities down to 0.8 times and up to 1.2 times the terminal velocity. Hindering of the fall velocity has also been observed for particles settling in a vertically oscillated container by Ho (cited in Nielsen [54]), by Tunstall and Houghton [70] and by Shöneborn [65]. The settling velocity of sub-Kolmogorov water drops in air submitted to a grid turbulence was found to increase for non-vanishing Stokes numbers in a study conducted by Aliseda et al. [1]). Similar trends were observed for solid particles in air by Yang and Shy [77]. In addition, for water drops in air, both an increase or a decrease have been observed in the recent experiments of Good at al [31]. Let us also mention experiments with light drops in water that exhibit either an increase or a decrease in their rise velocity depending on both Stokes and Rouse numbers from the study of Friedman and Katz [28].

Some theoretical results and numerous simulations (see Table 2.2) of inertial point particles in HIT (Homogeneous Isotropic Turbulence) or in kinematics fields mimicking turbulent flows are available. The simulations differ in the way DNS are implemented (forcing) and particle dynamics is accounted for (frozen field, one-way or two-way coupling, linear or nonlinear drag...). Yet they all predict an increase

Authors	Flow conditions	Dispersed phase	Behaviour of $\Delta V = V - V_{St}$
Ho 1964	container filled with water shaken along the vertical	particles characteristics not detailed, probably solid	the settling velocity scaled by the terminal velocity monotonously decreases with the ratio of acceleration of the tank over gravity.
Nielsen (1993, 1994)	oscillating grid turbulence	2-6 mm droplets in air and sand particles settling in a liquid phase.	-hindering at large Ro, V_p/V_{St} not varying much with Ro in the range of $0.3 - 4$ - enhancement at $Ro < 0.3$. The settling velocity V_p evolves as $\sim 0.2U\prime$
Zhou and Cheng 2009	oscillating grid turbulence	polystyrene particles $\sim$ 3 and 8 mm in size. Density ratio 1.07.	enhancement or hindering observed over a large range of St (0.001 to 1) and Richardson (10 to 10^4) numbers. The turbulent field not documented.
Friedman and Katz 2002	Experiments in box turbulence in water – weak but non negligible mean flow. The rise velocity is measured as $V_{slip} = V_p - V_{fluid}$	Light diesel fuel droplets, size $3 - 15$ larger than Kolmogorov length η. Presumably very dilute conditions.	- at high turbulent intensity, namely $U\prime/V_{St} > 5$, V_{slip} is larger than V_{St}, and V_{slip} is about $0.25U\prime$ whatever the St in the range $0.25 - 8$, - at lower turbulent intensity, namely $U\prime/V_{St} < 5$, V_{slip}/V_{St} can be larger or smaller than unity.
Aliseda et al. 2002	Experiments in grid turbulence using air at $Re \sim 75$	Polydispersed water droplets with the sizes $D < \eta$ conducted at $\phi_v = 1.5 - 7 \times 10^{-5}$	Velocity enhancement over the whole range of St $(0,01 - 5)$, with a maximum for St in the range $0.8-1.4$. The velocity enhancement increases with volume fraction ϕ_v due cluster dynamics and collective effects.
Yang and Shy 2005	Experiments on falling particles injected in a turbulent air zone generated by fans at $Re_\lambda \sim 75 - 120$	Monodispersed solid spheres with sizes $D < \eta$ at ϕ_v about 10^{-5} (fairly uniform at the entrance of the turbulent region)	Enhanced settling with a maximum at $St \sim 1$. The maximum in ΔV is about $0.13U\prime$.
Good et al. 2014	Experiments in box turbulence using air at $Re \sim 150 - 177$	Polydispersed water droplets at volume fraction ϕ_v of the order of 10^{-6} (not measured)	Enhancement for small St, Ro with maximum $\Delta V/u'$ about 0.22. Hindering observed for $Ro > 0.8$ for $St = 0.75$ and $Ro > 1$ for $St = 1.6$.

TABLE 2.1: Some key experiments addressing the question of the influence of a nearly homogeneous isotropic turbulence on the settling (or) rising velocity of small particles

in the settling velocity for inert ($St \neq 0$) dense particles, with some exceptions discussed below. They all obtain bell shape curves indicating that the enhancement $\Delta V = V - V_{St}$ scaled either by $U\prime$, by the Kolmogorov velocity v_η or by V_{St} first increases with the St number, reaches a maximum for St of order unity and then smoothly decreases down to weak, nearly zero values at large St. The typical magnitude of the maximum in ΔV is about $0.1 - 0.2U\prime$.

Authors	Base Flow	Dispersed phase	Main observations
Wang and Maxey 1993	DNS, $Re_\lambda \sim 20 - 60$. One-way coupling, linear and non linear drag	$\rho_p/\rho_f \sim 1000$. Presumably very dilute conditions	Enhanced settling for St in the range 0.2 to 3.2 and $Ro = 0.25 - 0.4$. The maximum $\Delta V \sim 0.12U\prime$ (or $\Delta V \sim 0.5V_{St}$) is observed at St between 0.5 and 1 (depending on Re_λ). A non-linear drag very slightly reduces the settling speed compared with a linear drag.
Yang and Lei 1998	DNS and LES. $Re_\lambda = 35.7, 65.3$ and 133. One and two-way coupling using non-linear drag assumption.	$\rho_p/\rho_f \sim 1000$. Presumably very dilute conditions	Enhancement predicted for St in the range (0 – 2.5) and Ro in the range (0 – 1.4) for Re_λ between 35 and 133. Maximum enhancement ΔV is of the order of $0.1U\prime$. This maximum arises at $St = 0.8, Ro = 0.5$; $St = 1, Ro = 0.4$ and $St = 1.2, Ro = 0.5$ respectively for $Re_\lambda = 35.7$; 65.3 and 133.

Tanaka et al. 2000	DNS. $Re_\lambda = 20$. One-way and two-way coupling	$\rho_p/\rho_f \sim 1000$. $\phi_v \sim 6 \times 10^{-5}$	Enhancement predicted for St in the range (0.5 – 4). Enhancement is larger when using two-way coupling for which $\Delta V/U\prime$ up to 0.25 compared with one-way coupling where $\Delta V/U\prime$ up to 0.15. The enhancement ΔV is linearly increasing with the local concentration.
Bosse et al. 2006	DNS. $Re_\lambda \sim 24$ to 42. One and two-way coupling, linear drag.	$\rho_p/\rho_f \sim 2000$ to 5000. ϕ_v from 10^{-6} to 10^{-4}.	Enhanced settling with a maximum at $St \sim 0.8$ and $V_{St}/v_\eta = 1$. The maximum ΔV is about $0.11U\prime$ in one way coupling simulations: ΔV increases when using two-way coupling. ΔV also increases with volume fraction and reaches $\Delta V \sim 0.5U\prime$ at $\phi_v = 15 \times 10^{-5}$ (for $St = 1, V_{St}/v_\eta = 1$). If the Re_λ is kept the same, then ΔV linearly growths with the volume fraction ϕ_v. Enhancement becomes weaker if Re_λ decreases at a given loading.

Dejoan and Monchaux 2013	DNS, $Re_\lambda \sim 40$. One-way coupling, linear drag	$Ro = 0 - 1$, $St = 0.36 - 6$	Cluster dimension is about 6η. Enhancement holds for St from 0.36 to 6 and Ro from 0.25 to 1. Maximum ΔV about $0.1U\prime$. But small particles are hindered in low concentration regions. Particle position happens to be correlated with regions of negative fluid velocity and of negative fluid acceleration.
Bec, Homann and Ray 2014	DNS, $Re_\lambda \sim 130$, 290, 460 and $Fr* = \epsilon^{3/4}/(g\nu^{1/4})$ from 0.01 to 2. No coupling, linear drag	St from 0 to 6. Presumably very dilute conditions	Enhancement observed over the whole range of parameters. In the limit $St \to 0$, the gain $\Delta V = (V - V_{St})/V_{St}$ is linear in St and nearly independent from Re and $Fr*$. The maximum enhancement occurs for $St = O(1)$: the abscissa of the maximum increases with $Fr*$ from about $St = 0.1$ to $St = 0.9$. The magnitude of ΔV increases with $Fr*$ and with Re_λ (with a saturation with Re_λ). ΔV is about $0.9V_{St}$ at $Fr* = 2$ and $Re_\lambda \sim 300{-}450$.

Good et al. 2014	DNS, $Re_\lambda \sim 105 - 227$, one-way coupling, linear and non-linear drag,	$\rho_p/\rho_f \sim 877$. Presumably very dilute conditions.	Simulations performed in the range St from 0.1 to 10 and Ro from 0.03 to $\sim$ 1.3. Enhancement only is observed when using a linear drag. Both enhancement and hindering are observed when using non-linear drag.
Rosa et al. 2016	DNS, $Re_\lambda \sim 28$ to 372. One-way coupling, linear and non-linear drag	$\rho_p/\rho_f \sim 500 - 10000$. Presumably very dilute conditions. St from 0.01 to 4.0.	Enhancement is observed for all conditions namely St from 0.02 to 1.8 and Ro from 0.06 to 7.3 at $Re_\lambda = 143.7$ (except for two conditions for which ΔV is within the uncertainty). The maximum of ΔV is about $0.14U\prime$ or $0.40V_{St}$. $\frac{\Delta V}{V_{St}}$ increases with Re_λ (for a fixd dissipation) and saturates at large Re_λ. $\frac{\Delta V}{V_{St}}$ increases and then decreases with the parameter $Fr_R = StS_v^2$ where $S_v = \frac{V_{St}}{v_\eta}$. The maximum is located near $Fr_R \approx 1$. Rosa et al. propose a fit of $\frac{\Delta V}{V_{St}}$ varying Fr_R and Re_λ.

TABLE 2.2: Some key simulations addressing the question of the influence of a purely homogeneous isotropic turbulence on the settling (or rising) velocity of small heavy sub-Kolmogorov particles

Among the exceptions, some particle-vortex interaction elementary models (e.g. Nielsen 1993 [54], Maxey 1987 [43], Eames and Gilbertson 2004 [22]) and kinematic simulations (Mei 1994 [46], Fung 1993 [29], Chan and Fung 1999 [14], Stout et al 1995 [67]) predict that, over some range of parameters, a decrease in the settling velocity can indeed occur. To our knowledge, in terms of direct numerical simulations, only the DNS of Good et al.[31] predict the occurrence of a velocity decrease at large Ro numbers when accounting for a non-linear drag law. Rosa et al.[63] repeated the simulations over longer run times (100 integral time scales compared with 10 in Good et al.[31]) using stochastic as well as deterministic forcing schemes. When changing from linear to non linear drag, they observed a very weak effect on the settling rate (1%). Moreover, they do not observe any hindering effect. Only when blocking horizontal particle motion to force quasi-vertical trajectories (that is disabling the preferential sweeping) did they found a reduction. Hence, the claim by Good et al. [31] that a non-linear drag suffices to observe hindering is probably not the correct explanation. From the numerical details provided by Good et al.[31] and by Rosa et al.[63], it is difficult to identify what were the differences between these two simulations, but it seem that (for some reason) particles were not sampling the same flow zones in the two DNS. The huge difference between these simulations remain thus to be clarified.

Besides, the impact of volume concentration is scarcely discussed except notably in the experiments of Aliseda et al. [1] and in the simulations of Bosse et al.[11] who considered two-way coupling. The incidence of the loading is also considered in the model proposed by Zaichik and Alipchenkov [79].

Let us first briefly summarize the main results reported in the literature by considering first the mechanisms proposed for single particles interacting with a turbulent field, and then for dense systems.

2.3.1 Mechanisms involving a particle interacting with the background turbulent field

In terms of mechanisms, most of the proposed explanations start from the interaction of a single dense particle with vortices. In the following, the discussion is organized according to the various scenarii available.

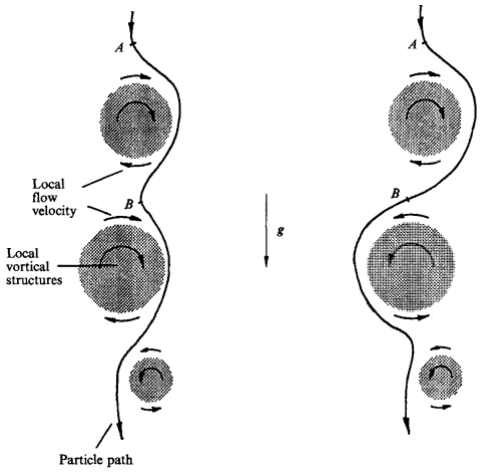

FIGURE 2.2: Sketch of a particle falling through an assembly of vortices from Wang and Maxey [73]

2.3.1.1 Fast tracking between vortices (or preferential sweeping)

A dense particle located in a vortex of a lighter fluid is expelled outside this vortex by centrifugation, mainly because of their inertia (with some exceptions, for example when, as notably discussed by Nielsen [54], the particle is initially located at a precise position within the vortex with horizontal vorticity. These positions are generally unstable as discussed by Maxey [43]. Besides vortex trapping events have a very low probability when considering particles dispersed in a turbulence field. Beside they are neutrally stable). Due to ejection, particles are mainly driven along the edge of vortices, where they acquire (possibly in part) the eddy outer velocity. Accordingly, they accumulate in between eddies i.e. high strain regions. The fast track effect, also called *preferential sweeping*, is the preferential selection of the downward side of eddies by falling particles, which leads to an increase in the settling velocity (Maxey and Corrsin [45], Wang and Maxey [73]). The fact that particles sample mainly the downward side is controlled by both inertia and terminal velocity. Let us discuss these two aspects here below:

- Without inertia, particles will sample equally the space with no effect on their settling velocity. Some amount of inertia is therefore required for ejection to take place. A small enough inertia will also allow the particle to follow (more or less) the outer streamlines of eddies, and thus to pick up their downward side. But if inertia becomes too large, the particle is no longer be entrained by the flow field induced by the nearby eddy. Instead, it will randomly select upward and downward sides, eliminating thus preferential sampling of the downward side (see fig.2.3).

The above-mentioned condition on inertia can be expressed in terms of a St number, but we have no clear quantitative answer. For example, the analysis of the rate of ejection of dense particles outside eddies by Bec and Chetrite [6] indicates that there is no clear cut-off in terms of St number. Indeed, these authors show that the ejection rate is maximum at St close to unity, and that it goes to zero as St when $St \to 0$ and as $St^{-\frac{1}{2}}$ when St becomes large. Hence, any particle with a finite St experiences ejection (although with contrasted ejection rates).

As for the ability to follow more or less the streamlines outside eddies, that is for particles to concentrate in low-vorticity regions (equivalent to small pressure gradient regions) which is the second ingredient of the fast track mechanism, some criteria is expected to hold.

Yet, quantitative results remain scarce. From simulations at $Re_\lambda = 185$, Bec et al.[8] have shown that preferential concentration in low vorticity regions is the driving mechanism up to $St \sim 0.3 - 0.4$. For larger St, the difference between fluid and particle dynamics is mainly due to a filtering effect by the finite particle response time. Similar conclusions were derived from simulations at $Re_\lambda = 139 - 187$ by Coleman and Vassilicos [17] with a St limit about 0.4. These authors also argue that the "sweep-stick" mechanism is expected to play a role in the range $1 < St < \frac{\tau_L}{\tau_\eta}$.

- A similar situation would occur if the settling velocity is fast enough compared to the carrier flow velocity so that the particle trajectory will not be significantly modified during its interaction with an eddy. Using a simplified model based on a fixed array of steady vortices, Maxey and Corrsin [45] show that interactions take place when the settling velocity is less than half the magnitude of the continuous phase velocity field. In other words, in the situation they examined, preferential sampling requires a $Ro = \frac{V_{St}}{U'}$ less than 0.5 to occur.

The combined role of the particle inertia and of its terminal velocity evoked here above can also be seen from the linearized equation of motion of a particle in the limit of small inertia as discussed in Section 2. Qualitatively, according to the preferential sampling scenario presented above, the increase in settling velocity is expected to scale with the characteristics velocities of the underlying turbulent field: both U' and v_η have been used in literature for that purpose.

From the above discussion, the fast track or *preferential sweeping* mechanism is therefore expected to be active:

- for particles with some inertia although no lower limit in Stokes can be defined,

- for Rouse numbers not too large, possible below some limit $Ro_{critical\ fast\ track}$.

These limits are expected to evolve with the characteristics of the turbulent field.

2.3.1.2 Loitering effect (also called "trajectory biasing" by Friedman and Katz) and vortex trapping

Consider a particle falling vertically through an assembly of vortices. That particle will experience up and down fluid motions whose average in space in zero. Yet, the particle will spend more time in upward directed regions than in downward directed regions because its instantaneous drag will be higher in the former case. Hence, the time average of its settling velocity is expected to be less than its terminal velocity, leading to a hindered settling velocity.

This so-called loitering mechanism is expected to be present for particles with

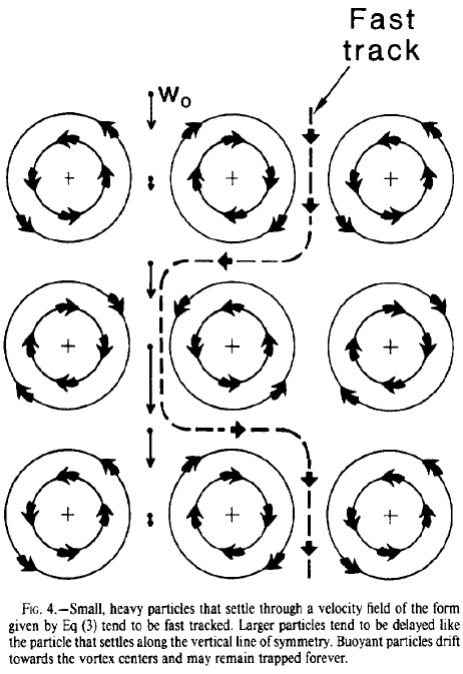

FIG. 4.—Small, heavy particles that settle through a velocity field of the form given by Eq (3) tend to be fast tracked. Larger particles tend to be delayed like the particle that settles along the vertical line of symmetry. Buoyant particles drift towards the vortex centers and may remain trapped forever.

FIGURE 2.3: Sketch of a particle falling through an assembly of vortices (from Nielsen[54])

close to vertical trajectories, that is for particles with enough inertia and/or with large enough settling velocity. Based on some experiments, Nielsen [54] tentatively proposed the criteria $\frac{U\prime}{V_{St}} < 4$ that translates into a $Ro > 0.25$ for loitering effect to occur. Hence, the loitering mechanism is expected to be active:

- for particles with some inertia, i.e. for non vanishing St numbers,

- for large enough Ro numbers, possibly above some limit $Ro_{critical\ loitering}$.

Clearly, loitering and fast tracking have opposite outcomes in terms of settling velocity. From the above scenarii, the preferential sweeping mechanism is expected to extinguish as Ro increases while the loitering effect should be enhanced. Therefore, the loitering effect when it occurs is often dominant. Yet, one expects that a range of Ro exists where both mechanisms are active and compete. This may tentatively be a possible explanation for the maxima observed when plotting the velocity difference versus St curves. Indeed, under gravity, St and Ro are connected so that by increasing the St, one may also cross the boundary in terms of Ro above which loitering becomes active. That boundary is not well known and we will come back to this question in Section 6.4. Note also that in polydispersed conditions, small particles may experience fast tracking while larger one may simultaneously experience loitering. The outcome in terms of the average settling velocity evaluated over all particle sizes will therefore strongly depend on the size distribution.

In the loitering scenario, it is not easy to identify the scales controlling the amplitude of the settling velocity modifications. Most authors simply consider the ratio $\frac{V}{V_{St}}$ to present the data. Nielsen, from a simple calculation, showed that the ratio $\frac{V}{V_{St}}$ should decrease with $\frac{U\prime}{V_{St}}$ and should reach an asymptote for $\frac{U\prime}{V_{St}} = O(10)$. No clear trend with the Ro number arises from the experiments of Murray [51] and of Nielsen [53], where $\frac{V}{V_{St}}$ was comprised between 0.4 and ~ 1. Good et al. considered both $\frac{V}{V_{St}}$ and $\frac{V-V_{St}}{U\prime}$ when presenting the data.

2.3.1.3 Fluctuations in acceleration and non-linear drag

The case of a particle settling through a vertically oscillating flow with an acceleration γ is another interesting situation to consider. Nielsen [53], among others, established that the settling velocity should decrease according to:

$$\frac{V - V_{St}}{V_{St}} \sim -(\frac{\gamma}{g})^2. \tag{2.12}$$

This prediction is in agreement with the settling experiments of Ho [35] in a container shaken vertically as a whole up to $\frac{\gamma}{g} \sim 3.5 - 4$. To derive the above equation, a non-linear drag must be accounted for, as also shown by Hwang [37], Ikeda and Yamasaka [38] and Mei [46]. Indeed, with a linear drag, the drag averaged over an acceleration period becomes zero so that the mean particle motion is unaffected. With a nonlinear law, the drag averaged over a period is no longer zero but it takes

some finite value, and the resulting particle motion is hampered. Although Nielsen estimated that mechanism negligible for sediment transport in coastal flows, the prediction from eq.2.12 can lead to significant hindering of the settling velocity in turbulent flows with strong dissipation.

Indeed, as it will be discussed in Section 6.5.2, the ratio $\frac{\gamma\prime}{g}$ where $\gamma\prime$ denotes the standard-deviation of the fluid acceleration could be as large as 5 in some available laboratory experiments.

These results provide an alternative option in terms of scaling that seems directly applicable to the loitering scenario since, along its trajectory, a particle will undergo fluctuations of the carrier fluid acceleration as well as of the fluid velocity. Indeed, from their simulations, Dejoan and Monchaux [20] noticed a strong correlation between particle velocities and fluid velocity but also between particle velocities and fluid acceleration.

2.3.1.4 Sweep-stick mechanism and settling speed

Although the sweep-stick mechanism has been amply discussed as a process leading to cluster formation, its implication on the settling velocity has not been addressed so far. When introducing gravity, the random sweeping argument still holds, so that particles are expected to stick on points where the fluid acceleration is equal to g. Such a trend is indeed observed in the simulations by Hascoet and Vassilicos [34] provided that the Ro remains small enough. At large Ro, the stick argument is not longer valid (in particular, the relative velocity cannot become very small), and mechanisms are expected to change. Let us also mention that Hascoet and Vassilicos [34] noticed that the clusters formed at high Ro become more columnar in the direction of gravity compared to those formed in absence of gravity. That feature is expected to have an influence on the cluster dynamics, and thus, on the settling speed.

2.3.1.5 Conclusion

As a summary, the trends discussed above and their effects on the settling speed are sketched in the fig.2.4 that represents ΔV versus St, with two behaviors (i.e. enhancement or hindering). This is clearly an over simplistic representation as the St number is not the only independent parameter governing the problem. Here, the fast track scenario is decomposed as preferential sweeping in the limit of low St and filtering effects at larger St, both leading to velocity enhancement. The

loitering effect starts above some Ro number (typically 0.2-0.3): its correspondence in terms of St depends on the turbulence characteristics. When loitering is active, it leads to velocity hindering. When it is absent or weak enough, only velocity enhancement is observed and ΔV is expected to go to zero at large St. The range of action of the sweep-stick mechanism has been indicated although its influence on velocity is unclear. Besides, collective effects, discussed in the next Section, are not represented.

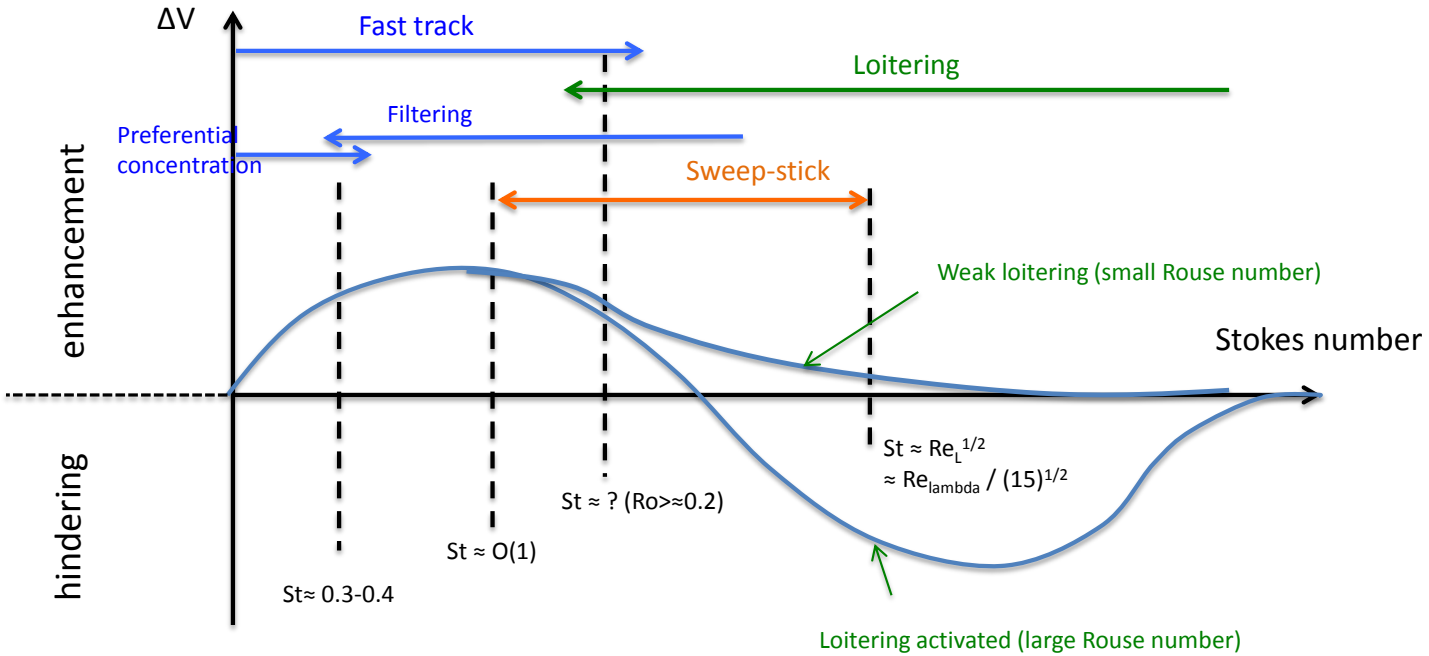

FIGURE 2.4: Sketch of observed variations in the settling (or rising) velocity and associated mechanisms.

2.3.2 Influence of mass loading and collective effects

Increasing the particle concentration can modulate the turbulent field: this effect will not be accounted for here. Indeed, we will restrict the discussion to loading conditions high enough to give rise to collective effects but low enough for the modulation of turbulence to remain negligible or small. For droplets in air, a typical limit for significant turbulent modulation to occur seems to be a mass loading above $8-10\%$, i.e. a volume concentration above about 10^{-4}.

Only a few authors discuss the role of concentration on the settling velocity, the latter being connected to the presence of clusters and their impact on the dynamics of both dispersed an continuous phases. Although it is not clear when the clusters start to appear significant (as it will be seen in Chapter 4 they are already present for $\phi_v = 2 \times 10^{-6}$ when considering water drop in air), their influence on velocity occurs by way of collective effects.

In the experiments of Aliseda et al.[1], these clusters gather all the particle sizes present in the flow (i.e. there is no significant size segregation). Clusters being denser than the average medium, they fall down through the continuous phase, entraining the particles they contain as well as the gas phase. Assuming that these dense regions behave as macro-particles, their fall velocity is expected to be proportional to $C_c \times {l_c}^2$ where C_c is their concentration and l_c their typical spatial dimension, namely:

$$V_{cluster} = \frac{K_T}{18} \times \frac{\rho_p}{\rho_f} \times C_c {l_c}^2 \times \frac{g}{\nu_f} \tag{2.13}$$

where the coefficient K_T depends on the shape of the macro-particle (typically $K_T \sim 0.3-0.5$). The above equation can be rewritten $\frac{V_{cluster}}{V_T} = K_T \times C_c (\frac{l_c}{D})^2$ where D is the particle diameter. A few experimental evidences support this interpretation (Aliseda et al. [1], see also fig.2.5). In a theoretical approach combining RDF modeling and Batchelor theory for suspension sedimentation addition, Zaichik and Alipchenkov [79] recovered a similar result by combining RDF modeling and Batchelor theory for suspension sedimentation. They obtained:

$$\frac{\Delta V}{V_T} \sim b(\chi) C (\frac{l_c}{D})^2. \tag{2.14}$$

where C is the concentration and $b = \frac{3|\chi|}{2(2+\chi)}$ is related to the exponent χ of the Radial Distribution Function. They show that for somewhat inert particles i.e. $0.01 < \mathrm{St} < 0.6$ and for large density ratio ($\frac{\rho_p}{\rho_f} > 103$). For the range of St, the prefactor $b(\chi)$ increases with the St number from 0.04 at $St = 0.01$ up to 1.04 for $St = 0.6$.

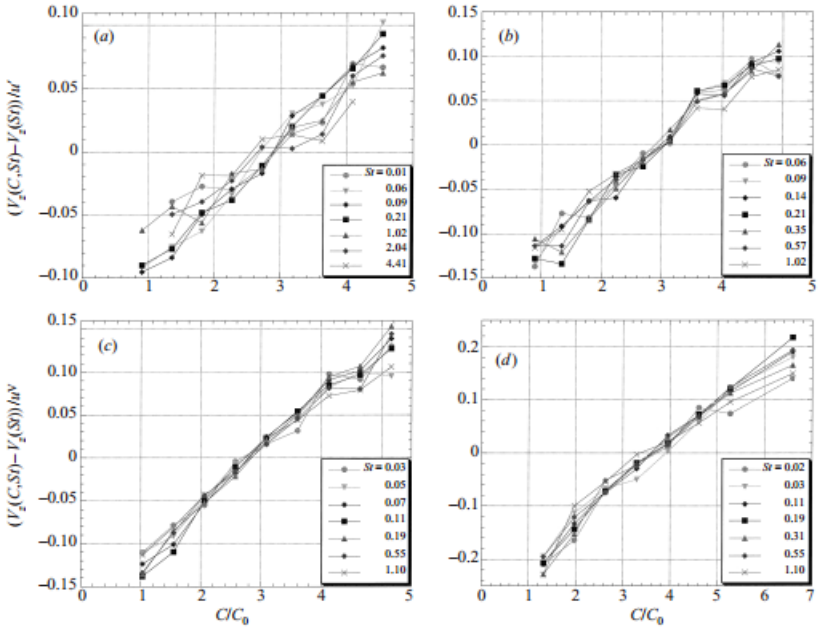

FIGURE 24. Enhancement of the settling velocity as a function of the local concentration. (*a*) $x = 100\,\text{cm}$, $\alpha = 6 \times 10^{-5}$. (*b*) $x = 100\,\text{cm}$, $\alpha = 7.5 \times 10^{-5}$. (*c*) $x = 200\,\text{cm}$, $\alpha = 5 \times 10^{-5}$. (*d*) $x = 200\,\text{cm}$, $\alpha = 7.5 \times 10^{-5}$.

FIGURE 2.5: The velocity of particles conditioned by the local concentration $\frac{C}{C_0}$ as found by Aliseda et al.[1]

In simulations, Wang, Ayala and Grabowski (2011) found that the coupling between preferential concentration and aerodynamic interaction induces a linear increase of the settling velocity with concentration. Boose et al.[12] using two-way coupling also recovered similar behaviors. On one hand, they show that the velocity enhancement increases with volume fraction with a maximum of $\Delta V = \overline{V} - V_{St}$ close to $0.25U\prime$ in the dilute limit and up to about $0.5U\prime$ at $\phi_v = 15 \times 10^{-5}$ (for $St = 1, Ro = 1$). Besides, if the Re_λ is kept fixed, ΔV linearly growths with the volume concentration, a behavior similar to the one predicted by eq.2.14. If Re_λ decreases (in their simulations Re_λ decreased when increasing the loading because of turbulence modulation), then the enhancement also decreases for a given volume loading, showing that the Re_λ is also an important parameter in the magnitude of the velocity modification. They also confirm that dense regions settle more rapidly than less concentrated zones: the increase of velocity with the local concentration is linear as in Aliseda et al. [1] experiments.

In addition, they do show that the continuous phase embedded in dense regions also settles in these zones, indicating that the gas phase is indeed entrained by particles. That effect is clearly captured thanks to two-way coupling, meaning that the flow field in the continuous phase is truly affected by the presence of particles. In

their simulations, Boose et al. [12] were not in position to define clusters, and thus, they did not link these velocities to clusters characteristics.

Moreover, Boose et al.[12] have also varied the Ro for fixed Re_λ, St and volume fraction (the gravitational constant g was adjusted in simulations to independently vary St and Ro numbers). They observe that the velocity enhancement ΔV decreases with the Ro when normalized by the terminal velocity while it increases when normalized by $U\prime$. They also observed some (limited) influence of the density ratio with a 20% increase in ΔV for $\frac{\rho_p}{\rho_f}$ varying from 2000 to 3500.

Overall their simulations under-predict Aliseda et al. [1] measurements while they over-predict those of Yang and Shy [77]. In the former case, a possible recirculation cell is evoked that could bias the data (that aspect will be discussed in Section 6.5.1). Globally, simulations and experiments are in qualitative agreement (including the magnitude of velocity enhancement) but there is no clear explanation of the observed quantitative discrepancies apart for differences in turbulent Re between experiments and simulations.

Dejoan and Monchaux [20] investigated the relation between clusters and settling velocity in a one-way coupling DNS accounting only for the drag force (linear) and gravity in the equation of motion for particles. They first show that the standard deviation of the Voronoï volumes (whose inverse represent the local concentration field) mainly depends on the St number and is weakly sensitive to the Ro number.

In addition, they report a significant size segregation: the fraction of large St particles ($St = 2$ and 6) increases with the local concentration with 40% of these particles present in regions of concentration about 6 times the average loading. On the opposite, particles of the St of the order of 1 are mostly present in regions with a local concentration in the range 0.6 to 2 times the average loading. Again, these results are insensitive to the Ro (from 0 to 1), indicating that the fall velocity has no role on cluster formation and characteristics nor on how particles are distributed (only inertia is at play).

In terms of settling velocity, velocity PDFs are nearly Gaussian in all cases considered i.e. Ro from 0 to 1, St from 0.36 to 6. Enhancement of the average (mean over all particles) settling velocity is observed in all conditions, with a maximum for ΔV about $0.1U\prime$ at $St = O(1)$ and Ro between 0.25 and 0.5. Interestingly, $\Delta V = V(St, Ro, C) - V_{St}$ happens to vary according to the local concentration. Most situations correspond to an enhancement (with values up to $0.2U\prime$) but a few correspond to hindering: the latter arise at low concentrations (below about 0.7-0.8 times the mean loading) whatever St and Ro numbers in the range considered. Hindering becomes more pronounced in void regions, and at large Ro numbers with a

Volume fraction	Density ratio	Turbulent Reynolds number	Stokes number	Rouse number	Size distribution
ϕ_v	$\frac{\rho_p}{\rho_f}$	Re_λ	$St = \frac{\tau_p}{\tau_\eta}$	$Ro = \frac{V_{St}}{U\prime}$	$P(\frac{D}{D_{10}})$

TABLE 2.3: Table of non-dimensional parameters

magnitude up to $0.15U\prime$. Let us note that hindering is also observed for the largest St number (~ 6) and in dense regions ($\frac{C}{C_0} \sim 5$) but the magnitude of ΔV is weak, comparable to their statistical noise, so that these observations at large St number may not be significant.

Going back to void regions, the velocity of particles is positive with respect to the mean velocity, i.e. particles are moving upward in a frame moving with the average settling velocity. Also, by correlating particle position and fluid statistics, Dejoan and Monchaux [20] clearly show that particles tend accumulate in regions where fluid velocities are aligned with gravity: this trend is fully in line with the fast track/preferential sweeping scenario based on particle centrifugation. But they show in addition that particles tend to accumulate in regions where the fluid acceleration is aligned with gravity.

2.4 Analysis of available data

2.4.1 Boundary between enhancement and hindering

According to the literature analysis, both velocity hindering and enhancement can occur. Anticipating on the non-dimensional analysis presented in Section 6.5, the outcome, in the limit of sub-Kolmogorov particles, is expected to depend on the following independent non-dimensional numbers (see table 2.3).

In an attempt to identify the limit between hindering and enhancement, it is worthwhile to report available data on a Stokes versus Rouse map with the Reynolds number as a third parameter. However, for large density ratio (1000 and above) the number of well-referenced data is very limited as only those of Good et al. [31] provide most of the required non-dimensional parameters quoted in the table above.

We therefore took advantage of Friedman and Katz's experimental results [28] that cover an extended range of Stokes and Rouse numbers. These data were obtained for a density ratio of order unity and for drops 3 to 15 times larger than the Kolmogorov length scale η. Concentrations were low enough to correspond to the very dilute limit, and the size distribution is probably unimportant in that limit. The conditions such that the settling velocity equals the terminal velocity, i.e. $V_p = V_{St}$,

are reported on a Ro versus St map in fig.2.6, each experimental condition being labeled by the turbulent Reynolds numbers (for future use, we also add on the label the Froude number defined as the standard deviation of the carrier fluid acceleration $\gamma\prime$ divided by g).

Note that, some odd behavior was observed in the data: for example, the condition $V_p = V_{St}$ holds over some range for the experiment labeled L4 while for the series L1, three data fulfill that condition. These somewhat odd trends are probably associated with the difficulty in measuring both particle and fluid velocities in these experiments (in particular, the mean fluid velocity were not strictly zero in the conditions considered) and with their associated uncertainty (unfortunately, the latter is not discussed in the publication). Without any indication concerning their reliability, all raw measurements have been reported in fig.2.6.

Clearly, hindering (respectively enhancement) in the rise velocity occurs above (respectively below) some limiting curve in the $Ro-St$ plane. Besides, as the turbulent Re_λ number increases, that limit is shifted toward lower Ro numbers as shown by the continuous lines. Note that, owing to the limited number of data, these lines are merely indicative. No such map exists for dense particles. The transition Ro number from experimental data is typically 0.3 (Nielsen [54]) and 0.8 to 1 (Good et al.[31]). This critical Ro number is expected to depend on the flow parameter but such dependencies remain to be clarified.

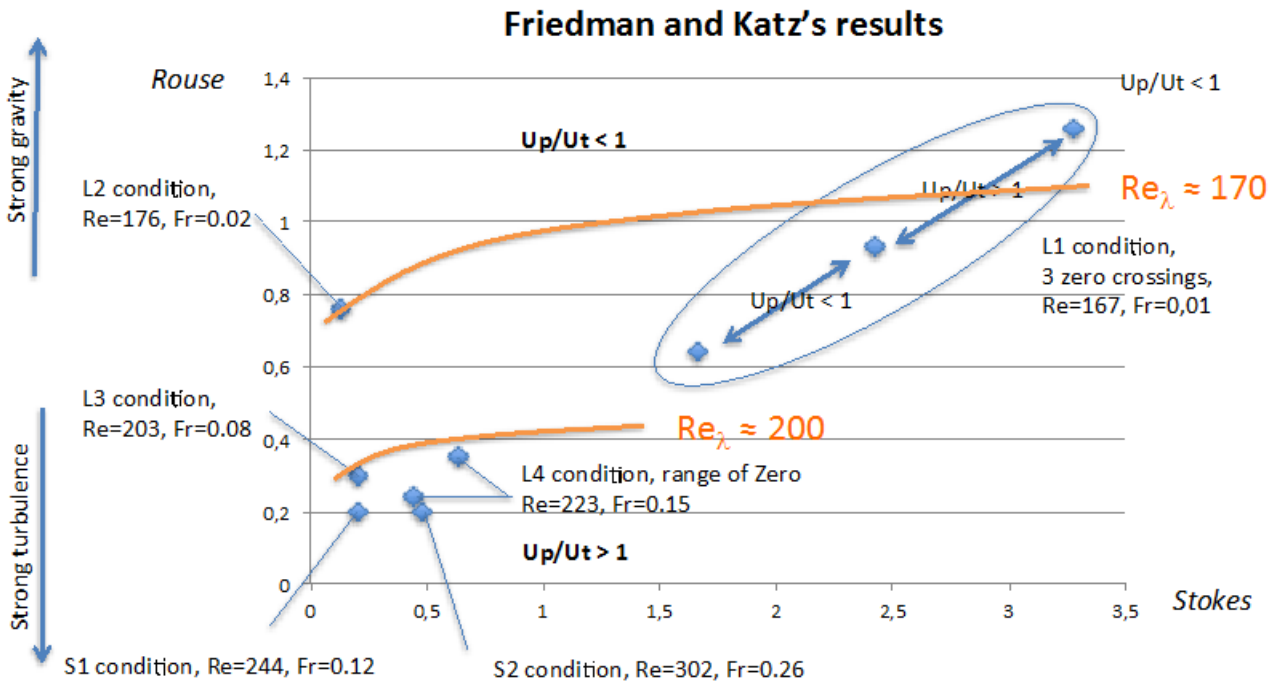

FIGURE 2.6: Flow conditions leading to $V_p = V_{St}$ in Friedman and Katz's experiments, reported on a *Ro-St* map with Re_λ as parameter.

2.4.2 Scaling of the velocity enhancement or of velocity hindering

One open question concerns what velocity scale or scales are relevant for an estimate of the velocity enhancement or hindering. As already mentioned, the results in terms of velocity modification are usually presented either scaled by $U\prime$, or by the Kolmogorov velocity v_η or by the terminal velocity V_{St}.

The combined role of particle inertia and of its terminal velocity evoked here above can also be seen from the linearized equation of motion of a particle in the limit of small inertia and small terminal velocity (small St number). In that limit, the particle velocity V approximately obeys (see for example Eaton and Balachandar [4]):

$$\mathbf{v} \approx \mathbf{u} + \mathbf{V_{St}} - \tau_p \times (\frac{d\mathbf{u}}{dt} + \mathbf{V_{St}}.\nabla\mathbf{u}) + higher\ order\ terms \tag{2.15}$$

where $\mathbf{u}$ is the fluid velocity at the particle position, $\mathbf{g} = g\mathbf{e}_z$ and $\gamma = \frac{d\mathbf{u}}{dt}$ is the Lagrangian acceleration of the fluid. Eq.2.15 is written here for dense particles in a light ambient fluid, and accordingly, the added mass has been neglected. Eq. 2.15 can be put in a non-dimensional form by introducing the terminal velocity $V_{St} = \tau_p g$ as the velocity scale:

$$\frac{\mathbf{v}}{V_{St}} \approx \frac{\mathbf{u}}{V_{St}} + \mathbf{e}_z - \frac{\gamma}{g} - \frac{\tau_p U\prime}{L}\mathbf{e}_z.\nabla^*\mathbf{u}^* + higher\ order\ terms \tag{2.16}$$

where the gradient ∇ has been scaled using the integral length scale L, the fluid velocity $\mathbf{u}$ (respectively the fluid acceleration γ) using the standard deviation $U\prime$ (respectively $\gamma\prime$) of velocity (respectively acceleration) fluctuations. In other words $\mathbf{u}^* = \frac{\mathbf{u}}{U\prime}$, $\gamma^* = \frac{\gamma}{\gamma\prime}$. The last group transforms as $\frac{\tau_p U\prime}{L} = \frac{\tau_p}{\tau_\eta}\frac{U\prime\tau_\eta}{L} = St{Re_\lambda}^{-\frac{1}{2}}$. Hence:

$$\frac{\mathbf{v}}{V_{St}} \approx {Ro}^{-1}\mathbf{u}^* + \mathbf{e}_z - \frac{\gamma\prime}{g}\gamma^* - \frac{St}{Re_\lambda^{\frac{1}{2}}}\mathbf{e}_z.\nabla^*\mathbf{u}^* + higher\ order\ terms \tag{2.17}$$

For a HIT field with no mean flow, the three parameters entering the above equation are $Ro = \frac{V_{St}}{U\prime}$, $Fr = \frac{\gamma\prime}{g}$ and $St = \frac{\tau_p}{\tau_\eta}$ combined with the turbulent Re_λ. We will see later that Fr defined as a $\frac{\gamma\prime}{g}$ is a unique function of Ro, St and Re_λ (see eq.6.16), and eq.2.17 can be rewritten:

$$\frac{\mathbf{v}}{V_{St}} \approx {Ro}^{-1}\mathbf{u}^* + \mathbf{e}_z - a_0^{\frac{1}{2}}\frac{St}{Ro}{Re_L}^{-\frac{1}{4}}\gamma^* - \frac{St}{Re_\lambda^{\frac{1}{2}}}\mathbf{e}_z.\nabla^*\mathbf{u}^* + higher\ order\ terms \tag{2.18}$$

Eq.2.18 clearly shows that both inertia (St) and settling velocity (Ro) play a key role in the particle dynamics. Moreover, in eq.2.18, the fluid acceleration appears as a driver of the particle motion, and therefore, the fluid acceleration may also provide a relevant velocity scale. Eq.2.18 can be also scaled with $U\prime$:

$$\frac{\mathbf{v}}{U\prime} \approx \mathbf{u}^* + Ro\ \mathbf{e}_z - Ro\frac{\gamma\prime}{g}\gamma^* - \frac{St \times Ro}{Re_\lambda^{\frac{1}{2}}}\mathbf{e}_z.\nabla^*\mathbf{u}^* + higher\ order\ terms \qquad (2.19)$$

2.4.3 Scalings of the velocity difference $V - V_{St}$

The velocity difference $V - V_{St}$ has been further attempted to scale with independent parameters characterising the particles inertia (St), acceleration of the flow with regards to gravity (Fr), turbulence (Re_λ) and gravitational settling (Ro).

The enhancement of the settling velocity difference $\Delta V = \frac{V - V_{St}}{U\prime}$ is predicted for St in the range [0 - 2.5] and for Ro in the range of [0 - 1.4] for Re_λ between 35 and 133 found by Yang & Lei [76].

Bec et al.[7] has obtained a following scaling of $\frac{V - V_{St}}{V_{St}}$ for $St >> {Re_\lambda}^{\frac{1}{2}}$ and

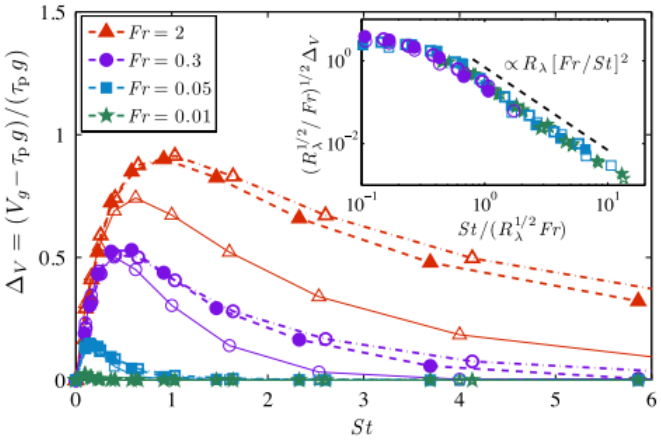

FIG. 2 (color online). Relative increase of the settling velocity Δ_V as a function of the Stokes number St for various Froude numbers, as labeled, and $R_\lambda = 130$ (thin symbols, plain lines), $R_\lambda = 290$ (filled symbols, dashed lines), and $R_\lambda = 460$ (open symbols, broken lines). Inset: $[R_\lambda^{1/2}/\mathrm{Fr}]^{1/2}\Delta_V$ as a function of $\mathrm{St}/[R_\lambda^{1/2}\mathrm{Fr}]$ for the same data.

FIGURE 2.7: Relative increase of the settling velocity ΔV as a function of St for various Fr [7], there $Fr = (\frac{\epsilon^3}{\nu})^{\frac{1}{4}}\frac{1}{g}$

.

$Fr << Re_\lambda{}^{\frac{1}{2}}$:

$$\frac{V - V_{St}}{V_{St}} \approx Re_\lambda{}^{\frac{3}{4}} Fr^{\frac{5}{3}} St^{-2}. \tag{2.20}$$

Here, Fr is defined as $(\frac{\epsilon^3}{\nu})^{\frac{1}{4}}\frac{1}{g}$. From 2.20 we see that the turbulence acceleration plays a dominant role in the enhancement of the settling velocity compared to that of the turbulent Re_λ and St. Fig.2.7 shows a relative collapse of ΔV when scaled with St, Re_λ and Fr.

Rosa et al.[63] attempted to find the scalings of velocity difference ΔV using a one-way coupling between the particle interaction and underlying turbulent flow. They found that there is a relative collapse of the quantity $\frac{V-V_{St}}{V_{St}\times St}$ versus Fr_R defined as $\frac{\tau_p^3\ g^2}{\nu}$ (see fig.2.8a) for one fixed $Re_\lambda = 143$. We have traced the fit of Rosa et al. [63] for other Re_λ varying from 75 to 500 (see fig.2.8b), and indeed, we see some collapse. The modified Froude number Fr_R for the particle was first introduced by Davilla & Hunt [19]. The Fr_R number represents the ratio of the inertial forces experienced by a particle to the buoyancy forces (see [19]). Both simulations done by Bec et al.[7] and Rosa et al.[63] demonstrate that both Fr and Re_λ are strongly affecting the magnitude of ΔV.

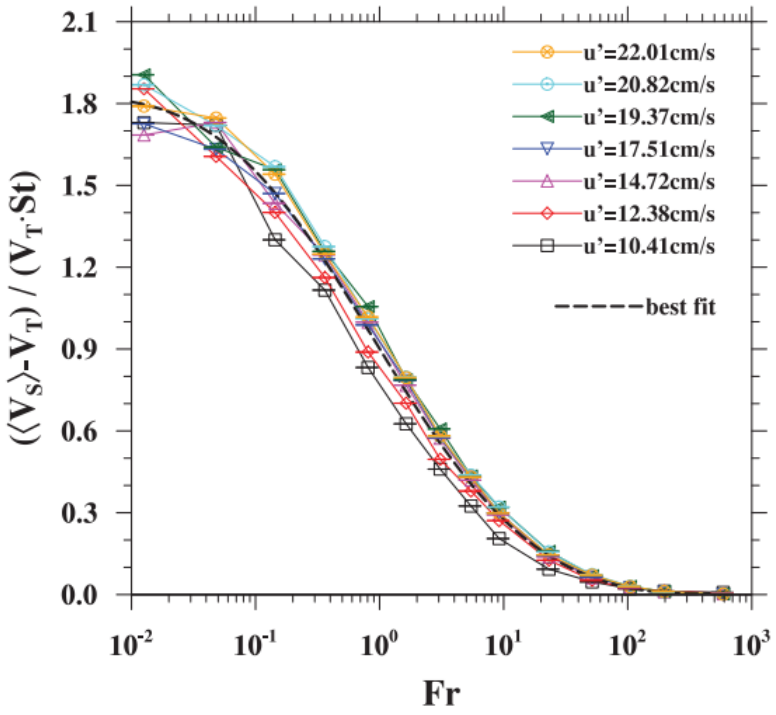

Fig. 4. The difference between the average settling velocity and terminal velocity normalized by terminal velocity and Stokes number as a function of particle Froude number.

(a)

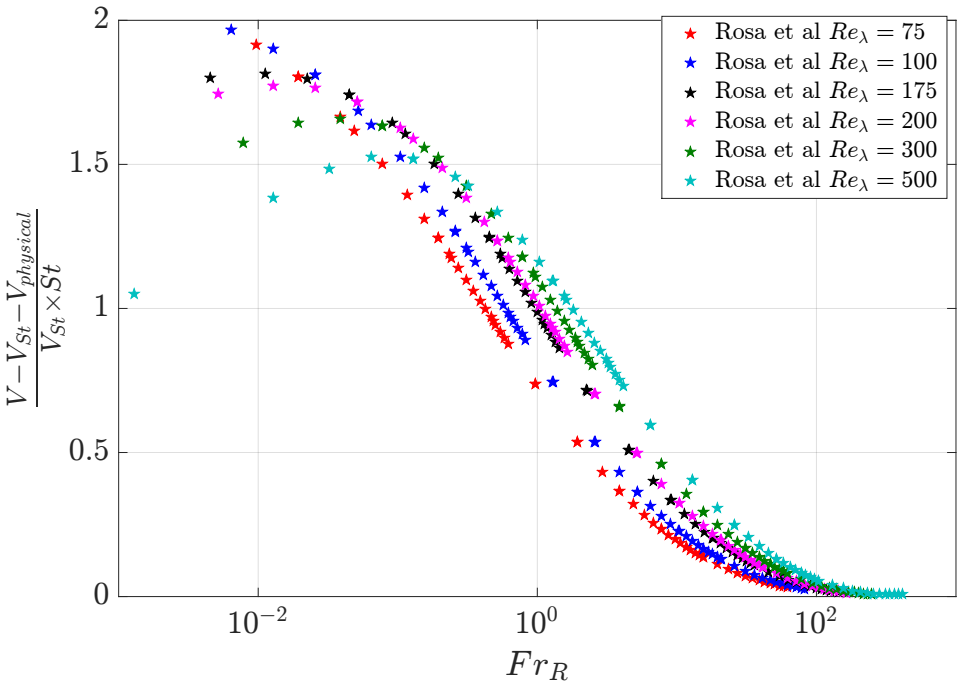

(b)

FIGURE 2.8: (a) Relative increase of the settling velocity ΔV as a function of Fr for various $U\prime$ [63] for fixed $Re_\lambda = 143$ and (b) same fit of Rosa et al.[63] traced for different Re_λ

.

2.5 Open Questions

From the previous discussion about clustering and settling velocity of inertial particles, many questions still remain open, in particular:

- how to disentangle the role of particles inertia given by St number, of gravitational settling represented by Ro number, of collective effects related to the volume fraction ϕ_v and the effect of turbulence given by Re_λ number or Fr number on the clustering of inertial particles? What is the importance of the collective effects when flow parameters are varied?
- both hindering and enhancement of the settling (or rising) velocity can take place, as seen by the previous studies, and the limit between the two behaviours is unclear,
- the scalings of the velocity modification due to turbulence and/or to clustering is still under debate.

These three questions will be addressed in this thesis by conducting new experimental studies.

2.6 Work program

In the attempt to find possible answers to the open questions about clustering and settling velocity of inertial particles, we decided to conduct experimental studies using two measuring techniques.

First experimental study was conducted using Particle Tracking Velocimetry, and it will attempt to give us the following measurements:

- 2D particle positions that will be used to define the local concentration field of inertial particles via Voronoii tesselations and analyse the level of clustering,
- characteristical geometrical properties of clusters and voids,
- the evolution of clustering levels and of the structures of clusters and voids by varying St number, volume fraction ϕ_v and Re_λ number,
- the behaviour of the settling velocity conditioned by the local concentration field with the goal to identify the presence of collective effects, where settling would show a dependency on the local concentration.

Second campaign of measurements was carried on using Phase Doppler Interferometry. The second campaign was primarily motivated by intrinsic experimental limitations of the PTV data (further discuss in Chapter 5), in particular regarding the high sensitivity to vertical alignment (crucial to address settling measurement) and the inability of PTV to distinguish particle of different size, hence not allowing to condition the settling velocity on particle size which is mandatory to address subtle Stokes and Rouse number effects previously discussed (in particular regarding the question of settling enhancement or hindering). The PDI measurement campaign was thus intended to provide us with the following measurements:

- the simultaneous measurements of the settling velocity, local concentration field and size of the inertial particles subjected to the turbulent flow,
- the evolution of the aforementioned quantities with the volume fraction and with turbulent Re_λ.

The measurements for the first campain (PTV) were done with varying turbulent Re_λ from 175 to 450, volume fraction ϕ_v from 0.2×10^{-5} to 2.0×10^{-5} and St number defined on the maximum probable D of the polydisperse spray from 0.1 to 5.0. The

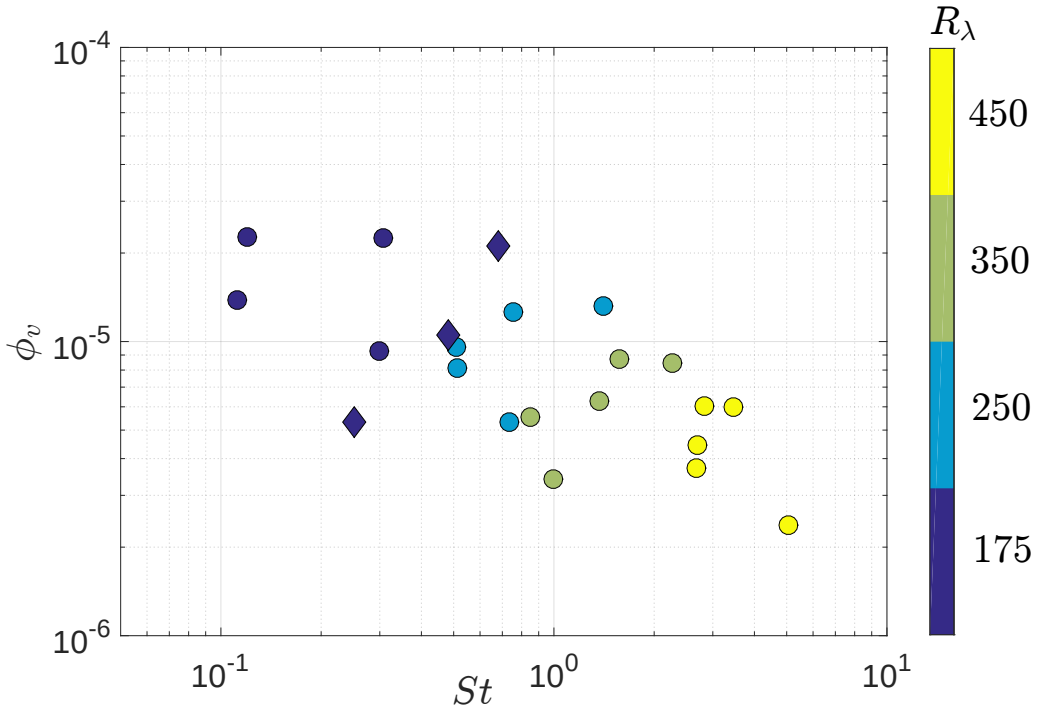

FIGURE 2.9: Experimental control parameter space in the scope of this thesis: round symbols are data obtained with PTV and diamond symbols are data obtained with PDI

.

second measurement campain was done at a fixed $Re_\lambda = 180$ and varying volume fraction ϕ_v from 0.5×10^{-5} to 2.0×10^{-5}. In these measurements the diameter of the particles D was measured in the range of $[0.5; 300]$ μm. Hence, the St number of the particles varied from 0.01 to 10. The selected St, Re_λ and ϕ_v parameters for the two measurement campaigns are given in fig.2.9.

Now we will give a quick overview of the organisation of this thesis. This thesis consists of 7 Chapters.

- Chapter 1 Introduction gives us the brief introduction of clustering and its role in natural and industrial processes.

- Chapter 2 Bibliography attempts to present a coherent and extensive bibliographical review of the previous studies conducted with regard to the clustering of inertial particles and their settling velocity in the presence of various physical factors such as the role of particles inertia, role of gravity, role of turbulence and collective effects.

- Chapter 3 describes the experimental facility i.e. the wind tunnel used to conduct the tests and the measuring techniques such as Particle Tracking Velocimetry (PTV) and Phase Doppler Interferometry (PDI). The generation of the polydisperse particle spray is also discussed as well as the generation of turbulence using an active grid.

- Chapter 4 examines how the clustering characteristics evolve with three control parameters namelly: particles inertia given by St number, Re_λ of the turbulent flow and volume fraction ϕ_v. This analysis is based on PTV measurements, and Voronoii 2D procedure is used to quantify the local concentration field.

- Chapter 5 investigates the settling velocity of the particles conditioned by the local concentration field $\mathcal{V}$ defined in the previous Chapter and obtained from PTV measurements.

- Chapter 6 investigates the settling velocity of inertial particles. To begin with, we eliminate the effects of alignment offset, and introduce the notion for the physical offset due to collective effects ϕ_v. Next, we investigate the behaviour of the settling velocity according to the size of the particle as well as the local concentration field using Voronoii analysis conducted in 1D. These data are further compared with the available experimental results, and their significance is discussed.

- Chapter 7 gives the conclusions of the work done notably on the clustering subject: evolution of the clustering levels of inertial particles, consequently, formed structures of the two-phase flow called clusters and voids with varying St, Re_λ and volume fraction ϕ_v. This Chapter also summarises the main findings for the settling velocity of the inertial particles. It discusses the enhancement and hindering of the velocity of inertial particles as a direct consequence of the gravitational settling, particles inertia and turbulence.

Chapter 3

Experimental Setup

Three series of measurements were taken to obtain information about clustering. Particle Tracking Velocimetry (PTV) was used to obtain Lagrangian statistics of the inertial particle field while Phase Doppler Interferometry (PDI) was supposed to provide us with information about Eulerian inertial particle field.
In all of experiments carrier fluid was an air flow generated in the wind tunnel, turbulence was generated with an active grid placed right before the entrance of the test section, inertial particles were generated from industrial injectors.

3.1 Wind tunnel

Experiments were conducted in a wind tunnel with a test section of 0.75 m×0.75 m×4 m (see fig. 3.3). Homogeneous isotropic turbulence is produced with an active grid located at the entrance of the test section. The mean streamwise velocity U in the wind tunnel was varied in the range $U \in [2.5 - 10]$ m/s (corresponding turbulence properties are given below in Table 3.2). Water droplets are injected 15 cm downstream of the active grid using an array of 18 pressure injection nozzles supplied with a controlled flow rate of water via a high pressure pump. Three injector sizes (with different orifice diameters $D_{inj} = 0.3,\ 0.4,\ 0.5\ mm$) were used in order to vary the size distribution of droplets injected in the flow. The droplet volume fraction can be further controlled by varying the flow rate of water F_{water} injected, which in our experiment evolves in the range $F_{water} \in [0.8 - 1.9]$ L/min. Overall, the combination of the three control parameters (U, D_{inj}, F_{water}) allows us to explore the parameter space (St, R_λ, ϕ_v). The main properties of the carrier turbulence, of the seeded water droplets and the accessible parameter space is described in the following subsection.
The details of the active grid in the wind tunnel have been published in [55]. Briefly, it is made up of eight vertical and eight horizontal shafts on which square wings are

mounted. Each axis is controlled individually by a stepper motor, so that the solidity of the grid can be actively and dynamically changed. This turbulence generation technique was first introduced by Makita [42] and has been reproduced in multiple studies in the literature ([52, 60], among others). When a random forcing protocol is used to drive the rotation of the shafts and flapping of the wings, it generates stronger turbulence than a passive grid (turbulence intensity in our active grid flow is of the order of 15-20%, while it is typically 2-4% in passive grid wind tunnel turbulence) while keeping good homogeneity and isotropy. Figure 3.1 shows a typical spectrum (measured with classical hot-wire anemometry) of the carrier flow velocity fluctuations for $U = 10\ m/s$, where a well defined inertial range can be clearly identified over about 2 decades in wavenumber space. Table 3.1 summarises the scalings of main turbulence characteristics such as turbulence intensity, R_λ and Kolmogorov scale η obtained through the calibration of the wind tunnel. Table 3.2 summarizes the main properties of the turbulence and the disperse phase, for the different values of mean stream velocity U.

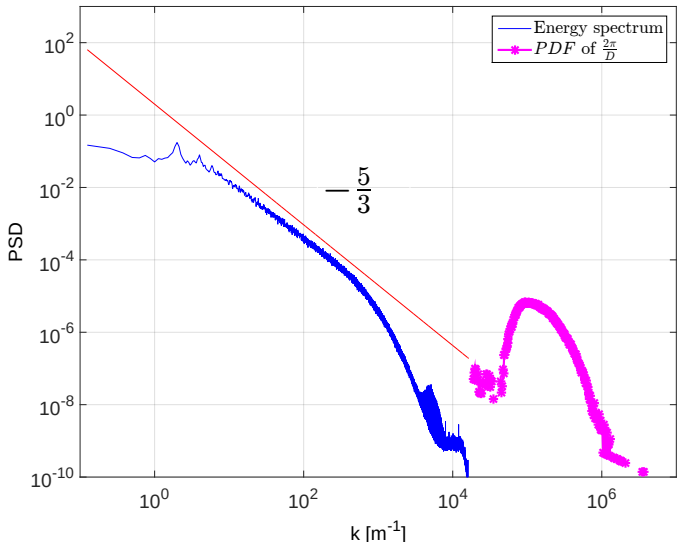

FIGURE 3.1: Typical Eulerian energy spectrum of velocity fluctuations produced downstream of the active grid, obtained from classical hot-wire anemometry, at a distance of 3.5 m downstream the grid, corresponding to the position where water droplets preferential concentration is investigated. The typical distribution of $2\pi/D$, where D is the droplets diameter, shown in magenta on this graph (with arbitrary units in the ordinate axis) demonstrates that all droplets are indeed smaller than the Kolmogorov length scale.

TABLE 3.1: Fitting exponents for the turbulent characteristics scaling as $A \cdot U^n$

A_{R_λ}	n_{R_λ}	A_λ	n_λ	A_ϵ	n_ϵ	A_η	n_η	$A_{L_{int}}$	$n_{L_{int}}$	A_{τ_η}	n_{τ_η}
95	0.71	9.2×10^{-3}	-0.38	0.011	3.4	1.0×10^{-3}	-0.98	0.07	0.49	0.057	-1.9

TABLE 3.2: Conditions of the experimental runs.

D_{inj} $[mm]$	F_w $[\frac{l}{min}]$	U $[\frac{m}{s}]$	$u\prime$ $[\frac{m}{s}]$	η $[\mu m]$	ϵ $[\frac{m^2}{s^3}]$	D_{max} $[\mu m]$	σ_D $[\mu m]$	D_{32} $[\mu m]$	St	ϕ_v $\times 10^{-4}$	Re_λ
0.3	0.8	2.36	0.30	431	0.20	35	17	60	0.3	0.09	175
		4.11	0.59	250	1.35	32	19	61	0.7	0.05	259
		6.42	1.00	162	6.12	24	18	60	1.0	0.03	356
		9.19	1.49	114	20.73	37	18	58	5.0	0.02	459
	1.2	2.37	0.33	429	0.21	21	17	52	0.1	0.14	175
		4.03	0.62	255	1.26	27	17	59	0.5	0.08	256
		5.95	0.92	174	4.74	24	17	57	0.9	0.06	337
		8.85	1.41	118	18.27	28	16	57	2.7	0.04	447
0.4	1.9	2.32	0.32	439	0.19	36	19	62	0.3	0.22	172
		3.95	0.56	260	1.17	45	20	65	1.4	0.13	252
		5.95	0.95	174	4.74	32	20	66	1.6	0.09	337
		8.64	1.40	121	16.83	30	20	69	2.8	0.06	439
	1.4	4.07	0.59	252	1.31	26	21	66	0.5	0.10	258
		6.27	1.00	166	5.64	28	21	67	1.4	0.06	350
		8.82	1.43	118	18.02	29	20	66	2.7	0.04	446
0.5	1.9	2.30	0.30	442	0.19	23	23	67	0.1	0.23	172
		4.13	0.58	249	1.37	32	23	72	0.8	0.13	260
		6.16	0.96	168	5.32	37	22	70	2.3	0.08	345
		8.68	1.40	120	17.05	33	21	70	3.5	0.06	440

3.2 Generation of inertial particles

Water droplets are injected with an array of 18 spray nozzles just downstream the active grid. The nozzles are fixed on 8 vertical bars, at the same transverse position than the vertical bars of the grid itself, in order to minimize the intrusion of the injectors array. Hot-wire anemometry shows that turbulence properties at the measurement location (3.5 m downstream the grid) when the injectors array is in place are undistinguishable compared to the case where it is not.

We have used three different classes of nozzles with three different orifice diameters D_{inj}. For a given class of injector, the size distribution of the produced spray depends weakly on the water pressure, which determines in contrast the water flow rate F_{water}, and eventually the volume fraction ϕ_v of the droplets population seeding

the flow. The inlet tube feeding the array with water is equipped with a rotary flow sensor used to monitor and control the water flow rate for every pressure set-point. Fig. 3.2 shows a typical size distribution of water droplets obtained from Phase Doppler Interferometry (PDI) measurements. The spray is strongly polydispersed, with a well-defined most probable diameter. The droplet size distributions have been measured using PDI for all the considered experimental conditions. The most probable diameter D_{max}, the Sauter mean diameter D_{32} and the standard deviation $std(D)$ are reported in Table 3.2. The most probable diameter evolves in a narrow range, from 21 to 45 μm. Otherwise, all conditions exhibit a comparable degree of polydispersity as $std(D)/D_{32} = 0.31 \pm 10\%$ and $std(D)/D_{max} = 0.66 + 50\% - 30\%$. The inset in figure 3.2 represents the distribution of particle Stokes numbers corresponding to the size distribution shown.The polydispersity of the spray naturally induces a polydispersity in Stokes number. The latter extends down to Values of Stokes span the range from 0.004 to 20.7, but the range 0.1 to 2.01 is consistently in every experiment reported here. A reference Stokes number for each experimental condition is defined using the most probable droplet diameter D_{max} in the distribution. Thus, for each experimental condition, the most representative particle Stokes number is estimated as $St_{D_{max}} = \frac{\Phi_{max}}{36}(1 + 2\Gamma)$, with $\Phi_{max} = (D_{max}/\eta)^2$ and $\Gamma = \rho_{water}/\rho_{air} \simeq 830$. Alternative choices are possible. For example, one may also refer to the most probable Stokes number, St_{max} (see inset in figure 3.2) that slightly differs from the Stokes number based on D_{max}. For the experimental conditions explored here, the difference between the most probable St_{max} and $St_{D_{max}}$ based on D_{max} varies between $12 - 75\%$ (see table 3.2). As pointed out earlier, since St depends both on D and η, for a given particle distribution the Stokes number varies with the flow Reynolds number. Thus, St is sensitive to both wind tunnel speed and injector orifice size as experimental controls.

3.2.0.0.1 Droplets volume fraction. The volume fraction ϕ_v of the droplet disperse phase in the wind-tunnel is given by the ratio between the water flow rate F_{water} through injector array and the total flow rate of air and water across the tunnel cross-section $F_{tot} = F_{air} + F_{water}$ with $F_{air} = S \cdot U$ (where $S = (0.75\ m)^2 \simeq 0.56\ \mathrm{m}^2$ is the area of the tunnel cross section): $\phi_v = \frac{F_{water}}{F_{tot}}$. Note that in all experiments $F_{water} < 2$ L/min while $F_{air} > 1.4\mathrm{m}^3/\mathrm{s} \gg F_{water}$, so that $F_{tot} \simeq F_{air}$ and $\phi_v \simeq \frac{F_{water}}{F_{air}} = \frac{F_{water}}{S \cdot U}$. Therefore, the volume fraction ϕ_v depends on both liquid injection flow rate and the wind-tunnel mean speed.

The measurement area is located 3 m downstream the injection of the droplets, where turbulence is well developed and what is expected to be sufficiently far away

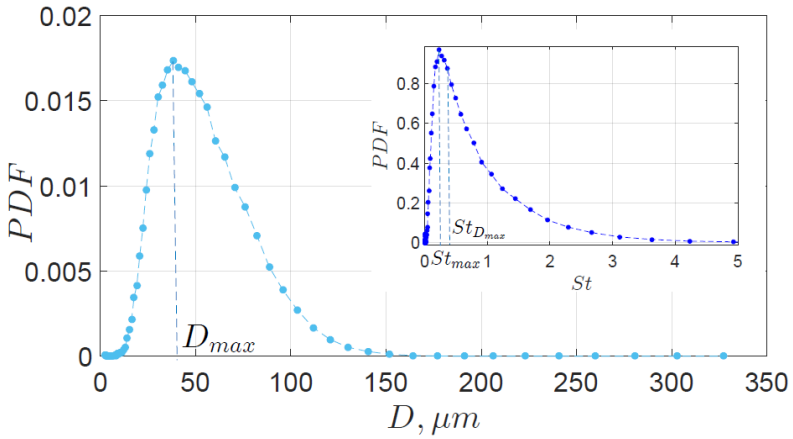

FIGURE 3.2: Typical diameter distribution of water droplets in the wind tunnel (produced by the 0.4 mm injectors at a flow rate of 1.9 l/min). Inset: corresponding distribution of Stokes numbers for $R_\lambda = 172$. Dashed lines indicate the Stokes number defined on the most probable diameter and the most probable Stokes number.

from the injection location for cluster formation to have reached a stationary state. Concerning the flow conditions, the duration required for clusters to form is indeed not well known. If as an estimate, we consider the duration of transients observed in direct numerical simulations, two proposals can be found concerning the time required for steady state to be achieved: either transients are of the order of the integral time scale T_{int} of the carrier turbulence (provided that the particle response time is much smaller than T_{int} [73] what is the case in our study), or they depend on a combination of turbulent and particle characteristic time scales (for instance, Yang & Lei [76] propose about 8 dissipation time scale τ_η plus 5 τ_p). In all our experimental conditions, the transit time of droplets between the injection plane and the measuring location amounts between 60 to 600 particle response times (based on the maximum probable diameter), and at least a few integral time scales (from 1.8 to 2.5). In such circumstances, such transit times are expected (subject to verification) to be large enough for clusters to be formed.

3.3 Particle Tracking Velocimetry

3.3.1 Experimental Setup

The wind tunnel is illuminated with a vertical laser sheet, in the streamwise direction of the test section, at midway between the front and the rear wall of the tunnel (fig. 3.3). The width of the laser sheet is of the order of 1 mm, that corresponds at

most to a few dissipative scale of the carrier turbulence. Because of the gaussian profile of the laser beam, the illumination is inhomogeneous in the vertical direction (a slight inhomogeneity also exists in the horizontal direction, mostly due to sheet formation near the waist of the laser). Therefore the laser intensity is maximum at mid-height. Sequences of images are recorded using one high-speed camera (Phantom V12 from Visual Research Inc., New Jersey). The camera was mounted with a 105 mm Nikon macro lens, with a Scheimpflug mount, allowing to visualize the laser sheet in forward scattering conditions to improve the brightness of the droplets while keeping good focusing conditions over the entire image. The dimensions of the visualization area are of the order of $L_x \times L_y$ with $L_x \simeq 10$ cm and $L_y \simeq 7$ cm (with the largest extension, L_x, in the streamwise direction covering a significant fraction of the integral scale of the carrier turbulence which is of the order of $L_{int} \approx 15\ cm$). For each experimental condition, defined by one triplet (St, R_λ, ϕ_v) in the parameter space in fig. 3.4 we record 20 movies at full resolution (1280x800 pixels) at a repetition rate of 2500 frames per second. This high repetition rate was chosen in order to have an inter-frame time step sufficiently short compared to the dissipation time scale τ_η of the carrier turbulence, with the perspective (not discussed in the present article) of performing particle tracking and estimating the Lagrangian velocity of the particles along tracks.The number of particles per image evolves typically between 500 and 2000 depending on flow conditions.

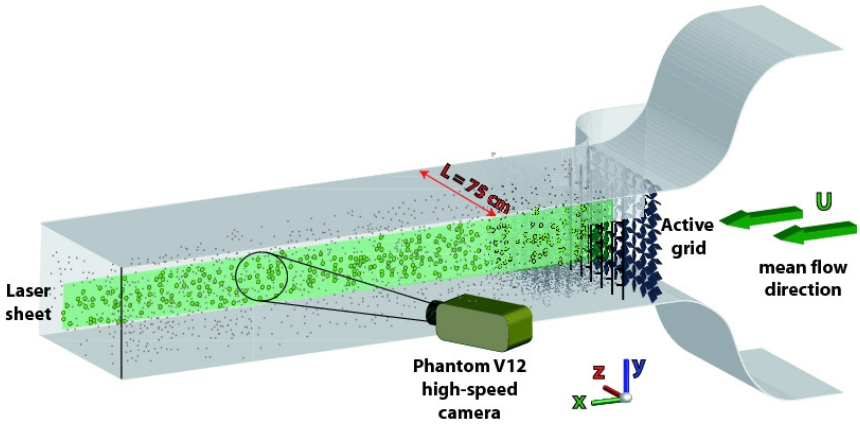

FIGURE 3.3: Schematic view of the experimental facility.

3.3.2 Method & Algorithm of PTV Tracking

The PTV tracking algorithm used is a 3 Frame minimum Acceleration procedure programmed by N. Oulette [58]. Possible trajectories for each particle are constructed through 3 frames, and the best one is found by the minimum acceleration requirement.
Hence, PTV data can simultaneously provide through Lagrangian trajectories both positions of the particles and their velocity. From this data it is possible to extract the information about:

1. 2D particle positions that reflect the local concentration field via Voronoï analysis which compared to the statistics of Random Poisson Process should yield the presence or absence of clustering

2. Lagrangian measurements of settling velocity of inertial particles which will be further conditioned by three of the control parameters

3. Lagrangian measurements of settling velocity of inertial particles conditioned by the local concentration field which should show qualitatively and quantitatively the dynamics of clusters and voids

4. Measurements of the size clusters and voids within the variation of experimental parameters

3.3.3 Parameter Space

The previous considerations show the difficulty to independently vary the three parameters (St, R_λ, ϕ_v) as they are fully entangled to the actual control parameters (U, D_{inj}, F_{water}). This has limited in previous studies the possibility to easily and systematically explore the parameter space. By independently varying the injectors diameter, the water flow rate and the mean stream velocity, we were capable in the present study to explore a significant fraction of the parameter space (St, R_λ, ϕ_v) (see fig. 3.4) in the ranges: $St \in [0.1, 5]$, $R_\lambda \in [170, 460]$ and $\phi_v \in [0.1 \times 10^{-5} - 2 \times 10^{-5}]$. Figure 3.4a&b represents the explored control parameters and experimental parameters which were accessible in the present study. This is still far from an ideal homogeneous exploration of the parameter space, as some systematic trends can be clearly seen:

1. For a given droplet diameter, the Stokes number increases with increasing Reynolds number (as a result of the dissipation scale decreasing with increasing

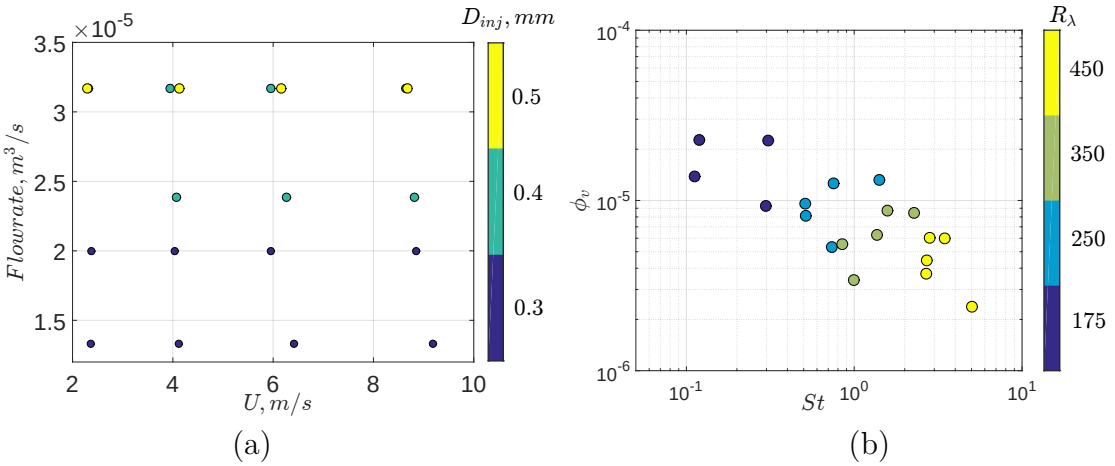

FIGURE 3.4: (a) Map of explored control parameters. (b) Corresponding map of experimental parameter space.

R_λ). In order to vary the Stokes number independently to Reynolds number, this trend can be partially compensated by using different injectors in order to vary independently the size of the droplets.

2. For a given water flow rate in the injectors, volume fraction decreases with increasing Reynolds number (as a consequence of the air flow increasing with U). In order to vary the volume fraction independently to Reynolds number, this trend can be partially (in the limit of accessible pressure set point of the pump) compensated by increasing the water flow rate in the injectors.

3. The combination of both previous effects results also in a global trend of volume fraction to decrease as Stokes number increases.

However, in spite of these trends, there are still interesting portions and sections of the parameter space where the influence of one parameter could be investigated limiting the variation of the 2 others. For instance, several horizontal lines in fig. 3.4b along variations of Stokes number at relatively constant volume fraction, with a moderate variation of Reynolds number can be identified. Similarly some vertical lines along variations of volume fraction at relatively constant Stokes number and moderate variations of Reynolds number can also be identified. Some points can also be found, with almost identical Stokes number and volume fraction and slightly different Reynolds number, hence allowing to explore some first trends of pure Reynolds number effects.

3.4 Phase Doppler Interferometry Procedure (PDI)

The role of polydispersity could hardly be discussed in terms of the LPT measurements, since it is difficult to determine the size of the particle from images. For example, a dim particle can either be a small particle or a big one at the edges of the laser sheet. To include the information about the particle size, we introduce PDI measurements which allow to determine at a given point the detection of particle as well as its size and velocities in both streamwise and vertical directions. Using a Taylor hypothesis, we can reconstruct a local concentration field along a line in the streamwise direction. In this respect, compared to LPT measurements that gave us 2D measurements but without any information about particle size, PDI data gives us additional information on the size but is restricted to a 1D measurement.

3.4.1 Principle of Phase Doppler Interferometry (PDI)

Phase Doppler Interferometry (PDI) schematized fig. 3.5 allows simultaneous and non-intrusive measurements of velocity and diameter of ideally spherical particles crossing a particular point in space. This technique is basically a single particle counter, i.e. only one particle passing through the measurement volume is measured at a time.

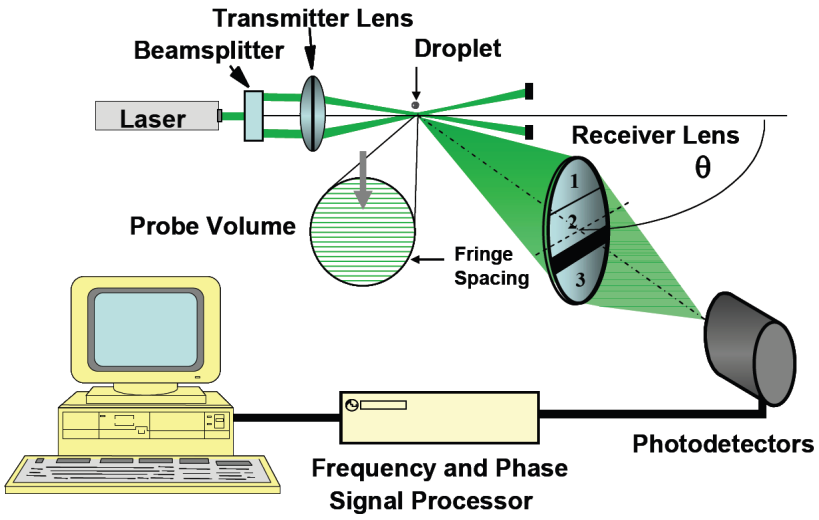

FIGURE 3.5: Operational schematics of PDI system (PDI-300 MD User Manual[59])

The probe volume is formed by the intersection of two coherent narrow (typically $< 1\ mm$ in diameter) laser beams. Besides, a fringe pattern is formed within

the probe volume as shown in fig. 3.6 (strictly speaking no fringes are formed in absence of intensity detector but the interpretation as a system of fringes will be here sufficient to expose the principle). The fringe spacing δ is related to the wavelength λ of the beams in the propagation medium and to the angle α between the two incoming beams, namely:

$$\delta = \frac{\lambda}{2sin(\frac{\alpha}{2})} \tag{3.1}$$

The light reflected by the particle passing through the measurement volume is mod-

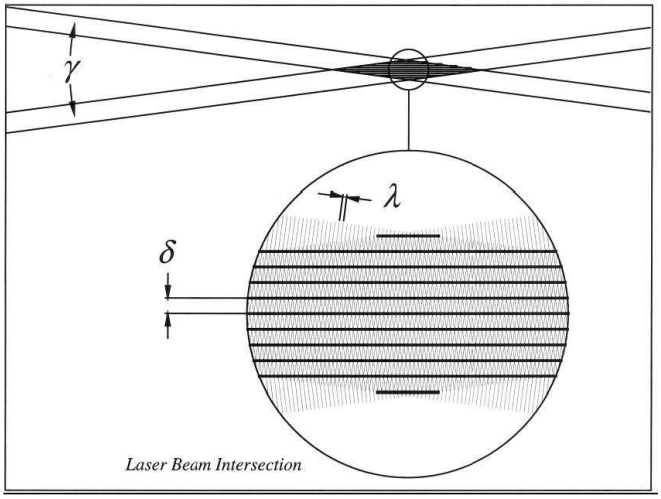

FIGURE 3.6: Interference fringe pattern (PDI-300 MD User Manual[59])

ulated by the intensity distribution in the fringe pattern. Hence, when a particle crosses the measurement volume, a photodetector fixed in space registers an amplitude modulated signal those so-called Doppler frequency f_D is proportional to the velocity of the particle U_x in the direction normal to fringes. Namely:

$$U_x = f_D \times \delta, \tag{3.2}$$

Note that the Doppler frequency does not depend on the detector position. When using two detectors, the phase shift between the pair of Doppler signals collected can be related to the particle radius. With two photodetectors fixed in space, the phase ϕ between the two signals happens to be linearly related with the particle radius R. Namely:

$$\phi = 2\pi C\frac{R}{\delta} \tag{3.3}$$

where C is a prefactor that depends on the spacing between the two detectors, on the diffusion angle with respect to the optical axis and on the relative refractive index of the particle when the diffusion exploits the refractive mode. The best optical settings of the PDI for analyzing water drops in air is a forward scattering arrangement with a 30 degrees diffusion angle in a plane perpendicular to the one defined by the incident laser beams (see fig. 3.7). Diffused light is then essentially a pure refractive mode, and the linearity between the phase and the size is a very good approximation of the system response.

3.4.2 Optical Settings of PDI

The PDI model used at LEGI is PDI-300 MD from Artium Technologies Inc (see fig. 3.5). In this system, two solid state lasers produce green (wavelength 532 nm) and blue (wavelength 473 nm) laser beams. Each laser beam is divided in two beams of equal intensity, and a transmitter lens ensures their focalization in space. The green beams provide simultaneous measurements of one velocity component and of the size of the particle, whereas the blue beams measures only one velocity component in a direction perpendicular to the former component. Although the two blue and green pairs of beams overlap fairly well, it is always tricky to ensure a perfect coincidence between the signals collected from the two wavelengths. To avoid any limitation in the signal processing and to maximize the validation rate, we choose to measure the settling velocity $V_{settling}$ simultaneously with the diameter D using the green laser beams, and to independently collect streamwise velocity measurement U using the blue laser beams. So doing, no criteria on coincidence was used in the processing. Accordingly, the green laser beams were set in a vertical plane and the blue beams in an horizontal plane.

The transmitter lens's focal length was set to 1000 mm, and the focal length of receiver was chosen to be 500 mm. These choices were made to obtain the best possible optical arrangement adapted to flows conditions and experimental set-up. Indeed for this optical arrangement, the fringe spacing for the green beams (channel 1) was $\delta = 8.9\ \mu m$ and the accessible diameters ranged from 3 μm to 300 μm: such an interval covers all the size distributions investigated so that any misleading phase interpretations were avoided. The fringe spacing for the blue beams (channel 2) was $\delta = 8.2\ \mu m$.

The dimensions of the probe volume formed at the intersection of the beams are primarily set by the beam waist: in the present systems, the latter is about $645.1 \mu m$

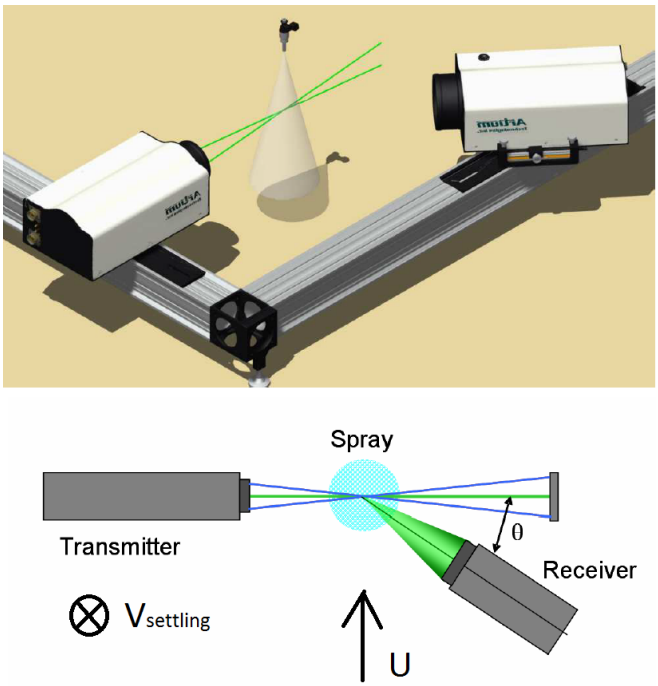

FIGURE 3.7: Chosen optical arrangement is forward scattering with diffusion angle of $\theta = 30$ degrees (PDI-300 MD User Manual[59])

that corresponds to 1.6η. Besides, the dimension of the probe volume along the optical axis direction is set by the aperture of the receiver. In the present system, aperture widths from 50 to $1000\mu m$ are available. A $200\mu m$ receiver aperture was selected that corresponds to about 0.5η. Thus, the measurement volume is of the order of 0.2 mm^3.

In practice, the optical axis of the transmitter was set perpendicular to the channel side walls and the receiver was located on the other side of the wind tunnel.

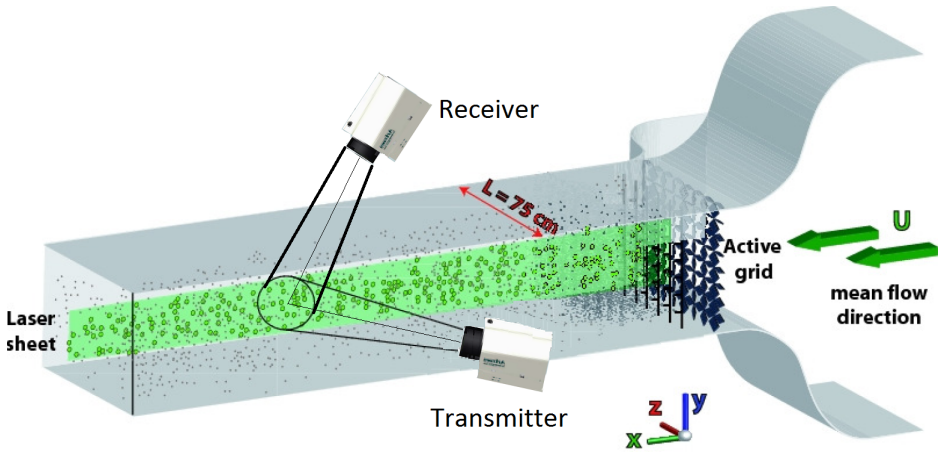

FIGURE 3.8: Experimental setup of PDI

During the experiments, droplets are continuously deposited on the internal side of windows and their accumulation with time leads to a significant decrease of the signal quality and thus of the data rate. On the emitter side, the window was cleaned at the start of each run and the run duration was adapted (depending on the concentration) to ensure moderate decay of the validation rate. Many of such runs were repeated to ensure convergence. On the receiver side, the problem was eliminated by way of a hole larger than the receiver optical aperture made in the wall. Also, black absorbing masks were installed where appropriate to eliminate spurious reflections that are a significant source of noise. In addition, optical adjustments were achieved before every measuring campaign to optimize the signal quality.

All measurements were performed at a distance $x = 3\ m$ (i.e. at the same streamise position than LPT measurements previously mentioned), from the injectors with the measuring point located in the middle plane between lateral vertical walls and at an altitude from the bottom of the channel of 35 cm.

3.4.3 PDI parameters adjustments

The objectives were to detect all the particles crossing the probe volume with a sufficient resolution on velocity and on size measurements. To approach these objectives, a number of parameters must be carefully adjusted to properly set-up the instrument. The following sections describe this process.

3.4.3.1 Detection of small drops

The first step consists in testing the ability of the system to detect the smallest drops present in the flow. In the selected flow conditions, we were interested in detecting droplets as small as a few micrometers that act as tracers of the gas flow. Since the laser power is fixed, the main variable is the amplification at detection, controlled here by the high voltage supplied to photomultipliers. A second parameter is the analog threshold that allows to distinguish small particles delivering low amplitude signals from background noise: indeed, any time the amplitude of the raw signal from a photomultiplier exceeds the threshold, the processor starts analyzing the waveform and possibly provides valid measurements of velocity and size. The amplification was first adjusted using a fine spray generator that delivers drop size in the range $3-5\ \mu m$ and considering a reasonable range of analog thresholds: a photomultiplier voltage of at least 700 V was required with the selected optical settings. This minimum amplification was kept for all experiments so that all size distributions contain data in that size range. Since an increase in the gain induces additional

noise, it is important to balance amplification and detection and in particular to finely adjust the analog threshold: this step is discussed later.

3.4.3.2 Selection of processing parameters and measuring uncertainties

The primary parameters to be selected by the user are the cut-off frequencies for a low pass filter and the digitalization frequency. To briefly explain how these parameters were selected, let us recall that a frequency shift f_{shift} $(40MHz)$ is imposed by way of Bragg cells so that the raw signal delivered at detectors has a frequency equal to the sum $f_{doppler} + f_{shift}$. This signal is high pass filtered to eliminate the pedestal component of Doppler bursts, and then mixed with a sinusoid at the so-called mixer frequency f_{mixer}. The resulting signal after low pass filtering contains the frequency $f_{doppler} + f_{shift} - f_{mixer}$: this is the signal that is sampled at a rate corresponding to twice or more (as recommended for size measurements) the maximum frequency $Max[f_{doppler} + f_{shift} - f_{mixer}]$ gathered at the highest velocity of the flow. The low pass filter is set accordingly. The frequency $f_{doppler} + f_{shift} - f_{mixer}$ is measured for each Doppler signal using an FFT performed over the interval $\pm f_{sampling}$ using 16384 bins. The velocity resolution of the system is therefore $\frac{2\delta f_{sampling}}{16384}$. When performing size measurements, it is advantageous to impose moving fringes in order to obtain Doppler signals containing more than 10-15 periods and thus to ensure more accurate period and phase measurements. Such a condition is absolutely needed in the present flow situation since the axial velocity is typically ten times higher than the vertical velocity (without any frequency shift, a droplet with a perfectly an horizontal trajectory would not produce any modulated signal). In practice, we selected $f_{shift} - f_{mixer}$ at least equal to the maximum velocity in the flow (see table 3.3). The resulting resolution in the streamwise direction is about 5 mm/s while it is 2.6 mm/s in the vertical direction. These numbers correspond to an ideal signal: in practice the actual resolution could be lower due to the presence of noisy and/or disturbed Doppler bursts.

A second set of parameters correspond to validation criteria. For the frequency detection, the signal to noise ratio of the DSP is the most stringent. The recommended value is 0.3, and as seen in table. 3.4 even better values were ensured thanks to the optimization of the optical adjustment. For sizes, the default criteria on the phase evolution within a burst and on the coherency between phases as detected from two pairs of detectors prooved efficient enough.

Concerning the size resolution, the range of diameters is set by the optical arrangement. The phase is detected with an accuracy about 1% (except for phases less

TABLE 3.3: Frequency settings for digitalization and filtering, $f_{shift} = 40\ MHz$

$\phi_v \times 10^{-5}$	Channel	$F_{sampling},\ MHz$	$F_{mixer},\ MHz$	$F_{filter},\ MHz$	$V_{min}, m/s$	$V_{max}, m/s$
0.5	Green	2.5	39.80	2.5	-1.060	1.223
	Blue	2.5	43.90	2.5	1.355	4.074
1.0	Green	1.25	39.58	2.5	-1.474	1.437
	Blue	2.5	43.95	2.5	1.192	4.129
2	Green	1.25	39.59	2.5	-1.293	1.388
	Blue	2.5	43.96	2.5	1.000	4.002

than 3° relative to 0° or 360°). This is also the uncertainty on size measurements. Spray particles will inevitably pass through the Gaussian beam which causes an important interference of scattered light intensity by reflection and refraction. For that reason Bachalo [3] proposed the optimal light scatter angle of 30° given that the refraction is about 80 times bigger than the reflection assuming a homogeneously illuminated sphere.

The key parameter to consider in the uncertainty of size measurements is the D_{drop} to beam waist diameter D_{beam}, $\Gamma = \frac{D_{drop}}{D_{beam}}$ [2]. If the $\Gamma << 1$ particles are much smaller than the beam waist, hence a homogeneous illumination of particles is assumed and trajectory crossing effect is not a major problem. If $\Gamma >> 1$ meaning that the particles size is larger than the beam waist, the sequel will depend on the particle trajectory since reflection will start to combine with refraction. The phase-radius relationship becomes much more complex, and eq. 3.3 may lead to significant error. Given that all particles of our spray are spherical (see Section 6.3) and the beam waist of 645.1 μm is twice larger than the largest particle size of about 300 μm, there should not be any major trajectory influence on the measurement. Moreover, the validation rate on diameter measurements was always in the range of $80 - 90\%$ indicating that the trajectory influence is not significant in our experimental condition.

3.4.3.3 Optimisation of the analog threshold

As the analog threshold allows distinguishing between signals and noise, that variable must be carefully optimized. In that perspective, we examined the sensitivity of the measurements to this parameter combined with amplification as shown on the fig. 3.9. Typical variations in the velocity standard deviation are low: they are about 5% for a gain varying from $700V$ to $800V$ at a threshold 50 mV for Channel 1 and 25 mV for Channel 2. Similar figures hold on both velocity components for a fixed gain at $700V$ and for a threshold varying from $25 - 100$ mV. In addition, changing the threshold affects the number of particles detected by second. It also affects the data rate (number of validation per seconds) because noisy signal may not pass through the selection criteria. It is thus interesting to examine the evolution of these quantities. These tests have been performed at the highest volume fraction ϕ_v for which the noise amplitude is maximum because of light diffusion by nearby droplets. From Table 3.4 we could see that several values of threshold for both Channels 1 (for the settling velocity $V_{settling}$) and Channel 2 (for the axial velocity U) were tested using overall validation rate of detected particles and data counts

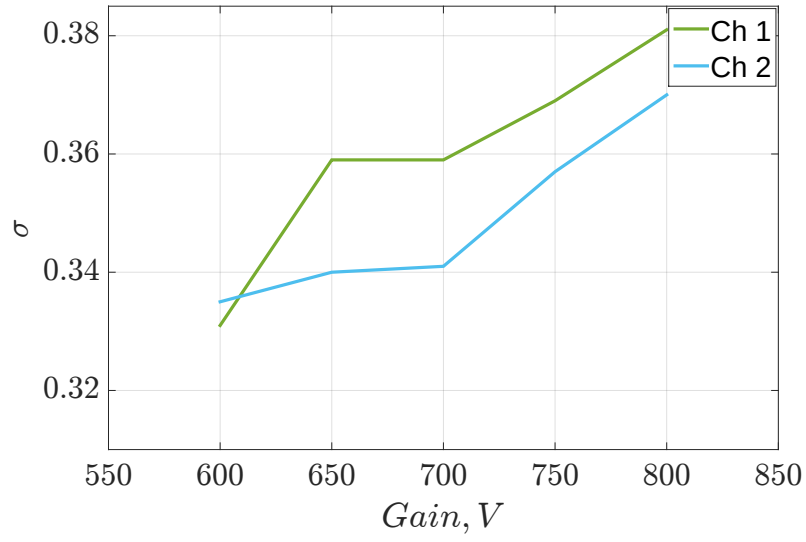

(a)

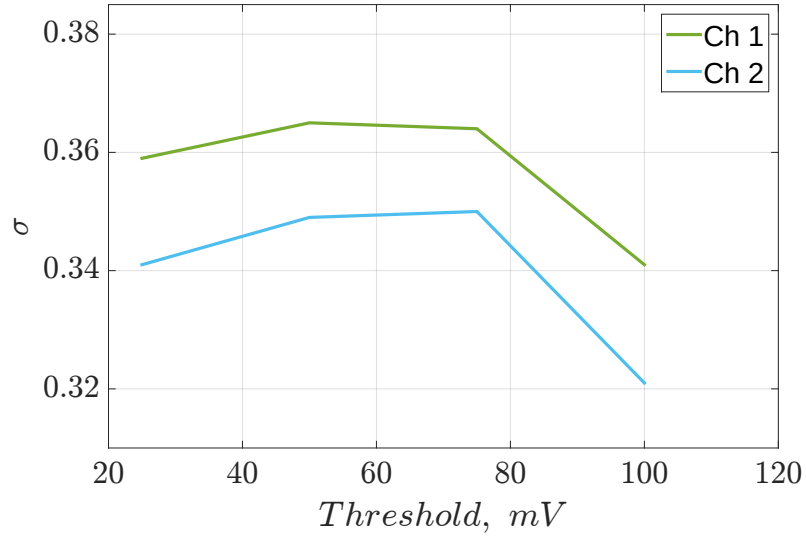

(b)

FIGURE 3.9: Sensitivity analysis on the velocity standard deviations (mm/s) changing (a) gain for a threshold of 50 mV for Channel 1 and 25 mV for Channel 2 (b) threshold for a gain of 700V

detected for a fixed measurement duration. In the case of Channel 1, the highest validation rate was achieved at the threshold of 100mV and data counts of 96000. For Channel 2 the validation rate was pretty much the same with a validation rate of 95% while the data counts was higher for the 75mV threshold. Thus, thresholds equal to 100mV for Channel 1 and to 75mV for Channel 2 were chosen.

We have already seen the photodetector gain was chosen to ensure the detection of very small particles. Yet, as increasing the gain adds up extra noise to that signal,

there is an optimum choice for the amplification. One way to test the correctness of the chosen gain is to look at the SNR (signal-to-noise-ratio) of collected signals. Table 3.5 summarises the settings which were tested to choose the appropriate gain. Clearly, the increase in the gain does not correspond always to better response. Hence, the optimum gain was chosen for both channels to be $700V$.

3.4.4 Test of the PDI on free of the fall velocity of isolated drops

To check the ability of the system to work with our water droplets, we decided to run a test with water droplets falling freely with no mean airflow nor turbulence involved. Free fall particle is subjected to gravity force

$$F_g = (\rho_p - \rho_f)\, g\, \frac{4}{3}\pi R^3 \tag{3.4}$$

where ρ_p is a density of particle, ρ_f is a density of fluid, R is a radius of spherical particle, g is a acceleration due to gravity. There is also a drag force F_d acting on a particle and using Newton's II law:

$$F_d = \frac{1}{2} \times c_D \times \rho_f \times {U_t}^2 \times \pi R^2 \tag{3.5}$$

where U_t is a terminal (Stokes) velocity and c_D is defined through Schiller-Neumann relationship:

$$c_D = \frac{24}{Re_p}(1 + 0.15 \times {Re_p}^{0.687}) \tag{3.6}$$

where $Re_p = \frac{2RU_t}{\nu}$ where ν is a dynamic viscosity of air.
Eliminating U_t from all equations above, we get:

$$U_t = \sqrt{\frac{4}{3}\frac{gD}{c_D}\frac{\rho_p - \rho_f}{\rho_f}} \tag{3.7}$$

TABLE 3.4: Testing analog threshold settings for the case of $\phi_v = 2.0 \times 10^{-5}$, gain=$700V$

Threshold, mV	50	75	100	150
Validation %, Ch1	20	65	75	70
Data Counts, Ch1	26000	114000	96000	85000
Validation %, Ch2	95	95	96	96
Data Counts, Ch2	106000	123000	110000	89000

TABLE 3.5: Testing gain settings for Channel 1 and Channel 2

Gain, V		Averaged SNR
Ch1	Ch2	
750	700	0.46
800	700	0.49
850	700	0.49
900	800	0.50
700	700	0.58

where $D = 2R$ is a diameter of the particle.
Using iterative procedure, the Stokes velocity $U_t = U_{St}$ can be determined. Using our system and just spraying the water droplets through the pulverisator in the wind tunnel with setting no mean flow, we were able to measure the terminal velocity U_{St} of the particles (see fig.3.10). In total there were 1000 statistics acquired for this

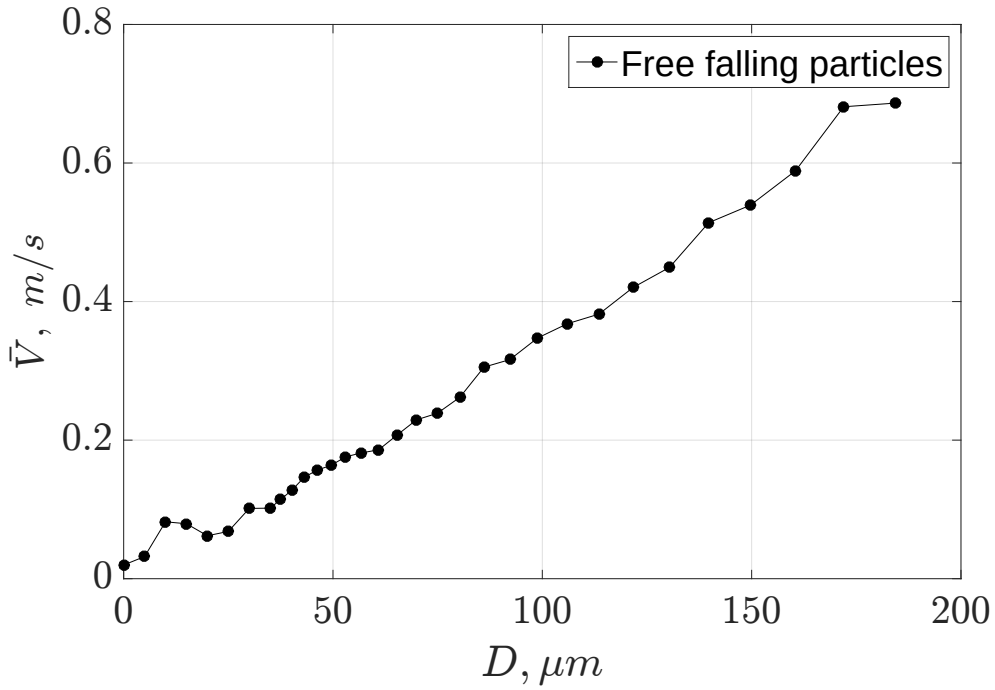

FIGURE 3.10: Velocity of drops under free fall measured with PDI

measurement. In this test, the droplets experience a free fall over a distance about $15 - 20$ cm before reaching the probe volume. Over such a distance, droplets of diameter larger than about $70 - 80$ μm do not reach 99% of their terminal velocity [16]. Besides, very few data were collected for drop sizes below about 20 μm. Hence, the size range corresponding to reliable measurements is comprised between 20 and 70 μm. Considering the interval between $D > 20$ μm and $D < 50$ μm (see fig. 3.11)

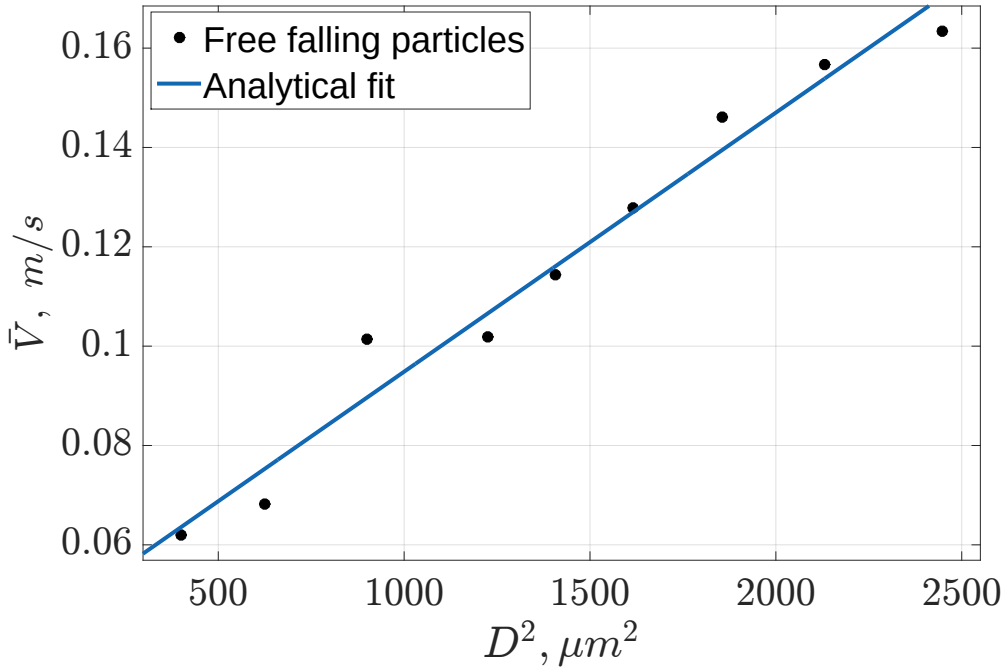

FIGURE 3.11: Fit of $\bar{V} m/s$ vs $D^2, \mu m^2$ of experimental data, D is in the interval [20 μm; 50 μm]

a fit was estimated:

$$V = 5.215 \times 10^{-5} D^2 + 0.0427 \tag{3.8}$$

where the constant value of 0.0427 is related to alignment issue (the latter is discussed in the Section 6.4.4). The trend for $D > 20$ μm & $D < 50$ μm is in a good agreement with the theoretical predictions that is $V \sim D^2$. The maximum difference between the fit and experimental measurements is 1.18 cm/s. The dispersion of the experimental data with regards to the fit is 6.3 mm/s. This value could be used as an indication of the actual uncertainty when measuring the settling velocity $V_{settling}$.

3.4.5 Convergence

The convergence of the collected data in the selected flow conditions was analysed by observing the behavior of $\bar{U}$, $U\prime$, $\bar{V}_{settling}$, $V\prime$ (see fig. 3.12, 3.13) according to the number of acquired statistics. The mean and standard deviation exhibiting a well converged behavior after sampling 4×10^5 data points. The values for convergence dispersion are presented in table 3.6. Convergence dispersion with regards to the mean velocity $\bar{U}$ is about 1.78%, and for the mean velocity $\bar{V}_{settling}$ it is about 4.98%. The values of $U\prime$, $V\prime$ are converged up to 0.58% and 0.65%. First 30 seconds of the

TABLE 3.6: Convergence dispersion with regards to the mean values of $\bar{U}$, $\bar{V}_{settling}$ and standard deviations $U\prime$, $V\prime$

$\phi_v, \times 10^{-5}$	$\delta\bar{U}, \%$	$\delta\bar{V}_{settling}, \%$	$\delta U\prime, \%$	$\delta V\prime, \%$
0.5	0.19	2.55	0.12	0.65
1.0	0.75	4.98	0.58	0.59
2.0	1.78	1.10	0.14	0.64

flow of injected particles were not sampled in order to allow the flow to develop to a stationary regime. The corresponding measurement duration was set to 60 seconds, that amounts for $300\tau_L$ where $\tau_L = 0.2s$. Hence the flow conditions are properly sampled.

The data rate of the acquisition for both Channels 1 (Green) and 2 (Blue) is given in Table 3.7. The data rate is minimum for both channels at $\phi_v = 0.5 \times 10^{-5}$ which could be due to droplets spray being very dilute, and it's maximum for $\phi_v = 1.0 \times 10^{-5}$ due to optimized experimental conditions for the PDI system (nor dilute, neither very concentrated). It is clear that the data rate for Channel 2 is systematically twice higher than Channel 1. It is noticeable that the validation rate for Channel 1 (measurement of settling V) is decreasing with an increase in the volume fraction ϕ_v which could be explained by light scattering due to the presence of more particles per unit volume. Meantime, validation rate for Channel 2 measuring the axial U velocity stays constant at around 99% meaning that there were less problems in detection of particles streamwise velocity.

TABLE 3.7: Acquisition parameters

$\phi_v \times 10^{-5}$	Data rate, Hz		Validation rate, %		N of points, $\times 10^6$	
	Ch 1	Ch 2	Ch 1	Ch 2	Ch 1	Ch 2
0.5	70	150	78	99	1.4	1.1
1.0	300	700	67	99	2.7	1.3
2.0	200	230	56	99	0.9	1.2

3.4.5.0.1 Parameter Space The parameter space for PDI data is shown on the fig. 3.14. The flow velocity was kept constant around $2.5m/s$, resulting in almost constant R_λ at around 185, and almost constant St at around 0.6. However, the volume fraction ϕ_v was changed 4 times from 0.5×10^{-5} to 2.0×10^{-5}.

This set of data is intended to give us an idea of effects of volume fraction ϕ_v on settling velocity $V_{settling}$. Furthermore, we should be able to obtain Eulerian

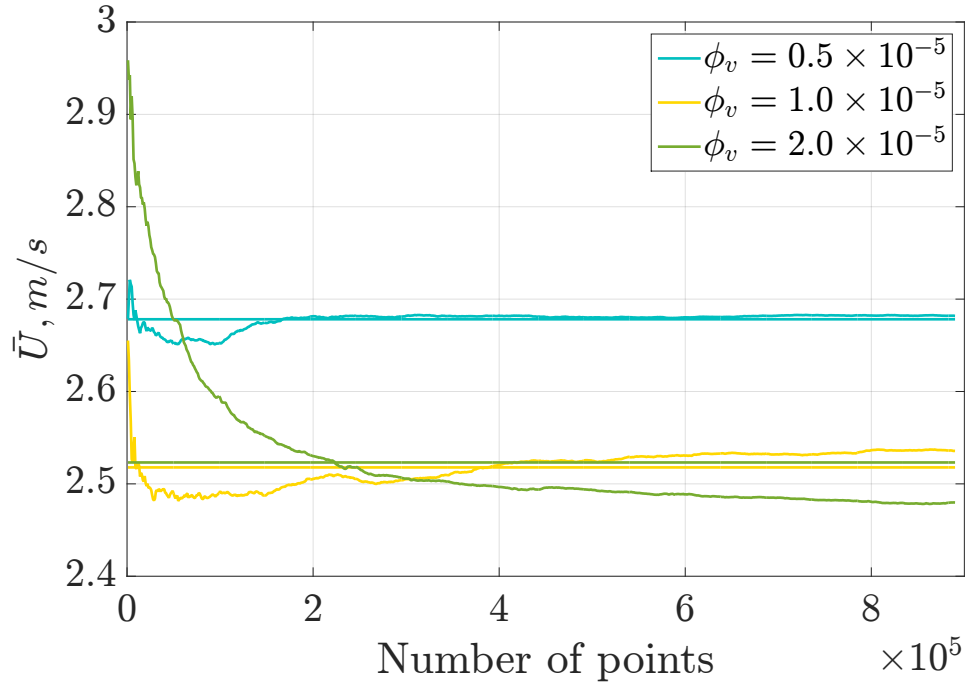

(a)

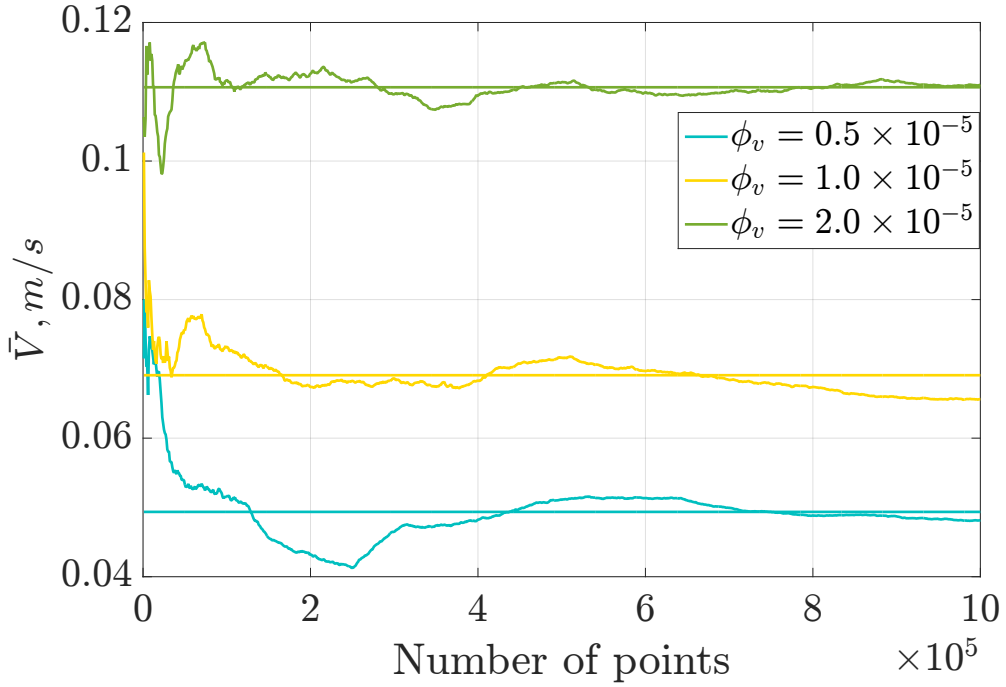

(b)

FIGURE 3.12: Convergence plots of mean velocity of (a) axial U (b) settling V

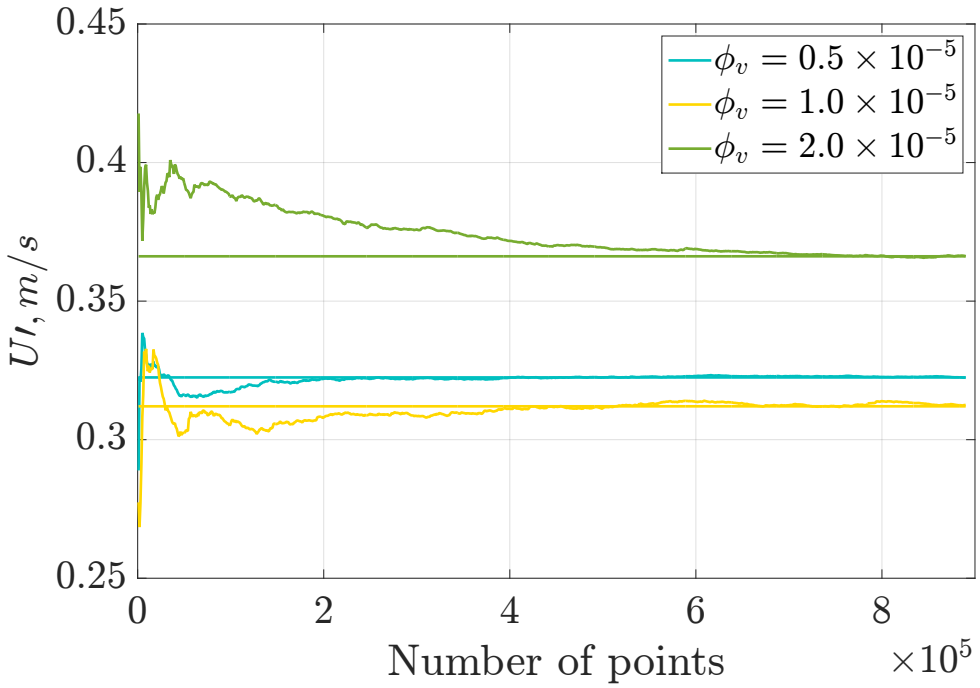

(a)

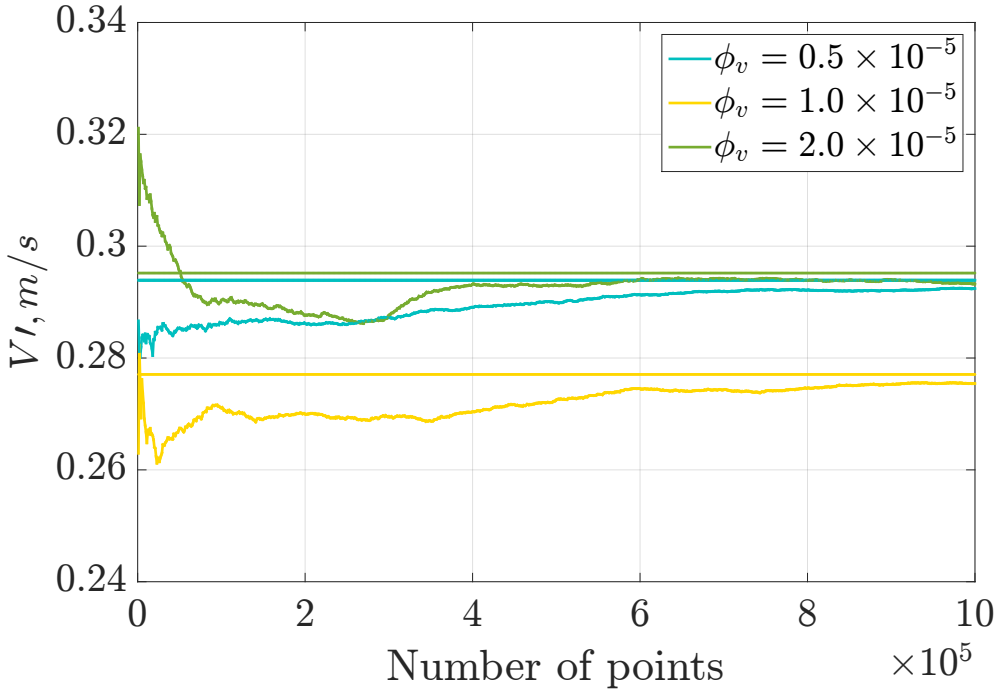

(b)

FIGURE 3.13: Convergence plots of standard deviation of velocity of (a) axial $U\prime$ (b) settling $V\prime$

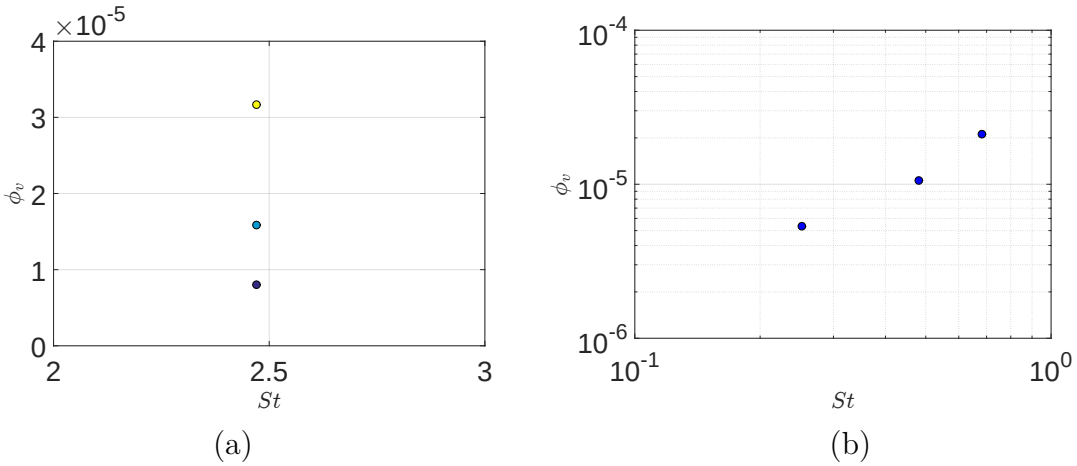

FIGURE 3.14: (a) Map of explored control parameters. (b) Corresponding map of experimental parameter space.

statistics of the particles detection time, axial U velocity, $V_{settling}$ measurements of velocity and simultaneous measurement of the diameter D. Additionally, we should be able to investigate the conditional statistics of velocity of the particles $V_{settling}$ with local concentration field ν in $1D$, and also conditional statistics of $V_{settling}$, concentration field ν and diameter of the particles $D, \mu m$.

Chapter 4

Structure of Clusters and Voids

4.1 Analysis of Clustering

In this Chapter we will present a diagnosis of clustering based on 2D LPT measurements, with the aim to disentangle the specific influence of particles inertia represented by St, turbulence characterised by Re_λ and collective effects given by the volume fraction ϕ_v in the explored parameter space shown on fig.4.1.

There are many different diagnoses for clustering that have been used in the scientific community in the past such Radial Distribution Function, fractal dimension D_2, box counting, Voronoï tesselations etc. In this analysis we will use Voronoï analysis, which has recently become a widely used technique to quantify clustering. This analysis allows us not only quantify the degree of clustering, but also easily identify structures as clusters and voids, and subsequently, analyse their geometry.

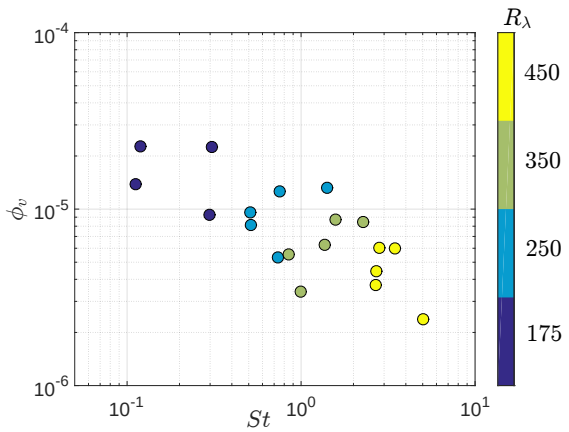

FIGURE 4.1: Experimental control parameter space for PTV data

4.1.1 Voronoï tesselation analysis of clustering

Voronoï tesselations, which have been proven to be a good estimator to quantify the clustering of particles [23, 47, 49, 68, 71, 55] is used to diagnose the appearance and the importance of preferential concentration.

Briefly, the main properties of Voronoï tesselation analysis relevant to clustering diagnosis are summarized as follows. For a given set of N particles $\mathcal{P}_{i\in[1,N]}$ with known 2D-positions (x_i, y_i) (the concepts are described here in 2D but they can be extended to any dimension), the associated Voronoï tesselation is the mapping of space into N cells $\mathcal{C}_{i\in[1,N]}$ (*Voronoï cells*) defined such as any point within the cell $\mathcal{C}_i$ is closer to the particle $\mathcal{P}_i$ than to any other particle $\mathcal{P}_{j\neq i}$. Figure 4.2a(top) shows an example of particles randomly distributed according to a standard Random Poisson Process (RPP) and the corresponding Voronoï tesselation diagram. The area $\mathcal{A}_i$ of the cell $\mathcal{C}_i$, is representative of the local seeding density around the particle particle $\mathcal{P}_i$: the smaller the Voronoï area, the larger the local density. The RPP case is considered as the reference situation, characteristic of a system free of any clustering and of any particular order.

Figure 4.2a(bottom) represents the probability distribution function (PDF) of the Voronoï areas for a RPP situation. There is no known analytical expression of the shape of this distribution for the RPP case, although it is known to be well approximated by a Gamma function [23]. The standard deviation of the normalized Voronoï area $\mathcal{V} = \mathcal{A}/\langle\mathcal{A}\rangle$ is however known analytically, and has a value $\sigma_\mathcal{V} \simeq 0.53$. Note that the mean Voronoï area $\langle\mathcal{A}\rangle$ does not carry any structural information and is simply related to the global seeding density of particles in the field of view. Statistics of Voronoï areas are therefore generally discussed in terms of the normalized area $\mathcal{V}$.

To illustrate how Voronoï analysis can be used to diagnose the spatial distribution of particles in space, figures 4.2b&c(top) represent respectively particles distributed on a regular grid (with a small local random displacement) and particles randomly distributed in the vicinity of a few given random locations, hence mimicking the existence of clustering.

Figures 4.2b&c(bottom) show that for the quasi-regular case, the PDF of Voronoï areas is narrower than for the RPP case (for a perfect regular arrangement of particles on a cartesian mesh, all cells will have the same Voronoï area, strictly equal to the mean), while for the clusterized situation the PDF of Voronoï areas is broader than for the RPP case. This is also expected, as small areas (high concentration regions) are expected to be over-represented within clusters, as well as large areas

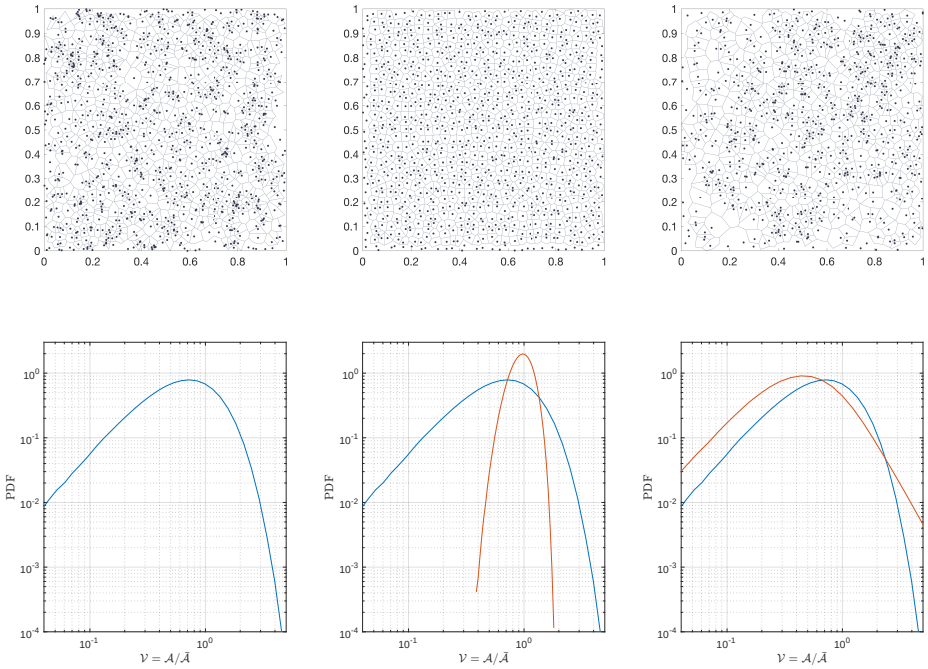

FIGURE 4.2: Voronoï tesselation diagram for synthetically-generated particle positions (top) and corresponding PDF of Voronoï areas (bottom) for (a) a Random Poisson Process (RPP) case, (b) a quasi-regular case (more ordered than random) and (c) a particle distribution with clusters and voids. In all the figures at the bottom, the blue line represents the PDF of the RPP case. The standard deviation of the normalized Voronoï area ($\mathcal{V} = \mathcal{A}/\bar{\mathcal{A}}$) are rank ordered as: $\sigma_{\mathcal{V}}^{regular} < \sigma_{\mathcal{V}}^{RPP} < \sigma_{\mathcal{V}}^{cluster}$.

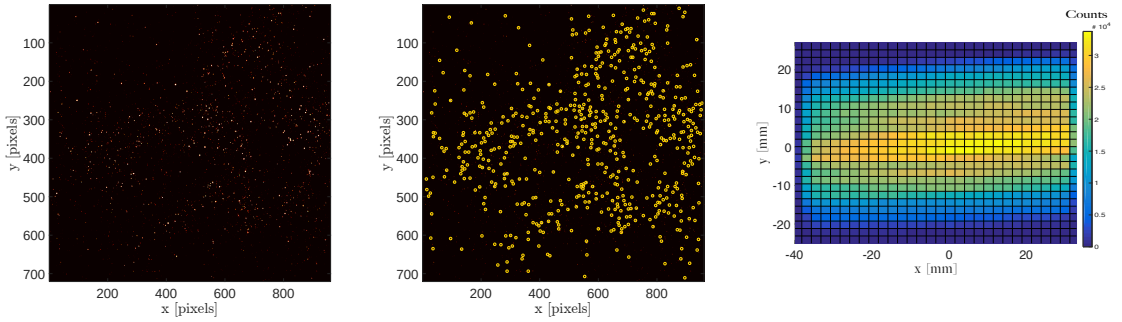

(a) (b) (c)

FIGURE 4.3: (a) Typical raw image, (b) detected particles, (c) probability of detected particles. The large scale inhomogeneity of the detection reflects the gaussian intensity profile in the laser illumination.

within voids. For a given (or measured) particle distribution, comparing the PDF of Voronoï areas to the RPP PDF therefore allows to diagnose the appearance of clustering. In particular, the width of the PDF, characterized by the standard deviation $\sigma_{\mathcal{V}}$ of the normalized Voronoï area gives a simple measure of the clustering level, the RPP value $\sigma_{\mathcal{V}}^{RPP} \simeq 0.53$ being the reference value characteristic of a pure random (non-clusterized) situation, while in presence of clustering we should have $\sigma_{\mathcal{V}} > \sigma_{\mathcal{V}}^{RPP}$.

4.1.2 Illumination inhomogeneity correction

Illumination inhomogeneity, shown in figure 4.3c, imposes additional image processing to unbias the particle detection prior to diagnosing preferential concentration. As a consequence of the Gaussian intensity profile across the laser plane, particles are statistically more probable to be detected in the center of the visualization domain. Figure 4.3a shows an example of a raw recorded image and figure 4.3b indicates the corresponding particle detection. The map of probability of particle detection (figure 4.3c), clearly shows that particles are more likely to be detected in the center of the image. Analyzing the clustering properties of particles in such conditions, without any correction, may lead to the errors in the diagnosis of the existence of clustering, simply because due to illumination issues.

To prevent such a bias, previous studies have cropped images [55], limiting the analysis to the central region, where illumination is relatively homogeneous. Doing so, however, requires many more images for statistical convergence of the analysis, and also biases the cluster/void analysis, as large structures cannot be detected.

We use an alternative approach, allowing the use of the full image with an appropriate correction to undo the bias in the estimation of the area of Voronoï areas where illumination is non-homogeneous. A corrective local *contraction* factor is applied to the raw Voronoï cells in regions with lower illumination to correct for them being statistically larger. We illustrate the method using a synthetically-generated random distribution of particles with a smooth gaussian modulation.

Figure 4.4a represents one realization of the synthetically-generated particle

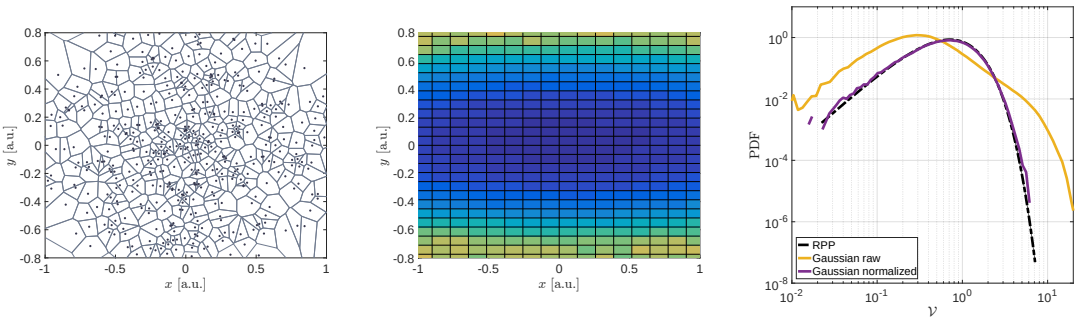

(a) (b) (c)

FIGURE 4.4: (a) Example of one realization of particles randomly distributed, with a large scale centered Gaussian modulation of the probability of presence (particles are more likely to be detected near the center than in the borders), mimicking the experimental illumination non-homogeneity due to the Gaussian profile of the laser sheet. (b) Coarse grained field of the average local Voronoï area $\mathcal{A}_{mean}(x, y)$, estimated from 1000 realizations as in figure (a). (c) PDF of Voronoï areas, estimated from 1000 synthetic images (with a few hundreds of particles in each image) for: (black dashed line) a random homogeneous RPP reference situation; (yellow solid line) a random but non-homogeneous distribution as illustrated in (a) and (purple solid line) the same random non-homogeneous distribution where Voronoï areas are locally corrected by the contraction field $\mathcal{A}_{mean}(0,0)/\mathcal{A}_{mean}(x, y)$ shown in (b).

field. Particles are randomly distributed following an RPP, but with a large-scale gaussian modulation mimicking the experimental bias in the center of the images. Figure 4.4c shows that, although no clustering mechanism is present, the PDF of normalized Voronoï areas $\mathcal{V} = \mathcal{A}/\langle\mathcal{A}\rangle$ deviates significantly from the RPP case, simply because of the large scale modulation of the probability of particle location. The standard deviation of $\mathcal{V}$ is $\sigma_{\mathcal{V}} \simeq 1.5 > \sigma_{\mathcal{V}}^{RPP} = 0.53$. To correct this bias, the coarse-grained field of the local average Voronoï area, $\langle\mathcal{A}(x, y)\rangle/\langle\mathcal{A}(0, 0)\rangle$ (Figure 4.4b) is estimated from an ensemble of 1000 realizations. The color of each rectangular zone in Figure 4.4b represents the average value of the Voronoï area of

particles detected within that zone. For smooth and large-scale inhomogeneities, as the one expected for instance for illumination inhomogeneities related to Gaussian profile of the laser, the number of zones used for the coarse-grained field is not a critical parameter. This coarse-grained field is then used as a contraction factor, normalized to be maximum and equal to one where the particle probability is maximum, so that the Voronoï area $\mathcal{A}$ of a particle $\mathcal{P}$, detected at a position (x, y) is corrected to become $\mathcal{A}^* = \mathcal{A} \cdot \langle \mathcal{A}(0,0) \rangle / \langle \mathcal{A}(x,y) \rangle$.

The PDF of the corrected Voronoï areas $\mathcal{V}* = \mathcal{A}^* / \langle \mathcal{A}^* \rangle$, is shown in Figure 4.4 and found to exactly match the reference RPP PDF, proving that this correction method effectively removes the bias. The same procedure is used to unbias the Voronoï area statistics from the experimental images.

4.2 Results

4.2.1 Deviation from Randomness of the Particle Concentration Field: Standard deviation σ_ν of the Voronoï area distributions

4.2.1.1 PDF of Voronoï areas

Figure 4.5 represents a typical Voronoï diagram from an experimental image. Colored structures represent detected clusters, further discussed below. Thousands of such tesselations are obtained for each experimental condition. PDFs of normalized corrected Voronoï areas are shown in Figure 4.6a, where the departure from the RPP case can be clearly seen. These experimental PDFs of Voronoï areas are significantly different from one experiment to another. This suggests an important influence of experimental control parameters (St, Re_λ, ϕ_v) on the degree of clustering.

Figure 4.6b shows the PDF of $\log(\mathcal{V})$ (centered by the mean and normalized by the standard deviation), emphasizing the quasi log-normal distribution of the statistics of Voronoï areas, as previously reported [47, 55]. This quasi-lognormality justifies the idea that the statistics of $\mathcal{V}$ can be described by a single parameter (recall that $\langle \mathcal{V} \rangle = \infty$ by construction), generally the standard deviation of $\mathcal{V}$, $\sigma_\mathcal{V}$, to quantify the departure from the RPP distribution.

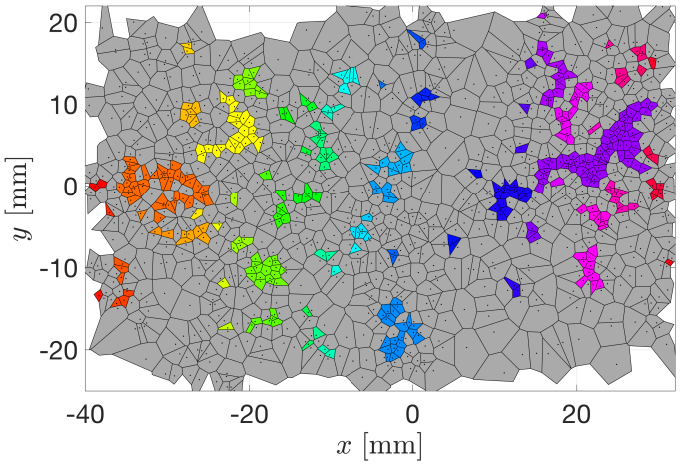

FIGURE 4.5: Example of Voronoï diagram for one typical image of our experiment. Colored regions indicate clusters, defined following the procedure described in sec. 4.2.3

4.2.1.2 Standard deviation of Voronoï

Figure 4.7 represents the difference between the experimental $\sigma_{\mathcal{V}}$ and the RPP value ($\sigma_{rel} = \left(\sigma_{\mathcal{V}} - \sigma_{\mathcal{V}}^{RPP}\right)/\sigma_{\mathcal{V}}^{RPP}$) as a function of Stokes number, Re_λ and ϕ_v. It is found that, for all experiments, $\sigma_{rel} > 0$, consistent with the existence of clustering. No clear trend with St can be identified. The most striking observation from these figures is the strong dependency of $\sigma_{\mathcal{V}}$ on the volume fraction.

This is highlighted in figure 4.7c where, for every Reynolds number, σ_{rel} is observed to increase quasi-linearly with ϕ_v. Trends with Reynolds number are more difficult to extract from this simple projection, although figure 4.7a, where the Reynolds number dependency is encoded in the color of the symbols, suggests an increase of $\sigma_{\mathcal{V}}$ with Re_λ.

To go further into the quantitative analysis of the dependencies of $\sigma_{\mathcal{V}}$ with the three parameters (St, Re_λ, ϕ_v), we consider the variable $\sigma_{rel} = (\sigma_{\mathcal{V}} - \sigma_{\mathcal{V}}^{RPP})/\sigma_{\mathcal{V}}^{RPP}$, which measures the relative deviation from the RPP case. We seek, as a first trial, for dependencies of σ_{rel} on (St, Re_λ, ϕ_v), as power law scalings:

$$\sigma_{rel} = K St^{\alpha} Re_\lambda^{\beta} \phi_v^{\gamma}, \tag{4.1}$$

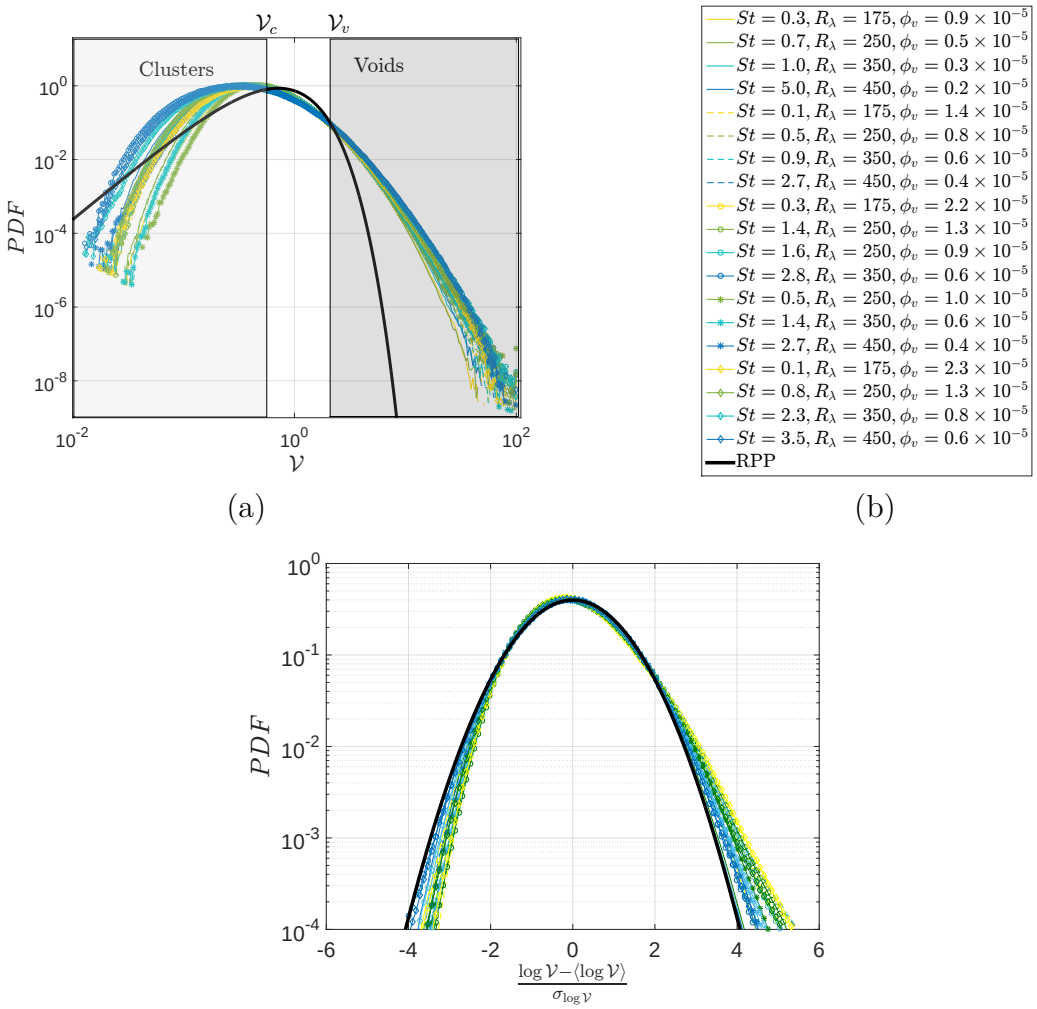

FIGURE 4.6: (a) PDF of the corrected normalized Voronoï areas $\mathcal{V}$ for all experiments. The solid black line shows the RPP distribution. (b) Centered, normalized PDF of $\log(\mathcal{V})$. The solid black line shows a gaussian distribution with variance 1.

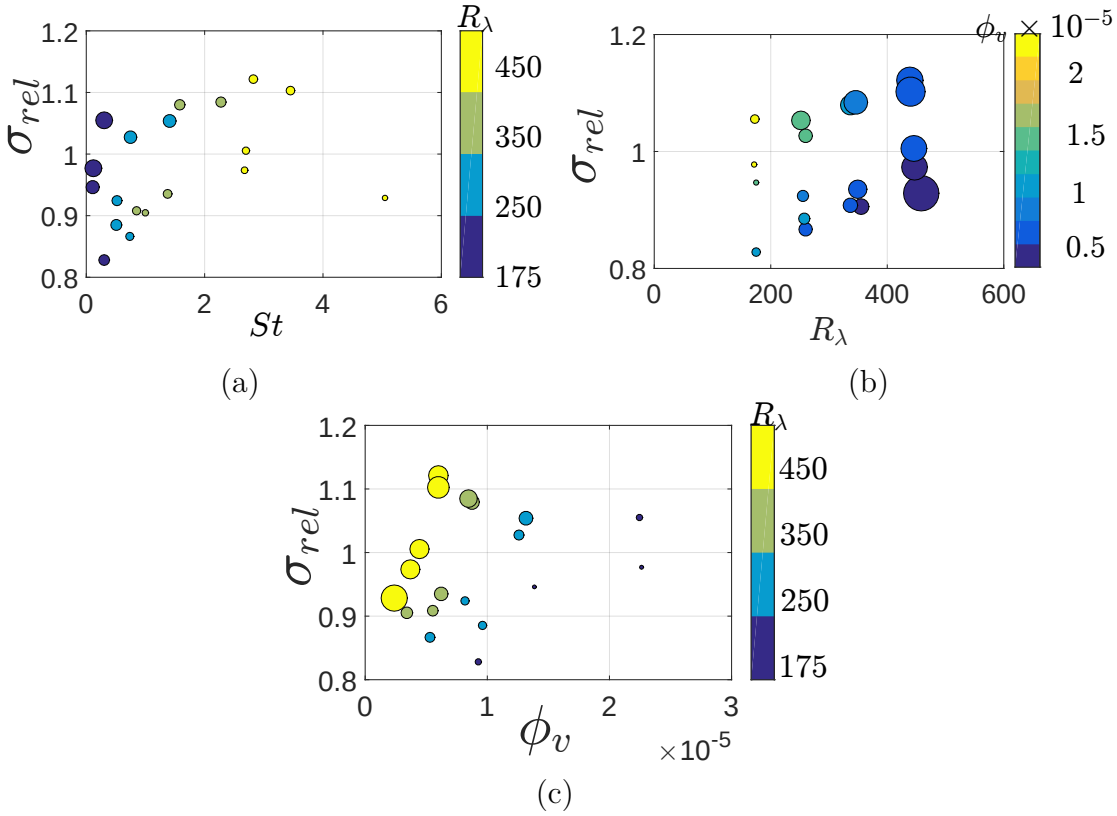

FIGURE 4.7: (a) Standard deviation σ vs St. Symbol colors represent the Reynolds number, while the size of the symbols encodes the volume fraction (larger symbols correspond to experiments at larger volume fraction). (b) Standard deviation σ vs Re_λ. Symbol colors indicate the volume fraction, while the size of the symbols encodes the Stokes number (larger symbols correspond to experiments with larger Stokes numbers). (c) Standard deviation σ vs ϕ_v. Symbol colors reflect the Reynolds number, while the size of symbols encodes the Stokes number (larger symbols correspond to experiments with particles at larger Stokes number).

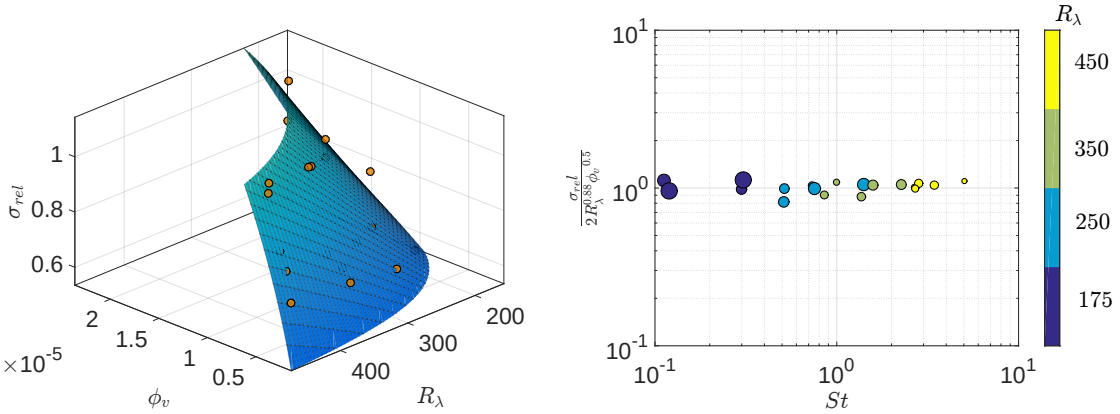

FIGURE 4.8: (a) σ_{rel} as a function of ϕ_v and Re_λ with a power law fit $\sigma_{rel} \propto Re_\lambda^\beta \phi_v^\gamma$. (b) σ_{rel} compensated by $Re_\lambda^\beta \phi_v^\gamma$. Best fit is obtained for $\beta \simeq 0.88$ and $\gamma \simeq 0.5$.

Based on the observations from figure 4.7, we first determine β and γ by a two-variables fit of the σ_{rel} data as a function of Re_λ and ϕ_v, neglecting the dependency on St in a first approximation. This is partially supported by the lack of a consistent evolution with Stokes number on figure 4.7a. The corresponding data and fit are shown in fig. 4.8a, where the best fit is obtained for $\beta \simeq 0.88 \pm 0.2$ and $\gamma \simeq 0.5 \pm 0.15$. The dependency of σ_{rel} with St is then explored by plotting the compensated quantity $\frac{\sigma_{rel}}{Re_\lambda^\beta \phi_v^\gamma}$, as a function of St in figure 4.8b. The data points present very little scatter, with no trend observed (best power law fit results in a exponent $\alpha \simeq 0.0 \pm 0.05$).

Overall, the dependency of the standard deviation of the Voronoï area distribution with the three controlling parameters (St, Re_λ, ϕ_v) results in the empirical scaling:

$$\sigma_{rel} = \frac{\sigma_\mathcal{V} - \sigma_\mathcal{V}^{RPP}}{\sigma_\mathcal{V}^{RPP}} \simeq 2\ St^{0.0} Re_\lambda^{0.88} \phi_v^{0.5}. \tag{4.2}$$

Interestingly, our results point towards a dominant dependency of the clustering on the turbulent Reynolds number, with a smaller dependency on volume fraction and no dependency on Stokes number. These observations will be further discussed in section 4.3.

4.2.2 Contribution of Clusters and Voids to the Standard Deviation of the Voronoï Area Distribution

So far we have presented only global statistics indicating the existence of clustering. Now we will identify clusters and voids to look in a more detailed way at contioned statistics in clusters, voids and intermediate regions between clusters and voids.

We define clusters and voids in fig. 4.6a, from the thresholds $\mathcal{V}_c$ and $\mathcal{V}_v$ [47, 49], corresponding to the points where the experimental Voronoï area PDF is above (more probable than) the RPP. Clusters are defined as particle ensembles with adjacent Voronoï cells whose area $\mathcal{V} < \mathcal{V}_c$ while voids correspond to cells whose area $\mathcal{V} > \mathcal{V}_v$. In the experiments reported here, the two cutoffs are insensitive to flow conditions, and their values, $\mathcal{V}_c = 0.6$ and $\mathcal{V}_v = 2.1$, are equal to those in previous studies at lower turbulent Reynolds numbers [55, 56]. The invariance of these intersections remains to be understood.

The standard deviation $\sigma_\mathcal{V}$ of Voronoï areas represents the second moment of the PDF of $\mathcal{V}$. One can therefore argue that large areas (*i.e.* voids) contribute more to $\sigma_\mathcal{V}$ than small areas (*i.e.* clusters). We can indeed write $\sigma_\mathcal{V}^2$ as

$$\sigma_\mathcal{V}^2 = {\sigma_c}^2 + {\sigma_i}^2 + {\sigma_v}^2 = \int_0^{\mathcal{V}_c} \left(\mathcal{V} - \bar{\mathcal{V}}\right)^2 PDF(\mathcal{V})\mathrm{d}\mathcal{V} + \int_{\mathcal{V}_c}^{\mathcal{V}_v} \left(\mathcal{V} - \bar{\mathcal{V}}\right)^2 PDF(\mathcal{V})\mathrm{d}\mathcal{V} + \int_{\mathcal{V}_v}^{\infty} \left(\mathcal{V} - \bar{\mathcal{V}}\right)^2 PDF(\mathcal{V})\mathrm{d}\mathcal{V}, \tag{4.3}$$

where the three terms give the contribution of clusters, intermediate areas and voids (denoted as σ_c, σ_i and σ_v), respectively, to the total standard deviation of Voronoï areas.

For the RPP, the three contributions are comparable: $\sigma_c^{RPP} = 0.29$, $\sigma_v^{RPP} = 0.30$ and $\sigma_i^{RPP} = 0.32$. Note that we used the experimental cluster and voids thresholds $\mathcal{V}_\rfloor$ and $\mathcal{V}_\sqsubseteq$ respectively to estimate the quivalent contributions for the RPP case. Obviously $\sigma_c^{RPP2} + \sigma_i^{RPP2} + \sigma_v^{RPP2} = 0.53^2$ as expected. The questions are: how do these contributions change for inertial particles and how do they evolve with the controlling parameters ?

The experimental data shows that σ_v^2 represents on average $\approx 75\%$ ($69\% - 78\%$, depending on the experimental conditions) of the total variance $\sigma_\mathcal{V}^2$, σ_c is only $\approx 17\%$ ($14\% - 18\%$) and $\sigma_i^2 \approx 8\%$ ($6\% - 12\%$). This partition clearly shows a stronger contribution of voids to the total variance compared to clusters, in contrast to the random case, and as expected from the extended tails of the inertial particle Voronoï PDF. The standard deviation of Voronoï areas, as commonly discussed in particle preferential accumulation, is therefore essentially a measure of the distribution of voids.

From this point of view, we have analyzed how each of the three contributions, clusters, voids and intermediate areas, evolve with flow parameters. For each contribution, the relative deviation is compared to the RPP case($\sigma_{rel,*} = \frac{\sigma_* - \sigma_*^{RPP}}{\sigma_*^{RPP}}$, with $* = c, i$ or v). Following a similar procedure as described above, we determine the scalings of these quantities with the experimental control parameters St, Re_λ and volume fraction ϕ_v:

$$\sigma_{rel,c} = 0.33 \times {Re_\lambda}^{1.05\pm0.44} \times {\phi_v}^{0.5\pm0.26} St^{0.01\pm0.07}, \tag{4.4}$$

$$\sigma_{rel,v} = 4.39 \times {Re_\lambda}^{0.79\pm0.18} \times {\phi_v}^{0.46\pm0.11} St^{0.01\pm0.03}, \tag{4.5}$$

$$\sigma_{rel,i} = 0.35 \times {Re_\lambda}^{0.66\pm0.17} \times {\phi_v}^{0.41\pm0.09} St^{0.00\pm0.03}, \tag{4.6}$$

These power law fits show that although the strongest contribution comes indeed from the voids, the dependencies with experimental parameters are comparable for all zones, with a leading role for the Reynolds number, a lesser influence of the volume fraction and practically no dependency on Stokes number, within the range of explored parameters.

4.2.3 Geometry of Clusters and Voids in the Particle Concentration Field

Figure 4.9 presents the PDF of cluster and void areas, before (top) and after (bottom) normalization. The cluster PDFs exhibit a distinct peak, indicating the existence of a typical characteristic cluster dimension, in agreement with other previous experimental findings [1, 55, 56]. Figure 4.9c shows that the PDFs of the normalized cluster areas $A_c / < A_c >$ follow an algebraic decay with an exponent $n_c \approx -5/3$, for areas larger than the most probable value.

Similar trends are observed for the void areas PDFs, although the range of sizes of the voids is naturally larger than that of the clusters (by a factor about 10). The exponent n_v for the decay of the PDF of normalized void area follows a similar trend to the clusters ($n_v \approx -5/3$). These qualitative features are found to be robust for all experimental conditions. Algebraic decay of the cluster and void areas have been previously reported in several previous experimental and numerical studies [10, 32, 47, 55, 56] and is in agreement with a simple model proposed in [32] which predicts

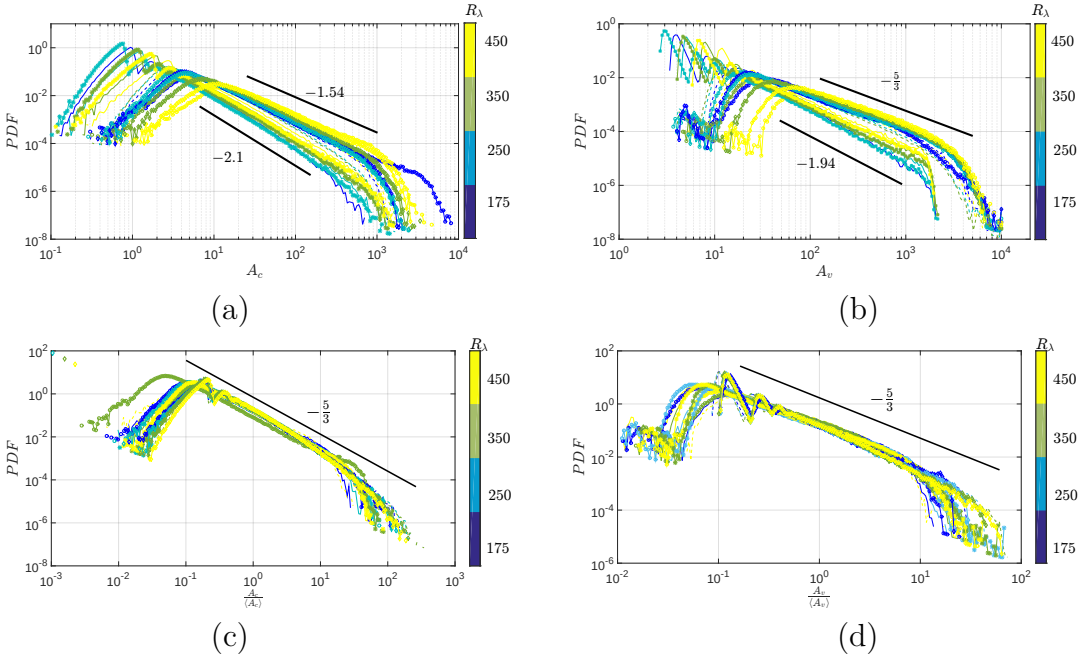

FIGURE 4.9: PDFs of clusters areas A_c (a) and voids areas A_v (b). Figs. (c) and (d) show the same PDFs for the areas normalized by the mean.

an algebraic decay for the PDF of void areas with a $-5/3$ exponent. In this model, the distribution of voids mimics the self-similar distribution of eddies across the turbulent energy cascade, suggesting that clustering (and voiding) of inertial particles is not only driven by small scales but reflects the self-similarity of the carrier turbulence. Unlike in the original work proposing the model, where it applied across the entire spectrum (from η to L_{int}), in these experiments, the $-5/3$ decay holds between a lower length scale comprised between 3 and 10η, depending on flow conditions, and an upper length scale slightly below L_{int}. The largest length scales are not fully resolved in the experiments since the images are about L_{int}, so the tails in the right hand side of the distributions (Figure 4.9) are not statistically significant.

Fig. 4.9 shows that the characteristic cluster size vary with the Reynolds number. Fig. 4.10 quantifies the dependency of the $\frac{\sqrt{\langle A_c \rangle}}{\eta}$ with St, Re_λ and ϕ_v. At first sight, these plots seem to suggest that cluster size increases with increasing Stokes and Reynolds number and decreases with increasing volume fraction. However, as for the previous discussion on $\sigma_\mathcal{V}$, these trends are quite complex. Fig. 4.10a shows that the increase of $\frac{\sqrt{\langle A_c \rangle}}{\eta}$ with St is very much connected to that in Re_λ (whose value is encoded in the colors of the symbols). Similarly, figs. 4.10b&c also point towards a direct connection between trends of $\frac{\sqrt{\langle A_c \rangle}}{\eta}$ on Re_λ and ϕ_v. To obtain better insight into the specific sensitivity to each controlling non-dimensional parameter,

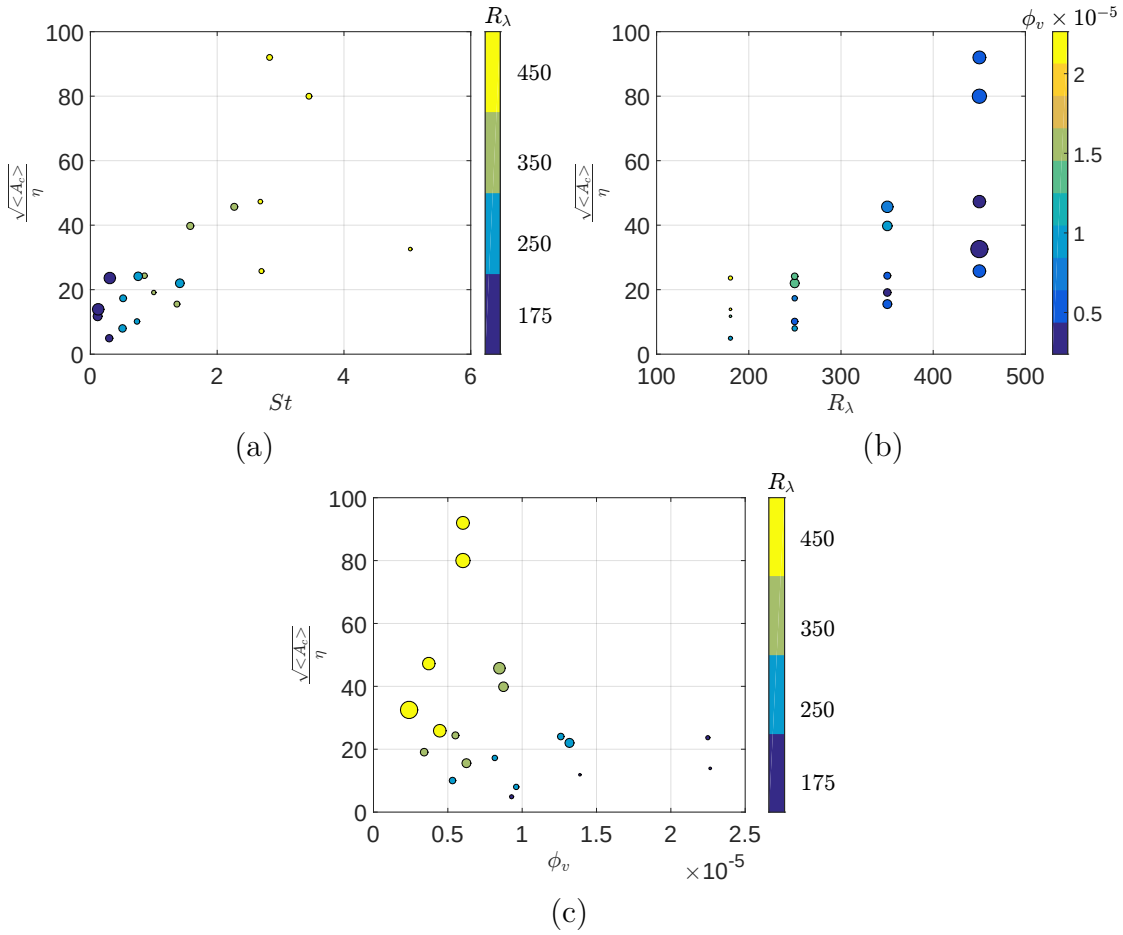

FIGURE 4.10: Dependency of the average cluster size on Stokes number (a), Reynolds number (b) and volume fraction (c). In (a), the color of the symbols indicates the Reynolds number and the size of the symbols reflects the volume fraction. In (b), the color of the symbols indicates the volume fraction and the size of the symbols reflects the Stokes number. In (c), the color of the symbols indicates the Reynolds number and the size of the symbols reflects the Stokes number.

as for previous study of σ_{rel}, power law fits are computed, in the form:

$$\frac{\sqrt{\langle A_c \rangle}}{\eta} = K' St^{\alpha'} Re_\lambda^{\beta'} \phi_v^{\gamma'} \tag{4.7}$$

First, the joint dependencies on Re_λ and ϕ_v, shown in fig. 4.11a, are computed.The best fit is obtained for $\beta' = 4.4 \pm 1.3$ and $\gamma' = 1.6 \pm 0.7$. The dependency of cluster size with volume fraction therefore appears to be lesser compared to the Reynolds number dependency. The remaining dependency on St is then probed by fitting the normalized quantity $\frac{\sqrt{\langle A_c \rangle}/\eta}{Re_\lambda^{4.4}\phi_v^{1.6}}$, shown in fig. 4.11b. The Stokes number dependency of the cluster size, $\alpha' = -0.2 \pm 0.25$, is marginal. Overall, the cluster size dependency on (St, Re_λ, ϕ_v) can be approximately quantified by the empirical expression:

$$\frac{\sqrt{\langle A_c \rangle}}{\eta} = 0.05 \cdot St^{-0.2} Re_\lambda^{4.4} \phi_v^{1.6}, \tag{4.8}$$

which shows the dominant role of the Reynolds number, a super-linear dependency on volume fraction and a negligible dependency on Stokes number. This suggests that the cluster size is primarily controlled by the carrier flow turbulence rather than by the disperse phase properties.

Similar trends are also obtained for the size of voids (see fig.4.12), with sensitivities to Re_λ and to ϕ_v similar to those obtained for the average cluster dimension. The Stokes number dependency is also weak. Since the spatial extension of the void regions is about ten times larger than that of clusters, this ratio carries into the prefactors in equations 6.7.2 and 7.3.

$$\frac{\sqrt{\langle A_v \rangle}}{\eta} = 0.45 \cdot St^{-0.09 \pm 0.1} Re_\lambda^{3.6 \pm 1} \phi_v^{1.3 \pm 0.55}. \tag{4.9}$$

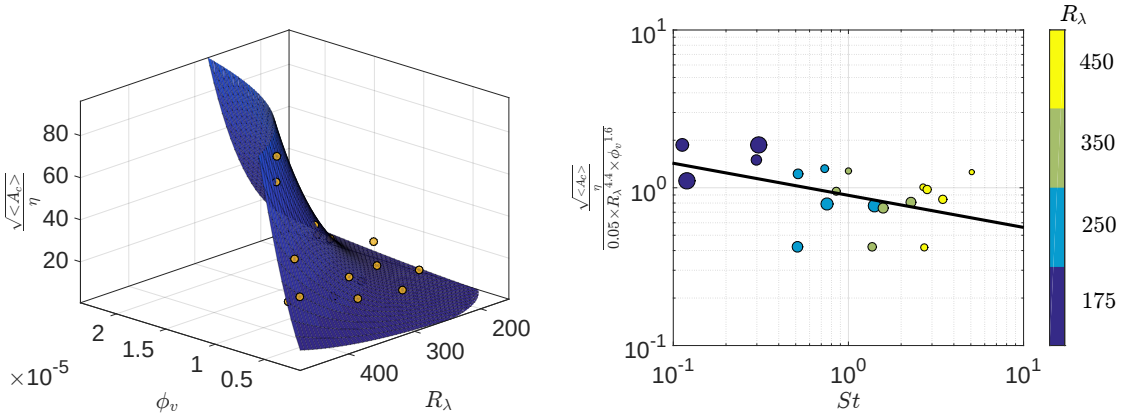

FIGURE 4.11: a). Scalings of $\frac{\sqrt{\langle A_c\rangle}}{\eta}$ vs ϕ_v and R_λ b). Reducing the original function of $\frac{\sqrt{\langle A_c\rangle}}{\eta}$ shows the weak dependence on St

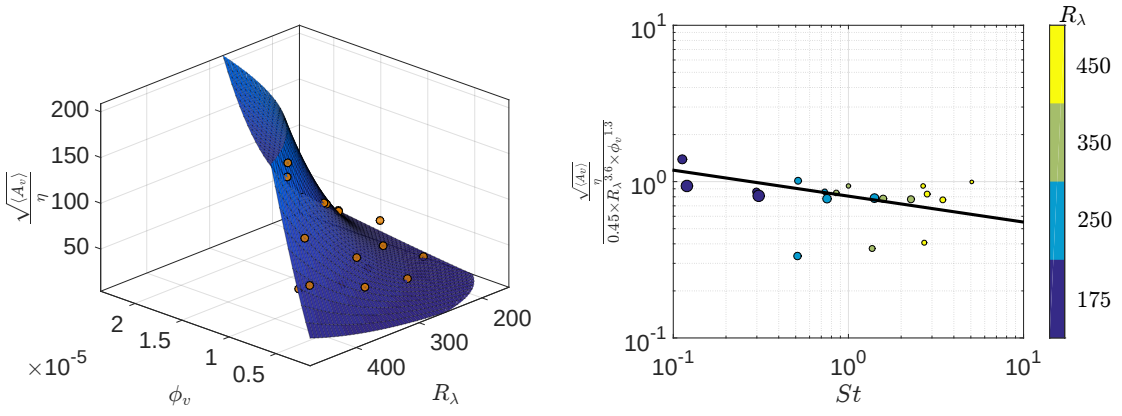

FIGURE 4.12: a). Scalings of $\frac{\sqrt{\langle A_v\rangle}}{\eta}$ vs ϕ_v and R_λ b). Reducing the original function of $\frac{\sqrt{\langle A_v\rangle}}{\eta}$ shows the weak dependence on St

4.3 Discussion

Application of Voronoï area statistical analysis to quantifying the degree of clustering and the geometry of cluster and voids of inertial particles in homogeneous isotropic turbulence has revealed the dependence of the preferential concentration on St, Re_λ and volume fraction ϕ_v. The standard deviation σ_ν of the statistics of Voronoï areas around particles, as well as the length scales of clusters and voids, have a strong dependency on Reynolds number, an intermediate dependency on volume fraction and no significant dependence (within experimental error) on the Stokes number.

This strong dependency of clustering on the Re_λ number reveals the dominant role of carrier flow turbulence in the clustering process, consistent with the assumption that the turbulent structures are the ones responsible for the formation of clusters.

The dependency of clustering on the particle volume fraction ϕ_v is very likely reminiscent of collective effects due to particle interactions, and is in agreement with previous observations of such collective effects [1, 47].

A very weak, almost inexistent, dependency of the degree of clustering and the cluster geometry on the Stokes number, (based on the maximum probability diameter in the polydisperse particle distributions used in these experiments), has been found. This contrasts with previous studies, where it has been consistently reported from DNS of mono disperse particle-laden flows [73, 24, 8, 9] that clustering is maximum for Stokes number of order unity, invoking a better resonance between particles response time and small turbulent eddies. It should be noted, however that, most metrics used to characterize the level of clustering are based on small scale quantities, for instance the correlation dimension that measures the increase of probability of finding two particles at vanishing distance compared to a random distribution. Such metrics are only relevant to quantify small scale clustering at sub-dissipative scales, which has been shown to be driven by Reynolds number and to be essentially independent of Stokes number [9]. This analysis is very different to that used in experiments with metrics that focus on inertial scales (most accessible Voronoï cells in experiments, such as the one shown in figure 4.5, have dimensions within the inertial range of scales).

In line of previous numerical studies [10, 9, 32], our experimental results point towards clustering of inertial particles being not only a small scale phenomenon, but one that occurs at all scales of turbulence. This is revealed, for instance, by

the algebraic decay of the PDF of cluster areas, and by the fact that average cluster dimensions, up to 100η, can be found for experiments at the highest Reynolds numbers. The importance of multi-scale clustering has also been recently emphasized by [17], who showed that the usual centrifugation mechanism [43], which is by essence a small scale preferential clustering mechanism based on the negative effective compressibility of high-strain/low vorticity regions of the carrier turbulence, is not the primary mechanism for preferential concentration of particles in turbulence when the Stokes number exceeds unity. Their numerical study shows that for particles with Stokes number larger than unity, clustering is primarily driven by the "sweep-stick" mechanism [17] by which particles tend to preferentially sample the zero-acceleration points of the carrier flow.

It is important to note that, contrary to the centrifugation mechanism which is indeed clustering mechanism, the "sweep-stick" is a preferential sampling mechanism, and clustering only emerges as a consequence of the low-acceleration points in a turbulent flow organizing in multi-scale clusters [32]. In this framework, clustering properties are driven by turbulence characteristics across scales, while particle properties only influence the ability of particles to preferentially stick to the aforementioned zero-acceleration points. The main constraint for particles to efficiently stick to zero-acceleration points is that their viscous relaxation time τ_p be small compared to the life-time of those zero-acceleration points. These points are known from numerical simulations to be very persistent [32], and this can be related to the experimental finding that the correlation time of the acceleration magnitude of tracer particles is of the order of the integral time-scale T_{int} of the carrier turbulence [50]. As a consequence, as long as $\tau_p \ll T_{int}$, no significant dependency of clustering by the "sweep-stick" mechanism on the Stokes number is expected. A significant decrease of the efficiency of the mechanism will only occur for particles with response times approaching the integral time scale of the flow. In our experiment, T_{int} is at least of the order of 100 ms or more. For water droplets, such high response times, would require particles with diameter of the order of 100 μm or more. Interestingly, the "sweep-stick" scenario also suggests that the impact of Stokes number should be more visible at lower Reynolds number as the condition $St \ll T_{int}/\tau_\eta$ becomes more stringent for lower Reynolds numbers. This may explain why, in low Reynolds number simulations [73], where $R_\lambda \approx 30$ and experiments [47], a decrease of clustering was indeed observed when Stokes number exceeds unity.

Finally, we also point out that the polydispersity of our droplet distribution would also be very likely to smear out possible weak Stokes number dependencies, in particular for the experiments at the lowest Reynolds numbers for which some

dependency may still have been expected.

4.4 Conclusions

Overall, our findings of a dominant role of the Reynolds number compared to the Stokes number is consistent with a leading multi-scale clustering process driven by a preferential sampling mechanism, such as "sweep-stick", in agreement with previous experimental results [55]. In a broader framework, this finding also supports the necessity to distinguish small scale mechanisms of clustering and multi-scale mechanisms [33].

The sensitivity of clustering to the volume fraction identified here is clearly beyond any measurement uncertainty. If, as discussed above, the sweep-stick mechanism is driving the cluster formation, any volume fraction influence is not captured in that picture. A possible scenario could rely on collective effects which are known to lead to denser regions sinking in the mixture with an enhanced settling velocity. Such denser regions could thus collect extra particles during their motion relative to the fluid, and therefore built up clusters of higher concentration and of larger size. Such a process would be clearly favored at higher volume fractions. In this scenario, the sweep-stick mechanism will act as the trigger of cluster formation, with subsequent growth driven by the collective dynamics. Another alternative view is that the presence of clusters modifies the local turbulent structure and favor the multiplication of sticking points in the flow (note that at the largest concentrations in clusters, the mass loading exceeds 0.1 and can even become close to unity): more particles could then either *activate* more zero acceleration points or help bring new particles in the sticking region. These scenarios, hypothetical as they are, may serve for planing new experiments to help understand how collective effects become efficient in clustering. Clearly, an investigation of the effect of disperse phase volume fraction on the micro scale mechanism for accumulation of particles would be worth undertaking.

We finish by emphasizing that due to intertwining of all three control parameters St, Re_λ and ϕ_v, the separation of their influence on clustering is an extremely difficult task. More experiments are being conducted to extend quantitative understanding to a broader range of parameter values, in particular regarding the role of volume fraction and collective effects.

The investigation of clustering in regards to its effect on settling of inertial particles is another important aspect that can be studied via conditioned joint statistics

of settling velocity and Voronoï analysis. This study should ideally provide the dependency of the settling velocity of inertial particles on turbulence fluctuations and a final expression for the connection between settling and clustering.

Chapter 5

Dynamics of clusters and voids. PTV data

In this chapter we investigate the dynamics of particles using the PTV data, with a particular focus on the conditioning of settling velocity to local concentration given by Voronoii statistics. The analysis proposed in this Chapter therefore combines the Voronoii data, already presented in the Chapter 4, and Lagrangian velocity statistics obtained from Particle Tracking. First sections in this Chapter describe the estimation of velocity statistics from PTV data, in particular from the prospect of filtering and alignment requirements. Then we investigate the unconditional velocity statistics before addressing the question of velocity conditioned to local concentration field. Dataset acquired using the PTV method covers a broad range of parameters, in particular regarding the Re_λ number.

5.1 Filtering of PTV tracked data

5.1.1 Tracks filtering

Lagrangian Particle Tracking allowed us to perform the Particle Tracking Velocimetry on the images acquired. Given an x, y coordinates of each particles, we were able to track our particles in space and time. Tracking was performed using the three frames best estimate algorithm by Nick Ouellette [58]. However, such a tracking results inevitably in the pixel-locking noise due to the resolution of the particle detection algorithms and white noise of both positions and then velocity statistics. Velocity statistcs are affected even worse because velocity is estimated as the first derivative of the position, what acts as a high pass filter which amplifies the noise present in the position data. To eradicate the noise or at least decrease its presence and its impact on statistical estimators, the positions and velocity statistics were

further filtered using two methods which we further discuss.

5.1.2 Gaussian Kernel Filtering

To define the appropriate length of the tracks at which we apply filtering procedure, we need to gather an idea of the typical time-scale at which the noise starts to emerge, the goal being to increase the signal to noise ratio by filtering most of the small scale noise, while preserving most of the actual singal.

To do that we first considered the usual strategy of applying a Gaussian filter of width ω with the following convolution kernel:

$$Kernel = A_p \times e^{-\frac{t}{w}^2}. \tag{5.1}$$

with

$$A_p = \frac{1}{\int e^{-\frac{t}{w}^2}} \tag{5.2}$$

where $-L <= t <= L$, and the support L of the kernel is taken to be 3ω. Convolution of each trajectory with the Gaussian kernel then gives the filtered trajectories. Filtered velocity is obtained by convolution of each trajectory with the derivative of the Gaussian kernel:

$$Kernel = A_v \times t \times e^{-\frac{t}{w}^2} \tag{5.3}$$

with

$$A_v = \frac{1}{\int t^2 \times e^{-\frac{t}{w}^2}}. \tag{5.4}$$

The normalization of the constants warrants that convolution with a pure linear signal $f(t) = t$, gives exactly one, as expected for a differentiating filter.

An important issue when filtering PTV data is to determine the optimal choice for the filter width ω. A Gaussian filter essentially behaves as a smooth low-pass filter with cut-off frequency of $\frac{1}{\omega}$. Hence the larger ω, the more filtered signal is. A compromise needs to be found where ω is large enough to filter most of the noise while keeping most of the signal. The traditional strategy for determining the optimal filter width consists of plotting the standard deviation of the sought quantity (in our case it is velocity) as a function of ω in order to find the smallest value of ω before the noise manifests as a rapid growth of standard deviation as ω is decreased.

Fig.5.1 a&b shows the evolution of estimated standard deviations of velocity

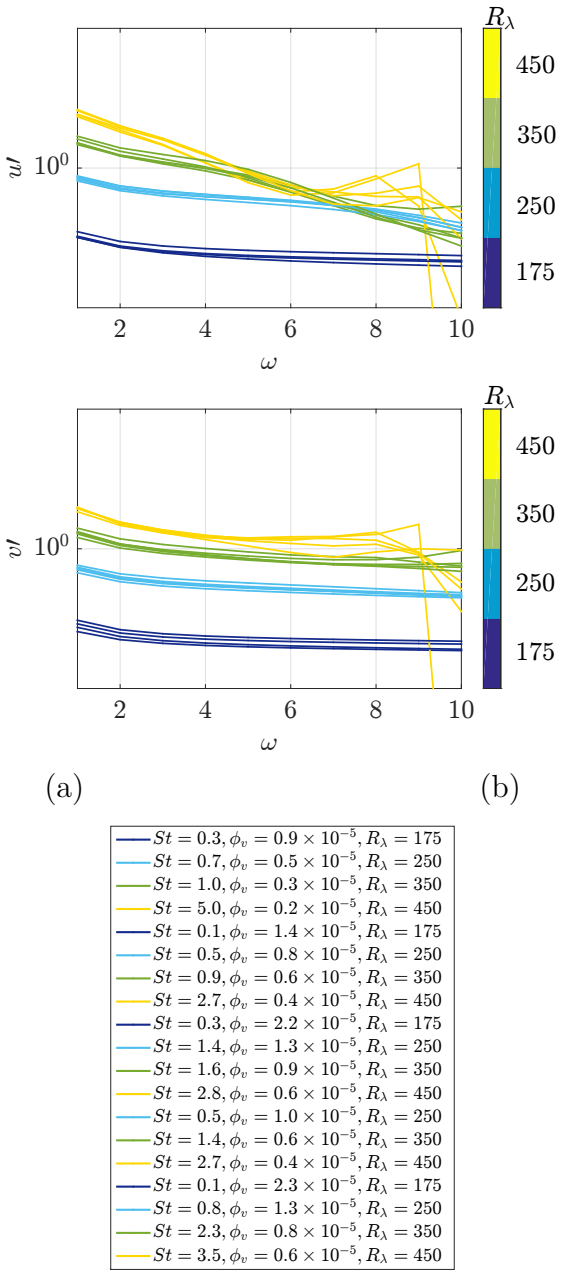

FIGURE 5.1: (a) $u\prime$ vs tracks length ω, (b) $v\prime$ vs tracks length ω. Note that ω here is given in units of a frame number. (c) Experimental parameters corresponding to a) and b)

fluctuations $u\prime$ and $v\prime$ as a function of ω for the filtered tracks using Gaussian velocity kernel for 19 experimental conditions (for more details of the experimental conditions see table 3.2 in Chapter 3).

We could see that values for both $u\prime$ and $v\prime$ are organised in the increasing Re_λ. We also see that for small values of ω $u\prime$ and $v\prime$ do increase although not drastically.

For intermediate values of ω, we see some sort of emerging plateau for all curves except the case of $u\prime$ at highest Re_λ. This plateau is typically what we look for when filtering. It represents a range of filter width for which the robust statistics (velocity variance here) is robust regarding to filtering parameters, suggesting that most influence of noise has been removed, while the signal has been preserved. For $u\prime$ the plateau becomes more shallow with increasing Re_λ. This is somehow expected as small scales are more easily resolved at lower Re_λ. For the highest Re_λ it seems that we lack a resolution to accurately resolve $u\prime$. It seems, however, we reasonably resolve $v\prime$ which shows a more robust plateau which is well presented for all Re_λ. This is probably related to the fact that a high streamwise velocity tends to make the horizontal pixel-beating completely uncorrelated between successive frames, while in vertical direction many particles move by less than a pixel which minimises the pixel locking. This means that purely horizontal tracks will have zero pixel beating in the vertical direction but still a lot in the horizontal one.

Another striking feature is the absence or scarce amount of tracks available with the length $w > 10$ for $Re_\lambda = 450$ what explains the poor statistical convergence for $u\prime$ and $w\prime$ when filtering with $w > 10$. This is related both to the lower brightness of the images recorded at the highest velocities (es exposure time had to be reduced to avoid motion blurring) which reduces the quality of particle detection and eventually of the particle tracking, and to the higher level of fluctuations which makes particles leave the laser sheet more frequently at higher wind speed.

To choose the optimal filter width ω, we analyse the plateaus for both $u\prime$ and $v\prime$ for all Re_λ. The plateau for $v\prime$ starts already from $\omega = 4 - 6$ for all datasets, for $u\prime$ the plateau starts from $\omega = 4 - 6$ for $Re_\lambda = 175 - 250$. For $Re_\lambda = 350$ there is at most an inflexion point around $\omega = 4$. For the highest $Re_\lambda = 450$, we can not see any inflexion point or plateau. However, we have to remind the reader that we are mostly interested in the settling velocity of inertial particles, and in our case the statistics of the vertical component are of an utmost interest. Hence, we decided to filter all available data for all Re_λ at $\omega = 5$ which in turn gives $L = 15$ in units of numbers of frames.

Fig.5.2a shows one long track with the track length of 80 frames. Fig.5.2b & c shows the instanteneous velocities U and V obtained after Gaussian kernel filtering

with the chosen $\omega = 5$. The regions of particle acceleration and deceleration could be clearly identified from these two plots. An intrinsic limitation of convolution filters is that they cannot be reasonably applied to signals shorter than the support L of the kernel. In the present case this would mean a major statistical loss as tracks shorter than 15 frames would be discarded from the analysis. To avoid losing statistics due to the length of the tracks, we have come up with another method of filtering short tracks which will be in the next Section 5.1.3.

5.1.3 Polyfit Filtering

To continue filtering of velocity data on short tracks, we have decided to simply use a polynomial fit of the tracks. This procedure will be applied to tracks shorter than 15 frames, which corresponds to about 6 ms i.e. this corresponds roughly to the order of τ_η, so that tracks at this scale are expected to be mainly straight (due to being assimilated to the local tangent of the actual trajectory), and with eventually a small quadratic correction due to acceleration. We have therefore considered a parabolic of the trajectories:

$$x = x_0 + u_0 \times t + \frac{1}{2} a_{x_0} \times t^2 \tag{5.5}$$

and

$$y = y_0 + v_0 \times t + \frac{1}{2} a_{y_0} \times t^2 \tag{5.6}$$

A small linear trend is therefore permitted for the velocity along this short tracks. Thus, a second order polynomial fitting of positions x and y is used to find instanteneous velocity statistics U and V with the number of points acquired: one such short track is shown on the fig.5.3a. The instanteneous velocities V and U obtained from the parabolic fit of the track ($u = u_0 + a_{x_0} \times t$ and $v = v_0 + a_{y_0} \times t$) are shown in fig.5.3b & c.

Note that this parabolic fit procedure is similar to the filtering method originally deployed by Voth et al. [72]. As done by Voth et al.[72], it could have been used instead of the Gaussian filter even for longer tracks (the equivalent of the filter width ω being the number of frames used to perform the parabolic fit). It is however much less efficient from the computational point of view. In the end, we have therefore chosen to use the Gaussian filter method with $w = 5$ for tracks longer than 15 frames, and the parabolic fit method for shorter tracks.

We should also mention that although some basic statistics of velocity fluctuations will be presented, we will essentially discuss in the sequel the average settling

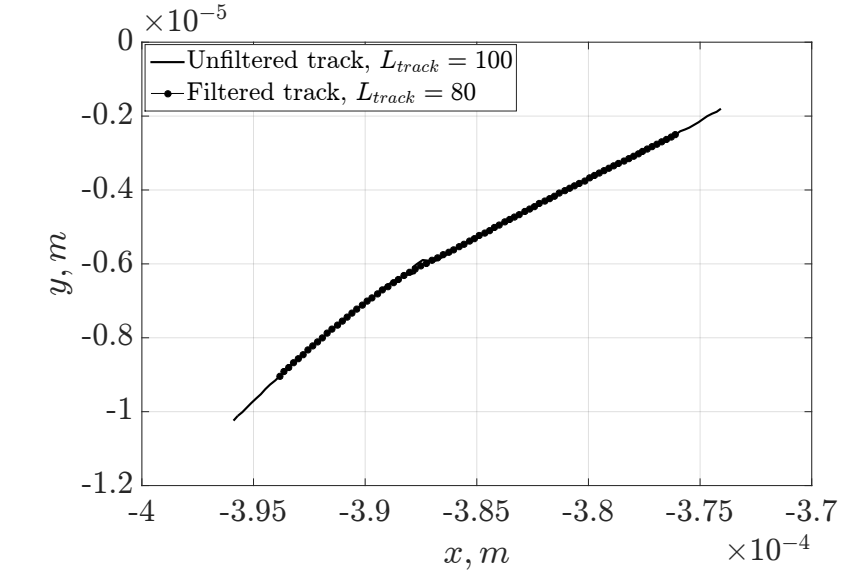

(a)

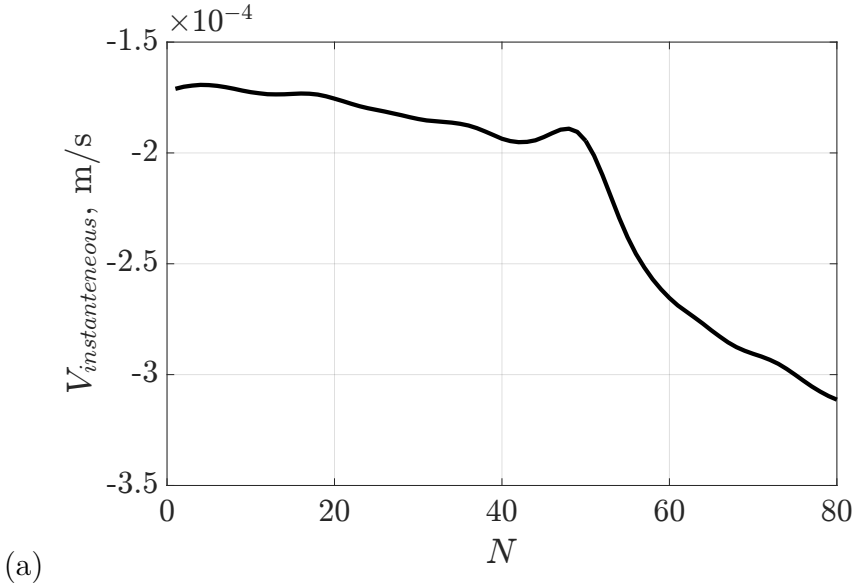

(b)

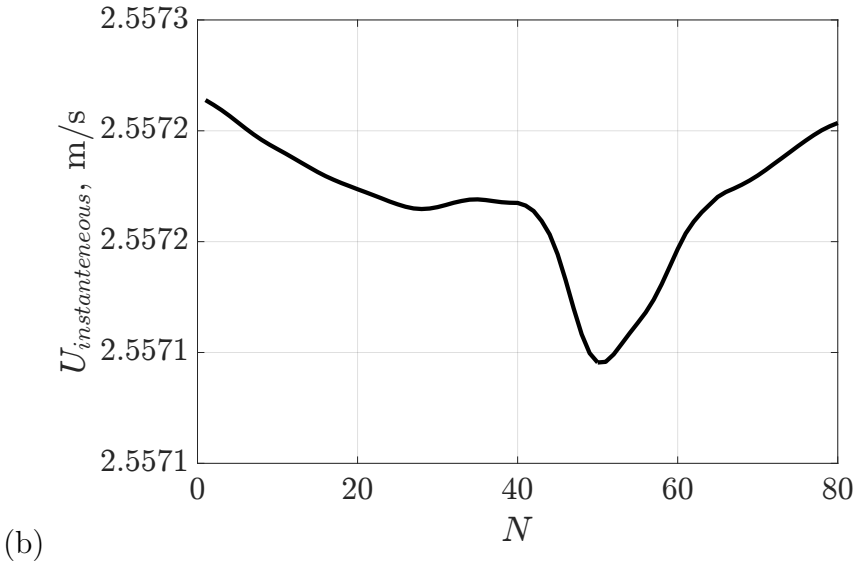

(c)

FIGURE 5.2: (a) the positions of x, y of the long track filtered using Gaussian Kernel, (b) instanteneous velocity axial U for the track provided, (c) instanteneous velocity settling V for the track provided

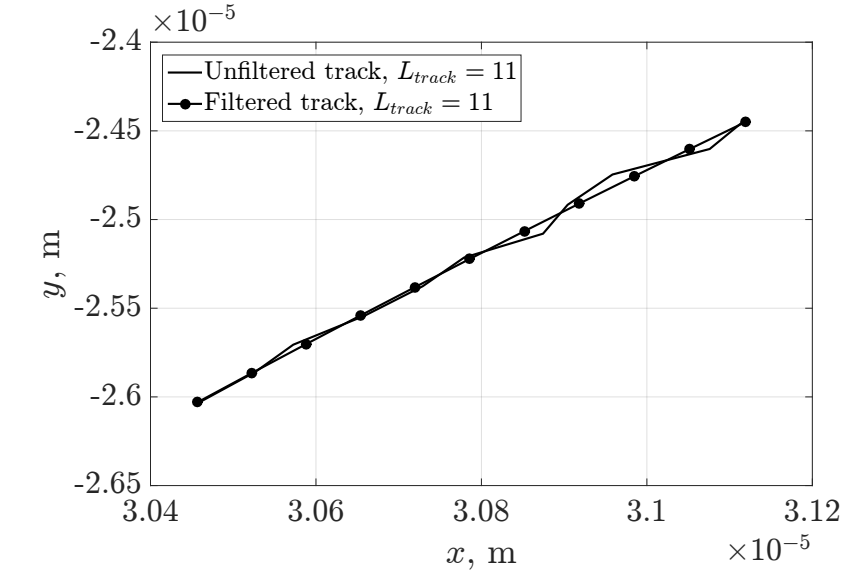

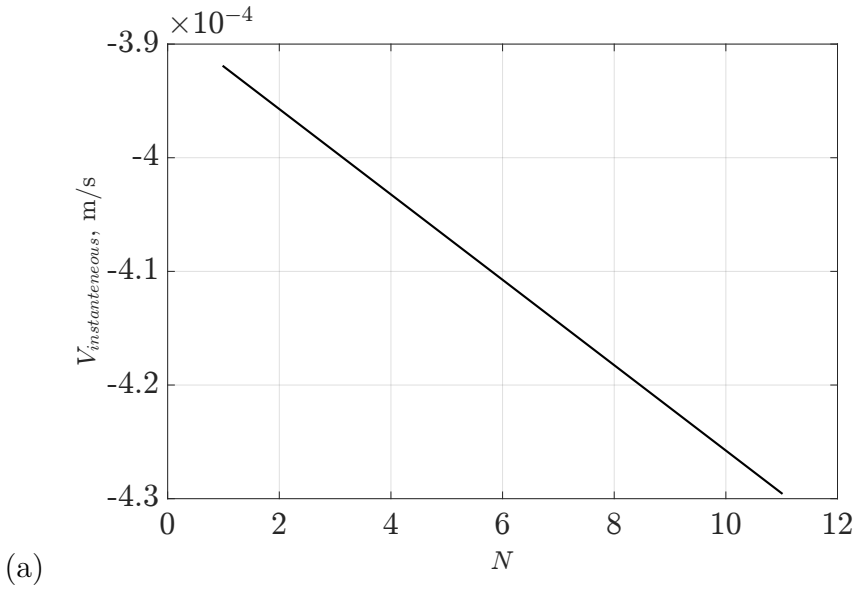

(a)

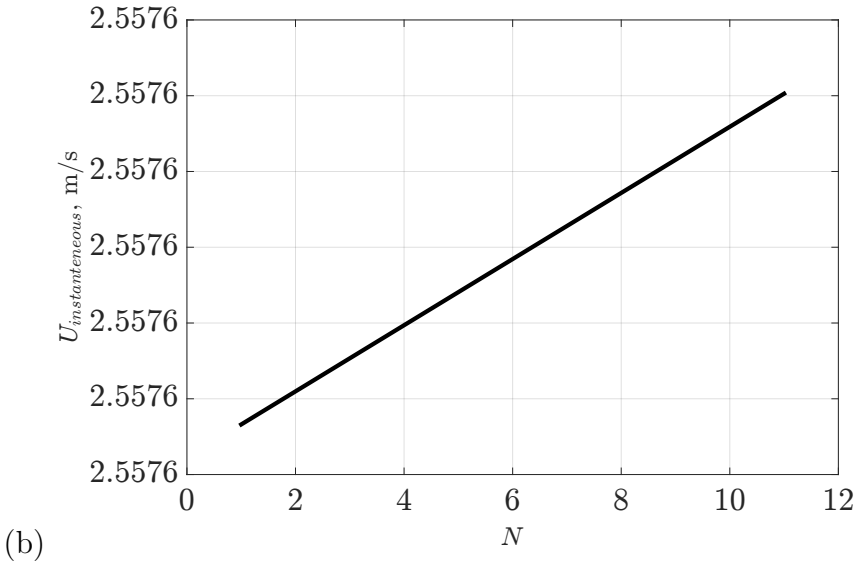

(b)

(c)

FIGURE 5.3: (a) the positions of x, y of the long track filtered using polyfit filtering, (b) instanteneous filtered velocity axial U for the track provided, (c) instanteneous filtered velocity settling V for the track provided

velocity V (and its connection with preferential concentration phenomenon) which is not expected to be highly sensitive to noise and filtering, contrary to fluctuations.

5.2 PDFs of Streamwise and Settling Velocities

Having performed filtering, we first briefly present the PDFs of the axial velocity U and settling velocity V of inertial particles for all 19 experimental cases.
Fig. 5.4 a&b shows the centered and normalised with σ of each distribution probability density functions for axial velocity U and settling velocity V. All PDFs for both U and V reasonably follow a Gaussian distribution (given in black) for fluctuations up to $\pm 4\sigma$ for lowest Re_λ and $\pm 3\sigma$ for the highest Re_λ. The departure from gaussianity for large velocity fluctuations (mostly affecting high order statistics, beyond the scope of the present study) is a classical signature of remaining noise. We stress that the present PTV measurements have been carried with the primary goal of investigating the mean settling velocity (and not high order moments of velocity fluctuations), which are not significantly affected by the tails of the PDFs. Future dedicated PTV measurements, focusing on high order and well-resolved small scale Lagrangian statistics, will be carried using an improved small-scale resolution, by zooming onto a smaller area (what allows to increase the spatial resolution and to reduce peak-locking noise and increasing the frame rate. This will allow a detailed investigation of multi-scale velocity fluctuations of inertial particles, although at the price of a reduced measurement volume, hence limiting the possibility to investigate clustering and clusters geometry (what was one of the goals of this work). Note that some aspects of velocity fluctuations will still be discussed in Chapter 6 of this manuscript (dedicated to Phase Doppler Interferometry measurements).

5.3 Limitations of PTV measurements to diagnose settling

The PTV measurements acquired during this thesis had the ambition to cover for the first time a broad range of multiple parameters where St, Re_λ and ϕ_v are varied independently (to some extent), with the goal to quantify the impact of these parameters on clustering and settling properties addressing also the interplay between clustering and settling in terms of collective effects. Covering such a broad parameter space carries however intrinsic difficulties when PTV diagnosis are considered, in particular regarding the determination of the absolute vertical velocity of the

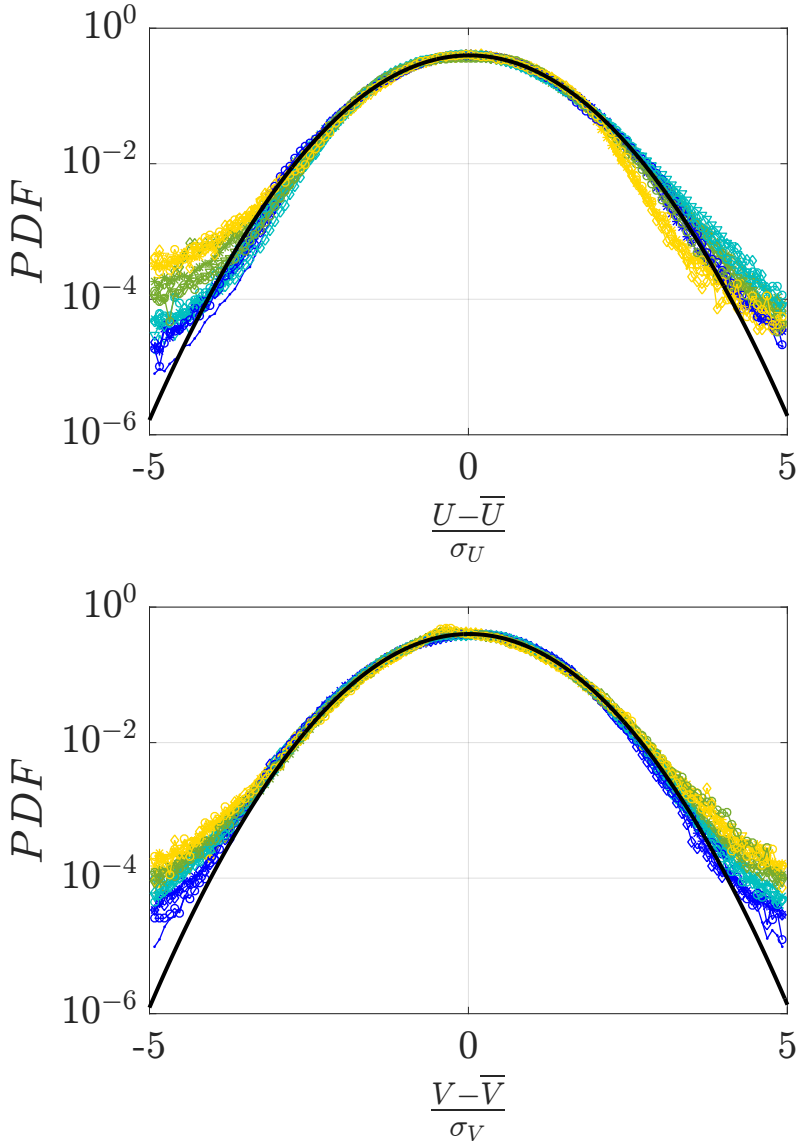

(a) (b)

$St = 0.3, \phi_v = 0.9 \times 10^{-5}, R_\lambda = 175$
$St = 0.7, \phi_v = 0.5 \times 10^{-5}, R_\lambda = 250$
$St = 1.0, \phi_v = 0.3 \times 10^{-5}, R_\lambda = 350$
$St = 5.0, \phi_v = 0.2 \times 10^{-5}, R_\lambda = 450$
$St = 0.1, \phi_v = 1.4 \times 10^{-5}, R_\lambda = 175$
$St = 0.5, \phi_v = 0.8 \times 10^{-5}, R_\lambda = 250$
$St = 0.9, \phi_v = 0.6 \times 10^{-5}, R_\lambda = 350$
$St = 2.7, \phi_v = 0.4 \times 10^{-5}, R_\lambda = 450$
$St = 0.3, \phi_v = 2.2 \times 10^{-5}, R_\lambda = 175$
$St = 1.4, \phi_v = 1.3 \times 10^{-5}, R_\lambda = 250$
$St = 1.6, \phi_v = 0.9 \times 10^{-5}, R_\lambda = 350$
$St = 2.8, \phi_v = 0.6 \times 10^{-5}, R_\lambda = 450$
$St = 0.5, \phi_v = 1.0 \times 10^{-5}, R_\lambda = 250$
$St = 1.4, \phi_v = 0.6 \times 10^{-5}, R_\lambda = 350$
$St = 2.7, \phi_v = 0.4 \times 10^{-5}, R_\lambda = 450$
$St = 0.1, \phi_v = 2.3 \times 10^{-5}, R_\lambda = 175$
$St = 0.8, \phi_v = 1.3 \times 10^{-5}, R_\lambda = 250$
$St = 2.3, \phi_v = 0.8 \times 10^{-5}, R_\lambda = 350$
$St = 3.5, \phi_v = 0.6 \times 10^{-5}, R_\lambda = 450$

(c)

FIGURE 5.4: PDFs of centered and normalised (a) axial velocity U and (b) settling velocity V. (c) Experimental parameters corresponding to a) and b)

particles, which requires a perfect alignment of the camera sensor with respect to gravity. To understand how crucial this is, let consider an angular misalignment of only $\alpha = 0.5°$. This results in a projection of the mean horizontal velocity U onto the measured vertical velocity $V_{offset} = U \sin\alpha \approx \alpha U$, so that the measured vertical velocity is $V = V_{actual} + V_{offset}$ (where V_{actual} is the actual vertical velocity). The mean measured settling velocity $\overline{V}$ therefore deviates from the actual mean settling velocity $\overline{V}_{actual}$ by $V_{offset} \approx \alpha U$. For a small misalignment of only 0.5° this uncertainty represents of the order of 2 cm/s for the lowest investigated velocity ($U \approx 2.5$ m/s) and about 8 cm/s for the highest investigated velocity ($U \approx 10$ m/s). The typical settling velocity for the investigated particles being of the order of 10 cm/s, the measurement uncertainty due to an alignement error as small as 0.5° is therefore crippling, in particular at the highest investigated velocities. Reducing the uncertainty to an acceptable level (of the order of 10%) would require to be able to warrant the accuracy and the stability of the orientation of the sensor to a precision below 0.1°, what turned out to be beyond experimental possibilities, even if the highest care was taken to properly align the camera as well as the calibration mask used to determine the correspondance between pixel and real world coordinates when setting up the experiment. As a matter of fact, after postprocessing the PTV data, for certain experiments the absolute mean vertical velocity was unphysically found to go upwards, in particular for the highest wind-speeds investigated (with typical values of the order of 10 cm/s upwards, while typical settling velocities were expected to be of the same order but downwards, suggesting an alignment error of the order of 1°).

A possibility to compensate the alignment error would consist in considering first only the trajectories of the smallest droplets (with $St \ll 1$), assuming they behave as tracers with negligible settling, and determine V_{offset} as their mean measured vertical velocity. Such a strategy is however unrealistic with PTV data as (i) particle size is not resolved (unless a high magnification is used, in which case the measurement domain has to be reduced) and (ii) minimum size of detected particles depend upon illumination and recording exposure time, which may vary from an experiment to another. This last point is particularly sensitive in the present experiment. PTV measurements were initially planed to be accomplished using a high-repetition / high-power pulsed laser, available in the group. Using a pulse laser has the big advantage of assuring a short (but powerful) exposure of the particles (i) what avoids motion blurring, (ii) warrants exposure time is identical (and fixed by the pulse duration, of the order of 100 ns) for all experimental conditions and (iii) particles are equally detectable for all experimental conditions. Unfortunately, the

pulsed ceased to work at the very beginning of the PTV measurement campaign, and had to be replaced by a continuous laser. Such a continuous illumination, results in a effective exposure time per pixel which depends both on the actual shutter speed of the camera and on the mean wind-speed. In particular, it has to be significantly reduced to avoir motion blurring at the highest wind speeds investigated. This results in dimmer images, where smallest particles are very likely not visible at high wind speeds.

Altogether, these limitations prevent to draw any conclusion from the present PTV dataset on the absolute value of settling velocity. In particular the eventual global enhancement or hindering of settling with respect to the Stokes velocity cannot be reasonably addressed. However, differential diagnosis of settling depending on local concentration can be robustly addressed (for instance in terms of the difference between the settling velocity of particles within clusters and particles in depleted regions, as the offset velocity cancels when taking the difference). We present in the sequel of this chapter such differential diagnosis, seeking for a global signature of collective effects. Results on the absolute enhancement or hindering of the settling will be discussed in Chapter 6, from PDI measurements, which allow a better handling of alignment uncertainties and which also allow a further conditioning of settling to individual particle size.

5.4 Conditional Statistics of Velocity by Concentration

PTV data allows us to possess two type of information about inertial particles in the explored parameter space. First, as it was discussed in Chapter 4 Section 4.2, the local concentration field of particles was analyzed. Second, having performed filtering on the PTV data, we obtained dynamical statistics of inertial particles, especially the one we are interested in is a settling velocity V. Combining the two, we performed an analysis of the average settling velocity $\overline{V} - V_{mean}$ conditioned by the normalized Voronoï area $\mathcal{V}$ (presented in previous chapter) in the explored parameter space. The choice of V_{mean} as a reference velocity is arbitrary and has been made purely to have a common compensation of the alignment issues previously discussed.

The plots of the average settling velocity $\overline{V} - V_{mean}$ as a function of Voronoï area $\mathcal{V}$ are shown in fig.5.5. Note that in this plot the convention of positive vertical velocities being in the direction of gravity is used. A first observation from these

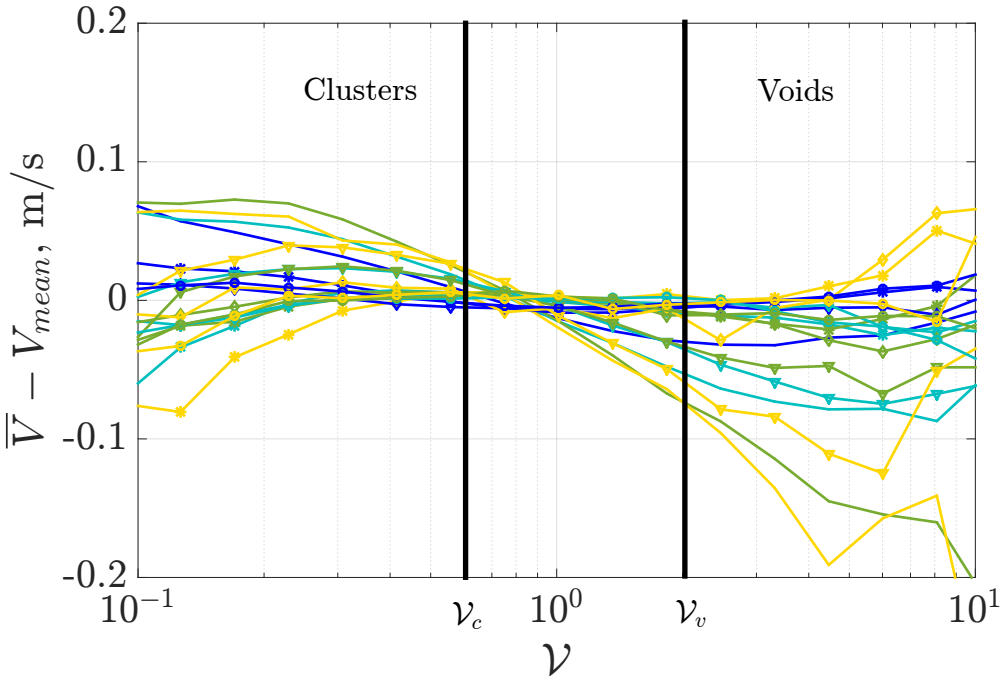

(a)

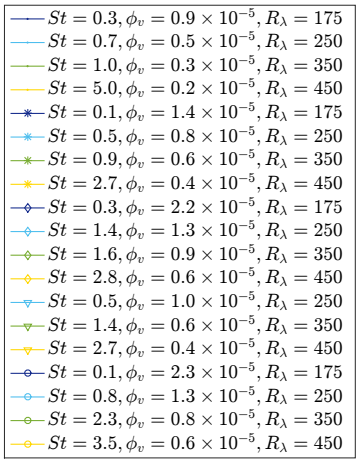

(b)

FIGURE 5.5: Averaged settling velocity (a) $\overline{V} - V_{mean}$ in m/s conditioned by the local concentration field $\mathcal{V}$, (b) experimental parameters corresponding to a). Positive V is in the direction of gravity.

curves is that for most experimental conditions particles with small Voronoï areas (i.e. particles in concentrated regions) tend to settle faster than the average and faster than particles in depleted regions (corresponding to large Voronoï areas) which settle slower than average. Using 2D thresholds for clusters and voids $\mathcal{V}_c = 0.6$ and $\mathcal{V}_v = 2.1$, we can further identify settling regimes of particles belongin to clusters and voids: for almost all experimental conditions clusters appear to settle faster than voids.

Fig.5.6 shows the average settling velocity $\overline{V} - V_{mean}$ normalised by $U\prime$, as often reported in previous studies, and in particular in the study by Aliseda et al. [1]. The previous trend, where clusters settle faster than voids is also clearly visible. The same observation was reported in the study by Aliseda et al. [1] (although their experiments covered a narrower range of parameters, in particular their Reynolds number was lower than in the present work), where particles in high local concentration regions were found to systematically settle faster. Aliseda et al. proposed an interpretation of this observation in terms of collective effects: the settling of particles in clusters resutls from the combination of the individual settling of the particle and of the global settling of the cluster itself. The trends reported in the present study are consistent with these previous observation and show that such a collective dynamics prevails over the entire explored parameter space.

In order to further quantify the difference between the settling of clusters and voids, taken as an indicator of collective effects on particle settling, we define $\overline{V}_{clusters}$ as the average settling velocity of particles with Voronoï areas below $\mathcal{V}_c$ and $\overline{V}_{voids}$ as the average settling velocity of particles with Vornoï areas above $\mathcal{V}_v$. Fig. 5.7a&b the difference $\overline{V}_{clusters} - \overline{V}_{voids}$ as a function of Reynolds number and of the global volume fraction. These plots confirm that clusters settle systematically faster than voids (the shown difference being positive for all experiments but one). It also shows that the settling difference between clusters and voids has a non-trivial dependency on experimental parameters. An important observation is that the influence of volume fraction ϕ_v increases with increasing Reynolds number, as shown by the larger spreading of the points at given increasing values of Re_λ in fig. 5.7a. The color code in this same figure represents the volume fraction and indicates a global trend where the velocity difference between clusters and voids seem to decrease with increasing values of ϕ_v. This global trend is confirmed in fig. 5.7b, where for given values of Re_λ the difference of settling velocities between clusters and voids is indeed found to decrease as ϕ_v increases.

This suggests, somehow counter-intuitively at first sight, that the impact of collective effects are reduced as the global volume fraction is increased. However, this

finding is in qualitative agreement with the results by Monchaux et al. [47] who reported that the over-concentration of particles within clusters with respect to the average particle concentration tends to decrease when increasing the seeding of the flow. In Monchaux et al. study this was interpreted as a collective effect, very likely triggered by enhance hydrodynamic interactions between particles within clusters, preventing the inner concentration within clusters to increase in proportion to the mean concentration. In such a scenario, the collective enhancement of settling within clusters, found by Aliseda et al. to be, at first order, proportional to the inner concentration within clusters with respect to the mean is also expected to be less important at increasing global volume fraction. At this point, a more quantitative analysis of this scenario and of the impact of the global seeding on the relative settling of clusters and voids would therefore require to explore the evolution of the inner concentration of clusters and voids for the different experimental conditions. Unfortunately, the illumination issues discussed previously (exposure time being different for different experimental conditions) related to the failure of the pulsed laser does not allow to unambiguously relate the count of particles on the image to the actual physical seeding. Although qualitatively the present results open however interesting perspective of analysis for future experiments where these technical issues of illumination will be solved.

We decided to evaluate the absolute difference between clusters and voids evolving with some of the experimental parameters that we have varied such as Re_λ and ϕ_v (see fig.5.7 a& b). We see two trends of the $\overline{V}_{clusters} - \overline{V}_{voids}$ plotted versus Re_λ in fig.5.7 a. One, where we do not see a lot of relative difference between velocity of clusters and voids, and the second one, where the increase in Re_λ follows larger and larger dispersion between velocity of clusters and voids.

The second plot fig.5.7 b shows the evolution of the difference $\overline{V}_{clusters} - \overline{V}_{voids}$ with ϕ_v. Here, we can clearly see there exists a non-trivial dependence of the settling velocity on the volume fraction ϕ_v. This dependence manifests itself strongly at high Re_λ.

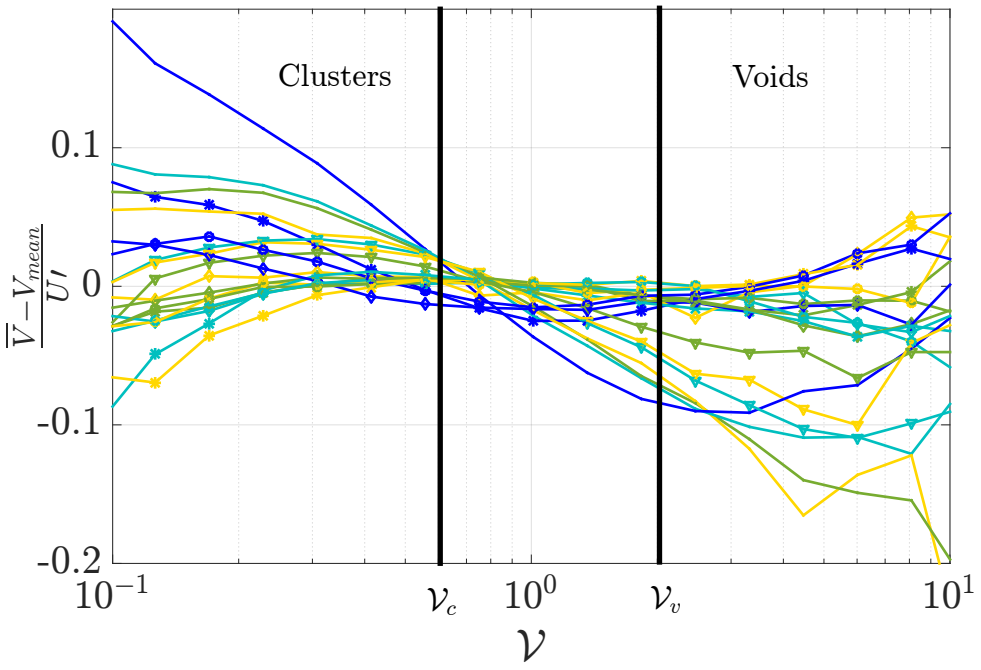

(a)

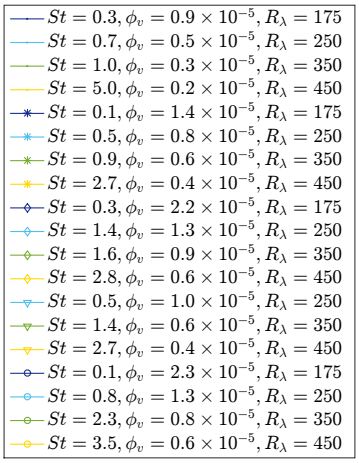

(b)

FIGURE 5.6: Averaged settling velocity (a) $\frac{\overline{V}-V_{mean}}{U\prime}$ conditioned by the local concentration filed $\mathcal{V}$, (b) experimental parameters corresponding to a). Positive V is in the direction of gravity.

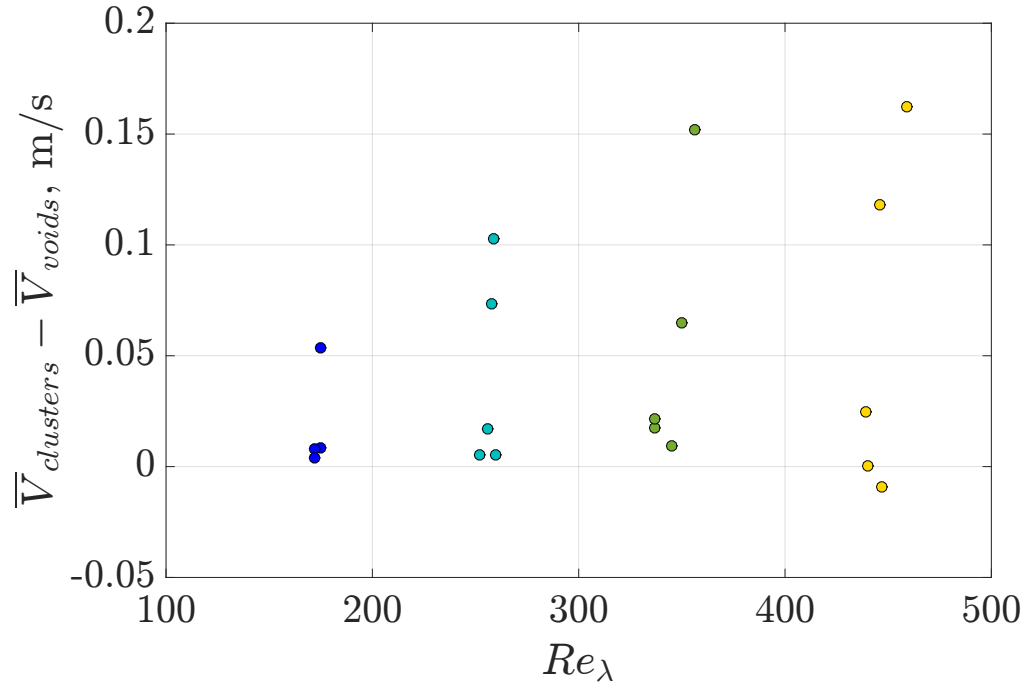

(a)

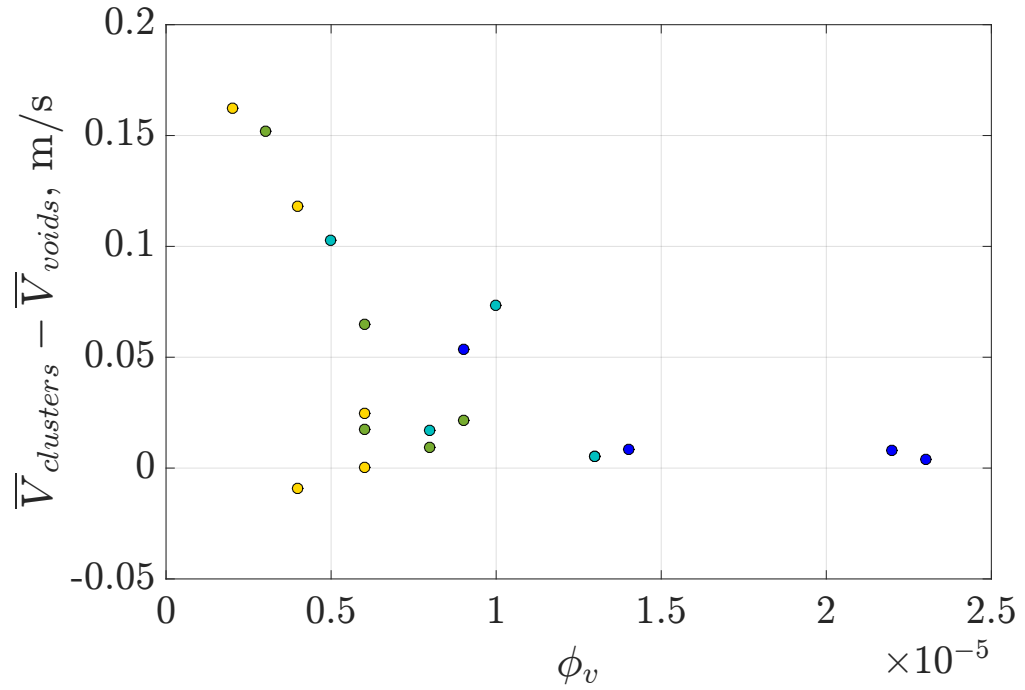

(b)

FIGURE 5.7: Difference between clusters and voids $\overline{V}_{clusters} - \overline{V}_{voids}$ plotted versus (a) Re_λ (volume fraction ϕ_v decreases both vertically and from right to left of the Re_λ). and (b) ϕ_v, the colors are attributed as follows: blue for $Re_\lambda = 175$, light blue for $Re_\lambda = 250$, green for $Re_\lambda = 350$, yellow for $Re_\lambda = 450$.

5.5 Conclusion

In this Chapter we have shown a simultaneous information obtained for the local concentration field with the aid of Voronoii tesselations, and the dynamical statistics of the inertial particles through the settling velocity V for explored parameter space. The data for the settling velocity V was further filtered to minimise the influence of the pixel-locking noise.

Next, we have looked at the PDFs of the streamwise U and settling V of the inertial particles for a given parameter space. Velocity statistics were found reasonably gaussian, with non-gaussian tails for extreme events, reminiscent of remaining noise. These tails preclude any serious analysis of high order velocity statistics, which were not the scope of the study aiming primarily at investigating the mean settling velocity. We have also pointed that several experimental constraint limited the diagnosis of settling to a differential diagnosis, not suitable to address global enhancement or hindering of settling with respect to Stokes terminal velocity, but relevant to identify the signature of collective effects on settling, such as the difference between settling velocity of particles depending on their belonging to clusters or voids.

With this in mind, we have combined the information about the local concentration field $\mathcal{V}$ obtained in Chapter 4 Section 4.2.1 and settling velocity statistics. We have confirmed the presence of collective effects as previously found by Aliseda et al [1], evidenced by the fact that particles within clusters settle systematically faster than particles in depleted regions. Non-trivial trends with Reynolds number and volume fraction were found. The sensitivity of collective effects on global seeding seems to be more profound at higher Reynolds number. For the lowest investigated Reynolds number, the difference between settling in clusters and voids remains small (a few cm/s) and marginally dependent on volume fraction, while the velocity difference reaches $\sim$ 10 cm/s at the largest Re_λ number. This dependency becomes more pronounced when increasing Re_λ number.

An interesting finding also concerns the difference between settling velocities in clusters and in voids being lesser for experiments carried at higher global volume fraction. This suggests, counter-intuitively, that the impact of collective effects is reduced at higher global seeding densities, what in turn may reflect the fact that the inner over-concentration increases less than the global seeding (as reported by Monchaux et al. [47]), leading to a smaller mixture density difference between clusters and the other regions of the flow.

Chapter 6

Dynamics of clusters and voids. PDI data

The added value of PDI measurements with respect to PTV measurements presented in the previous Chapter is that they allow to carefully correct misalignment issues, and to further condition settling statistics to individual particles diameter, hence providing a very detailed insight into the role of individual St and Ro numbers on settling enhancement and hindering. The objective of this chapter is to investigate the settling characteristics of particles of different diameters in the presence of turbulence and for varying volume fractions. First, we will conduct the analysis of the settling velocity at a fixed $R_\lambda = 185$ with changing volume fraction $\phi_v = 0.5 - 2.0 \times 10^{-5}$. We will look at the statistics of settling velocity and diameter D of the particles conditioned by the local concentration field.

6.1 Experimental Parameters

The map of experimental parameters is given in the table 6.1. Again, the reference Stokes number is based on the most probable diameter D_{prob} of each distribution. It is important to note that in other studies, the Stokes number is sometimes defined on the maximum probable D or D^2 or D^3 distributions that reveal the number of particles counted according to area or volume. Thus, one should take care in comparing flow conditions in terms of Stokes number. In our conditions, the St number fluctuates around 0.7. This is due to the fact that changing volume fraction ϕ_v by a factor of 4 does not affect significantly the diameter distribution D of droplets (fig. 6.1). In terms of polydispersity, the standard deviations evolve in the range of 41-53% of the mean diameter.

We introduce also the non-dimensional Rouse number $Ro = \frac{\tau_p \times g}{u'}$ that provides

TABLE 6.1: Experimental Parameters

ϕ_v	St	Ro	$u\prime$ $[m/s]$	D_{prob} $[\mu m]$	σ_D $[\mu m]$	R_λ	D_{10} $[\mu m]$	D_{32} $[\mu m]$	$D_{30}^{\frac{1}{3}}$ $[\mu m]$
0.5×10^{-5}	0.87	0.23	0.32	50	25	191	50.6	77.6	63.1
1.0×10^{-5}	0.58	0.18	0.31	43	23	184	43.8	70.7	56.1
2.0×10^{-5}	0.74	0.20	0.37	49	20	181	50.2	66.4	57.9

the ratio of the terminal velocity to $u\prime$. Here, the terminal velocity U_{St} considered is evaluated taking into account the non-linear Schiller-Neumann drag relationship. Mean Ro is defined on the most probable particle diameter D_{prob}, and it does not change much with the rise in volume fraction ϕ_v. R_λ for the three experiments stays around 185 (the velocity of the airflow was set to $U = 2.56 \pm 0.11\ m/s$).

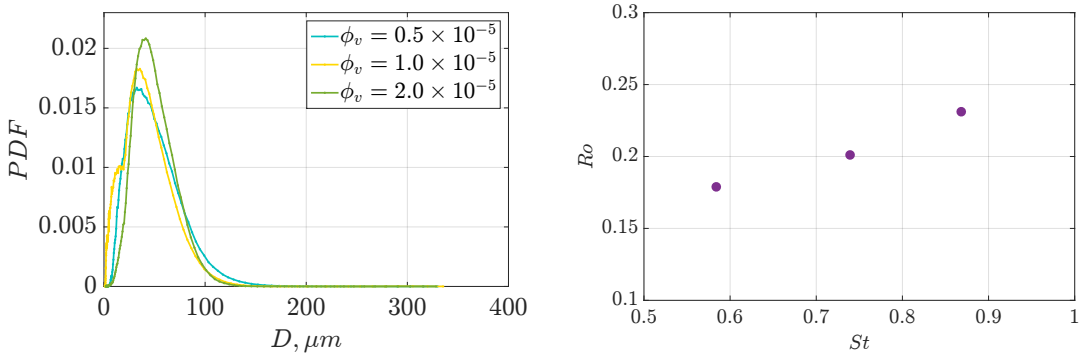

(a) (b)

FIGURE 6.1: (a) Diameter distributions (b) Mean St vs mean Ro scatter

6.2 Concentration evolution along the channel

We did not measured transverse profiles of concentration, nor analyzed its axial evolution. Instead, we exploited the PDI data to estimate the magnitude of water loss along the channel. Indeed, from the joint size-velocity distribution, one can deduce a number of parameters. In particular, the local volume flux of liquid along a vertical J_L is given by:

$$J_L = \int_D N \frac{4\pi}{3} V(D) \frac{D^3}{8} P(D)\, dD = \\ = \frac{4\pi}{3} N < VR^3 > = \frac{\phi_v < VR^3 >}{< R^3 >} = \phi_v \frac{< VR^3 >}{< R^3 >} \tag{6.1}$$

TABLE 6.2: Total number of data collected N_{counts}, volume fraction at injection ϕ_v in each experiment and the corresponding data rate and validation rate.

Flow rate, l/min	ϕ_v	N_{counts}	Data rate (Hz)	Validation rate %
0.47	0.5×10^{-5}	1.13×10^{6}	68	78
0.95	1.0×10^{-5}	1.30×10^{6}	310.2	67
1.9	2.0×10^{-5}	1.17×10^{6}	208.6	56

where N is the number density. The averages $< VR^3 >$ and $< R^3 >$ can be evaluated from PDI data. The mean vertical phasic velocity is defined as $\frac{J_L}{\phi_v}$, and thus, it is given by $\frac{<VR^3>}{<R^3>}$. The number density flux is the number density times the arithmetic mean vertical velocity $< V >$ that differs from the phasic velocity.

In principle N is available from PDI data provided that all droplets crossing the probe volume are detected and their signal validated. As shown in table 6.2, the data rate, even corrected with the validation rate, is not proportional to the liquid concentration. Thus, we used an alternate approach to evaluate the number density.

In the eq.6.1, we exploited the fact that the number density N can be deduced from the volume concentration ϕ_v from the knowledge of $D_{30} =< D^3 >= 8 < R^3 >$ (see values in Table 1.1) since N obeys $\phi_v = N\frac{4}{3}\pi < R^3 >$. The results are given in the table 6.3. They integrate the probe volume correction from the PDI manufacturer (the effective probe volume of PDI systems growths with the particle size) but otherwise they correspond to raw data, i.e. uncorrected from the validation rate.

As water deposition on the bottom wall was effective after ≈ 1 m from injection, the vertical flux was found to represent $10 - 12\%$ of the injected flow rate. When correcting for the validation rate, that proportion reaches 16% (20% for the highest flow rate). Hence, although the deposition of drops on lateral walls is not accounted for in the above estimate, the loss of water on the bottom wall due of settling does not significantly affect the water concentration along the channel.

Flow rate injected $[l/min]$	ϕ_v at injection $\times 10^{-5}$	Mean vertical phasic velocity $[m/s]$	Arithmetic mean vertical velocity $[m/s]$	Number density flux $[counts/m^2 s]$	Number density $[counts/m^3]$	Vertical volume flux per unit area $[m/s]$	Corrected vertical flux /horizontal flux
0.47	0.5	0.218	0.105	3.98×10^6	3.8×10^6	1.09×10^{-6}	4.7×10^{-3}
0.95	1.0	0.192	0.117	1.26×10^7	1.1×10^8	1.92×10^{-6}	1.7×10^{-3}
1.9	2.0	0.212	0.162	3.18×10^7	2.0×10^8	4.24×10^{-6}	1.2×10^{-3}

TABLE 6.3: Some characteristics of the drop for each experimental condition.

6.3 Sphericity of inertial particles

PDI system works very well with spherical particles. To check the sphericity of the droplets considered here, we evaluated two We numbers that are used to characterise the interface deformation as they compare a dynamic pressure with capillary pressure. The We number based on the terminal velocity is defined as

$$We = \frac{\rho \times V_p^2 \times D}{\gamma} \tag{6.2}$$

where ρ is the particle density, V_p is its terminal velocity, D is its diameter and γ is the surface tension. Surface tension γ was calculated for water using following formula

$$\gamma = 235.8 \times (1 - \frac{T}{T_c})^{1.256} \times (1 - 0.625 \times (1 - \frac{T}{T_c})) \times 10^{-3} \tag{6.3}$$

where T is the temperature in K and $T_c = 647.098K$ is the critical temperature of water.

Let's consider the droplets interface deformation due to the relative velocity in the absence of turbulence or collective effects. In this case, the terminal velocity V_p is the velocity U_{St} calculated for non-linear Schiller-Neumann drag law. The distribution of We number is plotted on the fig. 6.2a. It is clear that the majority of droplets are spherical with a few particles being non-spherical with probability of 10^{-5} approaching the critical limit of $We = 12$ [40]. The same conclusion holds when considering a We number based on the measured settling velocity (fig.6.2c).

Now let's consider the interface deformation due to turbulence. The relevant number is now defined on $U\prime$ of the axial velocity U of the particles (see Table 6.1):

$$We = \frac{\rho \times U\prime^2 \times D}{\gamma} \tag{6.4}$$

From fig. 6.2 b, the maximum of We number for all three experimental conditions is below 1 [39] i.e. below the critical limit which is here about unity. This signifies that the turbulence does not seem to deform the initially spherical form of droplets. These results mean that overall our inertial particles are spherical water droplets, except for the larger droplets which are statistically insignificant (probability below 10^{-5}).

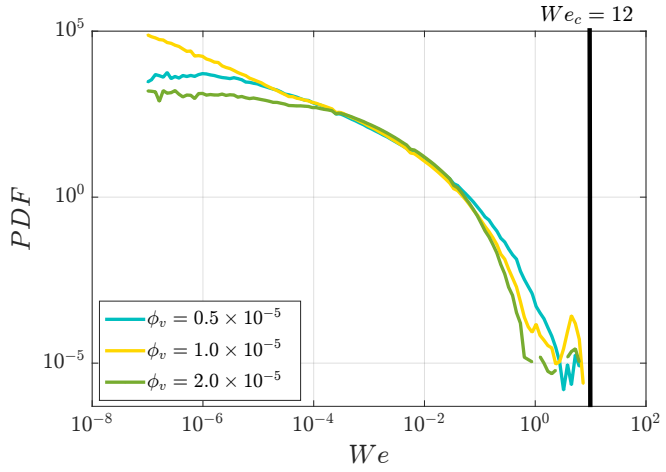

(a)

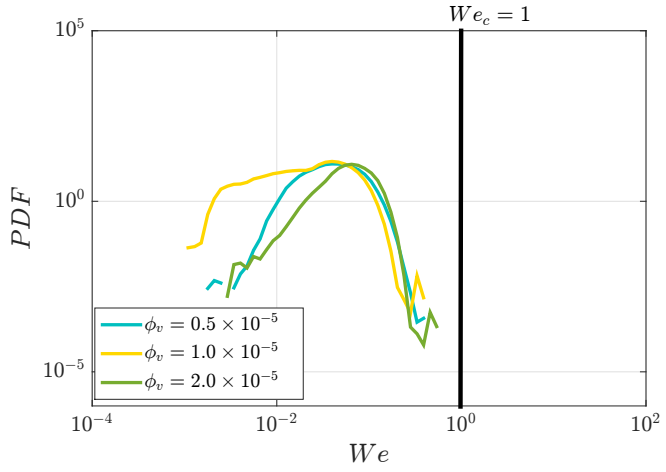

(b)

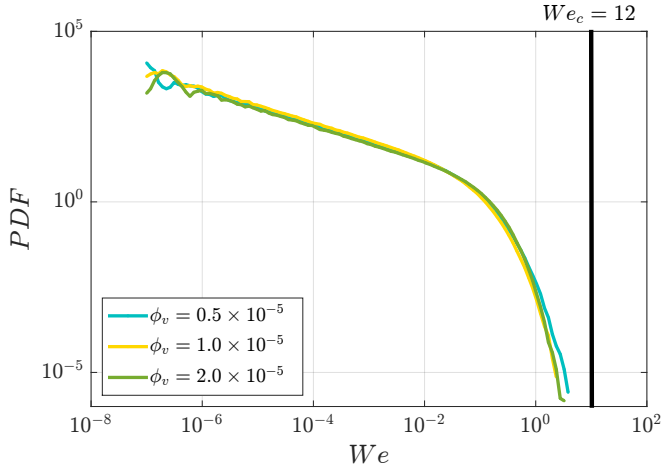

(c)

FIGURE 6.2: PDF distributions of We number for each experimental condition calculated (a) using $V_p = V_{St}$ (b) using $V_p = U\prime$, (c) using measured $V_p = V_{settling}$

6.4 Results

6.4.1 Statistics of measured velocities $V_{settling}$ and axial U

The pdfs of the axial U velocity and $V_{settling}$ are shown on the fig. 6.3. For all three conditions the mean U of the particles is around 2.56 m/s, which is the velocity of the mean airflow. This result is expected since there is no external force along the horizontal direction. This also means that the particles had enough time after injection to relax to the mean gas flow field. It was decided to substract the mean of each velocity distribution for both U and $V_{settling}$ and to normalise them with their respective standard deviations $\sigma_U = U\prime$ and $\sigma_V = V\prime$ (see fig. 6.4). Both normalised distributions seem to follow the Gaussian fit with standard deviations $\sigma = 1.4$ for U and $\sigma = 1.2$ for $V_{settling}$. This is pretty interesting, because the quasi-normal Gaussian distributions obtained through substracting the mean of the initial distribution and normalising with standard deviation of initial distribution tend to have a standard deviation σ close to 1. The ratio of standard deviations σ_U to σ_V is about 1.16, that means that our turbulent flow has a good degree of isotropy.

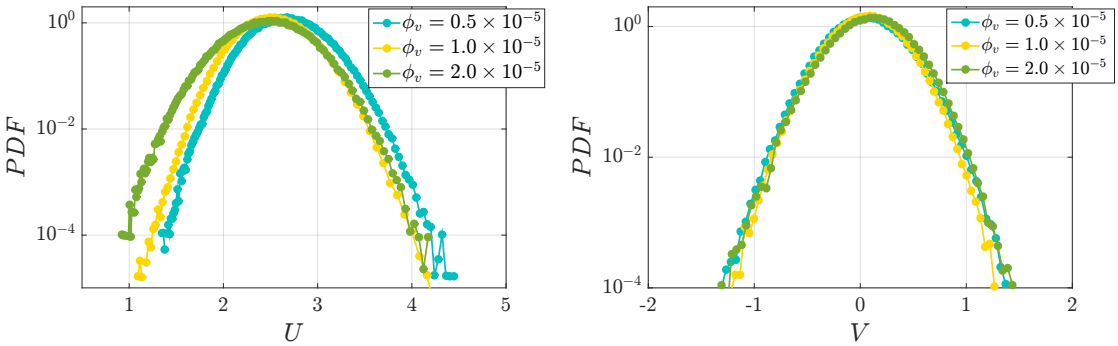

FIGURE 6.3: (a) Probability density function of axial U velocity (b) Probability density function of $V_{settling}$ (raw data), positive V is defined downwards. Data for all particle sizes.

The series of data for small particles $D < 15\mu m$ were obtained by using the coincidence procedure on axial velocity U and settling velocity V measurements with a 50% criteria (i.e. Doppler bursts from both components should overlap in time by at least 50%). The same analysis has been done for small particles of diameter $D < 15\mu m$ for velocities U and V. The PDFs of U and V for small particles are shown on the fig.6.5. Centered and normalised PDFs of U and V for small particles are plotted on fig. 6.6. As before, the standard deviations of both distributions are

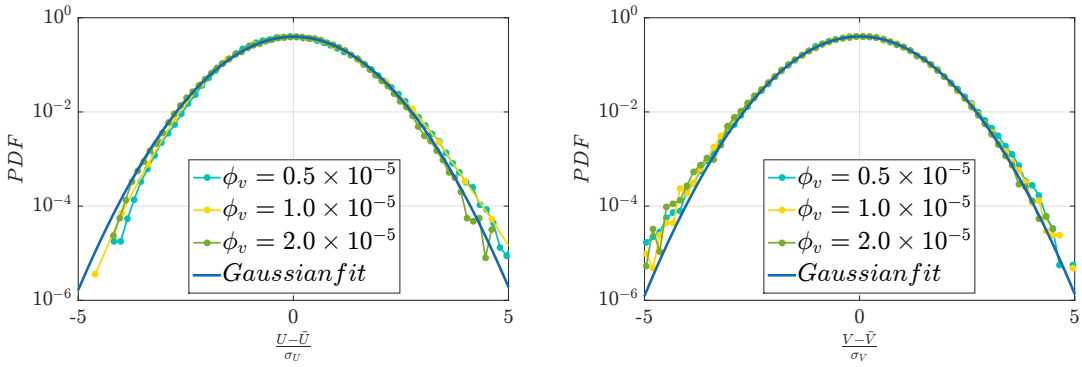

(a) (b)

FIGURE 6.4: (a) PDF of centered and normalised axial U velocity (b) PDF of centered and normalised $V_{settling}$. Data for all particle sizes.

1.4 compared to a quasi-normal distribution with a standard deviation unity.

Clearly the small particles have relaxed to the velocity of the flow (see Table 6.4). The fact that PDF distributions for both small particles only ($D < 15\mu m$) and for all particles are Gaussian with standard deviations that differ by most of $\Delta U_{max} = 0.09m/s$, $\Delta V_{max} = 0.08m/s$, $\Delta U\prime_{max} = 0.05m/s$ and $\Delta V\prime_{max} = 0.02m/s$ indicates:

- that the mean axial velocity of all particles is a good measure of the gas axial velocity,
- that the velocity statistics of axial U and $V_{settling}$ are quite well converged.

This result was used in experiments to set well-controlled flow conditions: in practice, for a given liquid flow rate, the wind speed was adjusted to maintain the actual gas velocity at a prescribed value thanks to PDI data. The values of U given in table 6.4 are obtained for a streamwise gaz velocity, set to a small value around 2.56 m/s. The differences with the set value are small, meaning that the wind speed did not need a lot of adjustment.

We checked the convergence of data by size bins (see Fig. 6.7) and the probability density functions of velocity V of particles over various diameter intervals (see Fig. 6.9). Fig. 6.7 shows that the statistics acquired for diameters $D < 10\ \mu m$ and above diameters $D \simeq 150\ \mu m$ all built on less than 10^3 counts, which could be not enough for a data analysis. The rest of the statistics contain up to 10^5 counts. Same trends could be confirmed from the PDFs of V for different diameters D. Fig. 6.9

TABLE 6.4: Mean and standard deviation of axial and settling velocities (in m/s) for small particles $D < 15\mu m$ and for all detected particles

$D < 15\mu m$ particles				
$\phi_v, \times 10^{-5}$	U	V	$U\prime$	$V\prime$
0.5	2.67	0.05	0.32	0.29
1.0	2.55	-0.01	0.31	0.27
2.0	2.38	0.07	0.36	0.32
All particles				
$\phi_v, \times 10^{-5}$	U	V	$U\prime$	$V\prime$
0.5	2.67	0.06	0.32	0.29
1.0	2.51	0.07	0.31	0.28
2.0	2.47	0.11	0.37	0.30

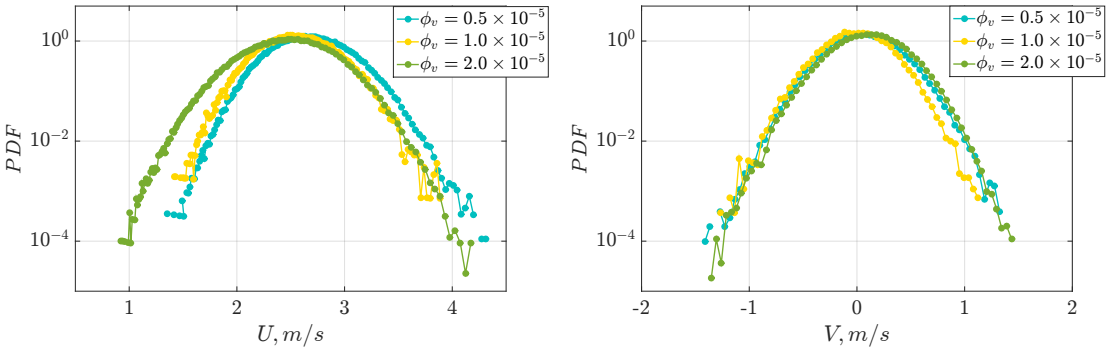

(a) (b)

FIGURE 6.5: (a) Probability density function of axial U velocity for small particles (b) Probability density function of $V_{settling}$ for small particles (raw data), positive V is defined downwards

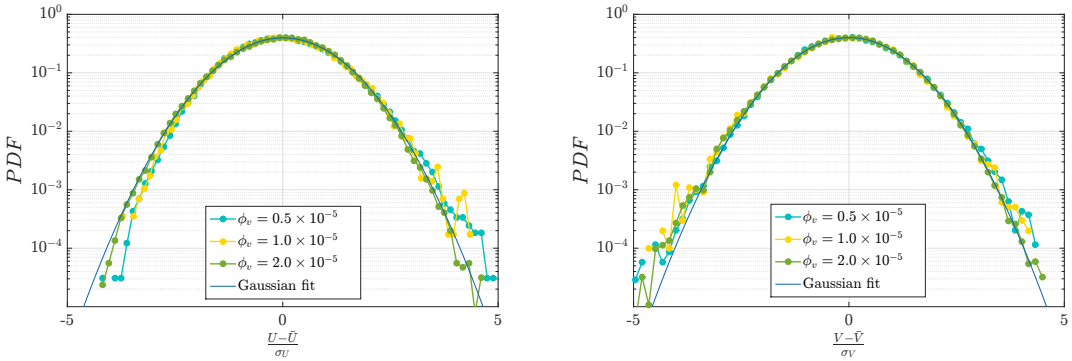

(a) (b)

FIGURE 6.6: (a) PDF of centered and normalised axial U velocity for small particles (b) PDF of centered and normalised $V_{settling}$ for small particles

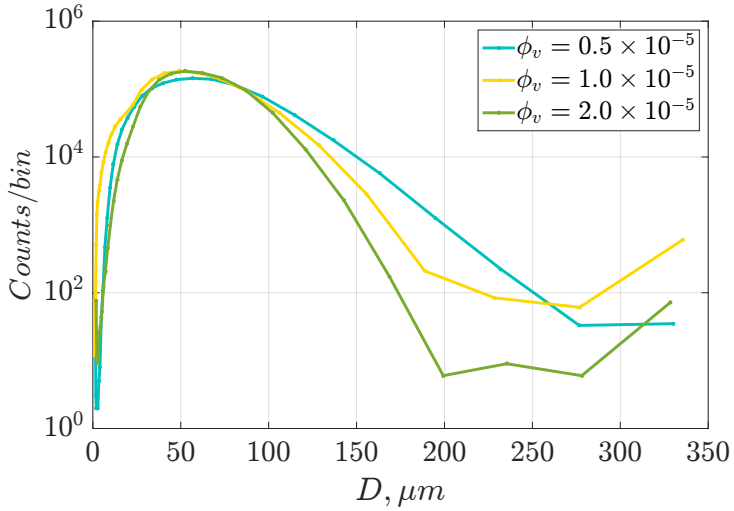

FIGURE 6.7: Counts of velocity statistics binned by diameter D μm. Table 6.5 provides the extent of the binning

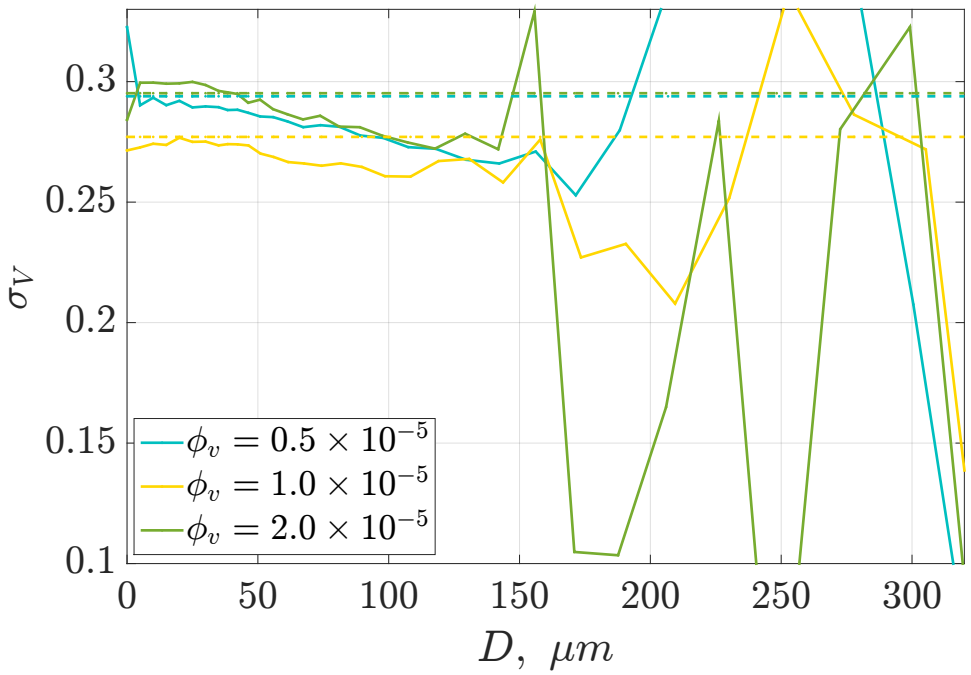

FIGURE 6.8: σ_V by diameter D, μm, dashed lines are the $V\prime$ average over of all particles

TABLE 6.5: Fluctuation $V\prime\ m/s$ by particle diameter $D, \mu m$

$\phi_v \times 10^{-5}$			
	0,5	1	2
bin, μm	$V\prime$	$V\prime$	$V\prime$
0-5	0.2823	0.2714	0.2842
5-10	0.3240	0.2727	0.2995
10-15	0.3201	0.2742	0.2996
15-20	0.3218	0.2737	0.2991
20-25	0.3216	0.2767	0.2993
25-30	0.3217	0.2750	0.2999
30-35	0.3225	0.2751	0.2986
35-38	0.3222	0.2735	0.2961
38-42	0.3230	0.2741	0.2955
42-46	0.3221	0.2740	0.2949
46-51	0.3216	0.2735	0.2912
51-56	0.3219	0.2701	0.2925
56-61	0.3228	0.2687	0.2886
61-67	0.3231	0.2666	0.2865
67-74	0.3216	0.2660	0.2843
74-81	0.3215	0.2651	0.2858
81-89	0.3204	0.2661	0.2813
89-98	0.3217	0.2646	0.2811
98-107	0.3226	0.2607	0.2775
107-118	0.3240	0.2606	0.2748
118-130	0.3247	0.2670	0.2722
130-142	0.3239	0.2679	0.2784
142-156	0.3196	0.2582	0.2719
156-171	0.3175	0.2760	0.3291
171-188	0.3243	0.2270	0.1048
188-207	0.3241	0.2327	0.1034
207-227	0.3011	0.2079	0.1650
227-249	0.3951	0.2516	0.2837
249-274	0.2705	0.3374	no data
274-301	0.2384	0.2863	0.2803
301-330	0.3948	0.2719	0.3227
330-360	no data	no data	no data

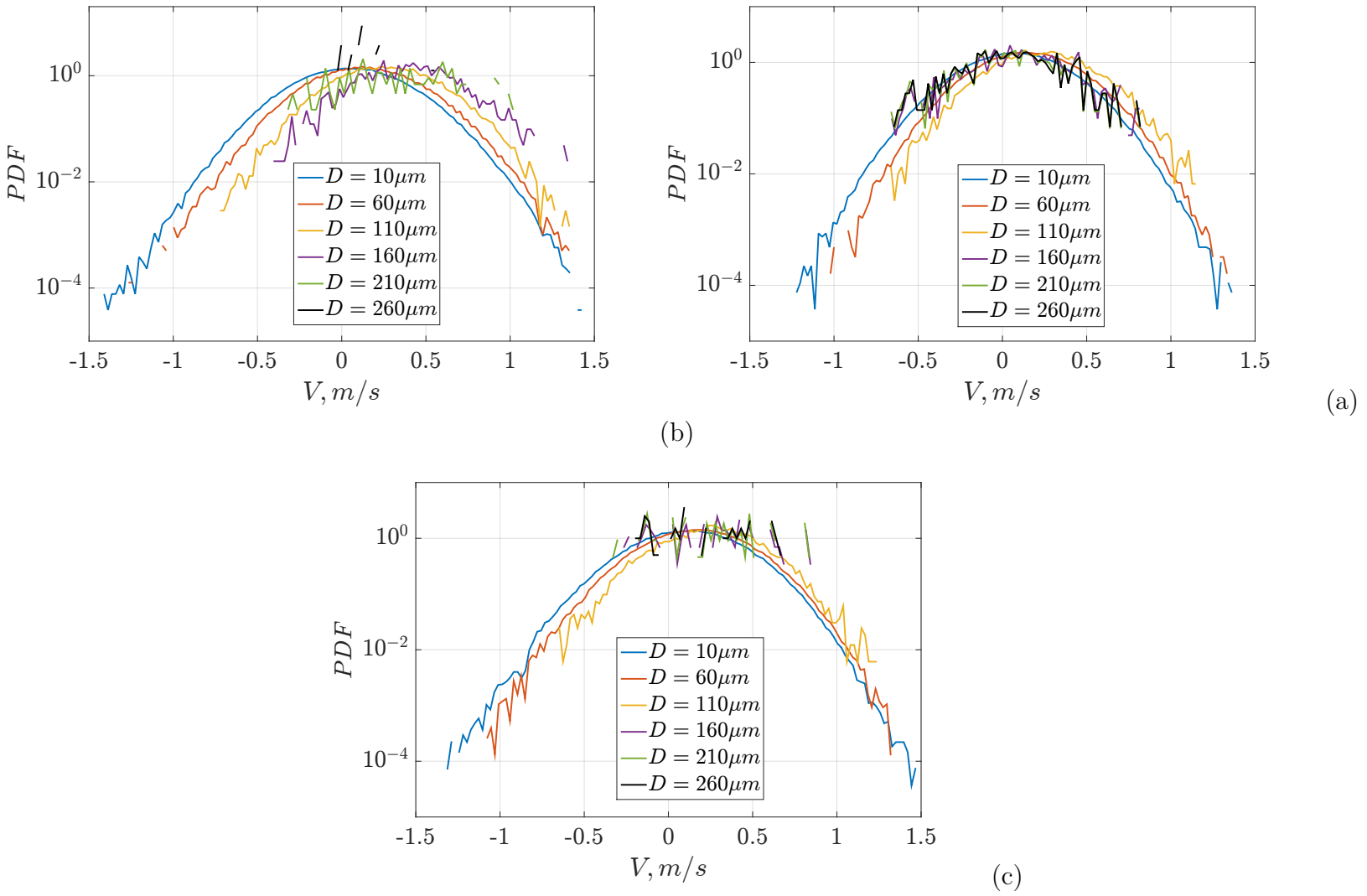

FIGURE 6.9: PDF of velocity V (raw data) for particles with different D (a) $\phi_v = 0.5 \times 10^{-5}$, (b)$\phi_v = 1.0 \times 10^{-5}$, (c) $\phi_v = 2.0 \times 10^{-5}$

confirms the presence of a convergence issue for $D > 110\ \mu m$. For all other diameters $D \leq 110\ \mu m$ the PDFs of V appear to be well-converged and resolved between $-1.5\ m/s$ and $1.5\ m/s$.
From the table 6.5 we could see that $V\prime$ is almost constant except in the first two bins $0 - 5, 5 - 10\ \mu m$ and for the bins after $142 - 156\ \mu m$. This means that the higher fluctuations are due to lack of detected statistics. We could see from the fig. 6.8 that the large fluctuations of the $V\prime$ starts from about $D = 150\ \mu m$. There is also some large fluctuations of $V\prime$ around small diameters $D = 5\ \mu m$. Thus, it is important to note that the data before $D = 5\mu m$ and past $D > 150\ \mu m$ are not statistically very well converged.

6.4.2 Comparison with Tchen-Hinze model

Given that we have information about particles time response, we can try to compare our data with the Tchen-Hinze model. Extended Tchen-Hinze model has been extensively investigated, best explained by Fevrier [25], and it provides the following result:

$$2{q_p}^2 = 2{q_{f@p}}^2 \frac{T_L^{L^{f@p}}}{T_L^{L^{f@p}} + {\tau_{12}}^F} \tag{6.5}$$

where ${\tau_{12}}^F$ is simplified to τ_p, ${q_p}^2$ is the particle's turbulent kinetic energy, ${q_{f@p}}^2$ is the turbulent kinetic energy of the fluid at the position of particle and $T_L^{L^{f@p}}$ is the Lagrangian integral timescale of the fluid at the particle's position. Wang & Stock [74] proposed a semi-empirical correction to estimate $T_L^{L^{f@p}}$:

$$\frac{T_L^{L^{f@p}}}{T_L^E} = 1 - (1 - \frac{T_L^L}{T_L^E})(1 + \frac{\tau_p}{T_L^E})^{-0.4(1+0.01\frac{\tau_p}{T_L^E})} \tag{6.6}$$

The Lagrangian integral timescale T_L^L is estimated by Sawford [64] as:

$$T_L^L = T_L^\infty (1 + {Re^\star}^{\frac{1}{2}}) \tag{6.7}$$

where $T_L^\infty = \frac{2}{C_0} T_L^E$ where C_0 is assumed to be 6 and T_L^E is the Eulerian integral timescale. Let's define our Re_λ as $(\frac{T_L^E}{T_\eta^E})^2$. Sawford [64] defines $Re_\star = 16\frac{{a_0}^4}{{C_0}^4} Re_\lambda$.
Now we have most of the parameters to compare with the Tchen-Hinze model. Yet, we have the measurements of $V\prime$ of particles by the diameter D, but we do not possess $U\prime$ or $W\prime$ (the transverse velocity component) by diameter D. Instead we make very strong hypothesis that $q_p^2 = 3V\prime^2$. In addition, we do not have the

measurements of ${q_{f@p}}^2$, the turbulent kinetic energy of the fluid at the position of particle. So three possibilities were suggested to calculate this quantity:

- assuming that ${q_{f@p}}^2 = {q_f}^2$ where q_f is the turbulent kinetic energy of the flow and equals to $3(0.15\bar{U})^2$ due to 15% fluctuation rate and isotropy of the turbulence.

- assuming that the turbulent fluctuation rate in z-direction $W\prime$ is the same as the turbulent fluctuation rate in x-direction $U\prime$ because the turbulent fluctuations in y-direction are affected by the gravity. Hence, ${q_{f@p}}^2 = 2U\prime^2 + V\prime^2$ where $U\prime$ is a standard deviation of the axial velocity U of all particles.

- assuming the Homegeneous Isotropic Turbulence and the equality of fluctuations rate in all three directions $U\prime = V\prime = W\prime$ holds. Hence, ${q_{f@p}}^2 = 3V\prime^2$. Here we have a choice between two estimations of $V\prime$ either one estimated for particles with diameter $D < 15\ \mu m$ or one estimated as a standard deviation over all particles ranges. From table 6.4 we could see that the maximum dispersion between two estimations of $V\prime$ is of 0.02 m/s which is about 6%. Therefore, we choose $V\prime$ calculated over the whole range of particles sizes.

Combining all these variables we plotted the extended Tchen-Hinze model shown on the fig. 6.11 using the three assumptions mentioned above. It is clear that there is a large dispersion for large diameters $D > 150\ \mu m$ i.e. smaller $\frac{\tau_L^{f@p}}{\tau_p}$ and owing to the lack of statistics. The trend obtained from experiments is in a good agreement with the theory (see fig. 6.11c), when using the very strong assumption ${q_{f@p}}^2 = 3V\prime^2$. The trend is greatly underestimated compared with the extended Tchen-Hinze model when using the assumption ${q_{f@p}}^2 = 3(0.15\bar{U})^2$ (see fig. 6.11a). This is expected as the turbulent intensity measured in the single phase condition nearly exceeds estimates using PDI data. The trend is in intermediary agreement with extended Tchen-Hinze model when using ${q_{f@p}}^2 = 2U\prime^2 + V\prime^2$ (see fig. 6.11b) meaning that accounting for the small anisotropy of the scales in x, y and z directions reduces the gap between the extended model and current results. Overall, from the best estimate obtained (see fig. 6.11c) we could conclude that, over the range where the fluctuations are well resolved, the trend is in agreement with Tchen-Hinze model. Finally, all particles present in the flow conditions experience velocity fluctuations close to those of the gas phase.

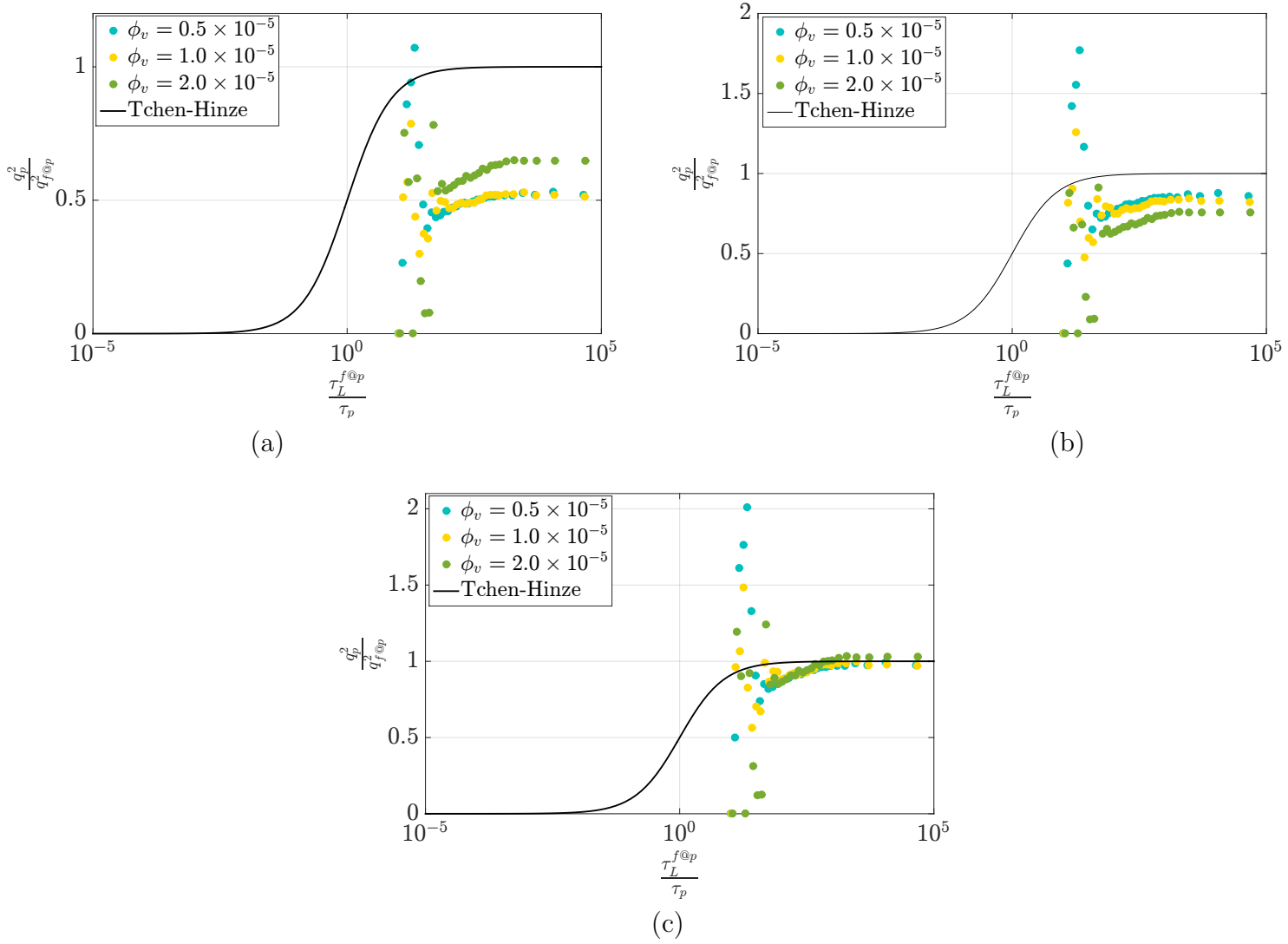

FIGURE 6.11: Tchen-Hinze model plotted using (a) ${q_{f@p}}^2 = 3(0.15\bar{U})^2$ (b) ${q_{f@p}}^2 = 2(U\prime)^2 + V\prime^2_{average}$ where $V\prime_{average}$ is the standard deviation of V over all range of particles (c) ${q_{f@p}}^2 = 3V\prime^2$. (Data below $\frac{\tau_L^{f@p}}{\tau_p} < 10^2$ correspond to $D > 150\ \mu m$ for which the statistical noise is very large, and thus, are not representative).

6.4.3 Measurements of settling velocity of inertial particles $V_{settling}$

PDI measurements allow registering dynamics of the particles with the simultaneous measurement of their diameter. The plot of $V_{settling}$ corresponding to raw data detected by the PDI system vs D is shown on the fig. 6.10 for the three volume fractions ϕ_v considered (see Table 6.1 for other parameters defining our experimental conditions)

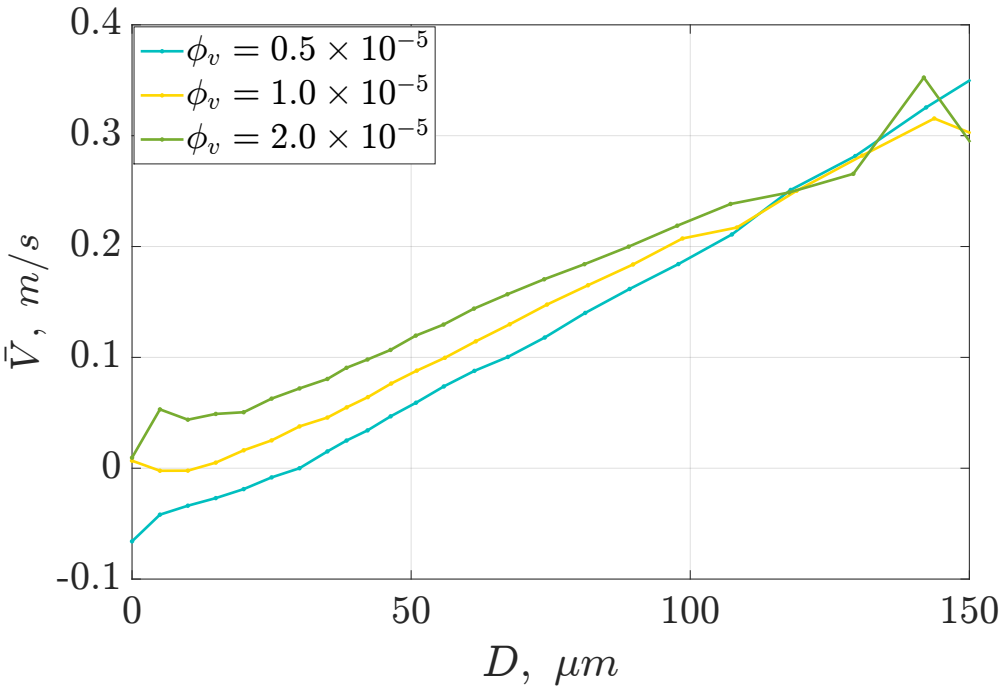

FIGURE 6.10: Settling velocity $V_{settling}$ vs D of all measured particles, positive V is defined downwards

From the fig.6.10, it happens that a velocity $V_{settling} \neq 0$ is measured in the limit of very small diameters although one expects the settling velocity to reach zero for tracers (i.e. as $D \to 0$) and in the limit of very dilute conditions. The presence of an offset velocity at small diameters holds at all three concentrations, and that offset velocity increases with the volume loading. Such trends correspond to two contributions:

1. In PDI measurements, there is always some uncertainty as to whether the system detects the velocity component perfectly aligned with the vertical: this bias due to alignment of the system is noted $V_{alignment}$.

2. With an increase in the concentration, another shift in velocity - most probably due to physical effects and hence noted $V_{physical}$ – is present. Note that such a shift has been already seen by Aliseda et al. [1].

Therefore, the offset in velocity can be written as:

$$V_{offset} = V_{alignment} + V_{physical} \tag{6.8}$$

The key point is to disentangle the above two contributions. One may try to do that based on a perfect optical alignment. Yet, as the ratio of axial to vertical velocities is large (factor of 10 to 100 depending on drop size), any slight misalignment of the green fringe system with an horizontal plane will bias the measurements of the settling velocity. In practice, the green beams were aligned along a vertical by considering their projections on a nearby wall: the beam position being estimated within $1mm$ for a beam separation of a few $10cm$, the resulting uncertainty on the angle is about $0.5°$. That angle leads to a bias about $0,009$ times the axial velocity, that is about $2\ cm/s$. Performing an optical alignment that would lead to a bias ten times lower ($\sim mm/s$) is therefore quite difficult. Instead, we decided to deduce the bias due to the alignment from raw data by considering that the settling velocity is zero for very small drops acting as tracers.

In principle, that detection should be achieved on extremely dilute conditions to get rid of any possible collective effect. Yet, in the present experiments, the experiment was not run at concentrations below $\phi_v = 0.5 \times 10^{-5}$ because the injectors were no longer working properly for lower liquid flow rates. Instead of considering the limit as $D = 0$ and a vanishing concentration, we somewhat arbitrarily assume that the lowest concentration considered was enough dilute. Hence the bias due to misalignment $V_{alignment}$ was determined the limit for of $D = 0$ from the measured settling velocity for the data collected at $\phi_v = 0.5 \times 10^{-5}$.

6.4.4 Determination of $V_{alignment}$

The bias $V_{alignment}$ has therefore been estimated as the limit of the velocity of particles whose diameter is approaching 0 for the experimental condition of $\phi_v = 0.5 \times 10^{-5}$. As the velocity is expected to increase as D^2, we considered linear fits of the curve $V_{settling}$ vs D^2 as shown on fig. 6.12. In addition, various diameter intervals were accounted for starting from a size D_{start} up to $25\mu m$: the corresponding estimates are given in table 6.6. The sensitivity of the fit happens to be about 4.8%

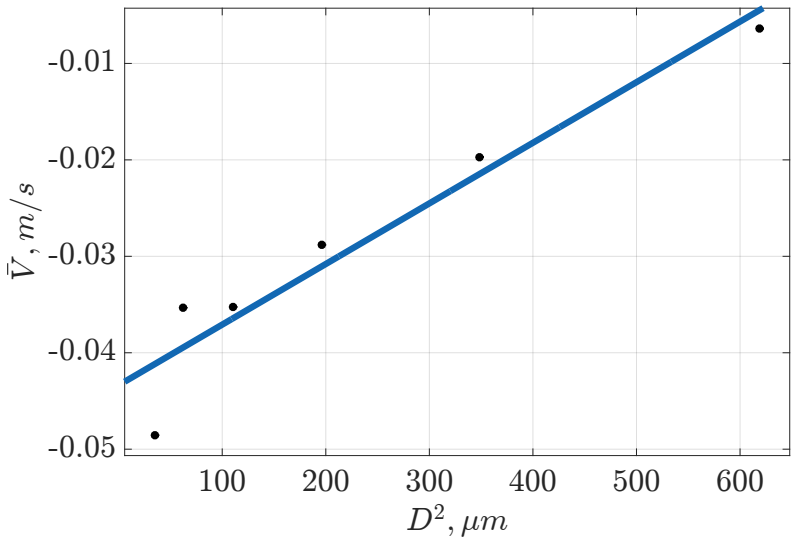

FIGURE 6.12: Extrapolation of the curve $V_{settling}$ vs D to determine $V_{alignment}$. Data for $\phi_v = 0.5 \times 10^{-5}$

TABLE 6.6: Fitting linearly $V_{alignment}$ m/s values by taking different ranges of diameters from D_{start} up to $25\mu m$

$D > 5\mu m$	$D > 6\mu m$	$D > 10\mu m$
-0.04034	-0.03962	-0.04337

with a mean value for $V_{alignment}$ around $-0.0411cm/s$. From that estimate, one can deduce the actual inclination of the fringe system with an horizontal plane. Putting

$$V_{alignment} = V_{axial} \times \alpha \tag{6.9}$$

where α is the misalignment angle and V_{axial} is the freestream velocity of the flow, $\alpha V_{axial} = -0.0411$ at $V_{axial} = 2.5m/s$ gives $\alpha = 0.0164rad = 0.94°$. Hence, the uncertainty on the alignment is about 1°, which is close to the magnitude estimated above.

In the following, the quantity $V_{alignment} = -0.0411cm/s$ will be deduced from all raw data. In particular, the settling velocity corrected for the alignment versus the drop diameter is now given in fig. 6.13. So, eq. 6.8 becomes:

$$V_{offset} = V_{axial} \times \alpha + V_{physical}(\phi_v, R_\lambda) \tag{6.10}$$

It is quite clear from fig. 6.13 that after substracting $V_{alignment}$, there is an additional offset $V_{physical}$ that will be determined in the next subsection.

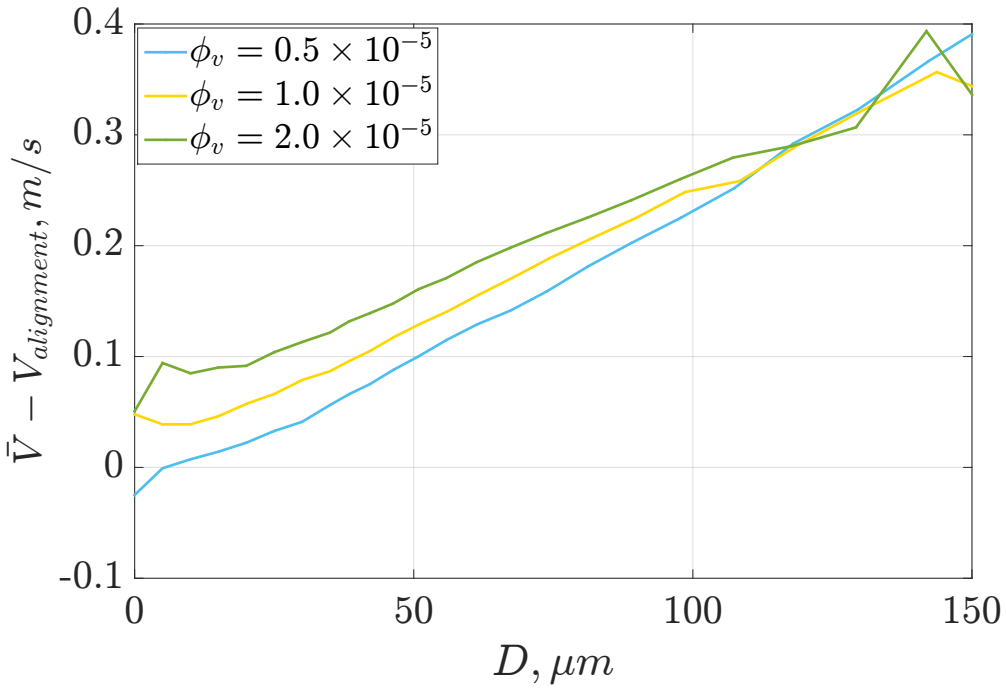

FIGURE 6.13: $\bar{V} - V_{alignment}$ vs D for three experimental conditions

6.4.5 Determination of $V_{physical}$

Substracting $V_{alignment}$ does not completely solve the issue on the offset since there is a second component $V_{physical}$, as shown on the fig. 6.14 supposedly due to change with volume fraction and possibly combined with turbulence effects.

It is worth examining how the quantity $\lim_{D\to 0} V_{Settling} - V_{alignment} - V_{St}$ evolves with the volume fraction. Fig. 6.14 shows that the component $V_{physical}$ is indeed present in our experimental conditions. Moreover, data with higher volume fractions exhibit higher deviations from 0 at $D < 10\mu m$. This could be owed due to the small number of detected data at these particular small diameters.
Hence, due to the limitations of the PDI system, it was decided to extrapolate the quantity $\lim_{D\to 0} V_{Settling} - V_{alignment} - V_{St}$ at $D = 0$.

Now that we have removed the alignment offset and the contribution due to non-linear drag, it is possible to determine the physical offset $V_{physical}$ (fig. 6.14). As before, the range of points in between D_{start} and $25\mu m$ is investigated using linear fitting, giving the values of offset due to physical conditions (see example of such a fit on the fig. 6.15). These offsets are given in the table 6.7. The offset for the most dilute experimental condition is 0 which is logical since this is the value that was used to compute the alignment offset and then substracted from the vertical

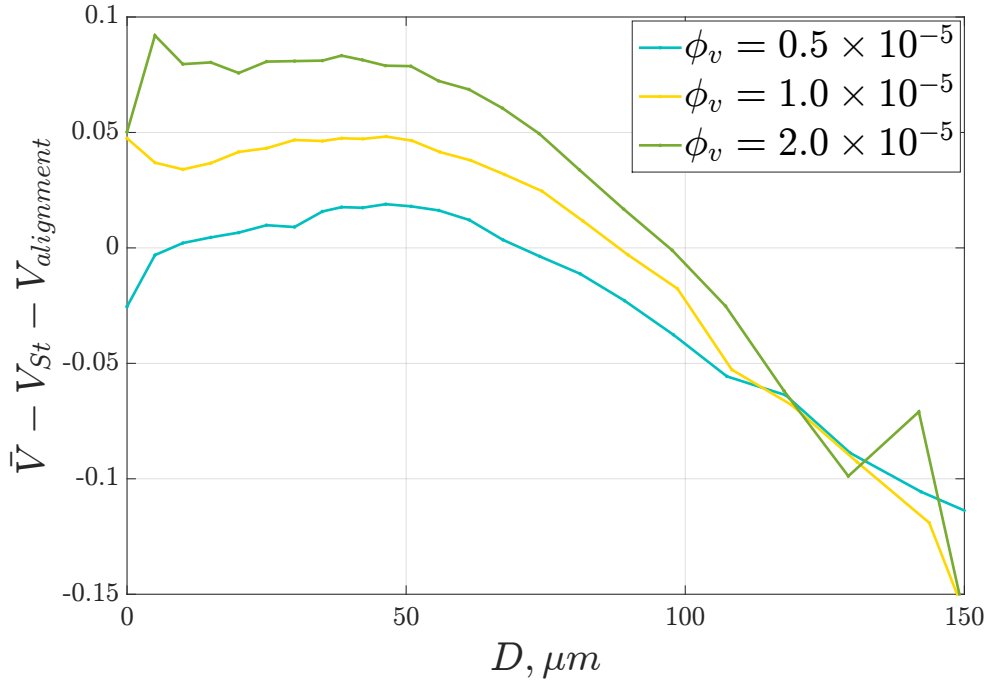

FIGURE 6.14: Raw $\bar{V} - V_{alignment} - V_{St}$ m/s vs D, μm of all particles. Positive V represents downward settling velocity

velocity measurement. The standard deviation of the estimated offset values for three experimental conditions is of the order of 5 mm/s. Let's look at the dependence of $V_{physical}$ on volume fraction plotted on fig. 6.16. The relationship between mentioned quantities is quasi-linear, yielding:

$$V_{physical}(m/s) = 4.86 \times 10^3 \phi_v - 0.0253 \tag{6.11}$$

The significance of $V_{physical}$ will be discussed in the Section 6.7.1 where the data on velocity conditioned by the local concentration and the size of the drops will have been made available. The fact that $V_{physical}$ goes to $\simeq -0.025$ m/s in the limit

ϕ_v	$D > 5$	$D > 6$	$D > 8$	$D > 9$	$D > 13$	$\bar{V}_{physical}$	$\sigma_{V_{physical}}$
0.5×10^{-5}	-0.0087	-0.0019	-0.0042	-0.0015	-0.0068	-0.0046	0.0031
1.0×10^{-5}	0.0344	0.0316	0.0258	0.0240	0.0218	0.0275	0.0053
2.0×10^{-5}	0.0593	0.0735	0.0724	0.0743	0.0715	0.0702	0.0062

TABLE 6.7: Values of offset $V_{physical}$ found by fitting linearly $\bar{V} - V_{alignment} - V_{St}$ vs D using different ranges of D_{start} to $25\mu m$

$\phi_v \to 0$ comes out from the fact that the zero was set for a finite volume fraction,

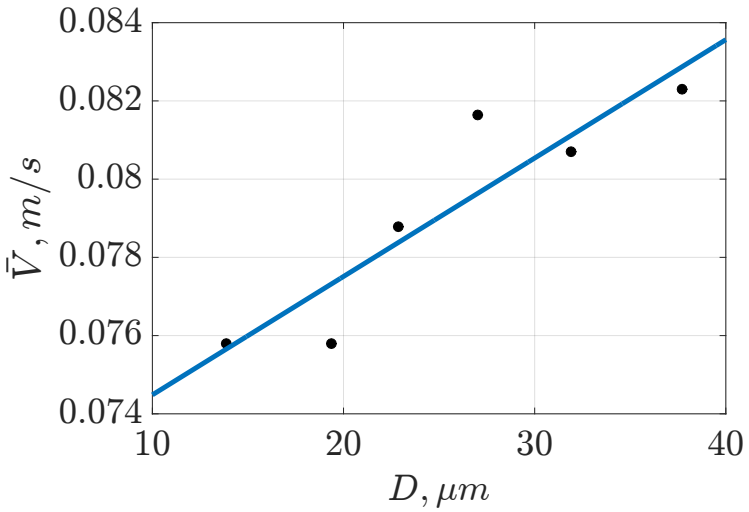

FIGURE 6.15: Extrapolation of the curves $V_{settling}$ vs D to determine $V_{physical}$. Data for concentration $\phi_v = 2 \times 10^{-5}$.

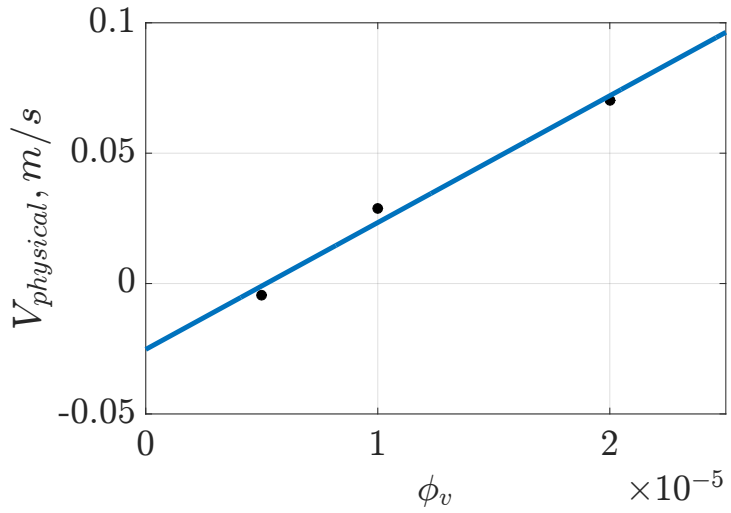

FIGURE 6.16: (a) $V_{physical}$ vs volume fraction ϕ_v

and this does not mean that $V_{physical}$ could be negative. This artifact is expected to disappear after performing the same analysis at a lower volume fraction.

6.4.6 Settling velocity of inertial particles $V_{settling}$

Let's substract now both offsets $V_{physical}$, $V_{alignment}$ and the terminal velocity V_{St} from $V_{settling}$ and plot it vs D. Fig. 6.17 indicates that the turbulence enhancement of the settling velocity V occurs for all three experimental conditions in the regions $0 < D < 60\ \mu m$ for $\phi_v = 0.5 \times 10^{-5}$ and $0 < D < 70\ \mu m$ for the other two higher volume fractions. However, past these limits velocity hindering takes place for higher

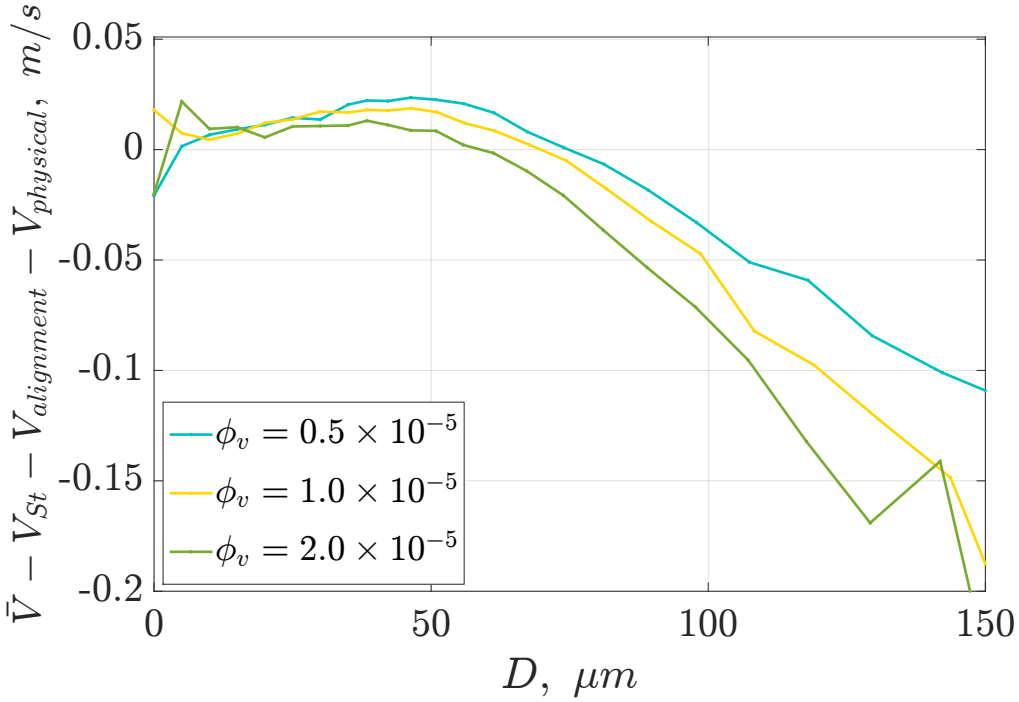

FIGURE 6.17: Settling velocity $\bar{V} - V_{alignment} - V_{St} - V_{physical} m/s$ vs D of all measured particles, positive V is defined downwards

diameters.

In addition, no collapse of the curves could be seen, indicating that $V_{physical}$ as defined in the limit $D \to 0$ is not a representative of the shift of curves over the whole range of diameters. In other words, the influence of the volume fraction on the settling velocity is not uniform over the range of sizes.

Fig. 6.18 shows the $\frac{\bar{V}-V_{alignment}-V_{St}}{V_{St}}$ vs St number where $\bar{V}$ is an averaged velocity by size of the particles. We could see that the enhancement of the settling velocity is quite large and evolves greatly with the rising volume fraction till $St <$ 1.6, 2.3, 2.6 respectively. However, past these critical values of St number hindering of particle velocity is noticeable for heavy particles. To better appreciate the limits between enhancement and hindering, we plot $\frac{\bar{V}-V_{alignment}-V_{St}}{U\prime}$ vs both St and Ro as shown on the fig.6.19 a&b. Here, we selected $U\prime$ over the whole range of particles as measured by PDI (see table 6.4). The behaviours of both curves versus St and Ro are quite similar due to the linear relationship between St and Ro:

$$St = \frac{\tau_p}{\tau_\eta} \tag{6.12}$$

$$Ro = \frac{\tau_p \times g}{U\prime} \tag{6.13}$$

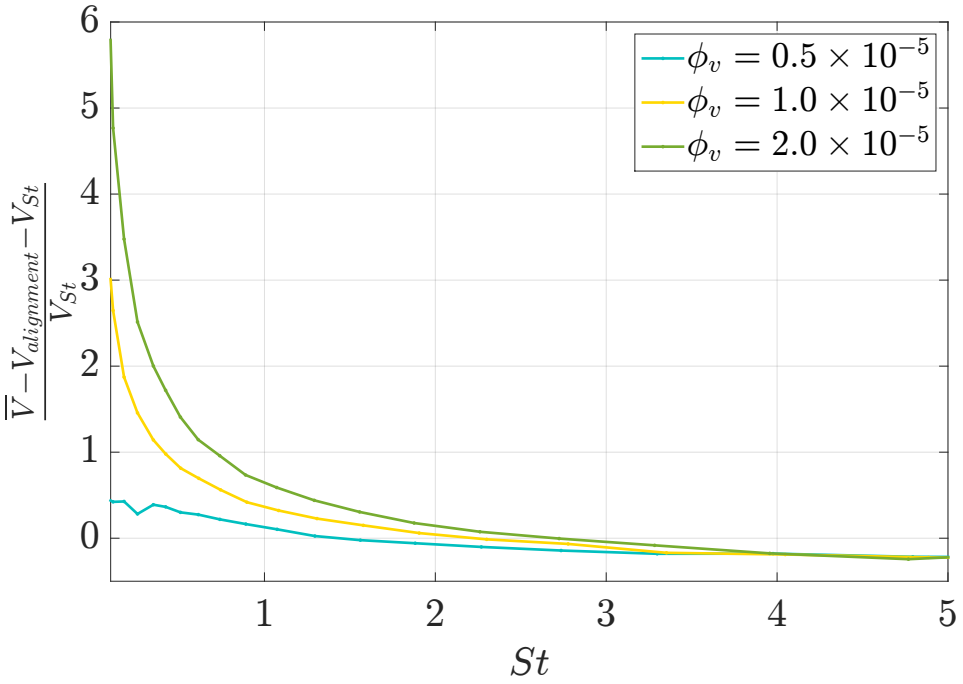

FIGURE 6.18: Corrected with alignment settling velocity $\frac{\bar{V} - V_{alignment} - V_{St}}{V_{St}}$ vs St of all measured particles

as $U\prime$ and τ_η are fixed for the present conditions.

Table 6.8 shows the abscissa of the maxima and their values. Maxima occur for St between $St = 0.4$ and $St = 0.7$ which is comparable to previous studies (see the discussion in Chapter 2). The enhanced settling velocity reaches up to 23% of the turbulent intensity $U\prime$ for the highest volume fraction $\phi_v = 2.0 \times 10^{-5}$. The maximum is 15.4% for $\phi_v = 1.0 \times 10^{-5}$. The lowest maximum enhancement of settling velocity is about 6% and happens for $\phi_v = 0.5 \times 10^{-5}$. Turbulent hindering happens to be significantly strong, reaching up to 50% of $U\prime$. This could be attributed to a loitering effect of heavy particles as suggested by Nielsen[54]. More about hindering of large particles will be discussed in the next Section 6.5.

Table 6.8 also provides the values of St, Ro for which the settling velocity equals the terminal velocity for a laminar flow for that particle size at the different volume fractions ϕ_v. Hindering of the particles dynamics happens for $St > 1.6, 2.3$ and 2.6 (respectively for Ro above 0.42 and $0.70, 0.70$) as the volume fraction ϕ_v increases.

From these plots we could also conclude that there is a clear effect of volume fraction on the settling velocity over the whole range of St and Ro considered.

The curves $\frac{\bar{V} - V_{alignment} - V_{St} - V_{physical}}{U\prime}$ (where $U\prime$ is the standard deviation of the streamwise velocity U_{axial} fluctuations of all particles which values are shown in the

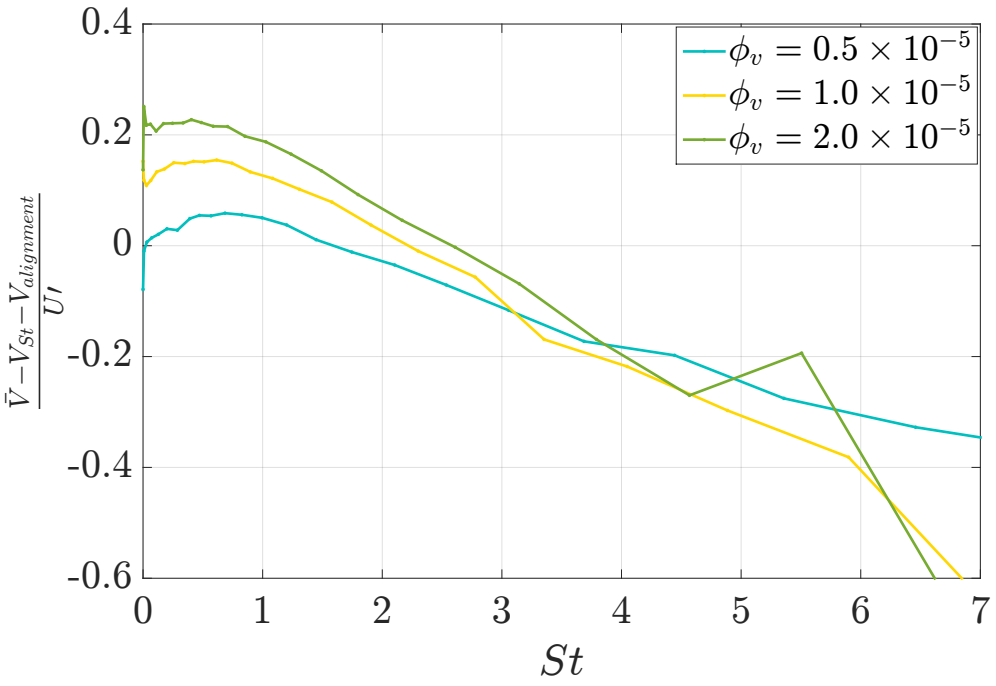

(a)

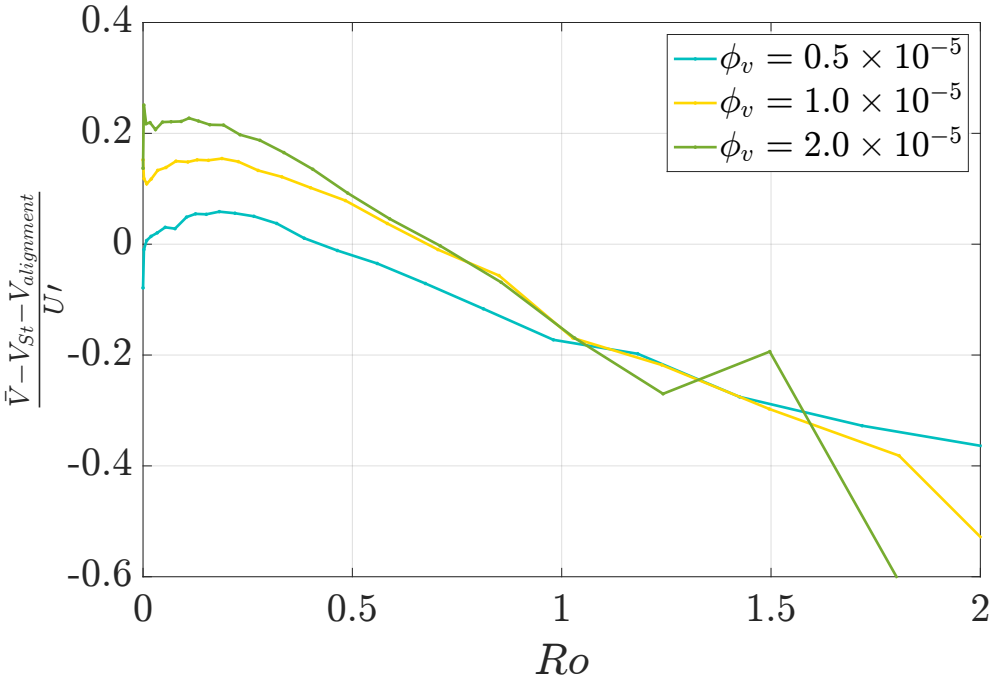

(b)

FIGURE 6.19: Settling velocity $\frac{\bar{V}-V_{alignment}-V_{St}}{U'}$ vs (a) St and (b) Ro, positive V is defined downwards

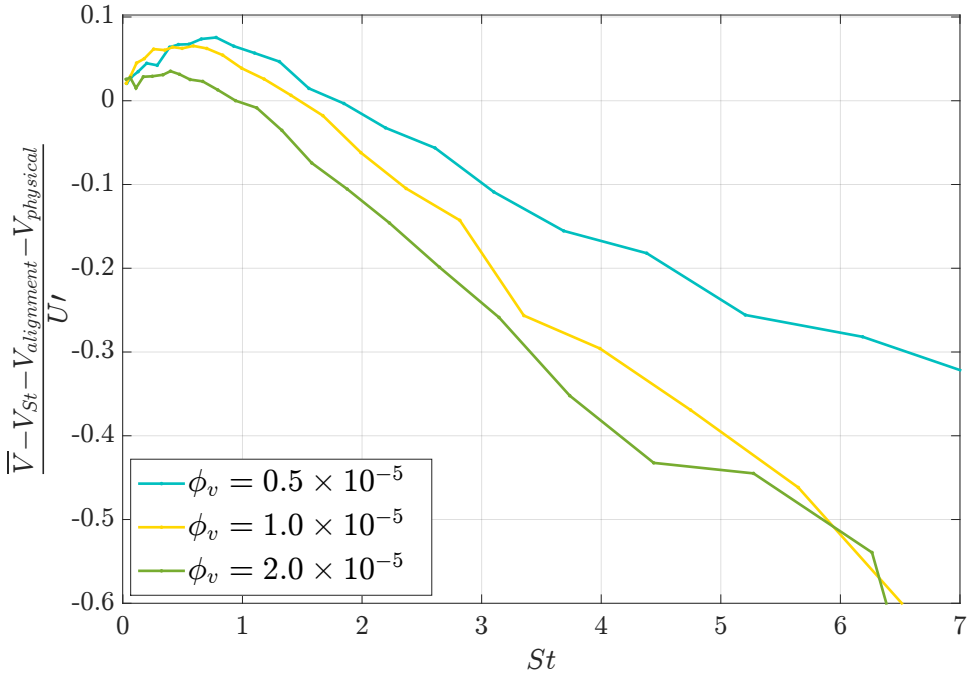

(a)

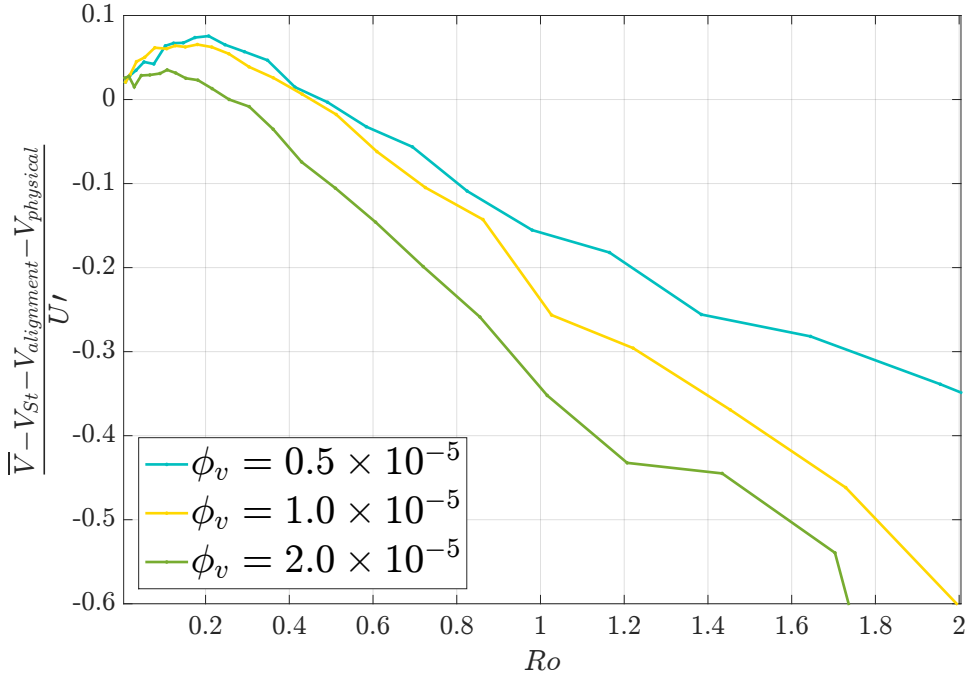

(b)

FIGURE 6.20: Settling velocity $\frac{\bar{V}-V_{alignment}-V_{St}-V_{physical}}{U\prime}$ vs (a) St and (b) Ro, positive V is defined downwards

table 6.4) versus St and Ro exhibit the same features (see also fig. 6.20). Yet, the fact that $V_{physical}$ does not represent the influence of ϕ_v over the whole range of sizes is made even more clear as the three curves deviate more and more from each other as St and Ro increase. A striking result is that in the hindering region at large Ro ($Ro > 1$), the volume fraction ϕ_v has no effect on the velocity change meaning that the clusters (the existence of which will be demonstrated in Section 6.6) are not affecting the way particle with large terminal velocity interact with turbulence. Again no collapse with $U\prime$ could be seen after substracting the effect of volume loading ϕ_v and Stokes drag. This means that the velocity statistics of inertial particles depend on more than just the turbulence intensity $U\prime$ of the carrier fluid, and that $U\prime$ could not be the appropriate variable to scale the effects of enhancement or hindering of the settling velocity V. We will go back on this question in Section 6.5.2.

TABLE 6.8: Maximum and zero-crossing values of curves $\frac{\overline{V}-V_{St}-V_{alignment}}{U\prime}$ versus St, Ro

$\phi_v, \times 10^{-5}$	St_{max}	Ro_{max}	Maximum value	$St_{zero\ crossing}$	$Ro_{zero\ crossing}$	$V_{mean},\ m/s$
0.5	0.69	0.18	0.059	1.6	0.42	0.105
1.0	0.62	0.19	0.154	2.3	0.70	0.117
2.0	0.40	0.11	0.227	2.6	0.70	0.162

We also considered the mean settling velocity V_{mean} as the arithmetic average evaluated over all particles present in the flow (i.e. considering all sizes up to $300\mu m$) according to:

$$V_{mean} = \int_{D_0}^{D_\infty} V(D)P(D)dD \tag{6.14}$$

Figure 6.21 shows the behaviour of $\frac{\bar{V}-V_{mean}}{V\prime}$ vs St. In the range of $0 < St < 2-4$ all three non-dimensionalised curves seem to almost collapse, showing invariant properties of quantity $\frac{\bar{V}-V_{mean}}{V\prime}$ with St and ϕ_v.

Interestingly, particles with St number below about 0.7 have a settling velocity lower than V_{mean}, while larger particles (at $St > 0.7$) have a velocity higher than V_{mean}. Hence, in a frame moving at the average fall velocity of the cloud of particles, small particles would rise while the rest of the drop population would fall. This trend is quite general and it is not due to size segregation between flow regions (see Section 6.6 where quantities conditioned by the local concentration will be presented).

Note that the change of the sign of $\overline{V} - V_{mean}$ happens at lower Stokes numbers compared to the transition between settling enhancement and hindering shown in fig. 6.19 or fig. 6.20. Indeed, we do not expect identical results when comparing to

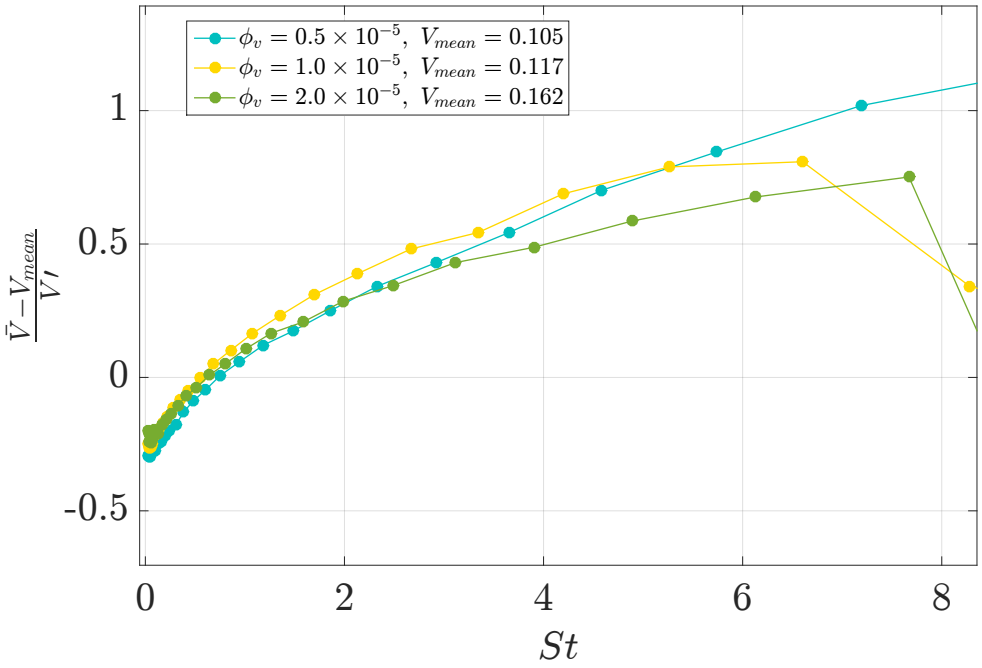

FIGURE 6.21: Settling velocity $\frac{\bar{V}-V_{mean}}{V'}$ vs St of all measured particles

the terminal velocity at a given size, and when comparing to the average velocity of the entire cloud of particles. The quantity V_{mean} is indeed dependent on the size distribution, and thus, it is not universal as it would change if another drop population is injected in the flow.

6.5 Discussion

The behaviour of settling velocity of inertial particles in the presence of turbulence and varying volume fraction has been attempted to be explained by a large amount of numerical and experimental studies. To remind the reader, we acquired the data for a high Re_λ regime, with the varying volume fraction of $0.5 - 2.0 \times 10^{-5}$ and with heavy subkolmogorov inertial particles. In such conditions, the presence of turbulence interacting with inertial particles results in the phenomenon of clustering of inertial particles. The role of turbulence and cluster formation is quite profound on the settling velocity of particles. While the enhancement of the settling velocity of the particles is expected for small particles, [73],[1], [28] a hindering of the settling velocity has been also observed for large particles [54], [31].

Moreover, the scaling of the enhancement of settling velocity has been proposed

with parameters such standard deviation of the velocity fluctuations $U\prime$ and the Kolmogorov velocity u_η.

It is worthwhile to focus first on the number of independent non-dimensional parameters chosen to characterise the two-phase flow. In a situation involving monodispersed fluid particles in a turbulent field, the following list of physical parameters can be tentatively established.

The physical parameters for the fluid are represented by:

- fluid density ρ_f,
- fluid kinematic viscosity ν_f,
- fluid integral length scale L (or alternatively the dissipation per unit volume),
- fluid turbulence intensity $U\prime$.

The physical parameters for the particles are the following:

- particle size D,
- particle density ρ_p,
- volume fraction ϕ_v,

in addition to

- gravity g,

where the dynamic viscosity of fluid particles and surface tension have been omitted neglecting any influence of the internal circulation within the drops as well as their deformation. Note that the turbulent field is fully characterised by L (or the dissipation rate ϵ), $U\prime$ and the fluid viscosity ν_f. These 8 physical parameters lead to five non-dimensional numbers. A possible choice is:

- volume fraction = ϕ_v,
- density ratio = $\frac{\rho_p}{\rho_f}$,
- turbulent Reynolds number based on L (integral scale) $Re_L = \frac{U\prime L}{\nu_f}$ (alternatively, one can use Reynolds number based on the Taylor scale λ),
- Stokes number = $\frac{\tau_p}{\tau_\eta}$ where τ_p is the particle response time and τ_η is the Kolmogorov timescale,

- Rouse number $= \frac{\tau_p g}{U\prime}$.

Note that in case of polydispersed systems, the distribution of normalized diameters $P(\frac{D}{D10})$ should be added to the above list.

Hence, we do not expect extra parameters to drive the response of particles (neglecting shocks or coalescence). For example, Good et al [31] introduced Fr as the ratio of the acceleration of the fluid r.m.s to the gravitational acceleration. However, such a use of Fr number is redundant with regards to the non-dimensional parameters we choose for the following reasons. Fr number is defined as:

$$Fr = \frac{\gamma\prime}{g} = \frac{{a_0}^{\frac{1}{2}}(\frac{\epsilon^3}{\nu})^{\frac{1}{4}}}{g} \tag{6.15}$$

where $\gamma\prime = {a_0}^{\frac{1}{2}}(\frac{\epsilon^3}{\nu})^{\frac{1}{4}}$ is the acceleration fluid rms, and one could express that as:

$$Fr = a_0^{\frac{1}{2}} \times Re_L^{\frac{1}{4}} \times \frac{U\prime^2}{gL} = a_0^{\frac{1}{2}} \times Re_L^{\frac{1}{4}} \times \frac{U\prime}{g\tau_p} \times \frac{\tau_p}{\tau_\eta} \times \frac{\tau_\eta U\prime}{L} = a_0^{\frac{1}{2}} \times \frac{St}{Ro} \times Re_L^{-\frac{1}{4}}. \tag{6.16}$$

Hence, from equation 6.16 we see that the information about particle response τ_p has been vanished by dividing St number by Ro number. In addition, a_0 is a function of Re_λ and is estimated as $a_0 = 0.13 \times Re_\lambda^{0.64}$ by Sawford[64]. Thus, the Fr number is not an extra parameter to consider.

The role of St and Ro numbers is not easy to disentangle as they are both built on the particle response time τ_p. Indeed:

$$\frac{St}{Ro} = \frac{U\prime}{g\tau_\eta} = \frac{U\prime^2}{gL} \times Re_L^{\frac{1}{2}} = \frac{U\prime^2}{gL} \times \left(\frac{U\prime L}{\nu}\right)^{\frac{1}{2}} = \frac{U\prime^{\frac{5}{2}}}{g(L\nu)^{\frac{1}{2}}} \tag{6.17}$$

does not depend on particle characteristics, so the question is in what circumstances can Ro and St be independently varied. The options left are changing gravity g, or the continuous medium ν_f or the turbulence characteristics ϵ (or $U\prime$) and L. Gravity can be modified in simulations but not in lab experiments. If one wants to maintain also the turbulence Re_λ number (since it is one of the independent non-dimensional parameters of the problem), then one must vary the parameter $\frac{U\prime^2}{gL}$ to obtain different St for a given Ro number (and vice versa). This is feasible by changing the ratio $\frac{L}{U\prime^2}$ while keeping $LU\prime$ constant, that is changing $U\prime$ and adapting L to maintain the turbulence Reynolds number Re_λ (for given carrier fluid and gravity). Alternately, one can keep $U\prime$ and change the integral length scale L. In other words, that means considering different experimental conditions. This can be put in an alternate form.

Indeed, the standard deviation of the fluid acceleration obeys.

$$\gamma\prime = a_0^{\frac{1}{2}}(\frac{\epsilon^3}{\nu})^{\frac{1}{4}}. \tag{6.18}$$

Using $\epsilon = \frac{U\prime^3}{L}$ eq. 6.18 becomes:

$$\gamma\prime = a_0^{\frac{1}{2}}\frac{U\prime^2}{L}Re_L{}^{\frac{1}{4}}. \tag{6.19}$$

Hence, the parameter introduced above, namely $\frac{U\prime^2}{gL}$, is proportional to $\frac{\gamma\prime}{g}$ multiplied by a function of Re_L. Thus, we need flow conditions such that $\frac{\gamma\prime}{g}$ is varied. Fortunately, different experimental conditions have been considered in the literature and we will take advantage of that to analyze the behavior of the unconditional average settling velocity. Given that there is some experimental and numerical data available for comparison, we have chosen to compare our results with the following contributions:

- the very first simulation of the enhanced settling velocity done by Wang & Maxey [73]
- experimental measurements of enhanced settling velocity of polydispersed water droplets in air for changing volume fraction by Aliseda et al.[1]
- recent measurements of droplets in air done by Good et al. [31] for three different Re_λ
- experiments with falling solid monodisperse particles injected in a turbulent zone generated by fans for three different Re_λ done by Yang and Shy [77]

The details of experimental conditions are given in table 6.9 and in table 2.2 of the Section 2.3. The range of Re_λ is from 75 to about 190. The range of velocity fluctuations is from 0.211 m/s to 0.470 m/s. Dissipation rate is from 0.2 to 2.3 m^2/s^3. Integral scale L varies from 2.7 cm to 15 cm. Volume fraction ranges from 0.1×10^{-5} to 7×10^{-5}. Although not an independent parameter, we provide also Fr (calculated using eq.6.15) in table 6.9 as well as the ratio $\frac{St}{Ro}$ as estimated from eq.6.17. Fr evolves from 0.9 to 9.9 leading to a significant range of $\frac{St}{Ro}$ ratio.

TABLE 6.9: Comparison of experimental conditions of available studies, * these are estimated values of volume fraction

Study	ϕ_v $\times 10^{-5}$	ϵ m^2/s^3	R_λ	$U\prime$ m/s	L cm	η μm	τ_η, ms	$(\frac{\epsilon^3}{\nu})^{\frac{1}{4}}$, m/s^2	Fr	$\frac{St}{Ro}$
Present	0.5	0.2	191	0.323	15	380	12	4.8	0.94	4
Present	1.0	0.2	185	0.312	15	402	12	4.8	0.94	3.7
Present	2.0	0.2	181	0.366	15	410	12	4.8	0.94	5.5
Aliseda et al	7	1	75	0.211	4.3	241	3.9	16.1	2.3	2.6
Aliseda et al	6	1	75	0.211	4.3	241	3.9	16.1	2.3	2.6
Aliseda et al	1.5	1	75	0.211	4.3	241	3.9	16.1	2.3	2.6
Good et al E1	0.1*	0.2	150	0.260	3.5	360	8.6	4.9	0.9	3.05
Good et al E2	0.1*	0.46	160	0.330	3.1	290	5.7	9.0	1.7	5.88
Good et al E3	0.1*	1.6	177	0.470	2.7	220	3.1	23	4.4	15.75
Yang & Shy	1.0	0.08	73	0.141	1.98	460	14	2.3	3.3	1.4
Yang & Shy	1.0	0.13	120	0.206	2.63	400	10.7	3.4	5.7	3.1
Yang & Shy	1.0	0.21	202	0.305	2.89	350	8.4	5.0	9.9	8.0

6.5.1 Comparing the offset due to volume fraction effects $V_{physical}$

Let us first focus on the influence of the global seeding on velocity enhancement. The first three sets of data in table 6.9 were conducted roughly at $\phi_v < 10^{-4}$. For all experiments considered the ratio $\Gamma = \frac{\rho_p}{\rho_f} = 833$ was the same (water droplets were injected in an air-flow). Good et al. estimated the volume fraction as $\sim 10^{-6}$ suggesting very dilute solutions used in their experiment but not giving a precise value. Thus, the data of Good et al.[31] can not be used for extracting values of $V_{physical}$.

Now let us compare $V_{physical}$ of our experiment with the one done by Aliseda et al.[1]. The physical offset due to the volume fraction has been estimated using the same analysis as given in Section 6.4.5. Their data are plotted on fig. 6.22 where the velocity change $\overline{V} - V_{St}$ has been diminished by $V_{physical}$. Fig. 6.22 does not show a collapse of the data. This means that the volume fraction effect can not be represented by $V_{physical}$ alone as it changes with St.

The offsets $V_{physical}$ corresponding to the three experiments of Aliseda et al. [1] were further plotted versus the volume fraction ϕ_v (see fig. 6.23) through following relationship:

$$V_{physical}\ m/s = 329 \times \phi_v + 3.3 \times 10^{-3} \tag{6.20}$$

Comparing this relationship with ours where $V_{physical}\ m/s = 4.86 \times 10^3 \phi_v - 0.0253$,

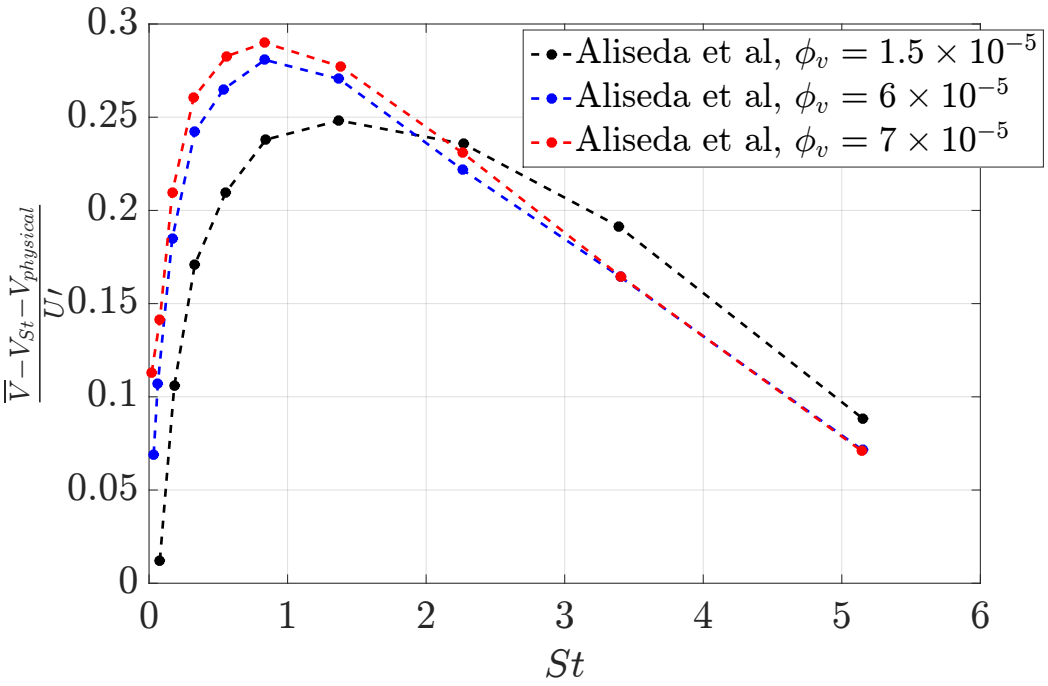

FIGURE 6.22: Settling velocity $\frac{\bar{V}-V_{St}-V_{physical}}{U\prime}$ vs St for experiments of Aliseda et al. [1]

we could clearly see that in both cases there is definitely a dependence on the volume fraction ϕ_v, but in Aliseda's case this dependence is about 15 times weaker than in ours. The reason could be that volume fraction itself is not the only factor responsible for the enhancement $V_{physical}$ of the settling velocity. The fact that both experiments were conducted at different Re_λ (see table 6.9) plays an important role too. So does the fact that we estimated $V_{alignment}$ due to alignment issue at the lowest concentration used in their experiments i.e. $\phi_v = 1.5 \times 10^{-5}$ compared to the lowest volume fraction $\phi_v = 0.5 \times 10^{-5}$ in ours. For a better estimate of $V_{alignment}$, an experiment at even lower volume fraction should have been ideally carried out.

Nevertheless, we decided to scale $\frac{V_{physical}}{U\prime}$ with both Re_λ and ϕ_v at the same time (see fig. 6.24). The evolution of $\frac{V_{physical}}{U\prime}$ with both ϕ_v and Re_λ scales as:

$$\frac{V_{physical}}{U\prime} = 2.2 \times \phi_v \times {Re_\lambda}^{1.6}. \tag{6.21}$$

This attempt to scale $\frac{V_{physical}}{U\prime}$ with both Re_λ and ϕ_v shows that the effect of additional velocity increase $\frac{V_{physical}}{U\prime}$ is due to both Re_λ and ϕ_v, and each of the two parameters contributes approximately equally to such an increase. Evidently, more data is required to obtain full scalings with Re_λ and ϕ_v. Moreover, it is clear that

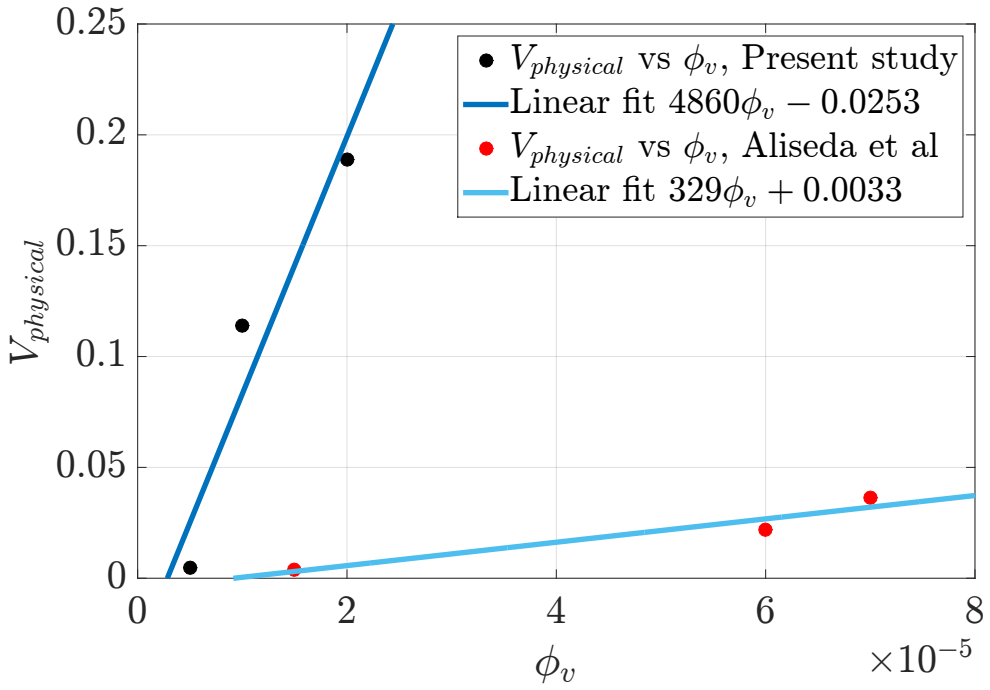

FIGURE 6.23: Offset $V_{physical}$ vs ϕ_v for experiments of Aliseda et al. [1] and our study

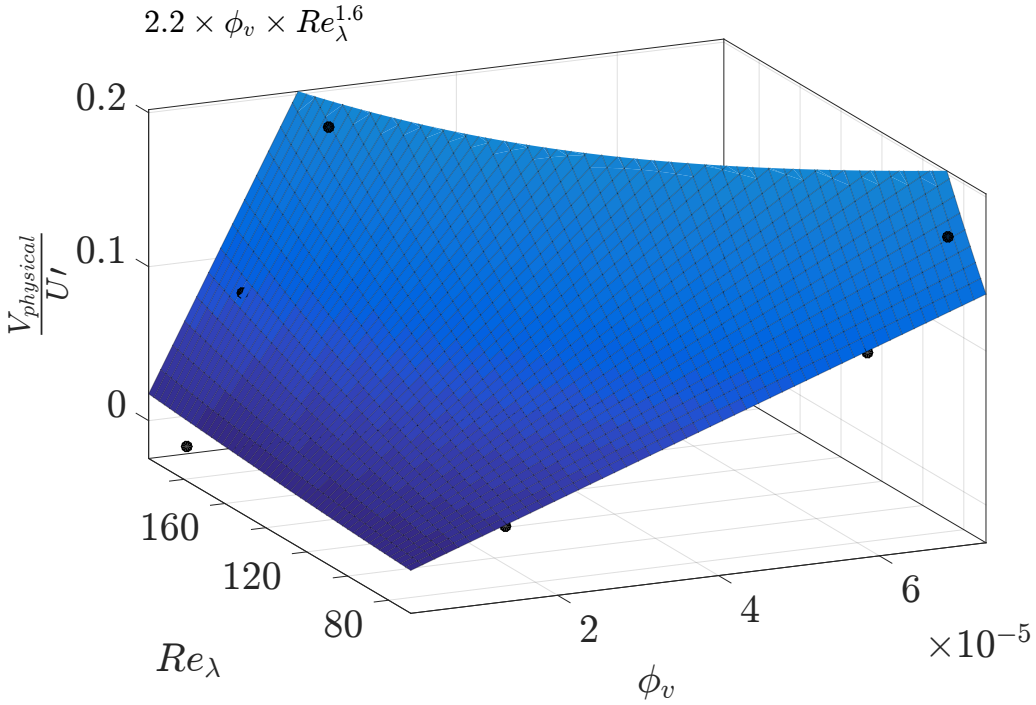

FIGURE 6.24: Evolution of $V_{physical}$ with Re_λ and ϕ_v from the experiments of Aliseda et al. [1] and from our study

the enhancement in the settling velocity is not the same when the size of particles is varied. We will discuss the probable origin of $V_{physical}$ in Section 6.7.1.

6.5.2 Scalings of the settling velocity: discussion

Now let's consider the quantity $\frac{\bar{V}-V_{alignment}-V_{St}}{U\prime}$ vs St and Ro. The corresponding measurements of settling velocity $\frac{V-V_{St}}{U\prime}$ were done by Aliseda et al [1], Good et al [31] and Yang & Shy [77]. We also added the simulations done by Wang & Maxey [73] for reference. The result are plotted on fig. 6.25 versus the Stokes number and in fig. 6.26 versus the Rouse number. Unfortunately, we could not extract the information about $V_{alignment}$ or $V_{physical}$ for the set of data of Good et al.[31], because the settling velocity measurements were not available for small St i.e. small particles sizes. Indeed, in the second and third experiments of Good et al [31] referred to as E2 and E3, the first measurement point does not start at $St = 0$ but at $St = 0.2$ and $St = 0.7$ respectively. In addition, for the third series of data Good et al. E3, a velocity change $\overline{V} - V_{St}$ equal to zero is observed at $St \sim 0.4$, that may be due an incorrect determination of the zero for their measurement technique. Despite these uncertainties, we will exploit the data of Good et al. as they are.

Fig. 6.25 shows $\frac{\bar{V}-V_{St}}{U\prime}$ vs St. From this figure we could see that the majority of curves reach a maximum enhancement in the settling velocity for $St \approx O(1)$ between 0.91 and 1.8 with one exception for the experiment E3 done by Good et al. [31] for which the maximum (if any as the curve is quite shallow) happens at a much higher value, for St between 4 and 6.

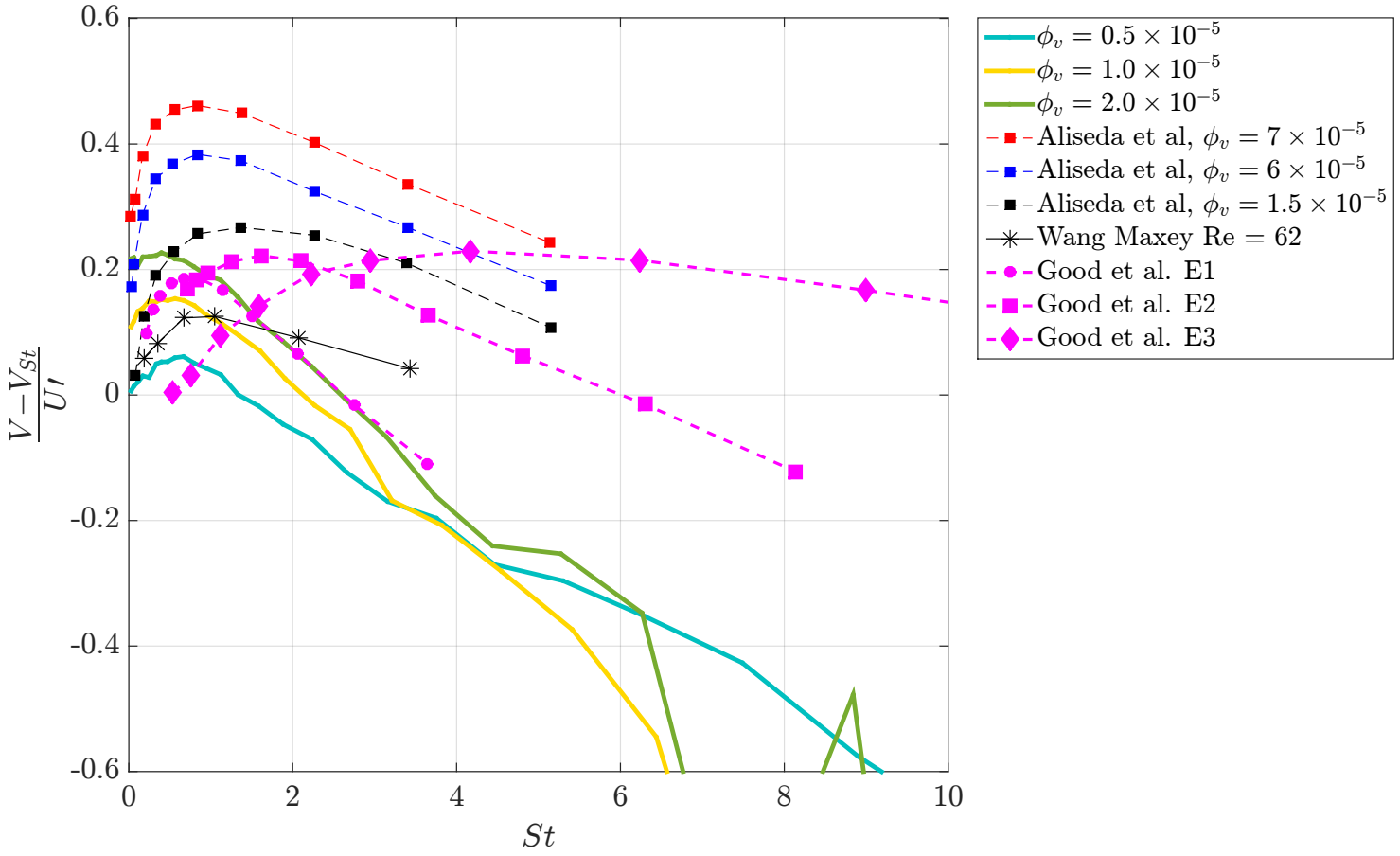

FIGURE 6.25: $\frac{V-V_{St}}{U\prime}$ vs St for present and previous studies

Hindering of the particles settling velocity could also be seen past the enhancement for some of these curves. Indeed, significant slow down of the particles is observed for our experimental data past $St = 1.6, 2.3$ and 2.6 with raising volume fraction ϕ_v (see table 6.8). Hindering was also reported by Good et al. [31]: they observe this effect at a comparable Stokes number, namely $St \approx 2.5$ for their condition E1 that happens to be close to our flow conditions. Indeed, for St above unity, there is an overlap of curves acquired in the present experiment at $\phi_v = 2.0 \times 10^{-5}$ and those of Good et al.'s acquired for E1 condition with $\phi_v = 0.1 \times 10^{-5}$. Except for the concentration, both experiments were performed at similar dissipation rates ($\epsilon = 0.2$ and $0.203\ m^2/s^3$) and Fr numbers (0.94 and 0.9) with slightly different Re_λ (191.03 and 150). Others flow conditions in Good et al.'s correspond to higher dissipation rate. For the flow condition E2, the Froude number is higher $Fr = 1.7$, and hindering happens at larger Stokes numbers, above $St \approx 6$. The observed hindering is most probably the mark of the "loitering" effect pointed out by Nielsen[54] for heavy particles with a large enough relative velocity interacting with turbulent eddies (see the discussion in the Section 2.3.1.2). Hence, aside the data of Good et al., this is the second experimental evidence that hindering happens for very dense particles ($\frac{\rho_p}{\rho_f} \approx 1000$) in a nearly homogeneous isotropic turbulent flow. Besides, this effect is quite strong as settling velocity reduction as large as $0.5U\prime$ are reported here (see Fig. 6.25).

A very interesting presentation of the same data $\frac{V - V_{St}}{U\prime}$ plotted now versus the Rouse number could be seen in fig.6.26. In particular, all datasets from Good et al. exhibit now similar behaviour while, when plotting versus St (fig.6.25), this condition E3 leads to a very shallow curve, quite different from of the other two. All curves exhibit a maximum enhancement of the settling velocity before $Ro \approx 0.3$. Past these maxima, all curves experience a steady quasi-linear decrease with the Rouse number. It is also remarkable that the slopes are nearly the same whatever the flow conditions. The boundary between enhancement and hindering evolves between $Ro \approx 0.3$ and $Ro \approx 1$ depending on flow conditions. Note that if the data of Aliseda et al. [1] or those of Good et al.[31] E3 are prolongated, the corresponding "critical" Ro number will be larger than unity. This boundary between hindering and enhancement is discussed in detail in the next section. According to fig.6.26, the curves are consistently shifted upward as the corresponding Fr number (see table 6.9) increases due to an increase in dissipation rate ϵ and/or Re_λ (the latter parameter affects the prefactor a_0 of the fluid acceleration standard deviation see eq.6.16). The only exceptions are the curves from Aliseda et al. ($Fr = 2.3$) that are above the curve for the condition E3 from Good et al. ($Fr = 4.4$): this is likely due

to the impact of the volume fraction which were not the same.

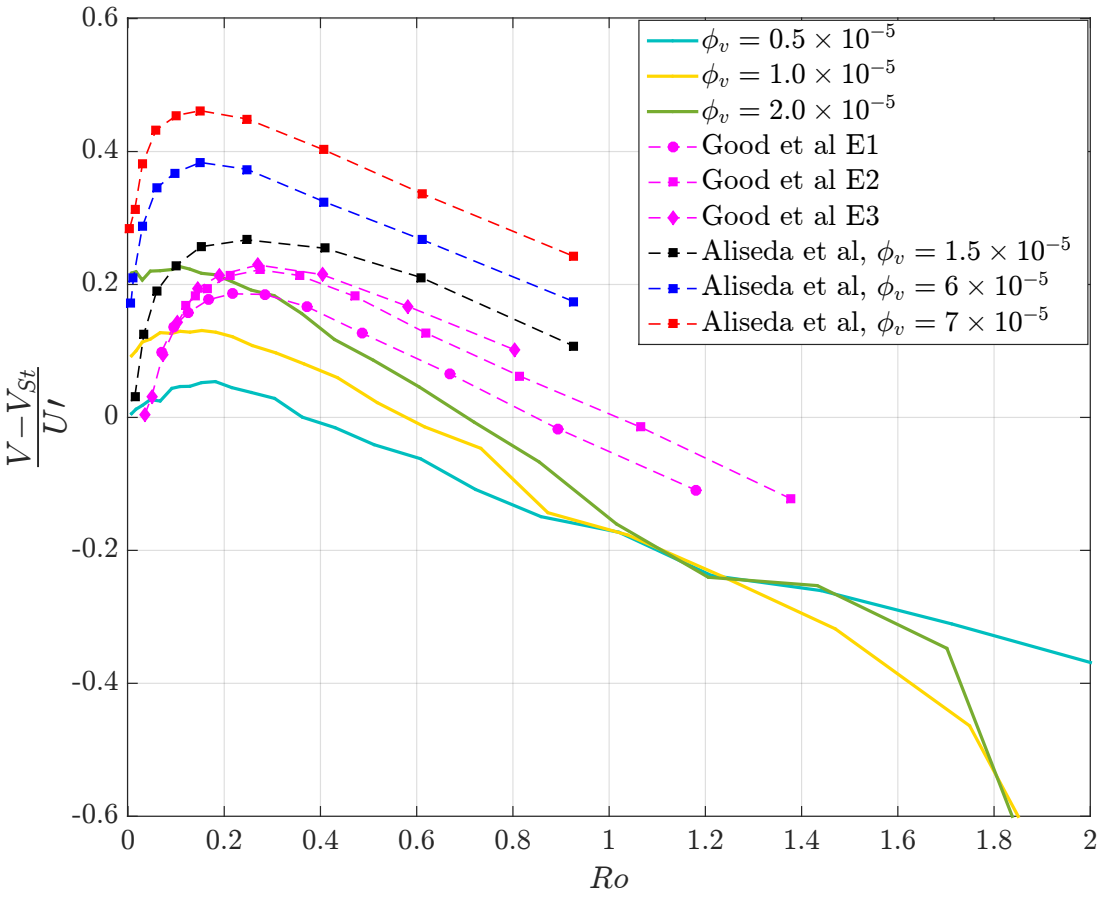

FIGURE 6.26: $\frac{V-V_{St}}{U\prime}$ vs Ro for present and previous studies

In the dataset of Aliseda et al. and in ours, which were obtained at fixed Fr numbers, increasing volume fraction ϕ_v increases the peak of each curve. An explanation for that is proposed by Aliseda et al. [1]: particles in clusters acquire the relative cluster velocity V_{cl} and this collective effect leads to an enhancement of the settling velocity.

Traditionally, the scalings of settling velocity enhancement were seeked by plotting $\frac{V-V_{St}}{U\prime}$ either versus St or versus Ro. Although the presentation of fig.6.26 exhibit an almost consistent organisation of the curves while varying the Fr number, no collapse could be observed when using $\frac{V-V_{St}}{U\prime}$ whatever the abscissa St or Ro considered. Moreover, if we compare the results of the present study conducted at $\phi_v = 0.5 \times 10^{-5}$ with the data of Good et al. E2 at fixed Ro number of $Ro = 1.066$, we see that for almost the same $U\prime$ (0.32 m/s in our case and 0.33 m/s in the case

of Good et al. E2), very similar Re_λ (191 here versus 160 for Good et al.) but different Fr (0.9 in our case and 1.7 in the case of Good et al. E2) which lead to a different St number using eq.6.17, the particle velocity $\frac{V-V_{St}}{U\prime}$ is -0.18 in our case and equals to -0.015 in the case of Good et al. E2, yielding the difference of 10 times between two values. Hence, $U\prime$ alone does not seem to be an appropriate parameter for estimating the magnitude of velocity enhancement or hindering. This also shows that velocity change is sensitive to Fr. The same conclusion would hold by considering the Kolmogorov velocity instead of $U\prime$.

Let us try now to find alternative parameters to scale the settling velocity $V-V_{St}$. As previously discussed, the standard deviation of the fluid acceleration seems to be a central parameter. Therefore, we can try to construct a velocity scale for the settling velocity $V-V_{St}$ based on the acceleration of the fluid $\gamma\prime$. We first considered a characteristic time of the fluid as $\frac{L}{U\prime}$. Using eq. 6.19, the proposed velocity scale becomes :

$$\frac{\gamma\prime \times L}{U\prime} = a_0^{\frac{1}{2}} \frac{U\prime^2}{L} {Re_L}^{\frac{1}{4}} \times \frac{L}{U\prime} = a_0^{\frac{1}{2}} \times {Re_L}^{\frac{1}{4}} \times U\prime \tag{6.22}$$

Using a_0 estimated as $0.13Re_\lambda^{0.64}$ given by Sawford[64] and $Re_\lambda = (15Re_L)^{\frac{1}{2}}$ in eq.6.22, we obtain:

$$\frac{\gamma\prime \times L}{U\prime} = 0.13^{\frac{1}{2}} \times 15^{0.16} \times U\prime \times Re_L^{0.41} \simeq 0.556 \times U\prime \times Re_L^{0.41} \tag{6.23}$$

This is the first scale of the settling velocity that we tried, and the results could be seen in fig. 6.27 plotted vs St and Ro. For the settling velocity we took $\overline{V} - V_{St} - V_{physical}$ except for the data of Good et al, since the $V_{physical}$ was not possible to estimate. Fig. 6.27a shows no collapse of any data of $\frac{\overline{V}-V_{St}-V_{physical}}{0.556\times U\prime\times Re_L^{0.41}}$ with St. Features similar to those seen in fig. 6.25 could be observed. Notably, the enhancement of the settling velocity of the particles achieves a maximum of 0.05, and the hindering of the settling velocity happens at the same St values as in the fig. 6.25. Essentially, what we have done here is a compression of the ordinate of the plot 6.25 by the factor $0.556 \times Re_L^{0.41}$ without changing the abscissa.

The same transformation could be applied to the graph $\frac{\overline{V}-V_{St}-V_{physical}}{0.556\times U\prime\times Re_L^{0.41}}$ vs Ro (see fig. 6.27b). However, here we witness some collapse of the respective datasets. For example, in the interval $0.4 < Ro < 0.8$ all the Aliseda et al. curves are narrowed down, so are the curves of Good et al. and the same holds for the curves of the present study. Yet, the three experimental sets do not collapse. This rescaling does no change the limits between enhancement and hindering previously determined from fig. 6.26 in terms of Ro.

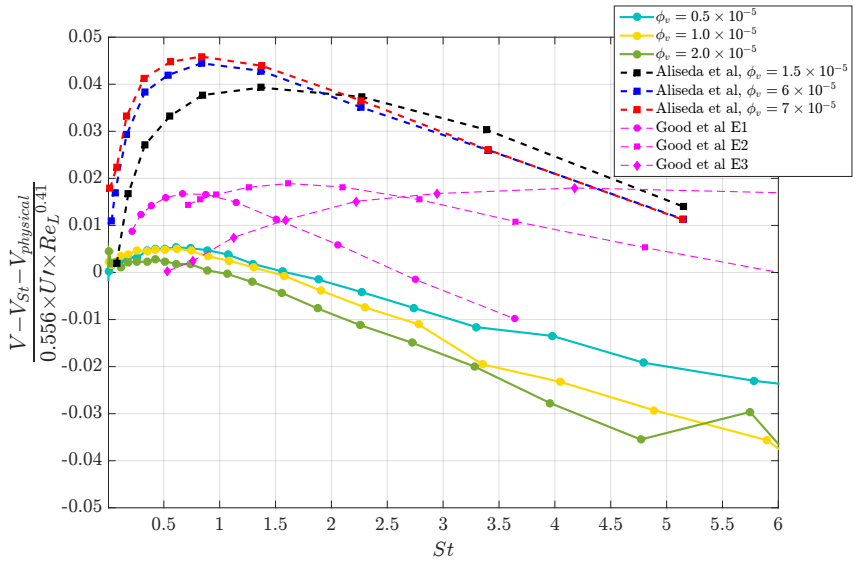

(a)

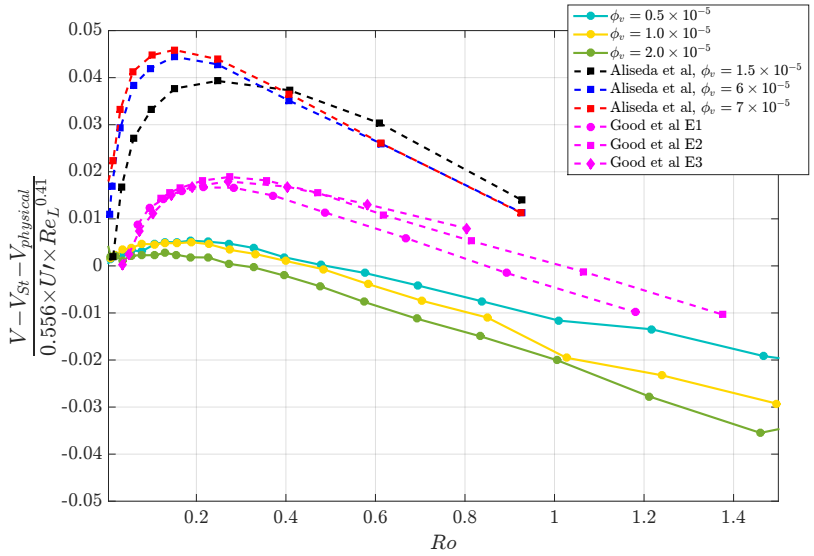

(b)

FIGURE 6.27: Scalings of settling velocity $\frac{V - V_{St} - V_{physical}}{0.556 \times U\prime \times Re_L^{0.41}}$ vs (a) St and (b) Ro

Another scale can be derived from the acceleration. We can seek out a scale for the settling velocity in terms of $\frac{\gamma\prime L}{V_{St}}$ where we use now a timescale corresponding to the time required for a particle to cross the integral length scale. Hence, we just multiply the expression found for the scale $\frac{\gamma\prime L}{U\prime}$ by $\frac{U\prime}{V_{St}}$. Thus, the new velocity scale becomes:

$$\frac{\gamma\prime L}{V_{St}} = \frac{\gamma\prime L}{U\prime} \times \frac{U\prime}{V_{St}} \simeq 0.556 \times Re_L^{0.41} \times U\prime \times \frac{U\prime}{V_{St}} \tag{6.24}$$

Using $\frac{U\prime}{V_{St}} = Ro^{-1}$ and substituting in eq.6.24, we obtain:

$$\frac{\gamma\prime L}{V_{St}} =\simeq 0.556 \times U\prime \times Re_L^{0.41} \times Ro^{-1} \tag{6.25}$$

To test this proposal, we plotted $\frac{V-V_{St}-V_{physical}}{0.556\times U\prime\times Re_L^{0.41}\times Ro^{-1}}$ vs St and Ro (see fig. 6.28 a&b). Now, and as Ro^{-1} enters the velocity scale, we introduce an effect of the abscissa St or Ro into the scaling of settling velocity. Looking at the fig. 6.28 a, we see that there is no collapse of the three available datasets. However, we could notice a collapse of each dataset relative to a given experiment, such as for those of Aliseda et al. and for ours. However, the data series from Good et al. do not collapse at all in this representation.

Let us now change focus on the same scaling of settling velocity $\frac{V-V_{St}-V_{physical}}{0.556\times U\prime\times Re_L^{0.41}\times Ro^{-1}}$ but vs Ro (see fig. 6.28 a&b). Here three distinct collapses one for each of the three datasets could clearly be identified. In particular, Good et al. data collapse better than in the representation versus the St number. The maxima values are as follows: 2% , 0.7% and 0.1% for Aliseda et al., Good et al. and present study respectively. However, no global collapse of all data could be obtained from this analysis. Thus, the proposed alternative velocity scales based on the fluid acceleration do not capture the magnitude of ΔV.

We have also tested the scaling provided by Bec et al [7] for the enhancement of the settling velocity only. In his paper, he develops a new scaling of the settling velocity $\frac{V-V_{St}}{V_{St}}$ with $Re_\lambda^{\frac{3}{4}} \times Fr_B^{\frac{5}{3}} \times St^{-2}$ where $Fr_B = (\frac{\epsilon^3}{\nu})^{\frac{1}{4}} \times \frac{1}{g}$. Here, Fr_B is essentially the ratio of fluctuation of the acceleration of the fluid over gravitational acceleration (the a_0 term due to turbulence is ignored). We plotted all three datasets of Aliseda et al, Good et al and present study in fig. 6.29 and 6.30.

No clear collapse of all datasets could be seen apart from the local ones with respect to the dataset from Aliseda et al or from the present study. The datasets of Good et al. are ordered with respect to increasing Re_λ but they do not merge, possibly because the effect of $V_{physical}$ was not accounted for. We also have to mention that the range of validity of the scaling proposed by Bec et al.[7] is defined for $St > (Re_\lambda^{\frac{1}{2}} Fr_B)$. The only data available in that range are ours, and they all correspond to hindering and not to enhancement (see fig.6.30). Hence this scaling does not capture the role of Fr and/or Re_λ on the magnitude of velocity enhancement.

We also tried to implement in our study the scaling provided by Rosa et al. [63] again valid for enhancement only as they do not observe hindering in their simulations unless the lateral motion of particles is blocked. In their numerical simulations,

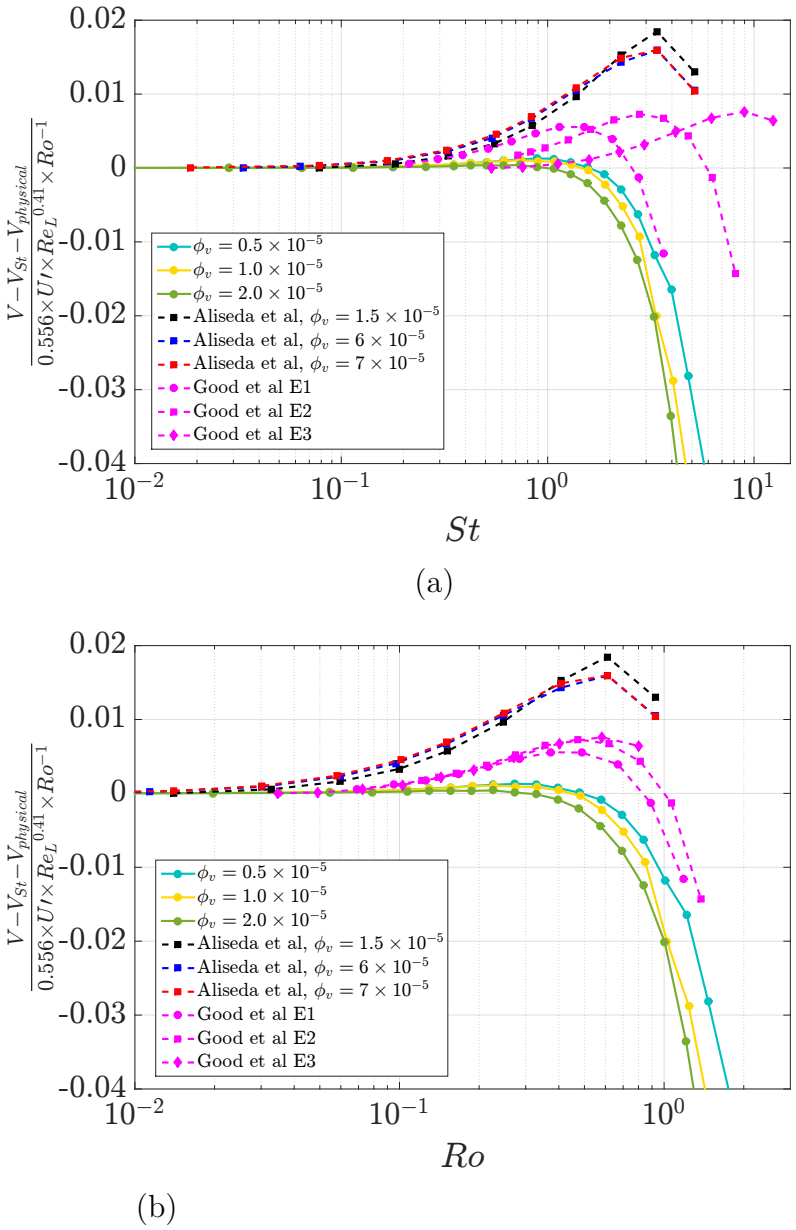

FIGURE 6.28: Scalings of settling velocity $\frac{V-V_{St}-V_{physical}}{0.556\times U\prime\times Re_L^{0.41}\times Ro^{-1}}$ vs (a) St and (b) Ro, positive V is defined downwards

they manage to obtain a consistent collapse of $\frac{V-V_{St}}{V_{St}\times St}$ versus Fr_R (the ratio of the inertial forces experienced by the particle to the buoyancy forces given by Davila & Hunt [19]) defined as $Fr_R = St \times \left(\frac{V_{St}}{V_\eta}\right)^2$ where $V_\eta = (\nu\epsilon)^{\frac{1}{4}}$ for a fixed $Re_\lambda = 143.7$. They then provide a fit of their numerical results as $\frac{V-V_{St}}{V_{St}}$ function of Fr_R and Re_λ. We tested Rosa et al. proposal on available experimental datasets: the results are shown in fig. 6.31. Two views are given on fig. 6.31 a & b showing the global view and local one restricted to 6 decades in Fr_R and from -0.2 to 1.5 in ordinate values.

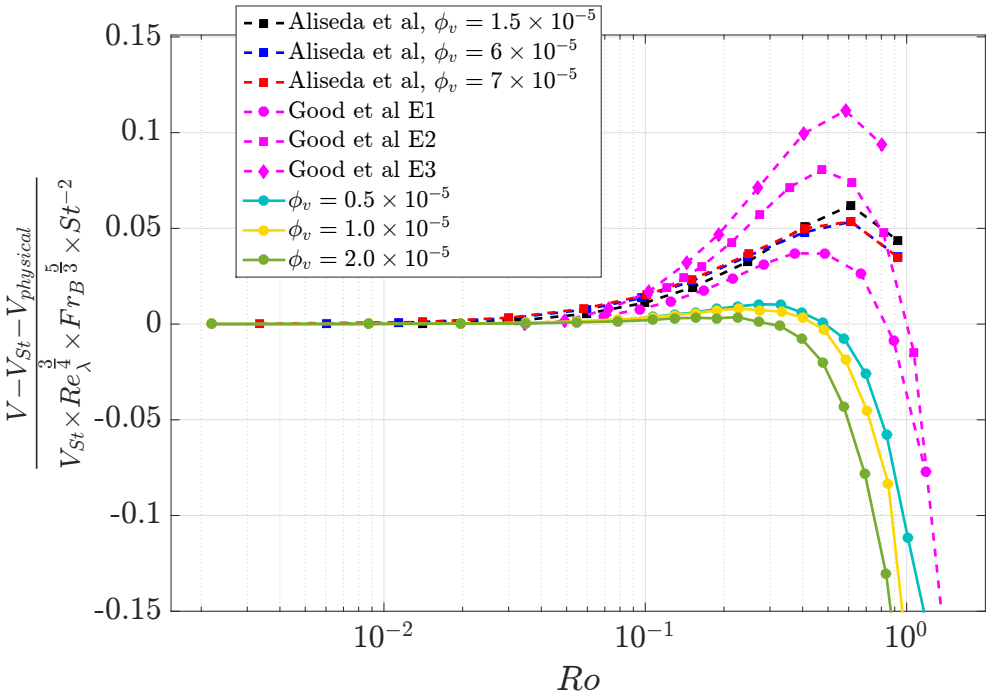

FIGURE 6.29: Scalings of settling velocity $\frac{V - V_{St} - V_{physical}}{V_{St} \times Re_\lambda^{\frac{3}{4}} \times Fr_B^{\frac{5}{3}} \times St^{-2}}$ vs Ro

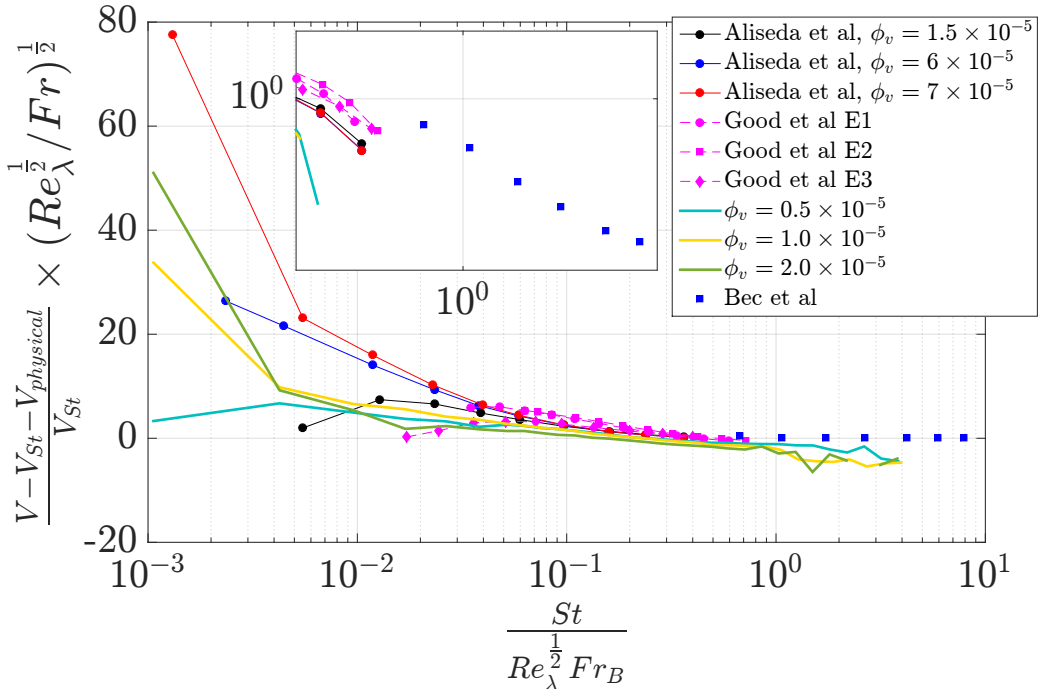

FIGURE 6.30: Same velocity $\frac{V - V_{St} - V_{physical}}{V_{St}}$ scaling of Bec but plotted in their representation (see fig.2 in [7])

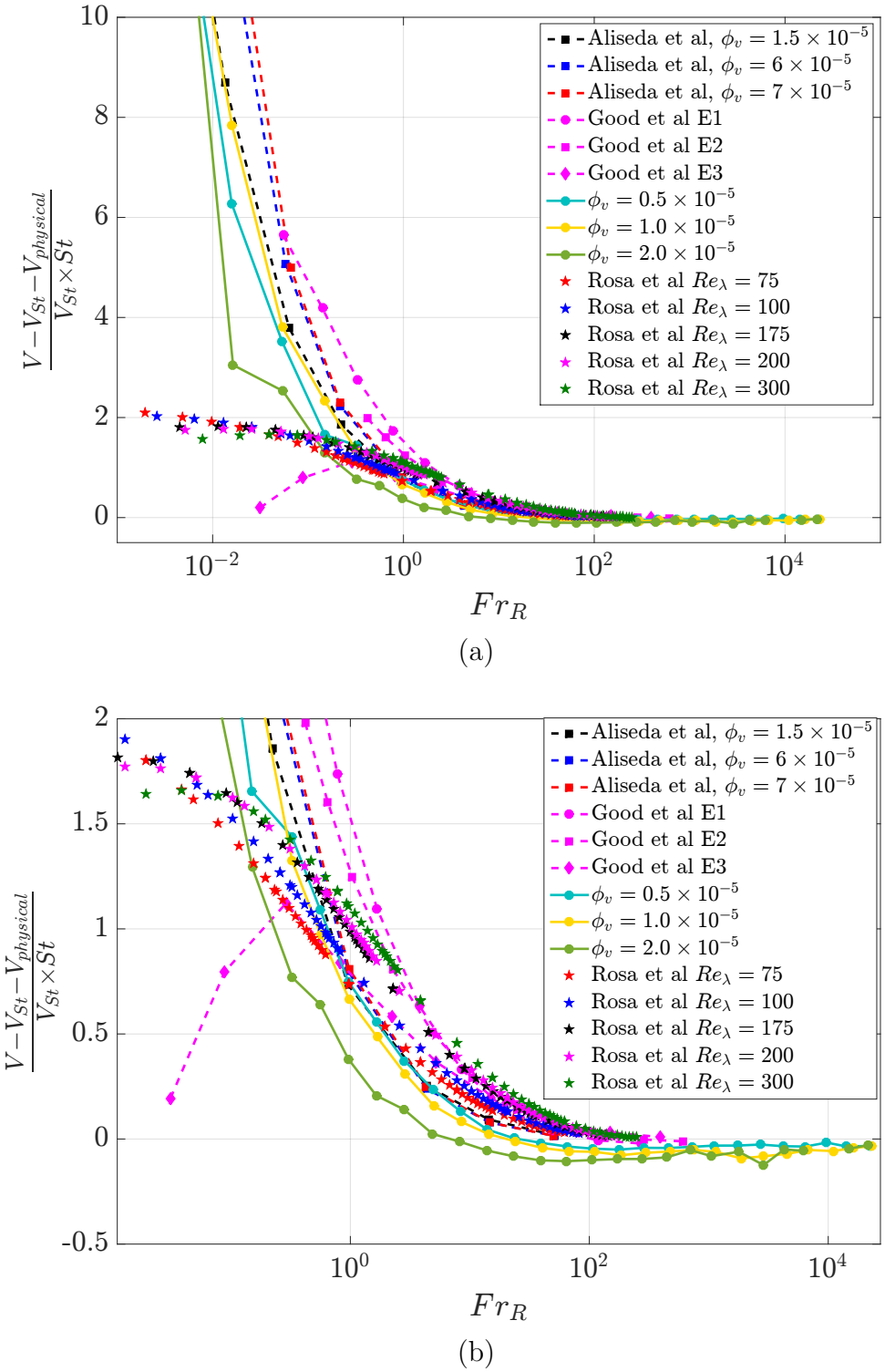

FIGURE 6.31: Scalings of settling velocity $\frac{V-V_{St}-V_{physical}}{V_{St}\times St}$ vs Fr_R (a) global view and (b) zoomed view, positive V is defined downwards

From the point of global view (see fig. 6.31 a) no collapse of the data can be seen. For small values of Fr_R, the function $\frac{V-V_{St}}{V_{St}\times St}$ exhibits large values because of dividing by small St. In the local view (see fig. 6.31 b) we could see a reasonable collapse of the dataset of Aliseda et al and two of our experimental conditions of the present study, while our third dataset - gathered at the largest concentration - does not collapse well . We also observe a very strong scatter of the data from Good et al. especially at low Fr_R. Yet, there is a « relative » collapse of all experimental data in the range $Fr_R = 3 - 100$ but, whatever the data serie considered the deviation between experimental data and Rosa et al. fit becomes quite large at lower Fr_R. In addition, the scaling proposed by Rosa et al. do not predict hindering while this happens in our flow conditions for Fr_R above about 8.

The last scaling we considered is relative to the hindering of the settling velocity and is inspired from Nielsen [54] analysis of the loitering effect. We have seen that, according to Nielsen, the quantity $\frac{V-V_{St}}{V_{St}}$ scales with $-(\frac{\gamma}{g})^2$, where γ is the maximum value of acceleration of fluid and g is gravity, when considering either a particle in a tank subjected to an acceleration or a particle in an oscillating grid. As we have seen that the fluid acceleration in the turbulent field affect the magnitude of velocity change, we have tried to scale $\frac{V-V_{St}}{V_{St}}$ with $-(\frac{\gamma\prime}{g})^2$ where $\gamma\prime$ is the fluid acceleration rms. To test this scaling we substracted Vphysical to get rid of the effect of volume fraction for the results of the present study and for the dataset of Aliseda et al. while the data of Good et al. have not been corrected for $V_{physical}$ since its estimation is not available. The results are shown in fig.6.32. A pretty good collapse could be seen for our data and for all curves of Aliseda et al., still with significant deviations for Good et al. E1 and E3 data series.

Overall, in the range of Rouse numbers above about 0.5, the trend appearing in Fig 6.32 is close to the following behaviour:

$$\frac{\Delta V}{V_{St}} \approx -kFr^2(Ro - Ro_{critical}) \tag{6.26}$$

where the slope k is slightly varying with flow conditions (typically, k ranges from 0.2 to 0.8), and where the critical Rouse number $Ro_{critical}$ corresponds to the abscissa of zero crossings. $Ro_{critical}$ also evolves with flow conditions: its behaviour is discussed in Section 6.5.3. The above proposal combines Fr and Ro numbers, and it indicates that both the velocity fluctuations and the standard deviation of the fluid acceleration control the magnitude of the change in the settling velocity. That result applies not only to the hindering regime but also to the moderate Rouse numbers where enhancement occurs (see fig.6.32, or the domain of linear decrease in

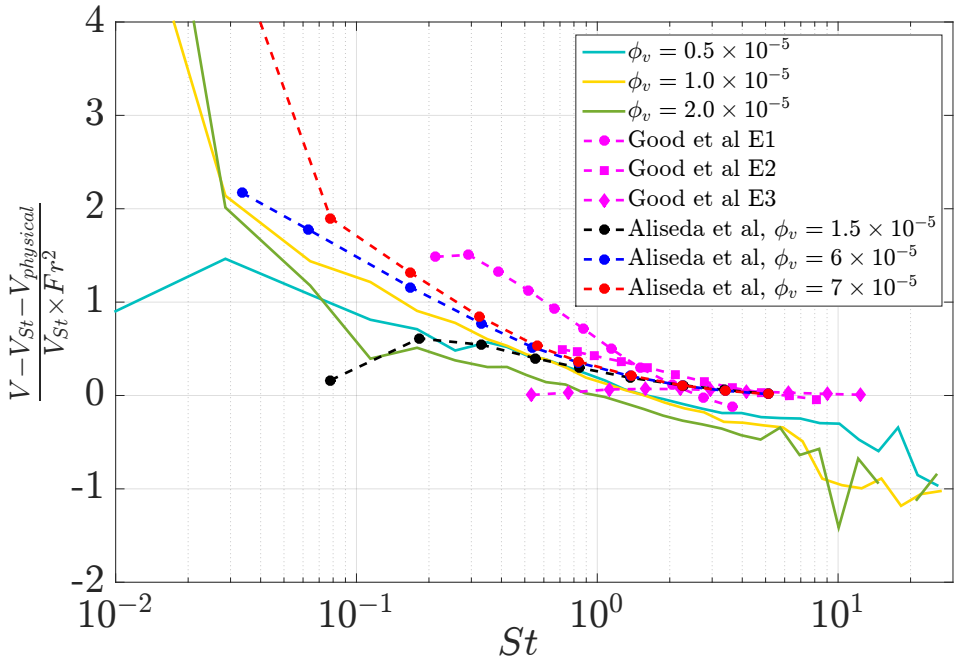

(a)

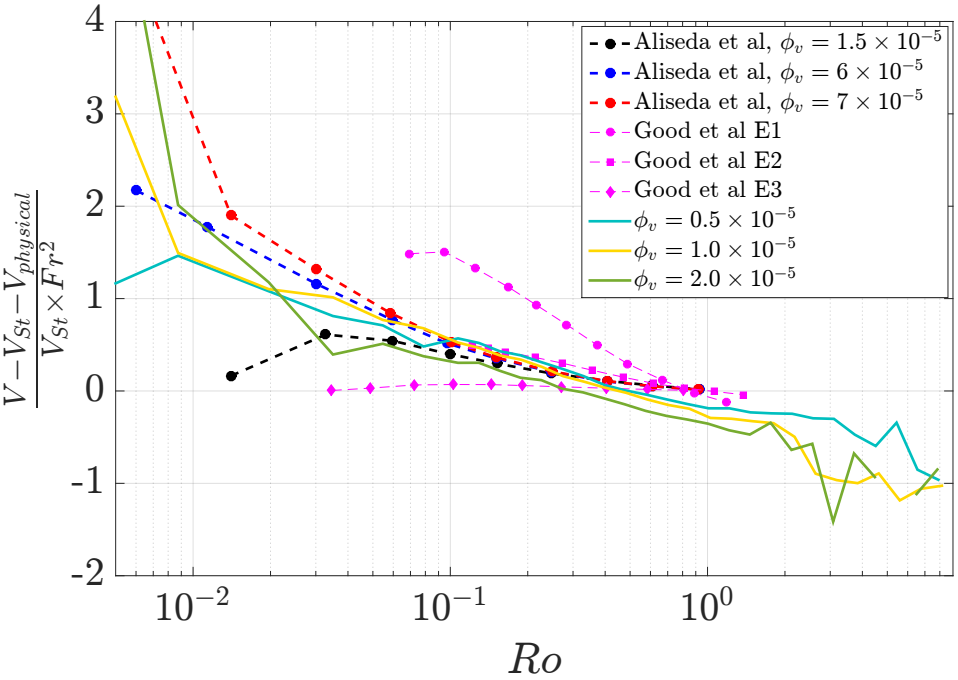

(b)

FIGURE 6.32: Scalings of settling velocity $\frac{V-V_{St}-V_{physical}}{V_{St}\times Fr^2}$ vs (a) St and (b) Ro

fig.6.26). However, it does not capture the maximum enhancement which is possibly controlled the competition between preferential sweeping and loitering.

In this section, we have discussed how the magnitudes of the settling velocity enhancement and of the settling velocity hindering evolve with flow parameters. Experimental evidence indicate that both velocity and accelation fluctuation in the fluids are important quantities controling the response of particles. Although no definite answer has been brought to this question, a proposition has been put forward that deserves to be tested further.

6.5.3 Boundary between enhancement and hindering

We have compiled the previous and current studies to analyse the boundary between enhancement and hindering of the settling velocity $V - V_{St}$. The details of the studies involved are given in the table 6.9. We decided to plot in coordinates Ro, St and Fr, the points of enhancement of the settling velocity in blue and the points of hindering of the settling velocity in red. The goal of this analysis is to find the boundary between enhancement and hindering of the settling velocity. There are two studies that have found hindering of the settling velocity: the present study and the study conducted by Good et al.[31]. The rest of the hindered data are extrapolated from plot such as fig.6.26 by extending the linear behaviour observed at large Ro numbers. This boundary is shown in fig.6.33, the corresponding views on St-Ro, Fr-Ro and Fr-St are shown in fig.6.34.

From fig.6.33 we could see that there is gradual transition from enhancement to hindering with the Fr number. Now, if we look in more detail on fig.6.34b, we see that the critical Ro_c would be probably located at around $Ro \approx 1$. The critical St increases with Fr as expected according to eq.6.15 and is dependent on the critical Ro_c (see fig.6.34a).

We estimated the critical $Ro_c \approx 1$ for the transition between hindering and enhancement to occur. There is a certain degree of possibility that loitering effect was present in the other studies where it has not been reported, but not detected because of the limit of the particles sizes available in the measurement. However, we see that with the increase of Fr, i.e. increase in the acceleration fluctuations, the presence of hindering is postponed more and more for a given Ro and St. This could mean that at high Fr the acceleration fluctuations are dominating gravity, and hence, to see the effect of loitering one has to consider much bigger particles corresponding to $Ro_c > 1$ in such an experiment.

Although these findings deserve to be confirmed by extra experiment, they provide the first quantative criteria of the onset of loitering of water droplets in a turbulent air flow.

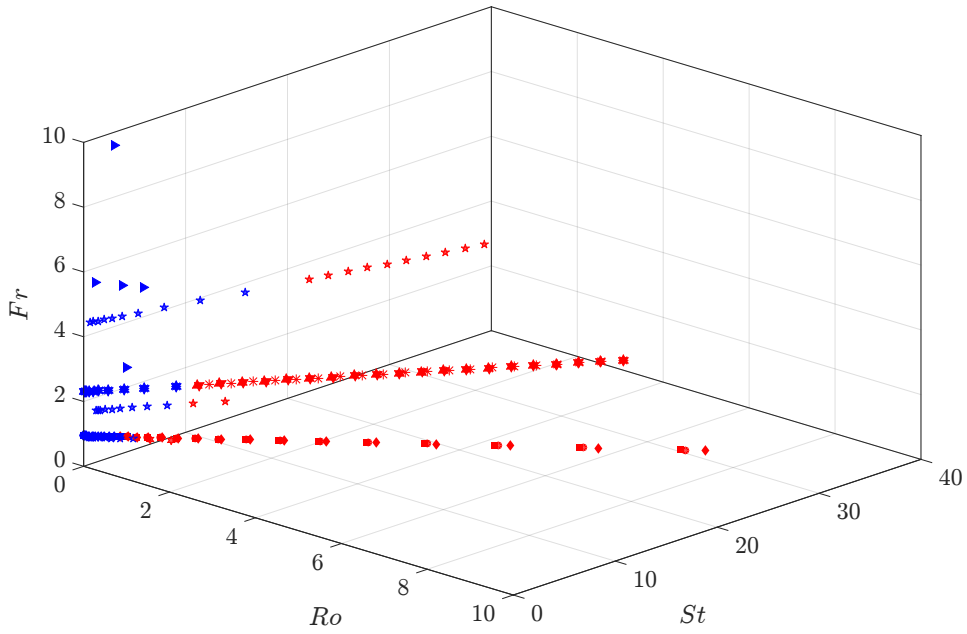

(a)

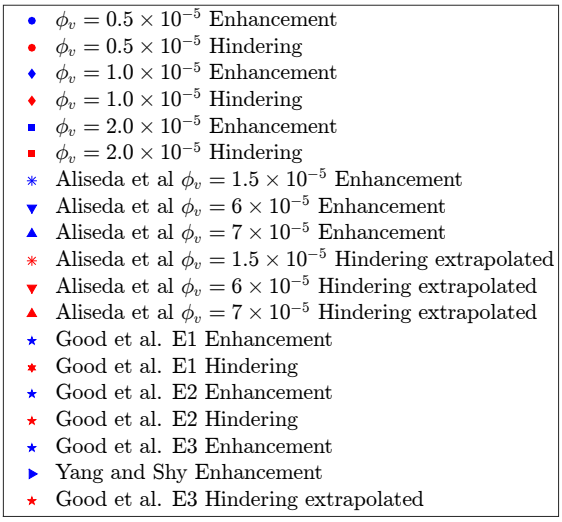

(b)

FIGURE 6.33: (a) Boundary between enhancement and hindering of the settling velocity with three control parameters St, Ro and Fr, (b) the legend corresponding to the studies involved.

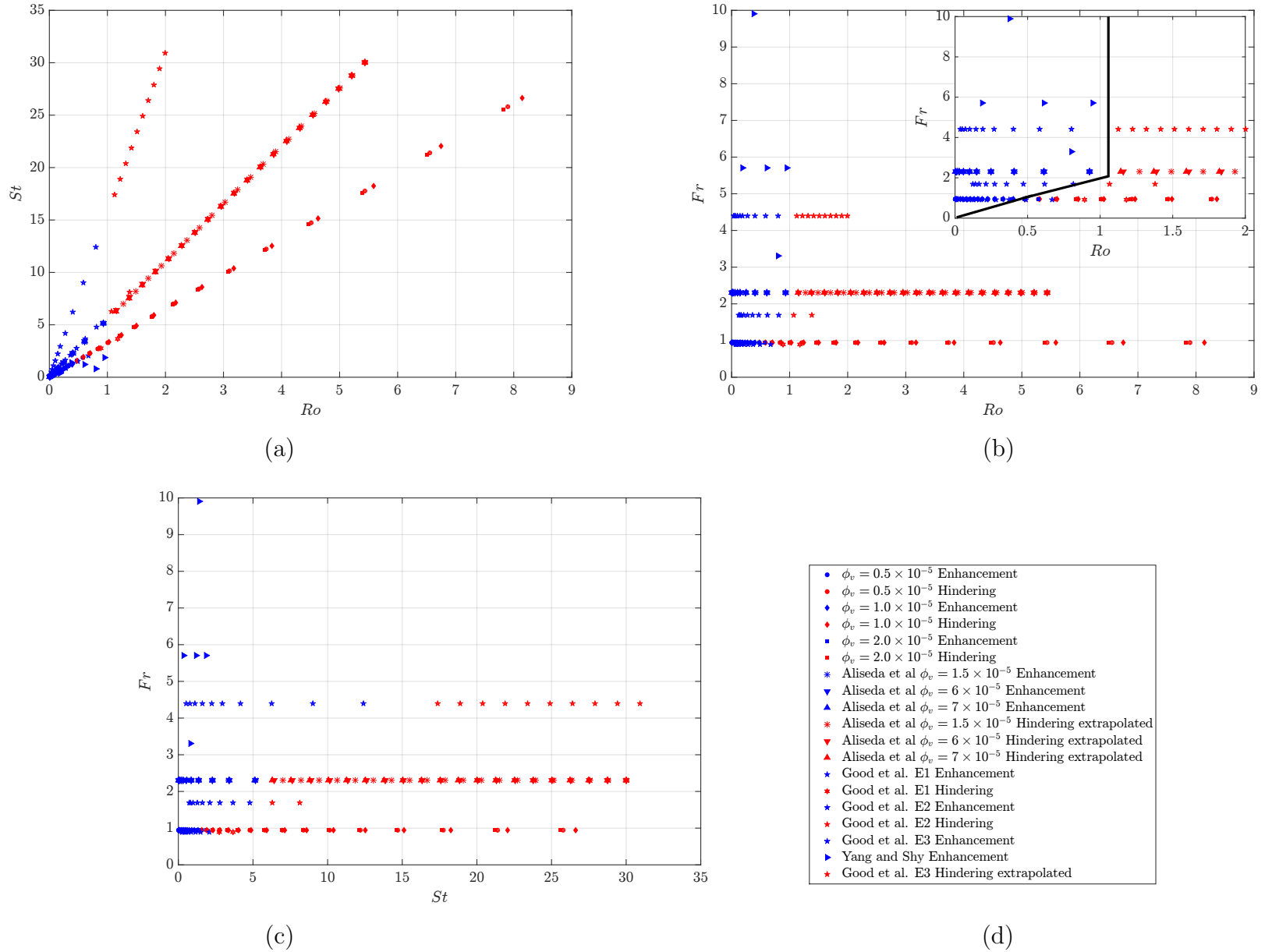

FIGURE 6.34: Boundary of enhancement and hindering of the settling velocity (a) *Ro-St* plane, (b) *Ro-Fr* plane, (c) *St-Fr* plane, (d) the legend corresponding to the studies involved.

6.6 Conditional analysis of the velocity on the diameter and concentration

We finish this Chapter by discussing the settling velocity conditioned by the diameter and local concentration.

6.6.1 Voronoii Tesselations 1D analysis

The method we use to analyse the local concentration field is the method of Voronoii tesselations. We have seen in Section 4.1, the application of Voronoii method in 2D space. In 2D, the Voronoii diagrams were used to transform the 2D field of x, y coordinates of the particles into the space tesselations where each Voronoii cell contains the points that are closest to the particle inside the tesselation than to any other particle in the flow. Let's apply the Voronoii procedure on our 1D PDI data using the method described by Ferenc et al. [23].

In the case of PDI data, we have the time of arrivals of our particles which allows us to deal with the 1D space. The principle of Voronoii tesselations in 1D is shown on the fig. 6.35. Each dot on the fig. 6.35 represents the arrival time of a particle.

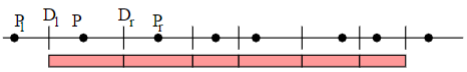

FIGURE 6.35: Principle of 1D Voronoii tesselations

So, the width of Voronoii cell is defined by the centers D_l, D_r of the two adjacent intervals and corresponds to the time $\delta T = T_{D_r} - T_{D_l}$ also equals to $\delta T = \frac{T_{i+1} - T_{i-1}}{2}$ of two consecutive centers. The characteristic variable of such a tesselation is $\nu = \frac{\delta T}{\bar{T}}$ where $\bar{T}$ is the mean of arrival time of particles. Potentially, we could transform $\frac{\delta T}{\bar{T}}$ into $\frac{\delta l}{\bar{l}}$ through U_{axial} using Taylor hypothesis to obtain lengths from times.

Now that we have constructed our Voronoii cells distribution, we can compare our distribution with the Voronoii tesselations of a Random Poisson Process. Ferenc et al [23] obtained an analytical expression using a gamma function that allows us to describe the probability density function (PDF) of the normalised Voronoii variable of Random Poisson Process (RPP) in n-D dimensions. The analytical expression for 1D [23] is given by:

$$f_{1D} = 4\nu e^{-2\nu}. \tag{6.27}$$

where $\nu = \frac{\delta T}{\bar{T}}$. The expression for the 2D case [23] is given by:

$$f_{2D} = \frac{343}{15}\sqrt{\frac{7}{2\pi}}\nu^{\frac{5}{2}}e^{-\frac{7}{2}\nu}. \tag{6.28}$$

where $\nu = \frac{A_v}{\bar{A}_v}$ and A_v is the area of Voronoii cell obtained through the Voronoii tesselation of the 2D x-y coordinate space.

Figure 6.36 shows the results for both 1D and 2D Voronoii tesselations of RPP. To remind the reader, the variable ν is representing a different dimensional object depending on the dimension chosen: the Voronoii cell ν in 1D is the time (or the length) between the detection of the arrivals of particles, in 2D - it is the area of the 2D Voronoii tesselations and in 3D - it is the volume. In all cases, the variables are scaled by their average.

From the fig.6.36 we could see that the Voronoii results in 1D and in 2D do not reflect the same behaviour. Interestingly enough the PDF curves of 1D and 2D RPP cross each other on the left at the point of $\nu_{left} = 0.50$ and on the right $\nu_{right} = 1.78$. The standard deviation of the PDF of RPP curves of 1D is $\sigma_{1D} = 0.71$ and of 2D is $\sigma_{2D} = 0.53$. To conclude, we can not compare both 1D and 2D Voronoii distributions on the same scale since in each of these dimensions, Voronoii cell is a different physical parameter. There does not exist a straight forward way to translate one of these PDFs into the other. To compare how statistics contribute to $\sqrt{\sigma^2_{RPP}}$ in each case, let us consider the contribution from dense (defined where $\nu < \nu_{left}$), dilute (where $\nu > \nu_{right}$) and intermediate regions (where $\nu_{left} < \nu < \nu_{right}$) in each RPP distribution separately.

We can write an expression for σ^2_{RPP} using three constituents:

$$\sigma^2_{RPP} = \sigma^2_{RPP_{dense}} + \sigma^2_{RPP_{dilute}} + \sigma^2_{RPP_{intermediate}} = \tag{6.29}$$

$$\int_0^{\nu_{cl}} (\nu-\bar{\nu})^2 PDF(\nu)d\nu + \int_{\nu_{cl}}^{\nu_{voids}} (\nu-\bar{\nu})^2 PDF(\nu)d\nu + \int_{\nu_{voids}}^{\nu_\infty} (\nu-\bar{\nu})^2 PDF(\nu)d\nu \tag{6.30}$$

We have calculated separately all three contributions of σ of all types of structures: dense, dilute and intermediate. From table 6.10, we see that the contribution of the dense regions towards the global σ_{RPP} is about 26% and 24% for 1D and 2D cases respectively, the contribution of the dilute regions to the global σ_{RPP} is around 59% in 1D case and 47% in 2D case, and finally, the contribution of the intermediate region towards the σ_{RPP} is around 14% in 1D case and is twice larger, 29%, in

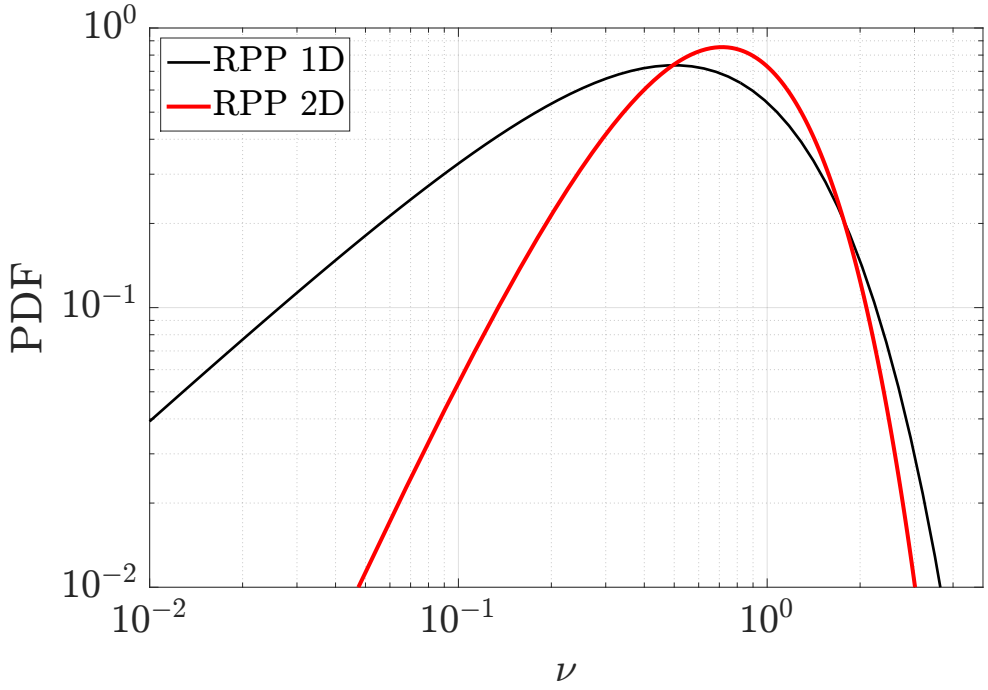

FIGURE 6.36: PDF of Voronoii diagrams of Random Poisson Process (RPP) in 1D and 2D

TABLE 6.10: Some properties of the σ of Voronoii distributions for $1D$ RPP and $2D$ RPP

Class	1D	2D	$\frac{\sigma^2_{class}}{\sigma^2_{RPP\_1D}}$, %	$\frac{\sigma^2_{class}}{\sigma^2_{RPP\_2D}}$, %
$\sigma_{RPP_{dense}}$	0.3635	0.2642	26	24
$\sigma_{RPP_{dilute}}$	0.5436	0.3655	59	47
$\sigma_{RPP_{intermediate}}$	0.2689	0.2869	14	29

the 2D case. We can see that the major contribution to the σ_{RPP} regardless of the case is the contribution of the dilute region. It is important to note that in this aspect the major bias towards the PDF of Voronoii cells would be the presence of a significant dilute region. Table 6.10 shows that 1D and 2D distributions are significantly different, and each type of structure contributes differently to the overal distribution in both 1D and 2D cases.

Let us apply now the 1D Voronoii procedure to PDI data: the results are shown in fig.6.37. We have to bear in mind that the validation rate for acquired statistics was not 100% meaning that some of the particles were missed by the PDI, and probably the data rate was not proportional to the volume fraction. All three PDF curves corresponding to our experimental measurement campaign of varying volume fraction ϕ_v show quite different behaviour compared with RPP. This means that we

TABLE 6.11: Contribution of σ of each class towards the global distribution

$\phi_v \times 10^{-5}$	$\frac{\sigma^2_{class}}{\sigma^2}$, %		
	Clusters	Voids	Inbetweeners
0.5	20	66	14
1.0	17	69	14
2.0	5	92	3

have clustering for every volume fraction tested. From the table 6.12 we see that all experimental PDFs cross the RPP curve at around $\nu_{cl} = 0.45 \pm 0.03$ on the left and $\nu_v = 2.22 \pm 0.12$ on the right. This is very interesting given that the points of crossing RPP curve in 2D are not very different from these limits: $\sigma_{left} = 0.6$ and $\sigma_{right} = 2.1$. As in 2D, these points of RPP crossing are conventionally considered to be the thresholds for clusters and voids. Note that owing to the comparison made between RPP in 1D and 2D, we are not sure that clusters and voids correspond to the same sets in 1D and 2D. As in 2D, we detect for the two largest volume fractions a third crossing of the RPP curve in the vicinity of $\nu = 0.04$ meaning that dense clusters essentially span the interval of $0.04 < \nu < 0.45$, and dense clusters 25 times the concentration ($\nu = 0.04$) are very rare.

From the table 6.12 we could also see the proportion of particles in each class: clusters, voids and inbetweeners (the points that are situated in between clusters and voids) calculated as $N_{class} = \frac{N_{datapoints}}{N_{total}}$ expressed in %. The largest population corresponds to the inbetweeners points yielding approximately 70% of all particles. The clusters contain around 22% of all particles, and the voids account for only 8% which is the smallest population. This is expected given that the probability of finding voids is extremely low since the expectation falls rapidly even for 1D or 2D Voronoii PDFs (see fig.6.36). Also from the fig. 6.37, the convergence issues of PDF past the limit of $\nu = 30$ could be clearly seen. Moreover, from table 6.11 we could see that both clusters and inbetweeners contribute roughly by a comparable amount to the global σ, and also, that their contributions decrease with the increasing volume fraction ϕ_v. While the contribution of both clusters and inbetweeners decreases, the contribution of the voids increases which means that σ is mainly a measure effect of the probability of voids. The same conclusion, with comparable figures, has been shown for 2D Voronoii analysis in Section 4.2.2.

The measure of clustering level is made by way of the standard deviation σ of the Voronoii distribution: σ is increasing with an increase of the volume fraction ϕ_v. We decided to check how the level of clustering evolve with both Re_λ and ϕ_v. From

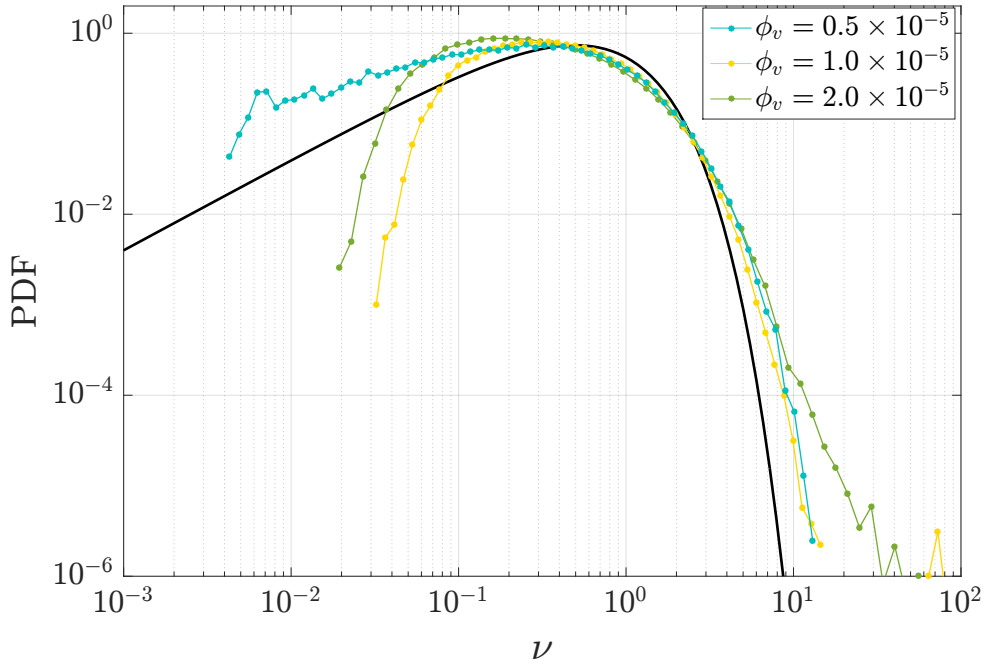

FIGURE 6.37: PDF of Voronoii diagrams of Random Poisson Process (RPP) in 1D and 2D

TABLE 6.12: Some additional characteristics of Voronoii distributions of our 1D analysis

$\phi_v, \times 10^{-5}$	ν_{cl}	ν_v	$N_{cl}, \%$	$N_v, \%$	$N_{inbetween}, \%$	$N_{total} \times 10^6$, points	σ
0.5	0.37	2.35	24	9	67	0.79	0.94
1.0	0.41	2.56	25	6	69	0.93	0.96
2.0	0.49	2.58	37	7	56	0.79	1.96

fig.6.38 we could see that the clustering level $\sigma_{rel} = \frac{\sigma - \sigma_{RPP}}{\sigma_{RPP}}$ fits as:

$$\sigma_{rel} = 2.03 \times Re_{\lambda}^{0.88} \times \phi_v^{0.48} \tag{6.31}$$

The same trend of the clustering level σ_{rel} vs Re_λ and ϕ_v was observed for the PTV data in 2D (see Chapter 4 Section 4.2).

6.6.2 Size segregation: diameter D of particles conditioned by the local concentration

Following the analysis of clustering, we look now at the size segregation of particles belonging to clusters and voids. Since we have the information about local concentration field, retrieved from the time arrivals of the particles, and the size of the

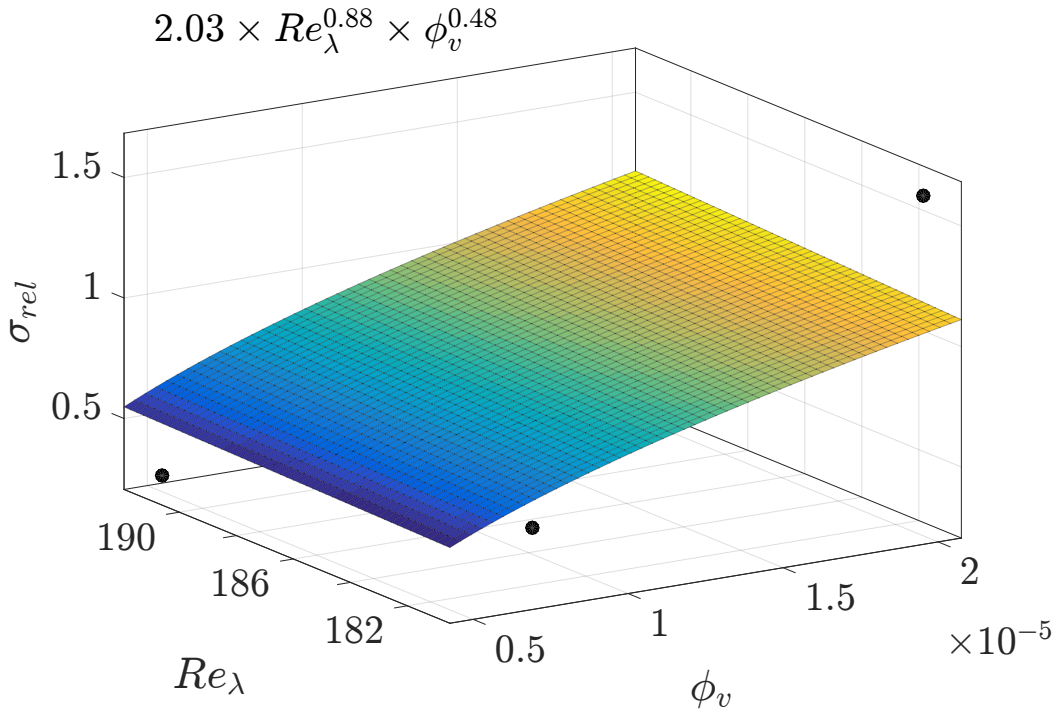

FIGURE 6.38: PDF of Voronoii diagrams of Random Poisson Process (RPP) in 1D and 2D

particles, we can classify three types of structures as particles would end up accumulating in clusters, voids and inbetweeners, and examine their corresponding size distributions.

After separating the three types of structures, the PDF of diameters D of each structure were computed for each experimental condition as shown in fig.6.39. Judging from these PDFs, no clear size segregation between these structures could be observed. This means that all particle sizes could be found in clusters, voids and points inbetween with comparable probability.

To analyse this in a more detailed way, we decided to look at the quantity $\frac{P(D_{classe})-P(D)}{P(D)}$ where $P(D)$ is a global inconditional probability of finding a particle with diameter D, and $P(D_{classe})$ is the probability of finding a particle with the diameter D belonging to a particular structure. This analysis is done to compare the relative tendency of each type of structures to possess a particular set of diameters D for each experimental condition (see fig. 6.40).

First of all, the inbetweeners region has a size distribution very close to the unconditional one with deviations $< 15 - 20\%$. For the lowest $\phi_v = 0.5 \times 10^{-5}$, the small particles up to 40 μm could be found with higher probability in voids than in clusters. The inverse is true for particles with a size between 40 μm and 150 μm,

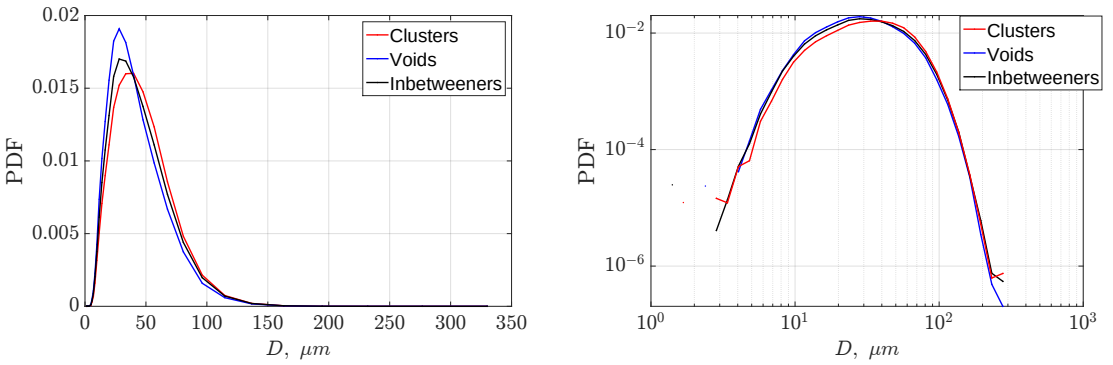

(a)

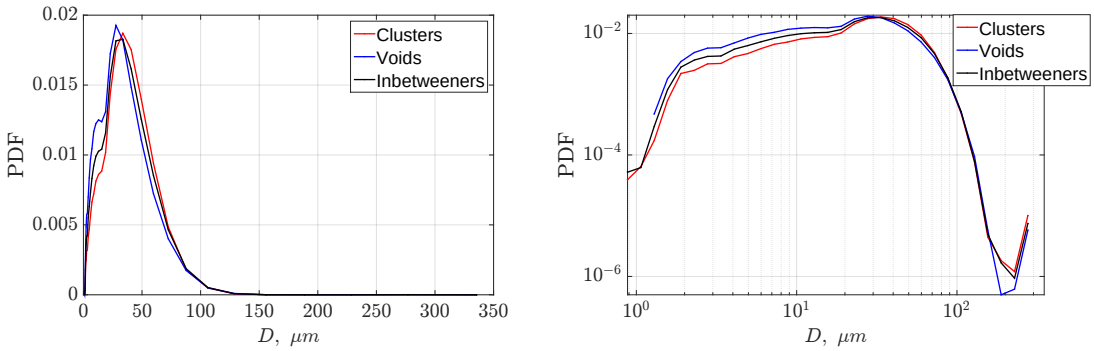

(b)

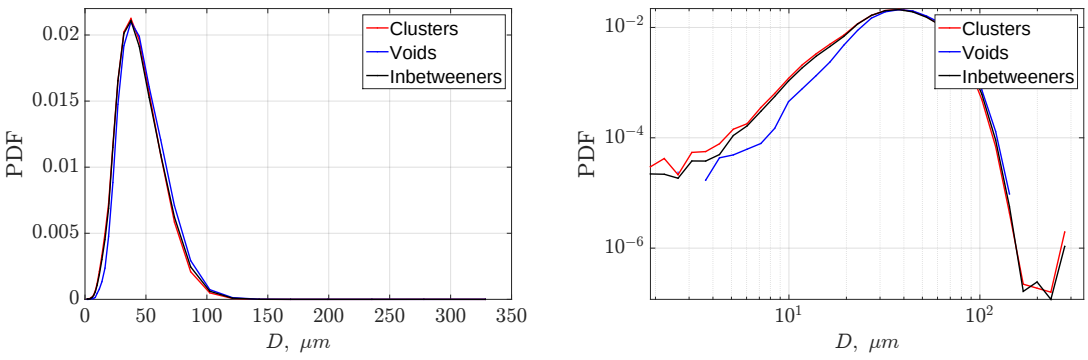

(c)

FIGURE 6.39: Diameter distribution of clusters, voids and inbetweeners for each experiment with volume fraction: (a) $\phi_v = 0.5 \times 10^{-5}$, (b) $\phi_v = 1.0 \times 10^{-5}$ and (c) $\phi_v = 2.0 \times 10^{-5}$

meaning that these larger particles accumulate more in clusters than in voids. The differences are quite small, about 20% at most. Note that, the figures above 20% observed at larger size ($> 150\ \mu m$) are not significant owing to the limited statistics. Increasing the volume fraction 2 times, shows the onset of inversing the trend of particles size accumulation depending on the type of structure they are in. The previous scenario is only true for small particles with diameter $D < 30\ \mu m$ and bigger particles with diameter $D < 95\ \mu m$. The trends for $D > 100\ \mu m$ are noisy, and thus, not clearly defined.

This inversion of the trend is more profound for the highest volume fraction $\phi_v = 2.0 \times 10^{-5}$ where smaller particles up to 40 μm are more probable to be found in clusters and larger particles up to 150 μm are more probable to accumulate in voids.

What is more interesting is the fact that for the highest volume fraction $\phi_v = 2.0 \times 10^{-5}$, the increase of the relative probability is the highest with 60% for the voids compared to the marginal increase up to 20% for the other two volume fractions. And the initial point of inflection of all curves for the diameter $D = 40\ \mu m$ changes marginally with rising volume fraction ϕ_v.

To conclude, we could see that there is a marginal change of $P(D|C)$ of particles to accumulate in clusters or voids with rising volume fraction compared to the overal distribution of the diameter D. However, on average no significant segregation of size by the local concentration ν is detected.

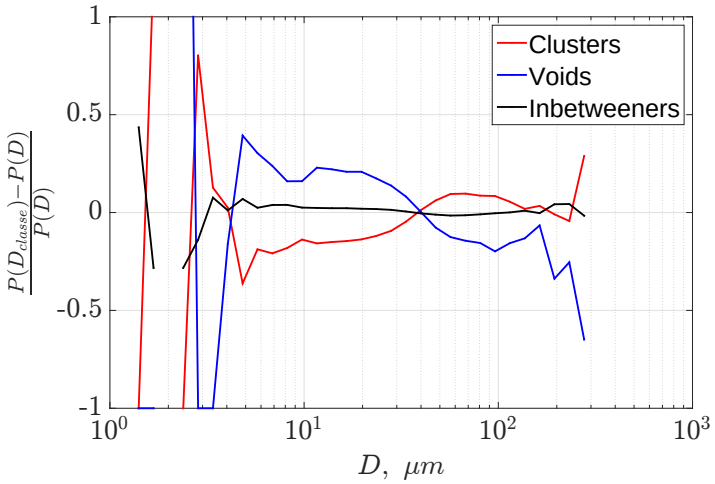

(a)

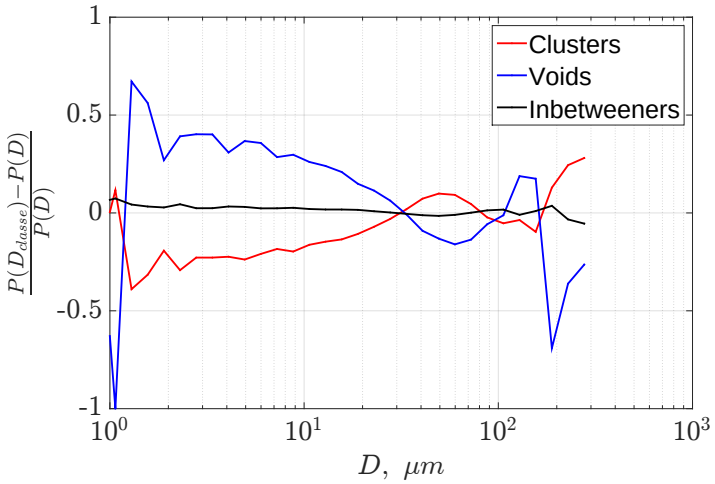

(b)

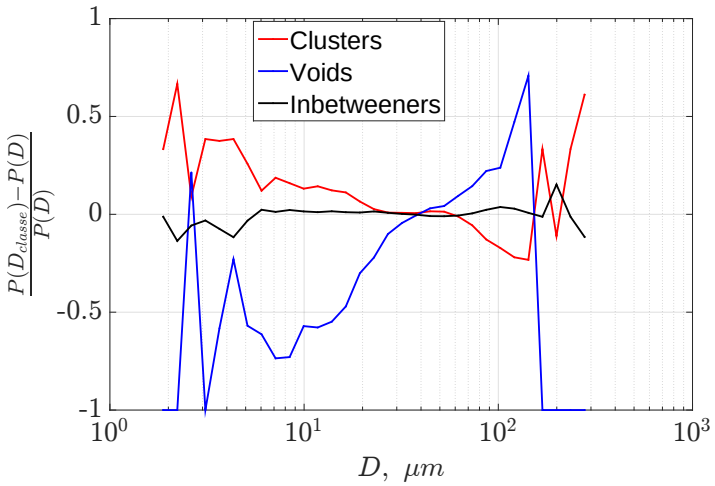

(c)

FIGURE 6.40: Quantity $\frac{P(D_{classe})-P(D)}{P(D)}$ vs D investigated for three experimental conditions: (a) $\phi_v = 0.5 \times 10^{-5}$, (b) $\phi_v = 1.0 \times 10^{-5}$ and (c) $\phi_v = 2.0 \times 10^{-5}$

6.6.3 Velocity statistics conditioned by the size of the particle and by the local concentration

The next point of our analysis is the conditional statistics of $\delta V = \bar{V} - V_{St} - V_{physical}$ by the diameter and by the local concentration ν. To start, we counted the amount of available statistics for a given local concentration ν (see fig.6.41). The majority of the velocity statistics are acquired for the interval between $\nu_{left} = 0.2$ and $\nu_{right} = 2.0$. Past these limits the loss of statistics is evident: this is notably so for $\nu < 0.06 - 0.07$ and for $\nu > 4 - 5$.

Next, we plotted the quantity $\delta V = \bar{V} - V_{St} - V_{physical}$ binned by the local concentration ν for a set of diameters ranging from $D = 12\ \mu m$ to $D = 97\ \mu m$ for three experimental conditions as seen on the fig. 6.42. The bins are defined as follows: linearly spaced 32 bins for D ranging from D_{min} to D_{max} and logarithmically spaced 32 bins for ν ranging from 10^{-2} to 10^{1}. To remind the reader, the thresholds for the clusters is $\nu_{cl} = 0.45$ and for voids $\nu_v = 2.22$. So, judging from the fig. 6.42, we do not observe any significant change of δV with the local concentration ν for any diameter chosen. It is striking that the flat trend is consistently observed through the 4 fold increase of volume fraction ϕ_v from 0.5×10^{-5} to 2.0×10^{-5}. Hindering of velocity (see discussion of velocity plotted vs D in Section 6.4.6) for the diameters larger than $D = 76\ \mu m$ for volume fractions $\phi_v = 0.5 - 1.0 \times 10^{-5}$ and larger than $D = 65\ \mu m$ for the highest volume fraction $\phi_v = 2.0 \times 10^{-5}$ is confirmed.

To further confirm the trends of velocity conditioned by both local concentration ϕ_v and diameter D of the particle, we decided to plot $\delta V = \bar{V} - V_{St} - V_{physical}$ binned now by the diameter D for given local concentration ν (see fig. 6.43). No clear trend with rising ν could be observed for any of the volume fractions tested. In terms of size we recover the trends observed on the average velocity (see fig.6.17 in Section 6.4.6). That is, hindering of the particle velocity occurs for large diameters ($D > 70\ \mu m$ for $\phi_v = 0.5 - 1.0 \times 10^{-5}$ and $D > 60\ \mu m$ for the highest $\phi_v = 2.0 \times 10^{-5}$) regardless of the local concentration ν, while enhancement happens at smaller sizes. This conclusion would be the same if the velocity $V_{physical}$ is accounted for as this quantity merely shift upward the curves by an amount smaller than the maximum velocity magnitude ($V_{physical} = -0.0046, 0.0275, 0.0702$ from fig. 6.16) also shown on fig. 6.43. This trend is opposite to the one found by [1] where collective effects were driving the enhancement of settling velocity. Here, each particle size maintains its proper behaviour irrespective of the local concentration as if each particle size were independently interacting with the background flow. This also holds for the three global concentrations combined.

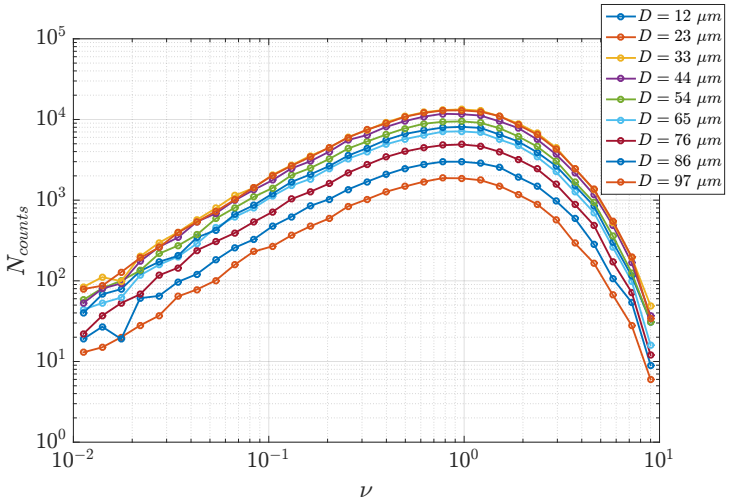

(a)

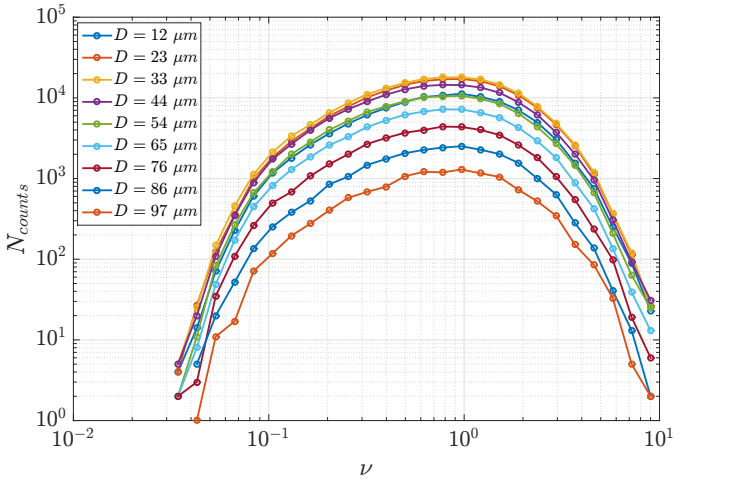

(b)

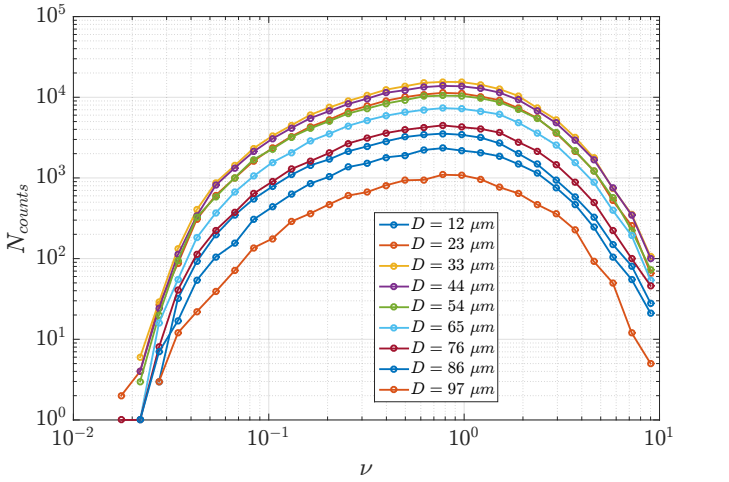

(c)

FIGURE 6.41: The N_{counts} of available statistics by concentration ν for particular diameters D for (a) $\phi_v = 0.5 \times 10^{-5}$ (b) $\phi_v = 1.0 \times 10^{-5}$ (c) $\phi_v = 2.0 \times 10^{-5}$

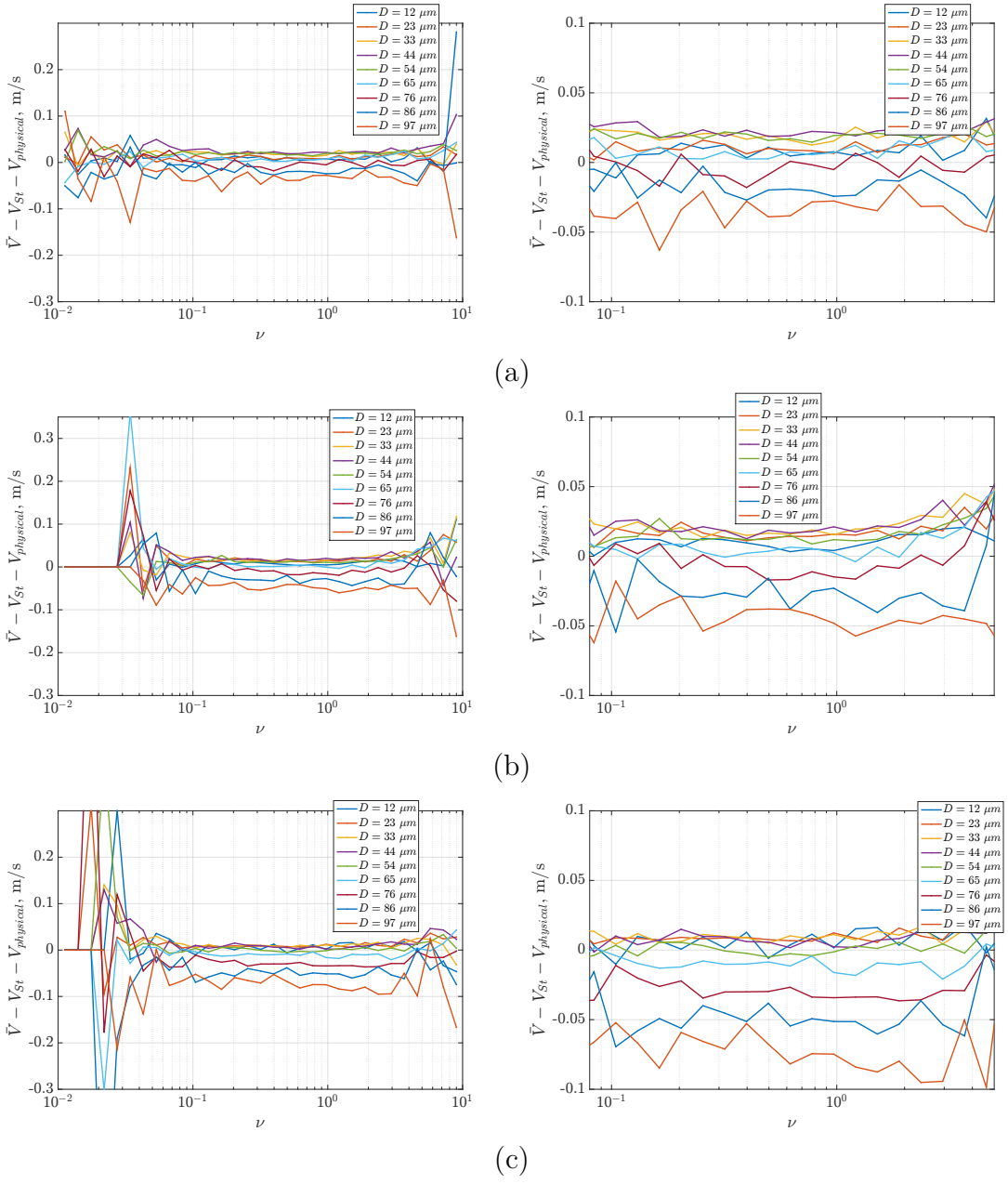

FIGURE 6.42: The quantity $\bar{V} - V_{St} - V_{physical},\ m/s$ conditioned by the concentration ν for particular diameters D for (a) $\phi_v = 0.5 \times 10^{-5}$ (b) $\phi_v = 1.0 \times 10^{-5}$ (c) $\phi_v = 2.0 \times 10^{-5}$. Right hand side figures correspond to the same data but zoomed over the interval $0.08 < \nu < 5$

The trend of velocity enhancement conditioned by the local concentration field has been documented in [1]. They observed the settling velocity enhancement with regards to the free falling regime of $\frac{V(C,St)-V(St)}{U\prime}$ for the particles at the higher local concentration and hindering of settling velocity with regards to the free falling regime of $\frac{V(C,St)-V(St)}{U\prime}$ for the particles with the lower local concentration. In other words, they have seen a significative enhancement of the settling velocity within the clusters.

What we see from our conditional analysis of the settling velocity is quite different compared to what was observed by that study. We have seen no size segregation or particle preference to the type of the structure they are in to as it was also shown in [1]. Meaning that all particle sizes are involved in both formations of clusters and voids. Secondly, no significant trend of $\delta V = \bar{V} - V_{St} - V_{physical}$ could be observed versus the local concentration ν or the diameter D. This means that all particles are interacting with the base flow irrespective of the presence of other particles. Increasing the volume fraction would result in the increase of effective number of particles seeded in the flow, however, it shows no sign of collective effects on the type of the structures the particles end up in. To further confirm this, the conditional analysis of $V(C|D) - V(D)$ vs ν is shown in fig. 6.44 for three experimental conditions. It is clear that there is no velocity change detected either in clusters or in voids. This confirms one more time that the signature of collective effects is absent in the present experimental condition.

We nevertheless detect a small influence of the global seeding. Indeed, we estimated the difference in the $\delta V = \bar{V} - V_{St} - V_{physical}$ between the particles with $D_{min} = 12\ \mu m$ and $D_{max} = 97\ \mu m$ for three volume fractions $\phi_v = 0.5, 1.0, 2.0 \times 10^{-5}$ as $0.0404, 0.0569, 0.0809$ m/s. Thus, there is a small increase of the relative velocity between small and large diameters with the increase in volume fraction ϕ_v.

In [1], the settling velocity of clusters was shown to evolve as $\delta V \sim C \times l^2$ where l is the length of the clusters and C is the concentration of particles in the clusters. Hence, the enhancement could be due to either denser clusters and/or due to the larger ones. In our case, the scenario of little effect of clusters on the enhancement of settling velocity is possible if the length of the clusters is small and/or if the clusters are less dense so that their settling velocity remains small in particular when compared to $U\prime$. To test this argument, we decided to track the clusters in time and obtain the length of the clusters in our experiment.

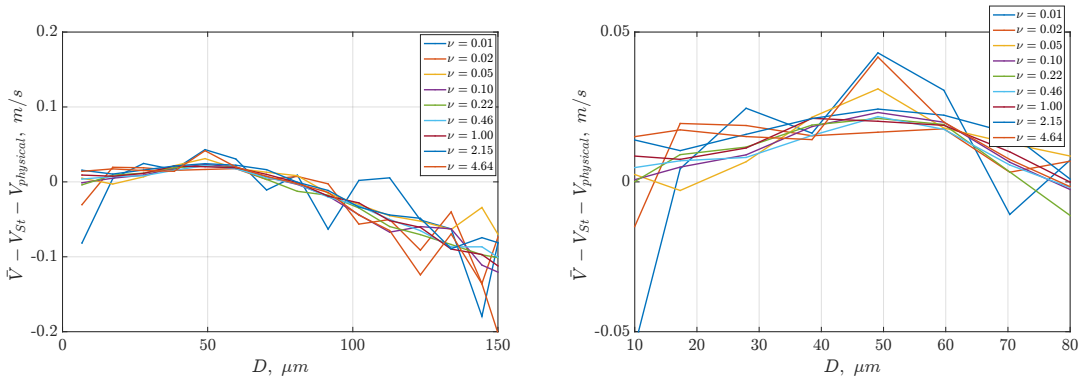

(a)

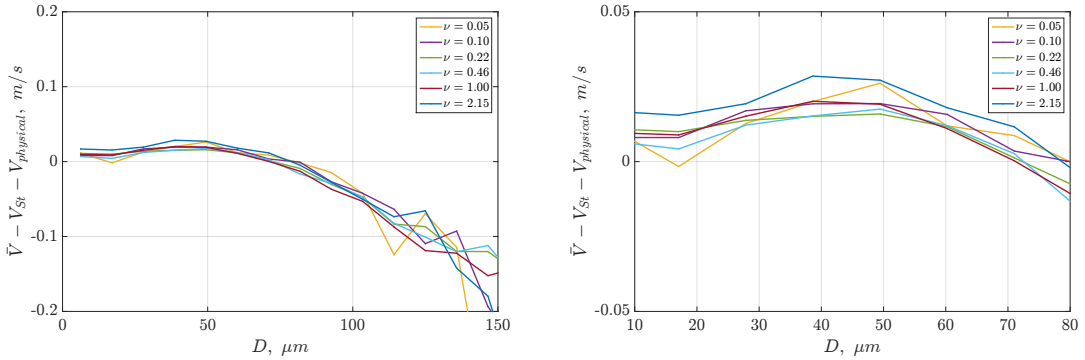

(b)

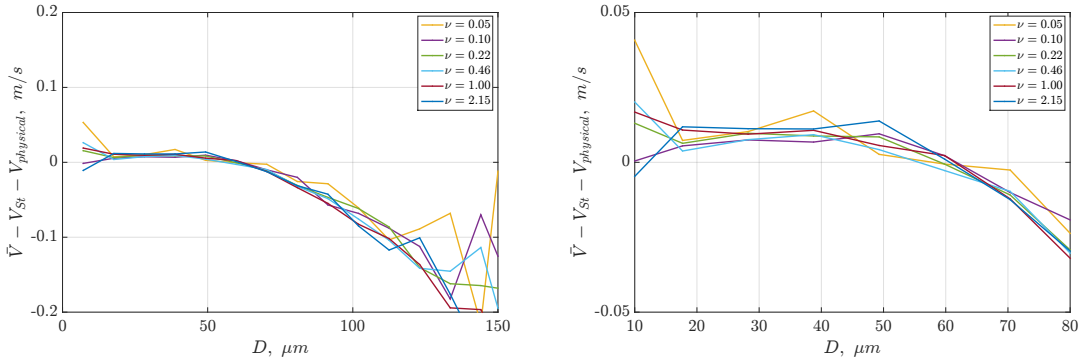

(c)

FIGURE 6.43: The quantity $\bar{V} - V_{St} - V_{physical},\ m/s$ conditioned by the diameter $D,\ \mu m$ for particular concentrations ν for (a) $\phi_v = 0.5 \times 10^{-5}$ (b) $\phi_v = 1.0 \times 10^{-5}$ (c) $\phi_v = 2.0 \times 10^{-5}$. Right hand side figures correspond to the same data zoomed for $10\ \mu m < D < 80\ \mu m$

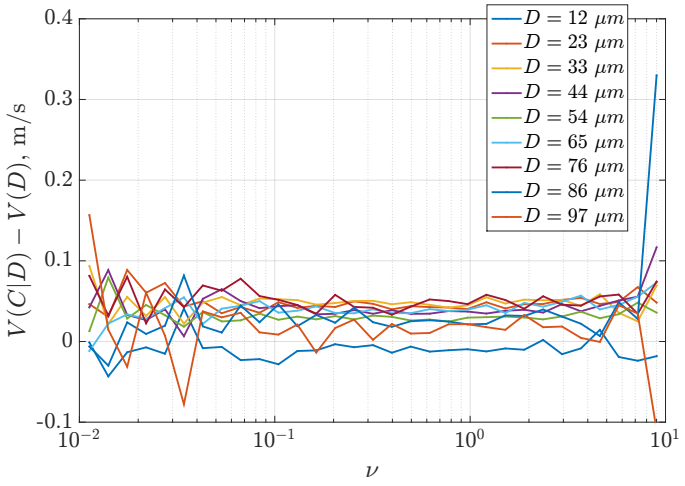

(a)

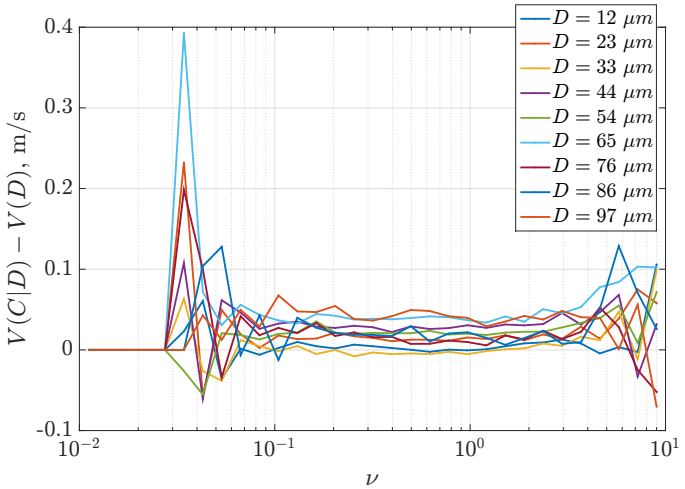

(b)

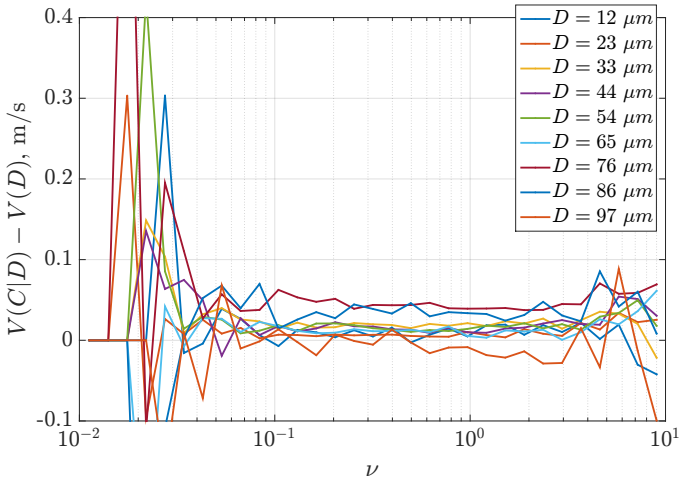

(c)

FIGURE 6.44: The $V(C|D) - V(D)$, m/s conditioned by diameter D, μm for a particular concentration ν for (a) $\phi_v = 0.5 \times 10^{-5}$ (b) $\phi_v = 1.0 \times 10^{-5}$ (c) $\phi_v = 2.0 \times 10^{-5}$

6.6.4 Length of the clusters l_c and their concentration $\frac{C_c}{C_0}$

Having achieved the simultaneous information about arrival times of the particles and their local concentration, we could track the clusters in 1D. We define the cluster as a structure of Voronoii cell with a minimum of two connected cells involved. By summing up the δT for each connected cell and converting it to a distance via $\delta T \times \bar{U}_{axial}$, the length of the clusters l is obtained.

The distribution of the length of clusters for each experimental condition is shown in fig. 6.45. From PDFs we observe that the range of estimated values of clusters length l are from 0.5 mm up to 10 cm. The PDFs of clusters length l corresponding to the experimental conditions $\phi_v = 0.5 - 1.0 \times 10^{-5}$ resemble each other, which could be also confirmed judging by the lowest mean clusters length $\bar{l}$ is 6 mm for $\phi_v = 1.0 \times 10^{-5}$, while the largest mean cluster length $\bar{l}$ is 2 cm observed for the lowest $\phi_v = 0.5 \times 10^{-5}$ (see table 6.13). The quantity $\frac{\bar{l_c}}{\eta}$ is also estimated as characteristic length of clusters and it can be compared with the quantity $\frac{\sqrt{A_c}}{\eta}$ from 2D PTV data (see results in Section 4.2.3). To recall, $\frac{\sqrt{A_c}}{\eta}$ evolves in the range of 5 - 25 for the $Re_\lambda = 175$ and $\phi_v = 0.5 - 2.0 \times 10^{-5}$. We could see that the estimations from 2D data and 1D data are yielding the same order of values. The biggest difference between $\frac{l_c}{\eta}$ and $\frac{\sqrt{A_c}}{\eta}$ occurs for $\phi_v = 0.5 \times 10^{-5}$. This could be due to missing some particles by PDI (validation rate $< 100\%$) or due to the fact that 2D and 1D Voronoii analysis is not the same procedure.

TABLE 6.13: Properties of clusters for three experimental conditions as detected by the 1D Voronoii analysis

$\phi_v \times 10^{-5}$	$\bar{l}_c$, m	C_0, particles/m	$\bar{l}_c/\eta$	$\bar{C}_c$, particles/m	$\frac{\bar{C}_c}{C_0}$
0.5	0.02	31	52	163	5.26
1.0	0.006	118	15	542	4.59
2.0	0.009	81	22	402	4.96

Next we estimated the pdf of concentration of particles per cluster C_c (see fig. 6.46). The range of particle concentration in clusters C_c is from 80 particles/m to 3000 particles/m. As can be seen from table 6.13, the highest mean concentration of particles per cluster length are achieved for volume fractions $\phi_v = 1.0 - 2.0 \times 10^{-5}$. The lowest mean concentration of particles per cluster length is achieved for the lowest volume loading provided (see fig. 6.46a). However, if we look closely at the quantity $\frac{C_c}{C_0}$, we see that all curves almost collapse showing the maximum at $\frac{C_c}{C_0} = 4$ independent of the volume fraction provided (see fig. 6.46b). The distributions are

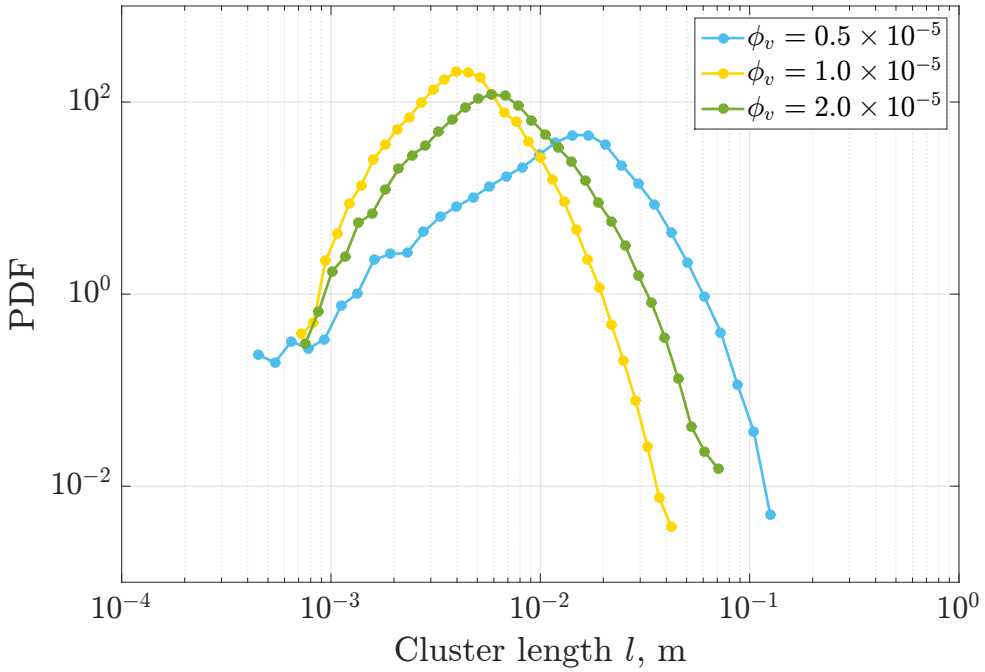

(a)

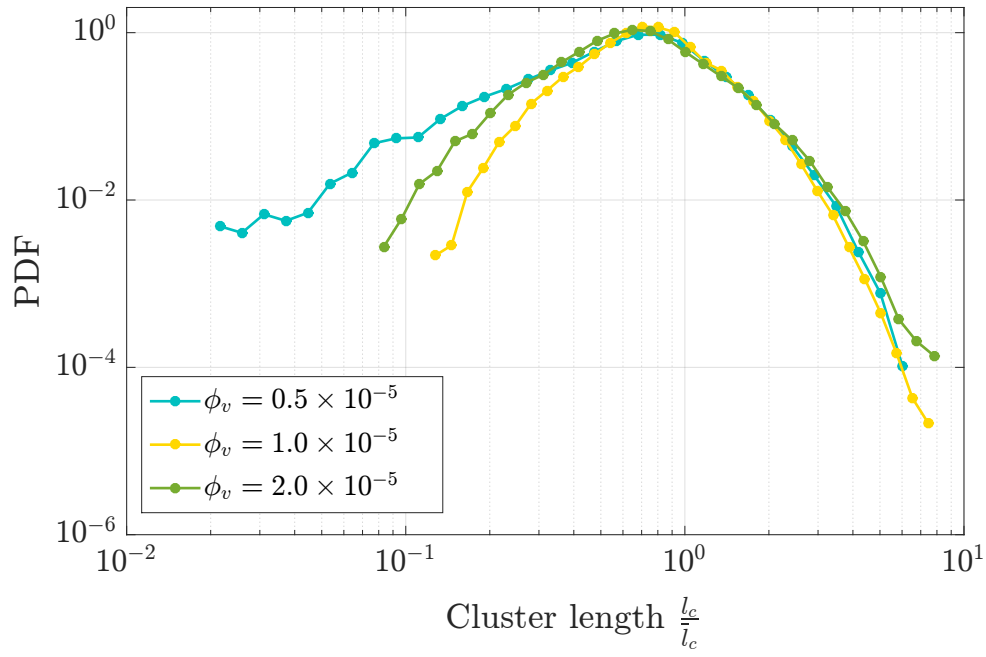

(b)

FIGURE 6.45: Distribution of (a) cluster length l_c and (b) cluster length $\frac{l_c}{\bar{l}_c}$ for three experimental conditions

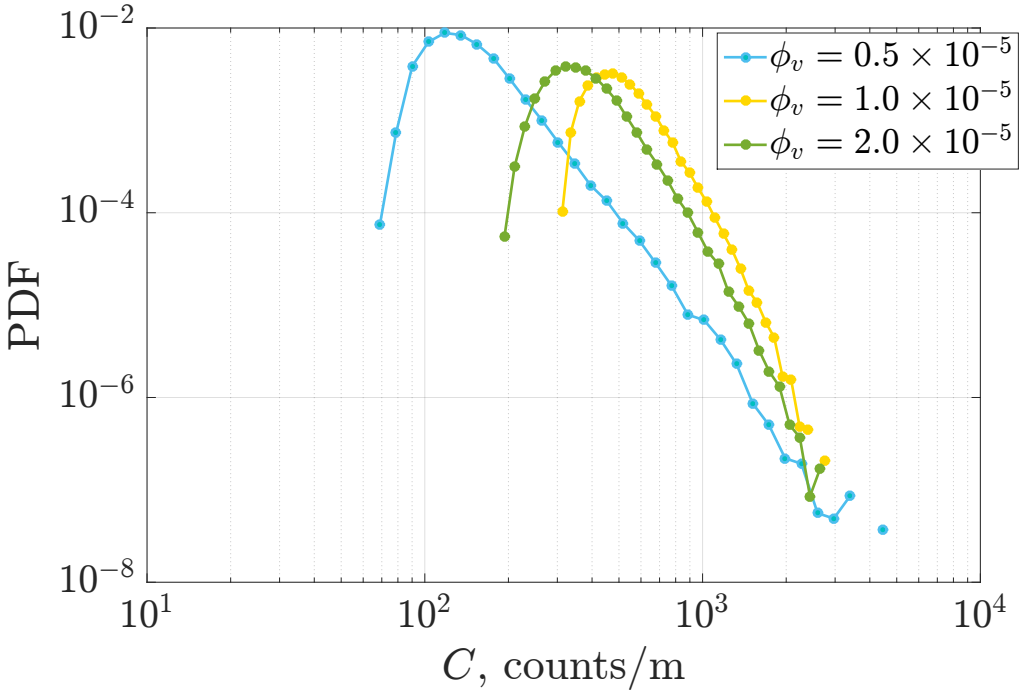

(a)

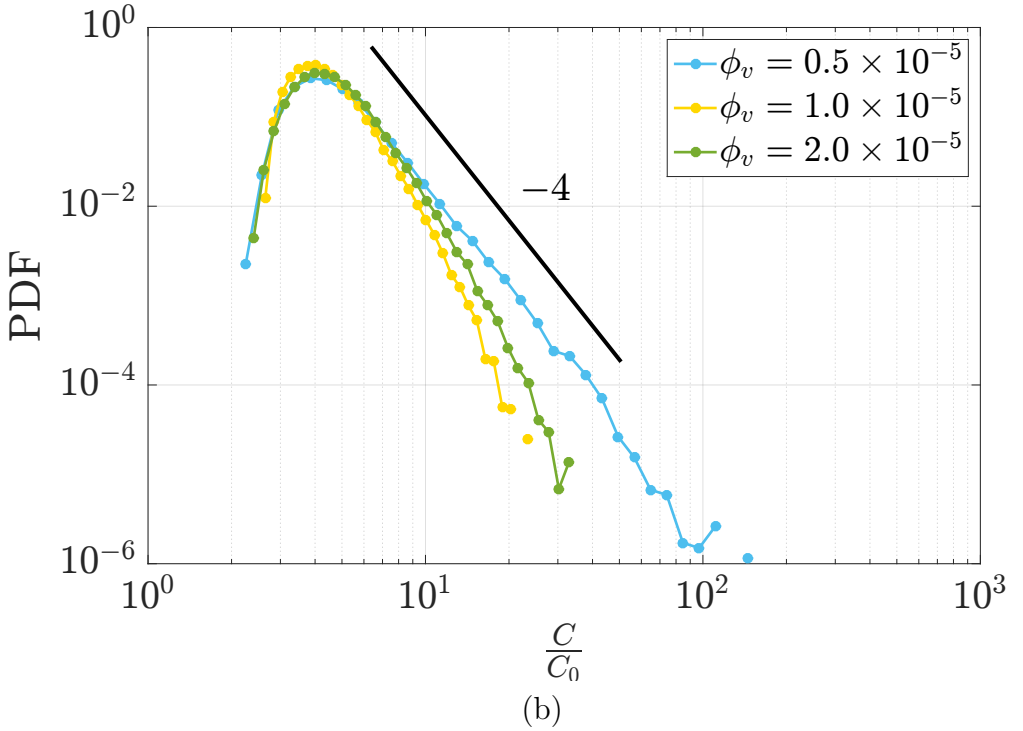

(b)

FIGURE 6.46: PDF of (a) concentration of particles in clusters C and (b) $\frac{C}{C_0}$ for three experimental conditions

strongly peaked with a strong decay of the probability for $\frac{C_c}{C_0} > 4$ with the slope of $\simeq -4$. The mean values of $\frac{C_c}{C_0}$ are almost the same around $\frac{C_c}{C_0} \simeq 5$. This is a very interesting result because we see that the maximum and the mean of $\frac{C_c}{C_0}$ i.e. the cluster packing capacity, are almost independent of the volume fraction ϕ_v. Cluster concentration evolves linearly with the volume loading. This result is in contrast with that obtained by Monchaux et al.[48] where the mean cluster concentration evolved as $C_0^{0.6}$.

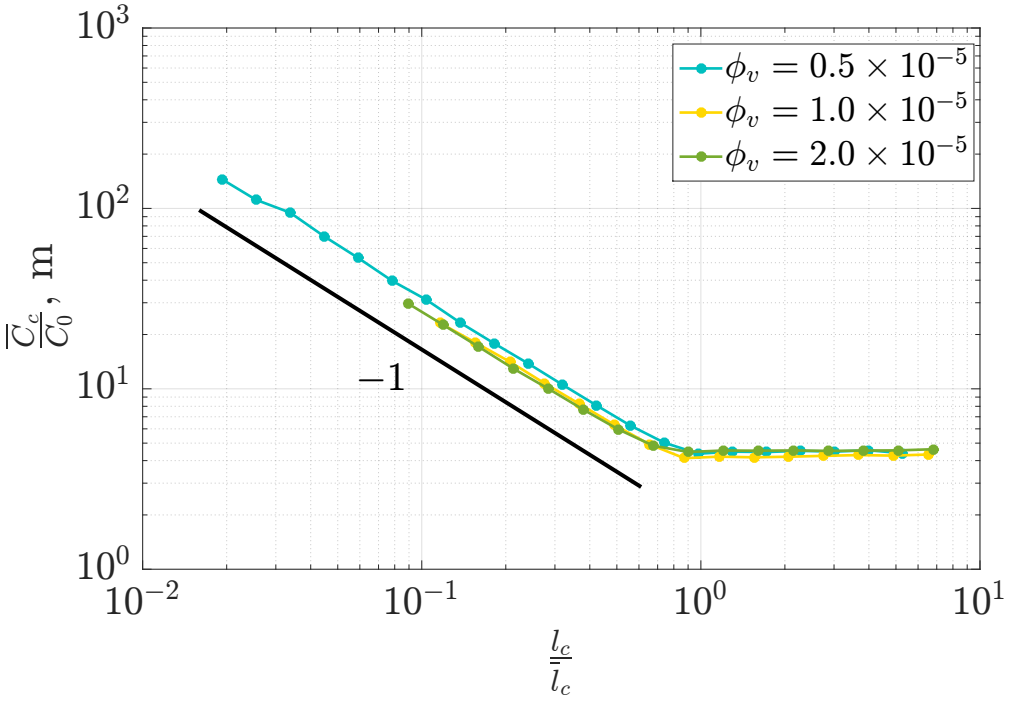

FIGURE 6.47: Concentration in clusters $\frac{\overline{C_c}}{C_0}$ versus the length of clusters $\frac{l_c}{\overline{l_c}}$ for three experimental conditions

We consider $\overline{C_c}$ as the average cluster concentration of cluster of size l. Fig. 6.47 shows $\frac{\overline{C_c}}{C_0}$ vs $\frac{l_c}{\overline{l_c}}$ for the three experimental conditions. We could see that there is no change in the quantity $\frac{\overline{C_c}}{C_0}$ with increase of the volume fraction ϕ_v. It is also remarkable that there is a critical length of $\frac{l_c}{\overline{l_c}}$ around 1 past which $\frac{\overline{C_c}}{C_0}$ stays constant. Meaning that the clusters have reached a saturation of length for the number of particles provided. The slope of decrease of $\frac{\overline{C_c}}{C_0}$ vs $\frac{l_c}{\overline{l_c}}$ is about -1 which means that the relative length of clusters $\frac{l_c}{\overline{l_c}}$ decreases linearly with the increase in $\frac{\overline{C_c}}{C_0}$.

Last but not least we have estimated the velocity of clusters V_{cl} as proposed by [1] as $V_{cl} = \frac{K_T}{18}\frac{\rho_p}{\rho_f}\frac{g}{\nu_f} C \times l_c^2$ where K_T is a degree of asymmetry of the particle shape and varies between $0.3 - 0.5$ and equals to 1 if the particle is a perfect sphere [1].

Since the shape of the clusters is unknown we assume a certain degree of asymmetry, meaning that clusters are not spherical, and we choose the value for $K_T = 0.3$. We take $\rho_p = 1000\ kg/m^3$ as the particles are water droplets, $\rho_f = 1.2\ kg/m^3$ as the fluid is air, $\nu_f = 1.5 \times 10^{-5}\ m^2/s^3$ as viscosity of air and $g = 9.81\ m/s^2$. In this formula, C is the concentration of particles in the cluster and l_c is its length. Hence, taking the mean values $\overline{C}_c$ and $\bar{l}_c$, the velocity of clusters V_{cl} is estimated as 0.09 m/s, 0.016 m/s and 0.075 m/s respectively with rising volume fraction ϕ_v of 0.5×10^{-5}, 1.0×10^{-5} and 2.0×10^{-5}. Let us remind that the PDI system was not delivering a data rate proportional to the volume fraction ϕ_v so that some bias may be present. A priori, one expects a random subsampling and then no serious bias on the statistics. What we can see is that the velocity of clusters V_{cl} decreases with the rising volume fraction ϕ_v which could be the case if either the length or concentration of particles in clusters decreases. Hence, we suppose that the velocity of clusters is not sufficient enough to significantly contribute to the enhancement of the settling velocity of particles. Also, the velocity of clusters V_{cl} is 3, 18 and 4 times weaker than the velocity of turbulent fluctuations $U\prime$, a feature that may also explain why particle turbulence interaction seem predominant over collective effects in our flow conditions. We will continue further a discussion for $V_{clusters}$ in Section 6.7.2.

6.6.5 Length of the voids l_v and their concentration C_v

Now let's perform the same analysis but with regards to the voids. The difficulty while analysing voids is the lack of statistics that could be acquired for voids in the experiment. To recall, the probability of finding a void is of the order of 10^{-4} and decreases rapidly with the size of the void.

We analysed the dimensions of voids for three experimental conditions. The PDFs of the length of voids are shown in fig. 6.48 a. We could see that the range of voids lengths is from $l_v = 0.3 \times 10^{-2}$ m to $l_v = 1$ m. There is some noise in the statistics acquired that could be clearly seen on the PDF for $\phi_v = 2.0 \times 10^{-5}$. In particular, the validity of the data for $l_v > 1$ m is questionable.These large values could be due to some particles missed by PDI due to reduced validation rate and/or because of the statistical noise due to the rarity of events detected.

Fig. 6.48 b shows the PDF of $\frac{l_v}{\bar{l}_v}$ for three experimental cases. We see a good collapse of the PDF curves which was also seen in 2D data (see fig. **??**). The peak is neatly marked with a strong decay (slope ~ -3) of the PDF after maximum. From table 6.14, we could see that the mean voids length decreases with the increase of volume fraction ϕ_v. We also compare the characteristic length of voids $\frac{\sqrt{A_v}}{\eta}$ obtained during 2D PTV campaigne and the values of $\frac{\bar{l}_v}{\eta}$. The characteristic length of voids $\frac{\sqrt{A_v}}{\eta}$ is varied from 12 to 38 for $\phi_v = 1.0 - 2.0 \times 10^{-5}$ and $Re_\lambda = 175$ which is not even within a range of the values of $\frac{\bar{l}_v}{\eta}$ estimated for our data (see table 6.14).

TABLE 6.14: Properties of voids for three experimental conditions

$\phi_v \times 10^{-5}$	$\bar{l_v}$, m	C_0, particles/m	$\bar{l_v}/\eta$	$\bar{C_v}$, particles/m	$\frac{\bar{C_v}}{C_0}$
0.5	0.263	31	691	9	0.29
1.0	0.067	118	166	35	0.29
2.0	0.136	81	330	22	0.27

We also looked at the concentration of particles in voids. Compared to those of clusters, the mean concentration of voids is about 18 times less than in clusters. Also from fig. 6.49, the range of voids concentration varies from 3 particles per m to 50 particles per m which is about 100 times less than in clusters. Normalising now with C_0 we could see some collapse of the pdf of $\frac{C_v}{C_0}$ for all three experimental conditions. The maximum occurs at $\frac{C_v}{C_0} = 0.3$ while the mean is consistently close to that value (see table 6.14). Again the maximum of the pdf is quite sharp with a -3 slope on the low concentration side. As for the relative concentration $\frac{\bar{C}_v}{C_0}$, the mean and the maxima happen to be proportional to the volume loading.

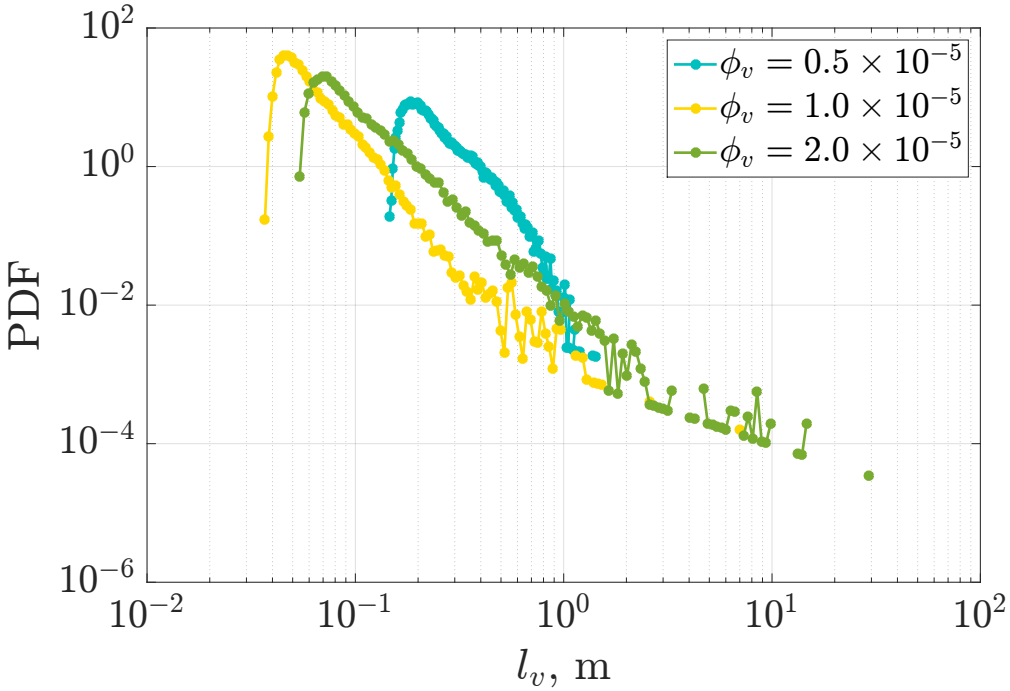

(a)

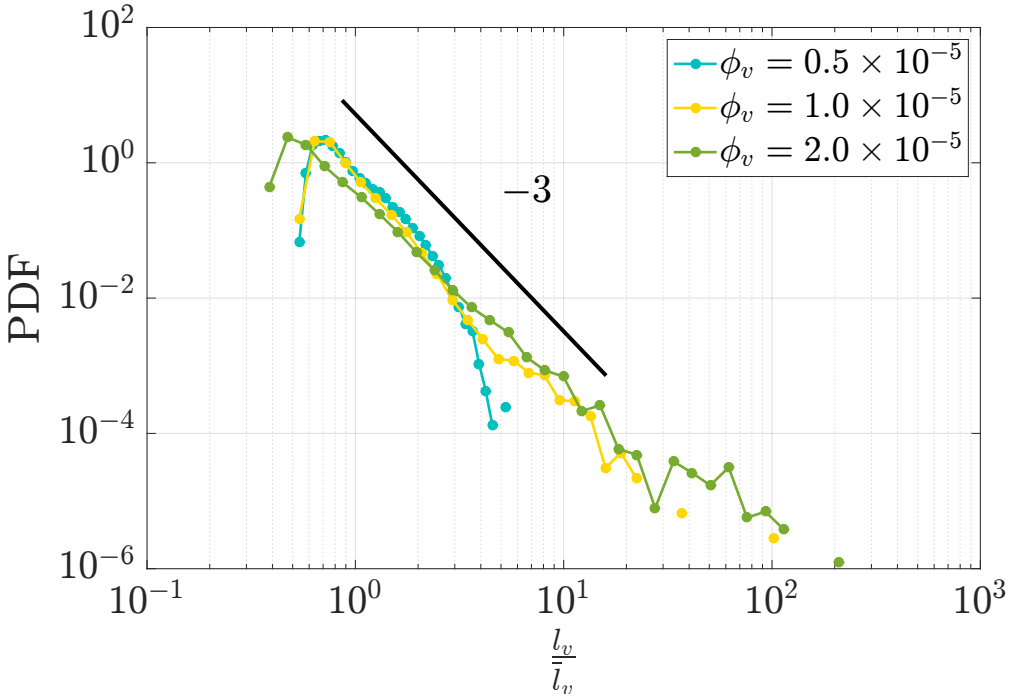

(b)

FIGURE 6.48: PDFs of length of voids (a) l_v and (b) $\frac{l_v}{\bar{l}_v}$ for three experimental conditions

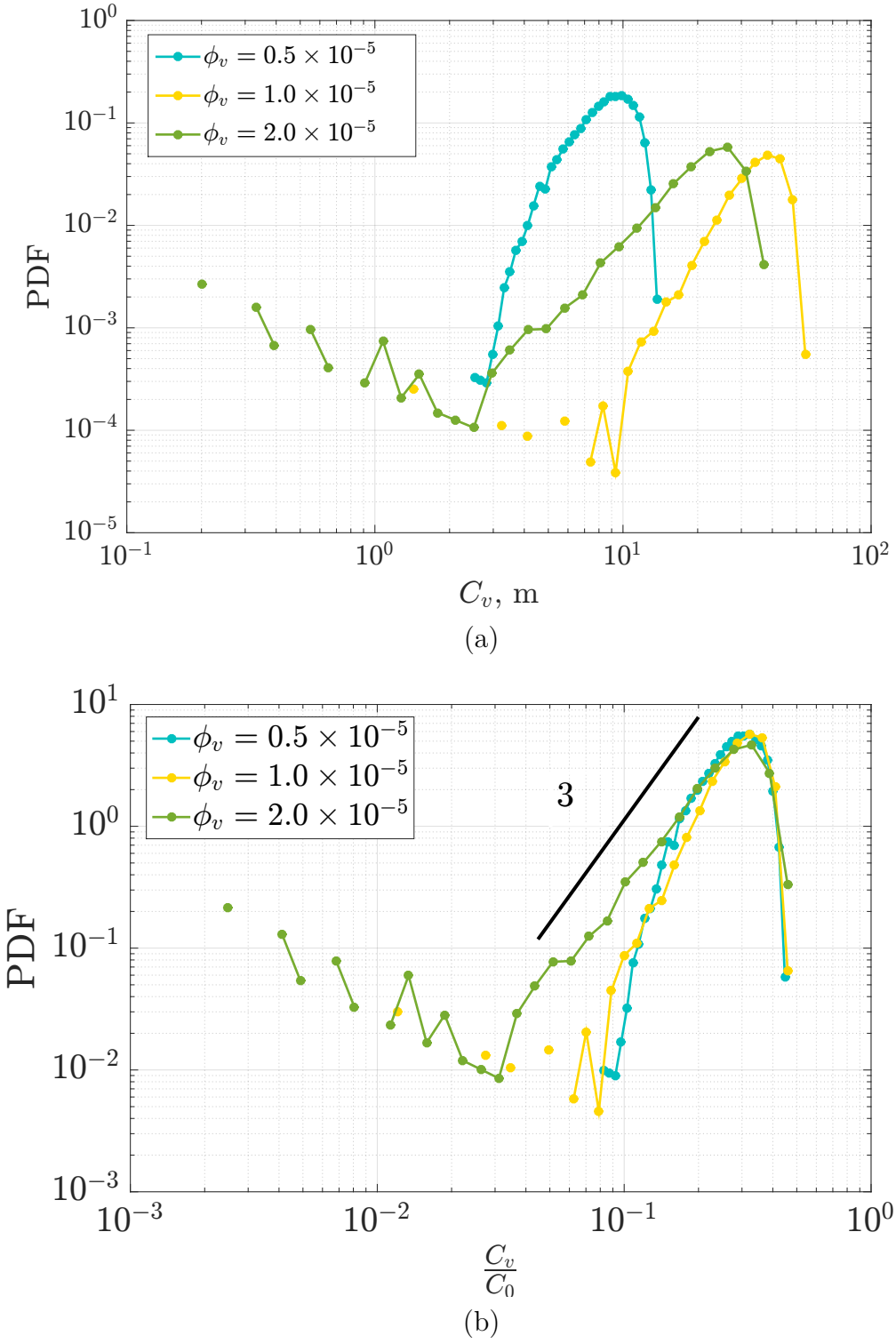

FIGURE 6.49: Concentration of particles in voids (a) C_v and (b) $\frac{C_v}{C_0}$ for three experimental conditions

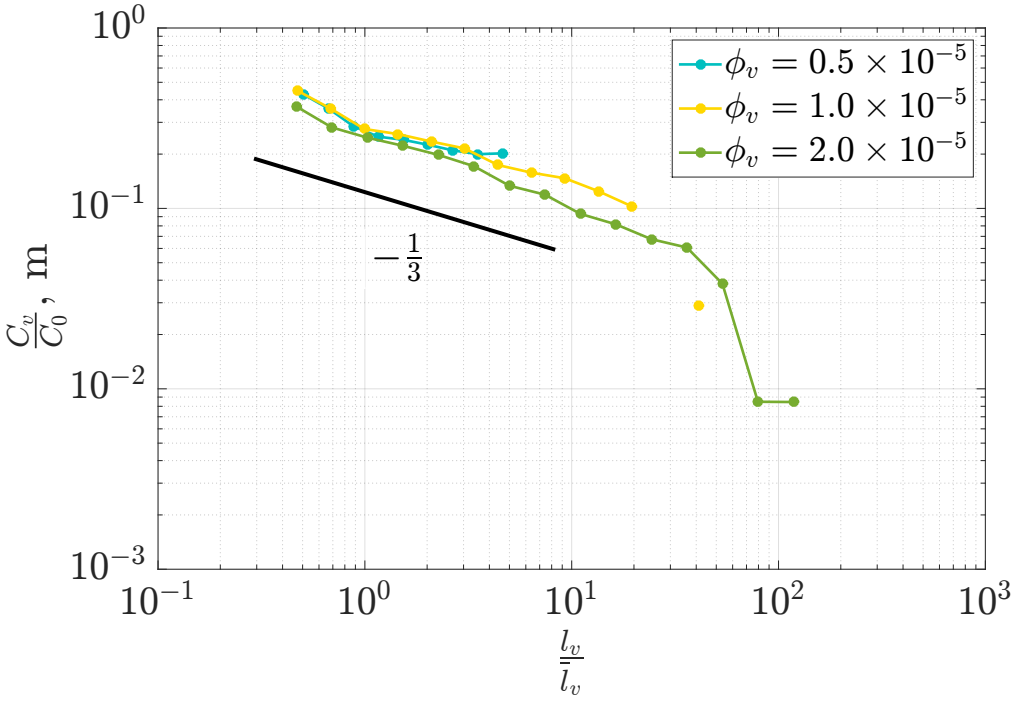

FIGURE 6.50: Concentration in voids $\frac{C_v}{C_0}$ versus the length of voids l_v for three experimental conditions

We have additionally plotted $\frac{\overline{C}_v}{C_0}$ with the length of voids $\frac{l_v}{\overline{l}_v}$ (see fig. 6.50). What we see is that the addition of particles to the voids does not affect greatly the length of the voids. The lack of data is evident for these estimations since the curves span just over one decade in both x and y direction of the plots. The shallow slope of $\frac{\overline{C}_v}{C_0}$ vs $\frac{l_v}{\overline{l}_v}$ is about $-\frac{1}{3}$.

6.7 Discussion

6.7.1 Velocity offset $V_{physical}$

It is worthwhile to go back to the meaning of the quantity $V_{physical}$ that has been presented in Section 6.4.5. $V_{physical}$ was estimated for the lowest volume concentration as the velocity shift observed in the limit of very small drops. To understand what $V_{physical}$ does represent, one must answer the question of where are these very small particles located? The analysis of PDI statistics indicates that approximately 60 to 70% of the particles are in the region between voids and clusters, $25-35\%$ are in clusters and less than 10% in voids (see table 6.11). In addition, there is a small excess (at low concentration) or a small deficit (at the largest concentration)

of small drops inside voids. But, the key point is that the velocity of small droplets is nearly the same whatever the local concentration (see fig.6.43).

Hence, in our conditions $V_{physical}$ is not an image of the fall velocity of clusters. Instead, since it is not biased either by size segregation or by particle positions, $V_{physical}$ is a faithful measure of the gas velocity, and it indicates that, in our flow conditions, the gas falls down at the same rate everywhere that is in clusters, in voids as well as in intermediate regions (this feature is represented by the arrows in the fig.6.51a).

Although PDI measurements have been performed only in the mid-depth of the channel, it can be guessed that they are representative of a significant fraction of the channel width. The global downward flux of the gas in the central part of the test section must then be compensated by an equivalent upward flux (or part of it as some flux may flow along the axial direction). It is quite probable that the gas is moving upward close to lateral walls (the latter may correspond to less dense regions if one consider that the area covered by injectors is less than the channel cross section). The existence of such a secondary motion has not been checked (this could be done by performing PDI measurements at different distances from the wall).

Yet, the fact that $V_{physical}$ increases with the volume loading is compatible with this scenario. If so, $V_{physical}$ is then an image of both the air entrainment by falling droplets and of the secondary motion induced by the confinement. The magnitude of that secondary motion would depend on the width of the central homogeneous region compared with that of the near wall layers. Without any information relative to spanwise velocity profiles, it is difficult to evaluate the relative contribution of these two effects, but this scenario should be kept in mind when examining the results.

Another consequence of this scenario is that the procedure to set the zero of the PDI-system could be incorrect. Indeed, we assumed that the zero of PDI velocity is given by smallest sizes and in the limit of a very small concentration for which we took $\phi_v = 0.5 \times 10^{-5}$. With a systematic recirculation, that concentration may not correspond to the zero gas velocity but instead to some finite value. A way to check that would have been to perform measurements at lower concentrations, but the incorrect functioning of injection at low liquid flow rates already mentioned, precluded such a test (at least with the present injector design). We can nevertheless evaluate the uncertainty associated with the procedure.

Indeed, fig.6.16 indicates that $V_{physical}$ would reach $-2.53\ cm/s$ in the limit $\phi_v = 0$. If that corresponds to the actual zero, then an absolute value of $2.53\ cm/s$

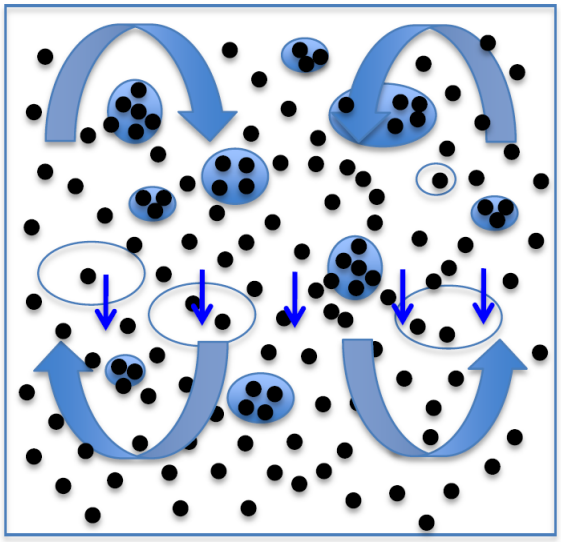

(a)

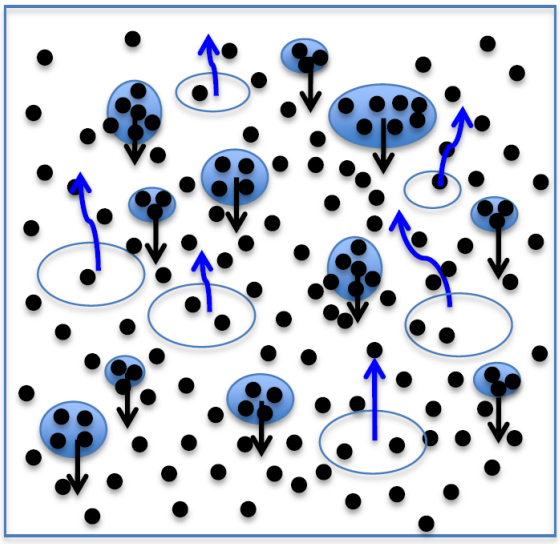

(b)

FIGURE 6.51: (a) Sketch of the particle organization in a channel cross-section, and of the induced gas recirculation in presence of an inhomogeneous repartition of clusters and voids in the cross section. The mean gas flows perpendicularly to the figure. (b) Sketch of the particle organization in a channel cross-section in presence of an homogeneous distribution of clusters and voids all over the channel cross-section. The mean gas flows perpendicularly to the figure.

should be added to all velocity data presented. Luckily, this velocity shift is comparable to the measurement uncertainty discussed in Chapter 3 Section 3.4.4, so that the data presented so far remain significant. Zero crossing on the plots such as fig.6.19 would be shifted to slightly higher St or Ro numbers, but they will be nevertheless present. All plots involving velocity differences, such as $V(D,C) - V(D)$ in fig.6.44, are unchanged whatever the interpretation given to $V_{physical}$ or its magnitude.

We have also seen in fig.6.23 that $V_{physical}$ takes a quite different magnitude in the present experimental conditions compared to those of Aliseda et al. [1]. In Section 6.5.1 we evoked the difference in turbulent Reynolds number between the two experiments, and the fact that the zero of the velocity measuring system was not established for the same concentration. Yet, the comparison is not straightforward.

On the one hand, a confinement effect similar to the one discussed above may have occurred in Aliseda et al experiments. Note that the experimental conditions were somewhat different from ours. In particular, the channel had a 20 $\times$ 20 cm^2 square cross-section and the injectors were occupying a 14 $\times$ 14 cm^2 area. Hence, injection was ensured over 70% of the channel width to be compared to 60% in our conditions: this small difference may possibly have favored the apparition of secondary flows in our test section. Besides, the mean axial velocity was about 10 m/s to be compared to 2.5 m/s in our conditions. For an arial entrainment as large as 10 m/s secondary motion is expected to be quite weak, which is indeed so as shown in fig.6.23.

An alternate option for Aliseda et al. flow conditions would be that the system was rather homogeneous, so that the air entrained downward by falling clusters was compensated by an upward flux distributed over the entire cross section, and notably in the void regions as sketched in fig.6.51b. In that case, $V_{physical}$ would result from up and down motions and it will be significantly lower compared to the situation with a recirculation: such a trend is compatible with the observations (see fig.6.23) that correspond to quite low velocities (less than 0.05m/s). Note that in a homogeneous situation the gas backflow would occur in between clusters, and thus, it should be detectable through concentration conditioning. Unfortunately, no statistics on particle velocity distribution in voids are reported in Aliseda et al.[1].

Thus, the meaning of $V_{physical}$ is quite different depending on the scenario selected. In the inhomogeneous case, $V_{physical}$ is a measure of the air entrainment and of the global induced recirculation. Consequently, it is preferable to subtract it from the vertical velocity measurements to properly evaluate the change in the settling velocity of particles. In the homogeneous case, $V_{physical}$ is a measure of the net gas

velocity as it results from a balance between downward and upward gas entrainment by the clusters and the voids present in the flow. In that situation, the vertical velocity measurements need no corrections. Transverse explorations and exploration of lower volume fractions are therefore highly recommended in order to discriminate between the two scenarii and to produce fully reliable data. Note that a break down of our PDI system precluded us to perform these tests as well as to explore the space of parameters further.

6.7.2 Velocity of clusters $V_{clusters}$

We have seen in the previous section that although clusters are formed in our experimental conditions, the settling velocity is not affected by the local concentration but only varies with the particle size. Hence, and contrary to Aliseda et al. findings, the presence of clusters does not modify the settling velocity, that is collective effects are either absent or weak. The question is why is there such a difference in the observed dynamics between these two experiments?

As a starting point, let us first set aside collective effects from the discussion. The turbulent Reynolds number (Re_λ) was 75 in Aliseda et al. to be compared with 180-190 in the present work. Owing to a much larger dissipation rate (see table 6.9), the Fr was significantly higher, about 2.3 against 0.94 here. The fluctuation in acceleration $\gamma\prime$ were therefore 2 times higher in Aliseda et al. than in the present work, leading to a reduced role of gravity in the former conditions. This is most probably the reason why, for a given Ro (which is almost equivalent to considering the same drop size as the velocity fluctuations $U\prime$ are close in the two experiments), no hindering was observed in Aliseda et al. while it does happen here (see fig.6.25). In other words, the loitering effect was weaker (or possibly negligible) in Aliseda et al.'s flow conditions, while it is strong in the present experiment: this comparison clearly illustrates the central role of the fluid acceleration on the magnitude of the loitering effect

To be more quantitative let us compare the data from each experiment at $Ro = 0.25$ and for comparable volume fractions ϕ_v (see data from Aliseda et al. at $\phi_v = 1.5 \times 10^{-5}$ and present experiments at $\phi_v = 1$ or 2×10^{-5} in fig.6.26). The velocity fluctuations $U\prime$ being about 0.3 m/s and 0.2 m/s in Aliseda et al. and in the present work respectively, that value of the Ro corresponds to similar drop sizes (41 μm and 59 μm respectively). At the same time, the St for such drops is smaller in the present experiments than in Aliseda et al. ($St = 0.94$ versus $St = 1.4$ respectively) mainly because of the change in the Kolmogorov time scale τ_η. Hence,

the filtering effect should be weaker in the present experiments than in Aliseda et al., and with preferential concentration in action the velocity enhancement should therefore be higher in the present conditions. What is observed is the opposite, that means that the loitering mechanism is already in action at $Ro = 0.25$ in our flow conditions and not in Aliseda et al. (since loitering is the only known mechanism able to diminish the magnitude of the velocity enhancement built up by the preferential sweeping scenario.) Moreover, as the Ro is fixed, the loitering happens to be much stronger in the present flow conditions because of a smaller St that made the particles more responsive to velocity fluctuations, and possibly also to acceleration fluctuations as discussed in Section 2.3.1.2) encountered along their trajectory than in Aliseda et al.'s flow conditions. This analysis put in evidence the impact of the Fr (combined with the Re_λ, see eq.6.16) that controls the ratio St/Ro. Indeed, from eq.6.16, $\frac{St}{Ro} = Fr \times \frac{{Re_L}^{\frac{1}{4}}}{{a_0}^{\frac{1}{2}}}$: that ratio is about 2.6 for Aliseda et al. flow conditions while it is about 4 in the present experiments.

According to the above discussion, two comments can be added.

First, as loitering is active at $Ro = 0.25$, it is then active for all larger sizes (larger Ro). As loitering gains in magnitude when increasing the terminal velocity, it counteracts the velocity enhancement due to preferential sweeping and leads, for large enough particles, to the hindering of the settling velocity (i.e. $V - V_{St} < 0$).

Second, this is not to say that loitering was absent in Aliseda et al.'s experiments but at least, that its magnitude was lower than in our flow conditions or that its onset in terms of Ro was delayed (this has been discussed in Section 6.5.3). In this regard, let us recall that drops were at most 60 μm in diameter in Aliseda et al experiments to be compared to about 300 μm here. Hence, the maximum Ro was limited to nearly one in Aliseda et al experiments, while we gather data up to $Ro \sim 9$. Since nearly all curves in fig.6.26 become more or less parallel at large Ro (> 0.5), it is possible that if larger particles have been present in Aliseda et al. experiment, velocity hindering may have been observed as well for these larger drops. By extrapolating the slopes, this may have occurred at Ro slightly less than 1.5, which is a magnitude comparable to those observed in the other two experiments.

So far, the above reasoning has not accounted for any collective effects. Let us recall that in Aliseda et al., the velocity enhancement was in part attributed to the presence of dense clusters whose fall velocity as a pseudo-particle was shown to be well approximated by eq.6.7.2 (see Section 2). The presence of clusters could therefore affect the settling velocity of particles in the following way. A particle of size D will acquire the cluster velocity in addition to its terminal velocity when captured (for some time) by a cluster of size l_c and concentration C_c. Hence, the mean fall

velocity of a particle of size D could be tentatively written:

$$V(D) = V_{St}(D) + \Delta V_{turb}(D) + \frac{\int_{C_c}\int_{l_c} P(D, C_c, l_c)\ V_{meso-scale}(C_c, l_c)\ dC_c\ dl_c}{\int_{C_c}\int_{l_c} P(D, C_c, l_c)\ dC_c\ dl_c} \quad (6.32)$$

In eq. 6.32, V_{St} represents the terminal velocity while $\Delta V_{turb}(D)$ represents the change in the settling velocity due to an isolated particle interacting with eddies as discussed in the fast track and loitering scenarii. The last term represents a contribution to velocity due to some extra mechanism at meso-scale, such as collective effects arising in presence of significant clustering. $P(D, C_c, l_c)$ denotes the probability to find a particle of size D in a zone of concentration C_c and of characteristic size l_c, and therefore, it accounts for size segregation if any, as well as for the partitioning of particles between voids, clusters and intermediate regions. The integral is achieved over all realizations in terms of concentration and size, which are the two parameters used to characterize voids, clusters and intermediate regions. That expression is adapted to the use of the cluster velocity given by eq. (that is $V_{meso-scale} = V_{cluster}$ in that case), but it also applies to any local concentration level including void zones and intermediate regions. For intermediate regions, the particles are nearly uniformly distributed in space as shown by Voronoii pdfs, and we do not expect any collective effect, that is $V_{intermediate}(D, C_c, l_c) \sim 0$. For the voids, some effect could be present. In particular, assuming an homogeneous repartition of clusters in the space (see the discussion in 6.7.1), if the clusters increase the settling velocity, the conservation of flux requires void zones to have an upward motion relative to cluster movement, and the latter must be accounted for. In the above formulation, the change in settling velocity can be therefore due to isolated particles interacting with eddies, to collective effects or to both mechanisms.

According to that simplistic model, we can identify three potential sources of differences from one experiment to another concerning the impact of collective effects:

- a strong size segregation between clusters, voids and intermediate regions, in which case $P(D, C_c, l_c)$ strongly depends on C_c and l_c.
- different repartitions of the particles between clusters, voids and intermediate regions, expressed through a strong dependence of $P(D, C_c, l_c)$ on C_c and l_c.
- different clusters and void characteristics (C_c, l_c) that would lead to different cluster and void meso-scale velocities.

The size segregation has been shown to be weak in both experiments (that is $P(D, C_c, l_c)$ is nearly independent on D), and thus, it cannot be retained as a plausible origin of the observed difference.

Concerning the partition of droplets, we have seen that the clusters defined from Voronoi tessellations correspond to local concentrations higher than 1.6 (in 2D) or 2.2 (in 1D) times the mean volume concentration. In average, the percentage of particles trapped in clusters is comprised between 24 to 37% in the 1D analysis (that proportion was not measured in 2D because we used an intensity renormalization technique see Chapter 4). In Aliseda et al.[1], the proportion of particles stored in regions with a local concentration above $2.2C_0$ was about 15% (39% for local concentration above $1.6C_0$). These figures are quite close in both experiments. Voids defined in 1D amount for 9% of all particles acquired. We do not have the data for the void and the intermediate regions from the experiments of Aliseda et al. The only data available is the fraction of particles in region of concentration higher than $1.1C_0$ and less than $2.2C_0$ which represents about 50%. From 1D Voronoï analysis, the intermediate region extends from $\frac{C}{C_0} = 0.38 - 0.42$ to $2 - 2.7$ and amounts for 56 to 69% of the particles (see table 6.12). Again, the figures from the two experiments are similar. Therefore, the partitioning can be said to be nearly the same in both flow conditions, and it cannot be at the origin of the observed difference.

The third argument to be considered concerns the magnitude of the meso-scale velocities $V_{meso-scale}(C_c, l_c)$. The data we have from Aliseda et al. concerns the meso-scale velocity within clusters. $V_{cluster}$ has been estimated in Section 6.6.4 using the phenomenological model proposed by Aliseda et al., and it ranges from 0.016 to 0.09 m/s in our flow conditions. These magnitudes are similar to those detected in Aliseda et al.'s experiments (where $V_{cluster}$ evolved between 0.06 and 0.09 m/s). This is not too surprising since the clusters characteristics in terms of length and concentration of particles within are not that different. Hence, the difference between the two experiments does not seem to stay on the cluster velocity. There could also be a difference in the dynamics of voids, especially if a homogeneous flow organization as discussed in the previous section was at play in Aliseda et al. experiments. As we do not have velocity statistics in voids for Aliseda et al. experiments, it is difficult to compare with our results and to draw any definite conclusion. Note that an issue that remains open in our experiments is that some of the estimates of $V_{cluster}$ are within the resolution of the measuring system, and yet no significant variation of the particle velocity when conditioned by the local concentration has been detected, implying that $V_{meso-scale}(C_c, l_c)$ is close to zero (see Section 6.6.3).

From the above discussion, it happens that the particle velocity modification

in our experiments relies mainly on the ΔV_{turb} term more than on some collective dynamics. As the maxima in velocity enhancement are much weaker here than in Aliseda et al. experiments, it is probable that the loitering effect is much stronger here, and that it overwhelms quickly the velocity change due to collective dynamics (if any). Also, the loitering effect starts to be active at much lower Rouse numbers possibly as low as $Ro \sim 0.1$. This trend is consistent with the limits between enhancement and hindering discussed in Section 2.4.1. Finally, the loitering effect seems poorly sensitive to the presence of clusters, notably as the largest particles experience large velocity change (up to $0.6U\prime$, see fig.6.19) compared with the expected clusters velocity (which is at most $\sim 0.2U\prime$). The above comment seems to be a plausible explanation why clusters do not affect much the settling speed in our flow conditions. It is therefore expected that the clusters would play a more significant role if loitering is not so strong, that is when velocity fluctuations overrun V_{St} (smaller Ro number).

According to the above discussion, collective dynamics may become more important at larger Fr numbers where gravity is less important. Indeed, we see a signature of collective effects in some of the data provided by PTV measuring campaign (see Chapter 5). The difference in velocity between clusters and voids becomes larger with increasing Re_λ, and hence, increasing Fr. However, to further test this idea and to identify the conditions for which clusters start to affect the settling velocity, it is necessary to conduct more studies investigating the velocity conditioned by the local concentration at higher turbulent Re_λ numbers using PDI. In particular, it would be necessary to test if the cluster velocity will evolve as $\overline{C}l^2$ as in Aliseda et al.[1]. We have seen that the cluster size increases with Re_λ but data are lacking concerning the behaviour of the mean cluster concentration with Re_λ.

6.8 Conclusion

We have analyzed the settling velocity of sub-Kolmogorov inertial particles using PDI measurements performed at a fixed $Re_\lambda = 180$ and for a volume fraction ϕ_v varying from 0.5×10^{-5} to 2.0×10^{-5}.

After having corrected the raw velocity data for the alignment issue, a remaining offset velocity $V_{physical}$ has been identified that growths with the volume fraction ϕ_v. We have suggested two scenarii for the origin of this offset. In one scenario, an

homogeneous repartition of clusters and voids regions over the whole channel cross-section is considered: in that case, $V_{physical}$ is mainly due to air entrainment induced by collective effects as discussed in Aliseda et al [1]. In the alternative scenario, we hypothesized an inhomogeneous repartition of clusters and voids that would lead to a vertical secondary recirculation in the channel cross-section because of the confinement by lateral walls. In that case, $V_{physical}$ would result both from collective effects and from that recirculation. Ideally, the contribution from that secondary recirculation is not to be accounted for when analyzing the settling velocity modification. In both scenarii, $V_{physical}$ is expected to increase with the volume concentration, in agreement with experimental evidence. Therefore, more information is needed to discriminate between the two scenarii and also to evaluate the relative importance of the recirculation if any. Luckily, the presence of this offset $V_{physical}$ does not alter the main conclusions which are presented hereafter.

We have first clearly shown that, in the present flow conditions, the settling velocity experiences either enhancement or hindering depending on the size of the particle considered. The enhancement effect could be attributed to the preferential sweeping mechanism, while the hindering is most probably due to loitering as it manifests itself for large particles corresponding to significant Ro numbers. With the data recently published by Good et al.[31], this is the second experimental evidence that hindering indeed occurs for dense particles in a nearly homogeneous isotropic turbulence background. Besides, we observed very significant settling velocity reductions with $V - V_{St}$ about $-0.5U\prime$ ($-0.6U\prime$ when accounting for $V_{physical}$) or $-0.21\ V_{St}$ ($-0.22V_{St}$ when accounting for $V_{physical}$) for a Rouse number about 1.7.

Clusters were identified in our flow conditions using a 1D Voronoï analysis of the arrival time of droplets as delivered by the PDI. Results are comparable with the 2D Voronoï analysis performed from images (see Chapter 4) except for void regions that were found to be significantly longer. In particular, we found that one third of the particles are located within clusters, and we obtained some estimations of the mean concentration in clusters ($\frac{\overline{C}}{C_0} \approx 4.6$ to 5.2) and in voids ($\frac{\overline{C}}{C_0} \approx 0.27 - 0.29$).

Using statistics conditioned by the local concentration, we observed a marginal size segregation between clusters, voids and intermediate regions. Surprisingly, and contrary to Aliseda et al. [1] findings, we didn't found any mark of collective effects as the settling velocity conditioned by the local concentration does not change with the local concentration. This result holds for all particles, i.e. whatever the Stokes number ranging from 0.03 to 2.7.

Moreover, by analysing available experimental data for sub-Kolmogorov and very dense particles ($\frac{\rho_p}{\rho_f} > 900$), we identified the onset of hindering, which also marks the

onset of loitering. The boundary is given as a critical Rouse number that increases first with $Fr = \frac{\gamma'}{g}$ from 0.3 to 1 and then remains stable at a value close to 1 for Fr above ≈ 2.

We also discuss the relevant velocity scale for the observed velocity modification $V - V_{St}$. The commonly used velocity fluctuation $U\prime$ or Kolmogorov velocity are clearly not adapted. We tried to built velocity scales based on the fluid acceleration considering either a fluid time scale or a particle time scale: both attempts lead to an independent collapse of each data series but were unable to gather the results acquired in different experimental conditions.

We have also tried two scalings proposed for the enhancement of the settling velocity by Bec at al [7] and by Rosa et al.[63]. Our range of acceptable St numbers is out of validity of Bec et al.'s [7] proposition, and no collapse of the experimental data takes place. Quite large scatter of the experimental data is obtained with the scaling law for the settling velocity proposed by Rosa et al.[63].

We also considered a scaling inspired from Nielsen proposition and observed a pretty good collapse of all curves, except for one serie from Good et al. Overall, for Rouse numbers above about 0.5 corresponding thus to a significant loitering mechanism, the trend is close to $\frac{\Delta V}{V_{St}} \approx -kFr^2(Ro - Ro_{critical})$, with a slope k slightly varying with flow conditions. That finding indicates that both the velocity fluctuations and the standard deviation of the fluid acceleration control the magnitude of the change in the settling velocity. That proposition needs to be confirmed over an enlarged parameter space. Besides, it does not capture the maximum enhancement which possibly arises from the competition between preferential sweeping and loitering.

Finally, we advance some explanations as why the clusters, although present in our flow conditions, do not affect much the measured settling velocity. We have assumed that the velocity of a particle will consist of its terminal velocity V_{St}, of ΔV_{turb} the settling velocity change due to particle interacting with eddies leading to the fast track and the loitering scenarii, and of the velocity imposed due to some extra mechanism at meso-scale such as collective effect arising in the presence of significant clustering. We have seen that comparing our data to the data of Aliseda et al.[1] (a dataset which contains similar to our estimations of the clusters length and their velocity) where the strong enhancement of the settling velocity with the increasing volume fraction due to presence of clustering has been identified, we do not witness any velocity difference between clusters and voids in our experiment. This suggests that the only term responsible for such a difference between two experiments to occur is the change of the velocity ΔV_{turb} due to loitering, which is

activated at much lower Ro in our experimental conditions than in those of Aliseda at al.[1]. It is necessary to point out that ΔV_{turb} changes sign past critical Ro number in our experiment due to loitering effect, whereas in Aliseda et al. experiments it remains positive at the same Ro. Moreover, the magnitude of ΔV_{turb} could be to up to $0.5U\prime$ (when not corrected for $V_{physical}$) at $Ro = 1.7$ which is much greater than the velocity of clusters estimated at most as $0.2U\prime$. Hence, the largest particles which are subject to loitering do not seem to be affected by the presence of clusters, possibly because their settling speed neatly exceeds that of clusters, so that their dynamics only result from their interaction with turbulent eddies.

According to this explanation, since loitering is stronger when the terminal velocity due to gravity dominates over turbulent velocity fluctuations, the impact collective effects may be reduced in the presence of higher Fr leading to higher Re_λ. Yet, we do not have fully investigated how the cluster velocity evolves when varying Fr or Re_λ. Yet, from PTV data, we have identified a significant increase (by a factor 2.6) of the difference between clusters and voids velocity as Re_λ increases from 200 to 450, and that increase could be tentatively attributed to collective effects. Therefore, the outcome of the competition between loitering and collective effets is not easy to predict and deserves to be analysed further.

Another possibility which could affect $V_{settling}$ is the time life of clusters and voids. If clusters live over a long time, the velocity of particles trapped in the cluster would be enhanced due to the acquired velocity of the cluster. However, if such an existence of the clusters is short, the particle would not acquire any additional velocity and the magnitude of its settling velocity would depend solely on the particle-flow interaction i.e. on the mechanisms of enhancement or hindering. Answering this question would require extra experiments and also different measuring campaigns.

Chapter 7

Conclusion

This thesis attempted to answer some of the open questions related to the clustering and to the settling velocity of heavy sub-Kolmogorov particles in homogeneous isotropic turbulent flows. In particular, our goal was to analyze:

- how the clustering characteristics evolve when varying the turbulence in the carrier flow, the inertia of particles and/or global volume loading ?
- what settling velocity modifications are to be expected according to flow conditions as litterature indicates that enhancement as well as hindering could possibly happen but there is no clear answer as to where is the frontier between these two behaviors and what are the parameters they depend on?
- and what are the parameters controlling the magnitude of settling velocity modifications?

To address these questions, we undertook experiments in a wind tunnel equipped with an active grid that provides turbulent fluctuations up to 15% and injecting water droplets just downstream that grid. All particle-laden flows considered correspond to very large density ratio $\frac{\rho_p}{\rho_f} >> 1$ and to sub-Kolmogorov droplets $\frac{D}{\eta} < 1$. These flows are expected to be driven by five non-dimensional and independent numbers, namely Re_λ representing the background turbulence, the volume fraction ϕ_v, the density ratio $\frac{\rho_p}{\rho_f}$, the St number accounting for particle inertia, the Ro number incorporating gravitational settling to which one should add the size distribution $P\left(\frac{D}{D_{10}}\right)$ since injected droplets are most of the time not monodispersed. In practice, we explored the experimental space from $Re_\lambda = 175$ up to $Re_\lambda = 450$. The volume fraction ϕ_v was varied from 0.2×10^{-5} to 2×10^{-5}: the corresponding mass loading were low enough to avoid any significant turbulence modulation by the dispersed phase. We also change the size of the injectors allowing some change in the drop size distribution. Overall, the resulting range in terms of St was from 0.1 to 5.0 and it was from 0.02 to 0.11 for the Ro number. Typical standard deviations on size

were around 31%.

During the PTV campaign we considered 19 flow conditions to explore the parameter space. For each of these conditions, 20 movies of 8500 images were acquired resulting in statistics from 85 million to 340 million particles per experimental run depending on flow conditions. Clustering characteristics were determined using a Voronoii analysis. In addition, Lagrangian tracking provided some estimates of the dynamical properties of clusters and voids. A PDI campain was also undertook in order to retrive joint size-velocity statistics, with typically about a million of particles detected per experimental condition. That campaign was achieved for a fixed Re_λ and for varying volume fraction ϕ_v four folds from $0.2 \times 10^{-5} - 2 \times 10^{-5}$.

Concerning **clustering**, the level of clustering was characterized by the standard deviation of Voronoï aera pdf as it is now classicaly done in the litterature (Chapter 4). We have shown that the standard deviation of Voronoï area PDF is mainly a measure of voids and that it increases with both Re_λ and ϕ_v according to:

$$\sigma_{rel} = \frac{\sigma_\mathcal{V} - \sigma_\mathcal{V}^{RPP}}{\sigma_\mathcal{V}^{RPP}} \simeq 2St^{0.0} Re_\lambda^{0.88} \phi_v^{0.5}. \tag{7.1}$$

Similarly, the average length scale of clusters $\frac{\sqrt{\langle A_c \rangle}}{\eta}$ and of voids $\frac{\sqrt{\langle A_v \rangle}}{\eta}$ are increasing with the same parameters according to the following trends:

$$\frac{\sqrt{\langle A_c \rangle}}{\eta} = 0.05 \cdot St^{-0.2} Re_\lambda^{4.4} \phi_v^{1.6} \tag{7.2}$$

$$\frac{\sqrt{\langle A_v \rangle}}{\eta} = 0.45 \cdot St^{-0.09} Re_\lambda^{3.6} \phi_v^{1.3}. \tag{7.3}$$

In particular, it is noticeable that the average length of clusters evolves from about 5η at $Re_\lambda = 175$ up to 80η at $Re_\lambda = 450$. The mean size of voids is typically ten times larger than that of clusters.

In all the above scalings for σ_{rel} and $\frac{\sqrt{\langle A_c \rangle}}{\eta}$ and $\frac{\sqrt{\langle A_v \rangle}}{\eta}$, the **dominant role is attributed to** Re_λ. This means that the clustering characteristics are mainly driven by the carrier flow turbulence which is consistent with the assumption that the turbulent structures are the ones responsible for the formation of clusters.

The weak dependence of the clustering characteristics on the Stokes number suggests a "sweep-stick" clustering mechanism. In a broader framework, this finding also supports the necessity to distinguish between small scale mechanisms of clustering and multi-scale mechanisms [33].

The neat dependency of clustering on the particle volume fraction ϕ_v is very likely reminiscent of collective effects. We have to mention that we did not try to scale these characteristics of the clustering with *Ro* number because we assumed that the *Ro* will affect mainly settling velocity whereas *St* would greatly affect the clustering. The absence of *St* dependency implies also no dependency on *Ro* as they are both built on the particle response times.

If the sweep-stick mechanism is driving the cluster formation, any volume fraction influence is not captured in that picture. A possible scenario could rely on collective effects which are known to lead to denser regions sinking in the mixture with an enhanced settling velocity. Such denser regions could thus collect extra particles during their motion relative to the fluid, and therefore built up clusters of higher concentration and/or larger size. Such a process would be clearly favored at higher volume fractions. In this scenario, the sweep-stick mechanism will act as the trigger of cluster formation, with subsequent growth driven by the collective dynamics. Another alternative view is that the presence of clusters modifies the local turbulent structure and favors the multiplication of sticking points in the flow (note that at the largest concentrations in clusters, the mass loading exceeds 0.1 and can even become close to unity): more particles could then either *activate* more zero acceleration points or help bring new particles in the sticking region. These scenarios, hypothetical as they are, may serve for planing new experiments to help understand how collective effects become efficient in clustering. Clearly, an investigation of the effect of dispersed phase volume fraction on the micro scale mechanism for accumulation of particles would be worth undertaking. In the same perspective, it would be worthwile to finely quantify how the concentration in clusters (and in voids) evolves notably when changing the volume loading and the Reynolds number. Very few data are available on that aspect, and their collection is not an easy task if one wants to get rid of any measurement bias.

The settling velocity of inertial particles has also been investigated for a constant $Re_\lambda = 180$ and varying volume fraction by a factor of 4 from $\phi_v = 0.5 \times 10^{-5}$ to $\phi_v = 2.0 \times 10^{-5}$. In all these experiments, the settling velocity happens to exhibit **enhancement** or **hindering** depending on particle size. More precisely, enhancement occurs below a critical *Ro* number while hindering happens above indicating that loitering is most probably at the origin of the observed decrease in the settling velocity. This is the second experimental data serie exhibiting hindering for water drops in a turbulent air flow. The observed hindering was especially strong with velocity differences $\Delta V = V - V_{St}$ up to $-0.6U\prime$ or $-0.2V_{St}$.

To evaluate the contributions of collective effects, we have analysed the settling

velocity conditioned by the local concentration field. No differences between the velocity of the clusters or voids could be detected in our case as opposed to the flow conditions considered by Aliseda et al.[1]. In an attempt to explain the origin of such a difference, we considered that the velocity of each particle is the sum of its terminal velocity, of the velocity modification ΔV_{turb} caused by an « isolated » particle interacting with turbulence settling mechanism (leading to settling velocity enhancement $\Delta V_{turb}(D) > 0$ when the particle is experiencing preferential sweeping, and to velocity hindering $\Delta V_{turb}(D) < 0$ when loitering takes place), and of a contribution of a meso-scale , $V_{meso-scale} = V_{clusters}$ which is assumed to be the clusters velocity due to collective effects. The reason why we do not find the same results consistent with the study conducted by Aliseda et al.[1] could be due to stronger loitering effect taking place in our study and not manifesting itself strong in the study of [1]. Thus, we suppose that the collective effects would become stronger when the loitering is delayed or suppressed completely due to higher influence of turbulence over gravity. Indeed, such a signature of collective effects at higher Re_λ has been seen in some of the PTV data.

We compared the settling velocity data of the present study with the data available from previous experiments by Aliseda et al. [1], Good et al. [31], Yand and Shy [77]. We have first identified the quantity $V_{physical}$ evolving with the volume fraction ϕ_v. The emergence of such a quantity with increasing ϕ_v has been previously seen by Aliseda et al.[1]. Two scenarii have been suggested responsible for $V_{physical}$:

- one, assuming an homogeneous repartition of clusters and voids all over the channel cross section, where $V_{physical}$ is then a measure of the velocity of clusters,
- second one, hypothetising the formation of a secondary motion in the form of a vertical recirculation in the channel cross section, where $V_{physical}$ becomes a measure of the recirculation velocity in addition to the contribution of the velocity of clusters.

However, we were not able to answer which scenario dominates in our case, and to which degree the effect of confinement is stronger compared to that of collective effects. An exploration along the transverse direction of the wind-tunnel would help getting an undisputable answer.

Next, we have seen that the change in settling velocity when scaled with $U\prime$ exhibits both enhancement and hindering. This led us to investigate the possible scalings for enhancement of settling velocity proposed by Bec et al.[7], Rosa et al.[63].

The scaling proposed by Bec et al.[7] was out of the available scope necessary for the scaling to work. The scaling of settling velocity proposed by Rosa et al. showed a large scatter of the experimental data involved.

A scaling of the velocity change versus the ratio of the standard deviation of the fluid acceleration fluctuations over gravity $\frac{\Delta V}{V_{St}} \approx -kFr^2(Ro - Ro_{critical})$ and inspired from Nielsen happens to gather pretty well most of the available experimental data. That result indicates that the fluctuations of the fluid velocity and of the fluid acceleration control the magnitude of the change in the settling velocity when loitering is active. Although encouraging, that proposition needs to be confirmed over an enlarged range of parameter, and also to be completed as it does not capture the maximum enhancement that is possibly controlled by the competition between preferential sweeping and loitering.

We also attempted to determine the **onset of velocity enhancement** using available experimental St, Ro and Fr space. We concluded that velocity enhancement occurs when the Rouse number exceeds a critical Ro number $Ro_{critical}$ close to unity. At small Fr the hindering of settling velocity happens at smaller Ro indicating that the loitering is the strongest when gravity is stronger than the rms acceleration of the fluid. The larger is the Fr, the further the onset of hindering moves with respect to Ro. The collective effects are expected to manifest themselves stronger at the higher Fr or higher Re_λ due to delay of the loitering or its possible suppression. This is a very important result meaning that more experiments would need to be conducted to define the proper evolution of the enhancement and hindering of the settling velocity with parameters such St, Ro and Fr. There is a need to perform additional DNS on the onset of loitering and to understand why the present DNS done by Good et al.[31] and Rosa et al.[63] do not agree with each other.

In terms of perspectives, and in addition to those already evoked here above, some extensions of these work deserved to be considered. It is first necessary to conduct more studies with PDI or PTV covering a broader range of parameters, in order to identify the regimes for which the clusters start affecting the settling velocity of particles. That would require a carefull determination of alignment offsets when increasing Re_λ to properly remove any bias on absolute velocity measurements In the same perspective, an estimation of the lifetime of clusters and voids may reveal additional effects on the settling velocity.

The question of the origin of $V_{physical}$ needs to be addressed in future studies because it is important to know which of the proposed two scenarii is present in order to properly interpret the raw velocity data. A precise quantification is required to

determine whether $V_{physical}$ is completely or partially driven by some possible secondary flow depending on experimental conditions.

The exploration of an enlarged parameter space is also required to determine without any ambiguity the repartition of particles between clusters, voids and intermediate regions change with flow conditions (and if so how it change with parameters). In the same perspective, additional measurements at higher Re_λ and ϕ_v would provide relevant data concerning particle size segregation (if any) depending on the type of structures these particles end in, and their possible impact. Aside cluster dimensions, reliable measurements of the concentration in clusters are also required, notably to test the existing phenomenological model of cluster velocity on an enlarged set of flow conditions. This again necessitates strong precautions to avoid any bias in the measurements.

Finally, the scalings of the settling velocity should be sought to be clarified further since in this work we have seen that the settling velocity does not scale only with $U\prime$, but that the strength of the rms of acceleration flow field is also an important parameter to consider.

References

[1] A Aliseda et al. “Effect of preferential concentration on the settling velocity of heavy particles in homogeneous isotropic turbulence”. In: *Journal of Fluid Mechanics* 468 (2002), pp. 77–105. DOI: 10.1017/S0022112002001593. URL: http://journals.cambridge.org/article%7B%5C_%7DS0022112002001593.

[2] WD Bachalo and SV Sankar. “Analysis of the light scattering interferometry for spheres larger than the light wavelength”. In: *4th International Symposium on Applications of Laser Anemometry to Fluid Mechanics*. Vol. 1. 1988, p. 1.

[3] William D Bachalo. “Method for measuring the size and velocity of spheres by dual-beam light-scatter interferometry”. In: *Applied Optics* 19.3 (1980), pp. 363–370.

[4] S Balachandar and John K Eaton. “Turbulent dispersed multiphase flow”. In: *Annual Review of Fluid Mechanics* 42 (2010), pp. 111–133.

[5] Alfred Barnard Basset. *A treatise on hydrodynamics*. Vol. 2. Deighton, Bell and Co., 1888.

[6] Jérémie Bec and Raphaël Chétrite. “Toward a phenomenological approach to the clustering of heavy particles in turbulent flows”. In: *New Journal of Physics* 9.3 (2007), p. 77.

[7] Jérémie Bec, Holger Homann, and Samriddhi Sankar Ray. “Gravity-driven enhancement of heavy particle clustering in turbulent flow”. In: *Physical review letters* 112.18 (2014), p. 184501.

[8] Jeremie Bec et al. “Acceleration statistics of heavy particles in turbulence”. In: *Journal of Fluid Mechanics* 550 (Mar. 2006), pp. 349–358. ISSN: 0022-1120. DOI: 10.1017/S002211200500844X.

[9] Jeremie Bec et al. “Heavy particle concentration in turbulence at dissipative and inertial scales”. In: *Physical Review Letters* 98.8 (2007), p. 84502. ISSN: 0031-9007. DOI: 10.1103/PhysRevLett.98.084502. URL: doi:10.1103/PhysRevLett.98.084502.

[10] G Boffetta, F De Lillo, and A Gamba. “Large scale inhomogeneity of inertial particles in turbulent flows”. In: *PHYSICS OF FLUIDS* 16.4 (2004), pp. L20–L23. ISSN: 1070-6631. DOI: 10.1063/1.1667807.

[11] Thorsten Bosse, Leonhard Kleiser, and Eckart Meiburg. “Small particles in homogeneous turbulence: Settling velocity enhancement by two-way coupling”. In: *Physics of Fluids* 18 (2006), p. 27102.

[12] Thorsten Bosse, Leonhard Kleiser, and Eckart Meiburg. “Small particles in homogeneous turbulence: Settling velocity enhancement by two-way coupling”. In: *Physics of Fluids (1994-present)* 18.2 (2006), p. 027102.

[13] Joseph Boussinesq. *Th{é}orie analytique de la chaleur: mise en harmonie avec la thermodynamique et avec la th{é}orie m{é}canique de la lumi{è}re*. Vol. 2. Gauthier-Villars, 1903.

[14] CC Chan and JCH Fung. “The change in settling velocity of inertial particles in cellular flow”. In: *Fluid dynamics research* 25.5 (1999), pp. 257–273.

[15] L Chen, S Goto, and J C Vassilicos. “Turbulent clustering of stagnation points and inertial particles”. In: *Journal of Fluid Mechanics* 553 (2006), pp. 143–154. ISSN: 0022-1120. DOI: 10.1017/S0022112006009177.

[16] Roland Clift, John R Grace, and Martin E Weber. *Bubbles, drops, and particles*. Courier Corporation, 2005.

[17] S W Coleman and J C Vassilicos. “A unified sweep-stick mechanism to explain particle clustering in two- and three-dimensional homogeneous, isotropic turbulence”. In: *Physics of Fluids* 21.11 (Nov. 2009), p. 113301. ISSN: 1070-6631. DOI: DOI10.1063/1.3257638.

[18] G. T. Csanady. “Turbulent Diffusion of Heavy Particles in the Atmosphere”. In: *Journal of the Atmospheric Sciences* 20 (1963), pp. 201–208. ISSN: 0022-4928. DOI: 10.1175/1520-0469(1963)020<0201:TDOHPI>2.0.CO;2.

[19] Javier Davila and Julian CR Hunt. “Settling of small particles near vortices and in turbulence”. In: *Journal of Fluid Mechanics* 440 (2001), pp. 117–145.

[20] A Dejoan and R Monchaux. “Preferential concentration and settling of heavy particles in homogeneous turbulence”. In: *Physics of Fluids (1994-present)* 25.1 (2013), p. 013301.

[21] T.\ Doychev and M.\ Uhlmann. "A numerical study of finite size particles in homogeneous turbulent flow". In: *ICMF 2010*. Ed. by S.\ Balachandar and J.\ Sinclair Curtis. Proc.\ 7th Int.\ Conf.\ Multiphase Flow. Tampa, USA: CDROM, 2010.

[22] I Eames and MA Gilbertson. "The settling and dispersion of small dense particles by spherical vortices". In: *Journal of Fluid Mechanics* 498 (2004), pp. 183–203.

[23] Jarai-Szabo Ferenc and Zoltan Neda. "On the size distribution of Poisson Voronoi cells". In: *Physica A-Statistical Mechanics and Its Applications* 385.2 (2007), pp. 518–526. DOI: 10.1016/j.physa.2007.07.063. URL: http://www.sciencedirect.com/science/article/pii/S0378437107007546.

[24] Jr Fessler, Jd Kulick, and Jk Eaton. "Preferential Concentration Of Heavy-Particles In A Turbulent Channel Flow". In: *Physics of Fluids* 6.11 (1994), pp. 3742–3749. DOI: 10.1063/1.868445. URL: http://scitation.aip.org/content/aip/journal/pof2/6/11/10.1063/1.868445.

[25] Pierre Fevrier, Olivier Simonin, and Kyle D Squires. "Partitioning of particle velocities in gas–solid turbulent flows into a continuous field and a spatially uncorrelated random distribution: theoretical formalism and numerical study". In: *Journal of Fluid Mechanics* 533 (2005), pp. 1–46.

[26] L Fiabane et al. "Clustering of finite-size particles in turbulence". In: *Physical Review E* 86.3 (2012), p. 35301. URL: http://pre.aps.org/abstract/PRE/v86/i3/e035301.

[27] Charmaine N Franklin, Paul A Vaillancourt, and M K Yau. "Statistics and parameterizations of the effect of turbulence on the geometric collision kernel of cloud droplets". In: *JOURNAL OF THE ATMOSPHERIC SCIENCES* 64.3 (Mar. 2007), pp. 938–954. ISSN: 0022-4928. DOI: 10.1175/JAS3872.1.

[28] P D Friedman and J Katz. "Mean rise of droplets in isotropic turbulence". In: *Physics of Fluids* 14.9 (2002), pp. 3059–3073.

[29] Jimmy Chi Hung Fung. "Gravitational settling of particles and bubbles in homogeneous turbulence". In: *Journal of Geophysical Research: Oceans* 98.C11 (1993), pp. 20287–20297.

[30] Renée Gatignol. "The Faxen formulas for a rigid particle in an unsteady non-uniform Stoke flow". In: *Journal de Mécanique Théorique et Appliquée* 2.2 (1983), pp. 143–160.

[31] G. H. Good et al. “Settling regimes of inertial particles in isotropic turbulence”. English. In: *Journal of Fluid Mechanics* 759 (Oct. 2014), R3. ISSN: 0022-1120. DOI: 10.1017/jfm.2014.602. URL: http://journals.cambridge.org/abstract%7B%5C_%7DS0022112014006028.

[32] Susumu Goto and J C Vassilicos. “Self-similar clustering of inertial particles and zero-acceleration points in fully developed two-dimensional turbulence”. In: *Physics of Fluids* 18.11 (Nov. 2006), p. 115103. ISSN: 10706631. DOI: 10.1063/1.2364263. URL: http://link.aip.org/link/?PHFLE6/18/115103/1%20http://scitation.aip.org/content/aip/journal/pof2/18/11/10.1063/1.2364263.

[33] K. Gustavsson and B. Mehlig. “Statistical models for spatial patterns of heavy particles in turbulence”. In: *Advances in Physics* 65 (2016), pp. 1–57.

[34] E Hascoët and JC Vassilicos. “Turbulent clustering of inertial particles in the presence of gravity”. In: *Advances in Turbulence XI*. Springer, 2007, pp. 482–484.

[35] HW Ho. “Fall velocity of a sphere in an oscillating fluid”. PhD thesis. PhD Thesis, University of Iowa, 1964.

[36] Holger Homann and Jeremie Bec. “Finite-size effects in the dynamics of neutrally buoyant particles in turbulent flow”. In: *JOURNAL OF FLUID MECHANICS* 651 (2010), pp. 81–91. ISSN: 0022-1120. DOI: 10.1017/S0022112010000923.

[37] Paul A Hwang. “Fall velocity of particles in oscillating flow”. In: *Journal of Hydraulic Engineering* 111.3 (1985), pp. 485–502.

[38] Syunsuke Ikeda and Masashige Yamasaka. “Fall velocity of single spheres in vertically oscillating fluids”. In: *Fluid dynamics research* 5.3 (1989), p. 203.

[39] JC Lasheras, E Villermaux, and EJ Hopfinger. “Break-up and atomization of a round water jet by a high-speed annular air jet”. In: *Journal of Fluid Mechanics* 357 (1998), pp. 351–379.

[40] Chang Sik Lee and Rolf D Reitz. “Effect of liquid properties on the breakup mechanism of high-speed liquid drops”. In: *Atomization and Sprays* 11.1 (2001).

[41] Francesco Lucci, Antonino Ferrante, and Said Elghobashi. “Is Stokes number an appropriate indicator for turbulence modulation by particles of Taylor-length-scale size?” In: *Physics of Fluids* 23.2 (2011), p. 25101. DOI: DOI10.1063/1.3553279.

[42] H Makita and K Sassa. "Active turbulence generation in a laboratory wind tunnel". In: *Advances in Turbulence 3*. Springer, 1991, pp. 497–505. URL: http://link.springer.com/chapter/10.1007/978-3-642-84399-0%7B%5C_%7D54.

[43] M Maxey. "The Gravitational Settling Of Aerosol-Particles In Homogeneous Turbulence And Random Flow-Fields". In: *Journal of Fluid Mechanics* 174 (1987), pp. 441–465. DOI: 10.1017/S0022112087000193. URL: http://journals.cambridge.org/article%7B%5C_%7DS0022112087000193.

[44] Martin R Maxey and James J Riley. "Equation of motion for a small rigid sphere in a nonuniform flow". In: *Physics of Fluids* 26.4 (1983), pp. 883–889.

[45] MR t Maxey and S Corrsin. "Gravitational settling of aerosol particles in randomly oriented cellular flow fields". In: *Journal of the atmospheric sciences* 43.11 (1986), pp. 1112–1134.

[46] R Mei. "Effect of turbulence on the particle settling velocity in the nonlinear drag range". In: *International journal of multiphase flow* 20.2 (1994), pp. 273–284.

[47] R Monchaux, M Bourgoin, and A Cartellier. "Preferential concentration of heavy particles: A Voronoi analysis". In: *Physics of Fluids* 22.10 (2010), p. 103304. DOI: 10.1063/1.3489987. URL: http://scitation.aip.org/content/aip/journal/pof2/22/10/10.1063/1.3489987.

[48] R Monchaux, M Bourgoin, and A Cartellier. "Preferential concentration of heavy particles: A Voronoı analysis". In: *Phys. ˜Fluids* 22.10 (2010), p. 103304.

[49] Romain Monchaux, Mickael Bourgoin, and Alain Cartellier. "Analyzing preferential concentration and clustering of inertial particles in turbulence". In: *International Journal of Multiphase Flow* 40 (2012), pp. 1–18. ISSN: 0301-9322. DOI: 10.1016/j.ijmultiphaseflow.2011.12.001. URL: http://www.sciencedirect.com/science/article/pii/S030193221100245X.

[50] N Mordant et al. "Long time correlations in Lagrangian dynamics: a key to intermittency in turbulence". In: *Physical review letters* 89.25 (2002), p. 254502. URL: http://prl.aps.org/abstract/PRL/v89/i25/e254502.

[51] Stephen P Murray. "Settling velocities and vertical diffusion of particles in turbulent water". In: *Journal of geophysical research* 75.9 (1970), pp. 1647–1654.

[52] Laurent Mydlarski and Zellman Warhaft. "On the onset of high-Reynolds-number grid-generated wind tunnel turbulence". In: *Journal of Fluid Mechanics* 320 (1996), pp. 331–368.

[53] Peter Nielsen. *Coastal bottom boundary layers and sediment transport*. Vol. 4. World scientific, 1992.

[54] Peter Nielsen. "Turbulence Effects on the Settling of Suspended Particles". In: *Journal of Sedimentary Research* Vol. 63.5 (Sept. 1993), pp. 835–838. ISSN: 1527-1404. DOI: 10.1306/D4267C1C-2B26-11D7-8648000102C1865D. URL: http://jsedres.sepmonline.org/content/63/5/835.abstract.

[55] Martin Obligado et al. "Preferential Concentration of Heavy Particles in Turbulence". In: *Journal of Turbulence* 15.5 (2014), pp. 293–310. DOI: 10.1080/14685248.2014.897710. URL: http://www.tandfonline.com/doi/abs/10.1080/14685248.2014.897710.

[56] Martın Obligado, Alain Cartellier, and Mickaël Bourgoin. "Experimental detection of superclusters of water droplets in homogeneous isotropic turbulence". In: *EPL (Europhysics Letters)* 112.5 (2015), p. 54004. ISSN: 0295-5075. DOI: 10.1209/0295-5075/112/54004. URL: http://stacks.iop.org/0295-5075/112/i=5/a=54004?key=crossref.67fc735adc13907fa5fbd6e8f39e16a8.

[57] Carl Wilhelm Oseen. *{Ü}ber die Stoke'sche Formel und {ü}ber eine verwandte Aufgabe in der Hydrodynamik:...* Almqvist & Wiksell, 1911.

[58] Nicholas T. Ouellette. *Particle Tracking Software*. 2016. URL: http://web.stanford.edu/~nto/software_tracking.shtml (visited on 11/04/2016).

[59] *PDI-300 MD User Manual. Operation of the Phase Doppler Interferometer (PDI) For Spray Drop Size and Velocity Measurement*. Artium Technologies, Inc.

[60] R Poorte and A Biesheuvel. "Experiments on the motion of gas bubbles in turbulence generated by an active grid". In: *Journal of Fluid Mechanics* 461 (2002), pp. 127–154. ISSN: 0022-1120. DOI: 10.1017/S0022112002008273.

[61] N. M. Qureshi et al. "Acceleration statistics of inertial particles in turbulent flow". In: *European Physical Journal B* 66.4 (2008), pp. 531–536. DOI: DOI10.1140/epjb/e2008-00460-x.

[62] Nauman M. Qureshi et al. "Turbulent transport of material particles: An experimental study of finite size effects". In: *Physical Review Letters* 99.18 (2007). DOI: DOI10.1103/PhysRevLett.99.184502.

[63] Bogdan Rosa et al. “Settling velocity of small inertial particles in homogeneous isotropic turbulence from high-resolution DNS”. In: *International Journal of Multiphase Flow* 83 (2016), pp. 217–231.

[64] B L Sawford. “Reynolds number effects in Lagrangian stochastic models of tur bulent dispersion”. In: *Physics of Fluids A* 3.6 (1991), pp. 1577–1586.

[65] P-R Schöneborn. “The interaction between a single particle and an oscillating fluid”. In: *International Journal of Multiphase Flow* 2.3 (1975), pp. 307–317.

[66] K D Squires and J K Eaton. “Preferential concentration of particles by turbulence”. In: *Physics of Fluids A* 3.5 (1991), pp. 1169–1178. DOI: 10.1063/1.858045. URL: http://scitation.aip.org/content/aip/journal/pofa/3/5/10.1063/1.858045.

[67] JE Stout, SP Arya, and EL Genikhovich. “The effect of nonlinear drag on the motion and settling velocity of heavy particles”. In: *Journal of the atmospheric sciences* 52.22 (1995), pp. 3836–3848.

[68] Yoshiyuki Tagawa et al. “Three-dimensional Lagrangian Voronoı analysis for clustering of particles and bubbles in turbulence”. English. In: *Journal of Fluid Mechanics* 693 (Jan. 2012), pp. 201–215. ISSN: 0022-1120. DOI: 10.1017/jfm.2011.510. URL: http://journals.cambridge.org/abstract%7B%5C_%7DS0022112011005106.

[69] Federico Toschi and Eberhard Bodenschatz. “Lagrangian Properties of Particles in Turbulence”. In: *Annual Review of Fluid Mechanics* 41 (2009), pp. 375–404. DOI: DOI10.1146/annurev.fluid.010908.165210.

[70] EB Tunstall and G Houghton. “Retardation of falling spheres by hydrodynamic oscillations”. In: *Chemical Engineering Science* 23.9 (1968), pp. 1067–1081.

[71] Markus Uhlmann and Todor Doychev. “Sedimentation of a dilute suspension of rigid spheres at intermediate Galileo numbers: the effect of clustering upon the particle motion”. English. In: *Journal of Fluid Mechanics* 752 (July 2014), pp. 310–348. ISSN: 0022-1120. DOI: 10.1017/jfm.2014.330. URL: http://journals.cambridge.org/abstract%7B%5C_%7DS0022112014003309.

[72] Greg A Voth et al. “Measurement of particle accelerations in fully developed turbulence”. In: *Journal of Fluid Mechanics* 469 (2002), pp. 121–160.

[73] L P Wang and M R Maxey. "Settling velocity and concentration distribution of heavy particles in homogeneous isotropic turbulence". In: *J. ˜Fluid Mech.* 256 (1993), pp. 27–68.

[74] Lian-Ping Wang and David E. Stock. "Dispersion of Heavy Particles by Turbulent Motion". EN. In: *Journal of the Atmospheric Sciences* 50.13 (July 1993), pp. 1897–1913. ISSN: 0022-4928. DOI: 10.1175/1520-0469(1993)050<1897:DOHPBT>2.0.CO;2. URL: http://journals.ametsoc.org/doi/abs/10.1175/1520-0469(1993)050%7B%5C%%7D3C1897%7B%5C%%7D3ADOHPBT%7B%5C%%7D3E2.0.CO%7B%5C%%7D3B2.

[75] Haitao Xu and Eberhard Bodenschatz. "Motion of inertial particles with size larger than Kolmogorov scale in turbulent flows". In: *Physica D* 237.14-17 (2008), pp. 2095–2100. ISSN: 0167-2789. DOI: 10.1016/j.physd.2008.04.022.

[76] C. Y. Yang and U. Lei. "The role of the turbulent scales in the settling velocity of heavy particles in homogeneous isotropic turbulence". English. In: *Journal of Fluid Mechanics* 371 (Sept. 1998), pp. 179–205. ISSN: 00221120. DOI: 10.1017/S0022112098002328. URL: http://journals.cambridge.org/abstract%7B%5C_%7DS0022112098002328.

[77] T S Yang and S S Shy. "Two-way interaction between solid particles and homogeneous air turbulence: particle settling rate and turbulence modification measurements". In: *Journal of Fluid Mechanics* 526 (2005), pp. 171–216.

[78] HIROSHI YOSHIMOTO and SUSUMU GOTO. "Self-similar clustering of inertial particles in homogeneous turbulence". In: *Journal of Fluid Mechanics* 577 (Apr. 2007), p. 275. ISSN: 0022-1120. DOI: 10.1017/S0022112007004946. URL: http://www.journals.cambridge.org/abstract%7B%5C_%7DS0022112007004946.

[79] Leonid I Zaichik and Vladimir M Alipchenkov. "Statistical models for predicting pair dispersion and particle clustering in isotropic turbulence and their applications". In: *New Journal of Physics* 11.10 (2009), p. 103018.

[80] Qi Zhou and Nian-Sheng Cheng. "Experimental investigation of single particle settling in turbulence generated by oscillating grid". In: *Chemical engineering journal* 149.1 (2009), pp. 289–300.

This PhD thesis investigates the phenomena of preferential concentration and settling of sub-Kolmogorov inertial particles transported in a turbulent flow. To this end, experiments have been carried out in active-grid-generated turbulence in a wind-tunnel, seeded with water droplets. Preferential concentration manifests itself as the emergence of spatial segregation of the particles, which were initially homogeneously seeded in the carrier flow, leading to clusters and voids. A particular effort has been put in disentangling the roles of particles inertia, of turbulence and of collective effects on the emergence of clustering and the modification of settling velocity and in investigating the interplay between clustering and settling. Four main non-dimensional parameters have been varied to establish the role of each in the clustering process and on the settling of the particles: the Rouse number $Ro,$ representing the ratio of the settling velocity of the particles to the fluctuating velocity of the fluid ; the Stokes number St , quantifying particle inertia as the ratio of the particle response time to the flow dissipative time scale; the Reynolds number Re_λ representing the degree of turbulence and the volume fraction φ_v representing the concentration of the particles in the two-phase flow.

Two experimental techniques (Lagrangian Particle Tracking and Phase Doppler Interferometry) are used to acquire data and diagnose the clustering and settling properties of the dispersed droplets.

2D-Lagrangian Particle Tracking has been performed using high-speed visualization of the dispersed droplets in a laser sheet. This gives access to simultaneous statistics of particles spatial distribution and velocity. Clustering has been quantified using Voronoï tessellation and quantitative scalings on the dependency of clustering intensity and clusters dimensions on St, Re_λ and φ_v are found. They show a strong influence of, Re_λ and volume fraction φ_v but a weak effect of St. This finding is consistent with a leading role of the “sweep-stick” mechanism in the clustering process, as proposed by Vassilicos. Furthermore, conditional analysis of the velocities of particles within clusters and voids has been performed showing that clusters tend to settle faster than voids, pointing to the role of collective effects in the enhancement of settling.

Phase Doppler Interferometry has then been used to further analyse velocity statistics, and particle concentration field conditioned on particle diameter. Enhancement of the settling velocity for small diameters is observed, in agreement with previous studies. On the contrary, for larger particles settling velocity is found to be hindered. This indicates a subtle intrication of several possible mechanisms affecting the settling, including preferential sweeping, loitering and collective effects.

Cette thèse étudie les phénomènes de concentration préférentielle et de sédimentation de particules inertielles transportées dans un écoulement turbulent. Pour cela, des expériences ont été menées en soufflerie dans une turbulence engendrée en aval d’une grille active et ensemencée avec des gouttelettes d'eau. La concentration préférentielle se manifeste par la ségrégation spatiale des particules qui bien qu’initialement ensemencée de façon homogène, tendent à se regrouper en amas, laissant en déplétion d’autres zones de l’écoulement. Un effort particulier a été consacré à séparer les mécanismes liés à l’inertie des particules, à la turbulence et aux effets collectifs impactant la formation des amas et modifiant la vitesse de sédimentation des particules. Quatre principaux paramètres non-dimensionnels ont été variés afin d’établir le rôle spécifique de chacun d’entre eux sur les processus de concentration préférentielle et de sédimentation: le nombre de Rouse Ro, représentant le rapport de la vitesse de sédimentation des particules à la vitesse fluctuante de l’écoulement; le nombre de Stokes St quantifiant l'inertie des particules comme le rapport entre le temps de réponse des particules et le temps dissipatif de l’écoulement; le nombre de Reynolds Re_λ représentant le degré de turbulence et enfin la fraction volumique de la phase dispersée φ_v.

Deux techniques expérimentales (suivi Lagrangien des particules et interférométrie à phase Doppler) ont été utilisées pour l'acquisition des données et pour le diagnostic de la concentration préférentielle et de la sédimentation des gouttelettes dispersées.

Le suivi Lagrangien de particules a été réalisé par visualisation à haute vitesse cadence des gouttelettes dispersées dans une nappe de laser. Cela donne accès aux statistiques simultanées de la distribution spatiale des particules et de leur vitesse. Le niveau de clustering a été quantifié à l’aide de tessélation de Voronoï. Nous établissons des lois d’échelles quantitatives caractérisant la dépendance du degré de clustering et de la géométrie des amas en fonction des paramètres de l’étude St, Re_λ and φ_v. Ces lois d’échelles indiquent une forte influence de Re_λ et de φ_v, mais un faible effet de St. Ce résultat est cohérent avec un rôle dominant du mécanisme « sweep-stick » comme origine de la concentration préférentielle, tel que proposé par Vassilicos. En outre, l'analyse conditionnelle des vitesses de sédimentation des particules en fonction de leur appartenance ou non à des amas montre que les zones à fortes concentration tendent à sédimenter plus rapidement que les zones peu concentrées, suggérant un possible rôle des effets collectifs dans l’augmentation de la vitesse de chute.

Les mesures par interférométrie de phase Doppler ont ensuite permis d’analyser plus en détail les statistiques de vitesse et de concentration de particules conditionnées à la taille des particules. Ces mesures montrent une augmentation de la vitesse de sédimentation pour les particules de petits diamètres, en accord avec des études précédentes. En revanche, la sédimentation est ralentie pour les particules de plus grand diamètre. Ceci indique une subtile intrication de plusieurs mécanismes possibles affectant la sédimentation turbulente de particules.